

Theoretical Modelling in Electrochemistry

A thesis submitted for the degree of

Doctor of Philosophy

in Physical and Theoretical Chemistry

Haonan Le

St Cross College

University of Oxford

Trinity Term 2021

Abstract

In this thesis, the studies of diffusion and the electrochemical systems based on the modelling and simulation of chronoamperometry and cyclic voltammetry for various novel electrochemical systems are reported and discussed.

In Chapter 1, fundamental and essential concepts and theories in electrochemistry are introduced to provide key background information and to assist the understanding of the later chapters. Similarly, Chapter 2 outlines the introductory aspects for the methodologies of electrochemical modelling and simulation by using the finite difference method to discretise the diffusion equations, together with the methods used for validating and testing the simulations.

Chapter 3 and 4 present the introduction and application of a new physicochemical parameter characterising mass transport, the ”diffusion indicator”, which offers sensitive and comparable information about the changes and trends in chronoamperometric current responses in a simple and straightforward form by distinguishing the relative contributions from linear and convergent diffusion. Based on the analytical and modelling studies of electrochemical systems with four different electrode geometries (spheres, discs, cylinders, and bands), the concept of the diffusion indicator is developed and discussed in Chapter 3. Chapter 4 applies this new parameter to chronoamperometric studies of several cylindrical and ring electrodes, where the comparative studies of the diffusive flux of the analyte toward electrodes with similar but different geometries from different spatial locations are presented.

Chapter 5 discusses the theoretical studies for a particular system regarding the nano-impact method, which involves the electrochemical process of depleting the dopant inside a spherical particle after the particle collides with the electrode and is adsorbed

on the electrode surface. Two different theoretical models are adopted and utilised, and a dimensional analysis is presented.

Chapter 6 investigates the cyclic voltammetry of a reversible one-electron-transfer reaction at electrochemical systems with different electrode geometries. A polynomial equation is introduced to describe the forward peak potentials at different scan rates for an 'infinitely long cylinder' electrode. Together with literature equations, this introduced equation enables us to produce an evaluation of infinite cylinder approximation for other cylinder-like electrodes of finite length and where the cylinder ends contribute significantly to the net flux.

Chapter 7 applies the diffusion-equation-based simulations to an adsorbed-enzyme-mediated electrochemical system together with the theoretical analysis of cyclic voltammetric current responses on both flat and porous electrodes to understand the role of the Michaelis-Menten kinetics under both diffusional regimes and, in particular, to explore the role of nano-structure in the enzyme-based catalytic reaction. In this study, literature reports of the *apparent* potential dependent Michaelis constants are explained. Four classes of voltammograms are identified corresponding to qualitatively different current responses. The conditions under which porosity can usefully aid the electro-catalysis are determined providing a basis for scale-up of the enzyme-catalysed redox processes.

Acknowledgements

First and foremost, I would like to thank Prof. Richard G. Compton for his greatest support and guidance during my D.Phil. study. His extraordinary motivation, expertise, patience, kindness, and sense of humour have given the best experience of D.Phil. study I could ever hope to get. I have greatly benefited from his ways of thinking, working, and communicating. What I learned from him will be continuously helping and teaching me even after my D.Phil. study. Words cannot adequately express my gratitude to him, and I sincerely wish him great happiness and health from the bottom of my heart.

I would like to express my deep gratitude to Dr. Enno Kätelhön for kindly sparing a great amount of his time to teach me in both electrochemistry and programming.

It has been a pleasure and privilege to be in such a great group. I would like to thank Chuhong, Lifu, Xiuting, Chris for their kind guidance and help. I would also like to thank Ruochen, Jake, and Danlei for their helpful support and discussion. Thanks to everyone else in the group, including but not limited to Yuki, Crystal Jiao, Giorgia, Hatem, Bertold, Wallans, Azhar, Dia, Korbua, Alex, Hannah, Crystal Chan, Lihua, Yuqi, Xin, Ruiyang, Yuanzhe, Yanjun, Annie, Raphael, Yifei, Yuanyuan, Haotian, Archana, Junling, and Joe, for creating a friendly and heart-warming environment.

I would like to thank Unilever-St Cross Scholarship and the Great Britain-China Educational Trust for their financial support. I am also grateful to be a member of St. Cross college and Department of Chemistry at University of Oxford.

Last but not the least, I would like to thank my family, especially my parents. I could not enjoy my life and study here without their unconditional love and support. I would also like to express my thanks to my love, Kezi Yao, for her continuous love. You supported me in every aspects of my life. What a pleasure to be Dr. together with you!

Contents

Abstract ..... **i**

Acknowledgements ..... **iii**

Contents ..... **iv**

Chapter 1: Introduction **1**

1.1 Mass transport in electrochemistry 1

1.1.1 Sources for mass transport 1

1.1.2 Fick's laws 3

1.1.3 Diffusion layer 4

1.2 Electrochemical fundamentals 4

1.2.1 Electrochemical cell 4

1.2.2 The Nernst equation 6

1.3 Electroanalytical techniques 7

1.3.1 Chronoamperometry 8

1.3.2 Cyclic voltammetry 9

References 13

Chapter 2: Electrochemical Simulations **15**

2.1 Modelling of electrochemical systems 15

2.1.1 Diffusion equations 15

2.1.2 Boundary conditions 17

2.1.3 Dimensionless coordinates 18

2.2 Solution of diffusion equations 19

2.2.1 The finite difference method 19

2.2.2 Spatial derivatives 20

2.2.3 Time Derivatives 22

2.2.4 The Thomas Algorithm 23

2.3 Simulation of electrochemical processes 25

2.3.1 1D simulations 25
2.3.2 Non-uniform grids 25
2.3.3 2D simulations 26
2.3.4 Validation and convergence studies 28
References 29
Chapter 3: The Diffusion Indicator: Comparative Chronoamperometry 30
3.1 Introduction 30
3.2 Simulation methods 33
3.2.1 Simulation models 33
3.2.2 Dimensionless parameters 37
3.2.3 Expanding simulation grids 38
3.2.4 Computational Methods 39
3.3 Theoretical analyses 39
3.3.1 Microsphere electrode 39
3.3.2 Microdisc electrode 40
3.3.3 Microcylinder electrode 40
3.3.4 Microband electrode 41
3.4 Results and discussion 41
3.4.1 Literature analytical and empirical equations 42
3.4.2 Simulated concentration profiles 44
3.5 Conclusions 52
References 53
Chapter 4: The Diffusion Indicator: Microcylinder and Microring Electrodes .. 55
4.1 Introduction 55
4.2 Theoretical methods 56
4.2.1 Simulation models 56
4.2.2 Dimensionless parameters 63
4.2.3 Expanding simulation grids 64
4.2.4 Computational methods 65

4.3 Results and discussion 66
4.3.1 Testing numerical simulations 67
4.3.2 The ‘annular band’ electrode model 73
4.3.3 The cylinder electrode models 80
4.3.4 The ‘embedded ring’ electrode model 88
4.3.5 Physical insights 89
4.4 Conclusions 91
References 92
Chapter 5: Single-entity Electrochemistry: Diffusion inside a Particle 95
5.1 Introduction 95
5.2 Theoretical models 97
5.2.1 The ‘truncated-sphere’ model 99
5.2.2 The ‘undeformed-sphere’ model 100
5.2.3 Dimensionless parameters 102
5.2.4 Computational methods 103
5.3 Results and discussion 104
5.3.1 Testing numerical simulations 104
5.3.2 The ‘truncated-sphere’ model 109
5.3.3 Comparison between two models 114
5.3.4 Dimensional analysis and fitting parameters 116
5.4 Conclusions 120
References 121
Chapter 6: Reversible Cyclic Voltammetry at Cylindrical Electrodes 124
6.1 Introduction 124
6.2 Theory and simulation 126
6.2.1 Theoretical models 126
6.2.2 Dimensionless parameters 131
6.2.3 Simulation grids 132
6.2.4 Computational methods 134

6.3 Results and discussion 134
6.3.1 Testing numerical simulations 134
6.3.2 The ‘infinitely long cylinder’ electrode model 143
6.3.3 Determining minimum values of *L* 150
6.3.4 The ‘annular band’ electrode model 151
6.3.5 The ‘full cylinder’ electrode model 154
6.4 Conclusions 156
References 157
Chapter 7: Electrochemical Processes Mediated via Adsorbed Enzymes: Flat and Porous Electrodes Compared. 160
Understanding Nano-confinement. 160
7.1 Introduction 160
7.2 Theory 163
7.2.1 The ‘Non-Porous Immobilised-Enzyme’ Model 163
7.2.2 The ‘Nanopore’ Model 168
7.2.3 Computational Methods 170
7.2.4 Simulation Grids 171
7.2.5 Calculations of parameters for the ‘Nanopore’ model 172
7.3 Results and Discussion 173
7.3.1 Testing Numerical Simulations 173
7.3.2 The ‘Non-Porous Immobilised-Enzyme’ Model 179
7.3.3 The ‘Nanopore’ Model 189
7.3.4 A Comparison of Flat and Nano-Porous Electrodes: Appreciating the Role of Nanoporosity and Optimising Substrate Conversion to Product 194
7.4 Conclusions 200
References 201
Appendices 204
A. Simulation Grids 204
A.1 Expanding time grids 204

A.2 Expanding space grids 204
B. Testing and Validating Simulations 205
B.1 Errors of mass conservation 205
B.2 Convergence studies 205
C. Supplementary Figures for Chapter 7 206

Chapter 1: Introduction

In this chapter, an overview of the essentials in the study of diffusion is presented together with the fundamental concepts, theories, and techniques of electrochemistry, which together provide important background information for later chapters of this thesis. Readers are referred to two introductory textbooks, *Understanding Voltammetry* [1] and *Electrochemical Methods: Fundamentals and Applications* [2] for more comprehensive and detailed guidance in these research areas.

1.1 Mass transport in electrochemistry

The transport of electrochemically active species from the bulk solution to the electrode-solution interface is of particular interest in electrochemistry as the mass transport determines, together with the electrode kinetics, the rates at which redox reactions happen at the surface of the electrode [1, 2].

First, three types of mass transport in a typical electrochemical system are introduced. Then a detailed background on the studies of diffusion processes in the electrochemical systems is discussed as, in an electrochemical system well-supported by electrolytes, the diffusion contributes to the major part of the total mass transport due to the dominance of pure Brownian motion in the corresponding mass transport processes [1].

1.1.1 Sources for mass transport

There are three sources for the mass transport for the electrochemically active species in the bulk solution: diffusion, migration, and convection [1, 2]. The total mass transfer flux, $j_T(x)$, at spatial point x can be described by the *Nernst-Planck equation* [2] along the x-axis for a one-dimensional system:

$$j_T(x) = -D_i \frac{\partial c_i(x)}{\partial x} - \frac{z_i F}{\boldsymbol{RT}} D_i c_i \frac{\partial \phi(x)}{\partial x} + v(x) c_i \qquad (1.1)$$

where D_j, c_j, z_j are the diffusion coefficient, concentration, and charge of species i, respectively. F is the Faraday constant, $\boldsymbol{R}$ is the universal gas constant, $\boldsymbol{T}$ is the temperature, $\phi(x)$ is the potential at spatial point x, and $v(x)$ is the velocity with which a volume element in solution moves at spatial point x. The three terms on the right-hand side represent the flux components of diffusion, migration, and convection, respectively.

Diffusion refers to the process where the analytes move spontaneously from a high-concentration zone toward a low-concentration zone due to the Brownian motion [3]. The diffusion processes can be well-described by Fick's First and Second Laws which depict the diffusion by relating the changes in concentration to space and time [4, 5]. More details about the model of diffusion are presented in the next section.

Migration represent the phenomenon where the electrochemically active species moves to/from the electrode because of the external electrical field according to the signs of their respective charges [1]. To minimise the influence of migration, an excess of supporting electrolyte consisting of non-electroactive ions whose concentrations are high enough should be used to compress the interfacial potential drop to a very low level. This enable us to neglect the migratory term in Eqn (1.1) due to the trivial value of $\frac{\partial \phi(x)}{\partial x}$ at the electrode surface. It is worth noting that the supporting electrolyte also decreases the resistance of the solution which minimises the undesirable potential drop between the working electrode and the reference electrode.

Convection describes the movement rendered by addition forces such as thermal convection, stirring, or magnetic forces [1]. Therefore, additionally attention should be paid in experiments to keeping the experimental conditions constant such as maintaining a constant temperature, minimising system vibration, and using a Faraday cage by reducing the influence of $v(x)$ in the third term in Eqn (1.1). Notwithstanding, in the theoretical researches in this thesis, convection is considered to be negligible.

As discussed above, diffusion is assumed to be the only source of the mass transport in all theoretical models investigated in this thesis. It is worth noting that neglecting migration and convection could result in the difficulties in the analysis of current responses and the comparison between the simulated results and the experimental data. Migration effect usually take place near to the electrode surface and influence the current responses at shorter timescales while convection usually have an impact on the current responses at longer timescales [1, 2, 6, 7]. However, by comparing between the simulated results and the experimental data, the effects of migration and convection could potentially be studied in the future using the diffusion indicator introduced later.

1.1.2 Fick's laws

As mentioned in the previous section, Fick's First and Second Laws are used in this thesis to depict the diffusion processes [4, 5]. By applying an analogy to the heat equation to diffusion processes, Fick's First Law gives the proportional relationship between the diffusive flux of the analyte and the concentration gradient of the analyte with the diffusion coefficient *D* of the analyte:

$$j = -D\frac{\partial c}{\partial x} \tag{1.2}$$

where *j* is the flux of the analyte, and $\frac{\partial c}{\partial x}$ is the concentration gradient. Note the negative sign rise from the fact that the diffusive flux occurs down the concentration gradient.

Fick's Second Law further relates the temporal evolution of the analyte concentration to the spatial gradient of the concentration:

$$\frac{\partial c}{\partial t} = D\nabla^2 c \tag{1.3}$$

where *c* is the analyte concentration at a certain space point, and *t* is the time. ∇ is the vector operator related to the coordinate system chosen. Specific diffusion equations are introduced in later sections for corresponding models.

1.1.3 Diffusion layer

According to the diffusion model above, the diffusive distance from a certain point to an area around increases as the diffusive time proceeds. It was described by Einstein that the probability density of species evolves with time due to Brownian motion [8]. Furthermore, the root-mean-square displacement *x* of an analyte particle corresponds to the diffusion coefficient *D* and diffusive time *t* in a one-dimensional system:

$$\sqrt{|x^2|} = \sqrt{2Dt} \tag{1.4}$$

which suggests the size of thickness δ ($\sqrt{|x^2|}$) of the *diffusion layer* or *diffusion domain* of the diffusion of the analyte to/from the electrode surface in electrochemical processes. Later in the simulations of the selected models, an excessively large spatial spaces are chosen to ensure the systems are not influenced by the limitation of the simulation areas.

1.2 Electrochemical fundamentals

To present the studies of the diffusive processes using electrochemical methods, it is necessary to introduce some basic concepts in electrochemistry in this section.

1.2.1 Electrochemical cell

As illustrated in Figure 1.1, an electrochemical cell often consists of the electrolyte and three electrodes: the working electrode, the reference electrode, and the counter electrode [1, 2]. The electrolyte refers to charged species in the solution phase that does not interfere with the electrochemical reaction of interest, but provides the conductivity for the bulk solution. The concentration of electrolyte is kept at a sufficiently high level for the models in this thesis, as discussed above, to prevent any influence of migration [9, 10].

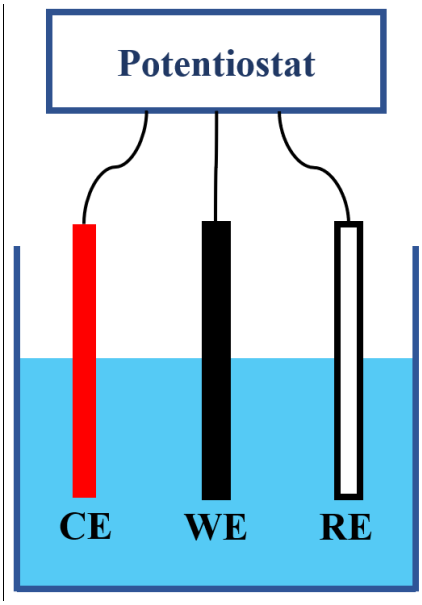


Figure 1.1: Illustrations of a typical electrochemical cell. Black: working electrode (WE), white: reference electrode (RE), and red: counter electrode (CE).

The working electrode (WE) is the electrode where a potential with respect to the reference electrode (RE) is applied to drive the current. The RE is designed with a known electrochemical equilibrium kept at a stable potential, e.g. a standard hydrogen electrode (SHE), a saturated calomel electrode (SCE), or a silver/silver chloride electrode [2]. The applied potential *E* between the WE and the RE is distributed as:

$$E = (\phi_e - \phi_s) + IR - (\phi_e^r - \phi_s^r) \tag{1.5}$$

where ϕ represents the electrical potential. The term ϕ_e is the potential of the WE and the term ϕ_s is the potential of the solution close to the WE. ϕ_e^r and ϕ_s^r are the electrical potentials of the RE and of the solution adjacent to it respectively. The *IR* term results from the passage of a current, *I*, through the electrical resistance of the bulk solution. It is worth noting that there is no current passing through the RE. There are two reasons for this of which the first is to maintain the fixed potential for the RE. Second, no current flowing leads to the fact that the *IR* term in Eqn (1.5) is reduced which ensures that changes in *E* reflect the changes in the potential drop $(\phi_e - \phi_s)$ at the WE, which drives the electron transfer.

The counter electrode (CE) is utilised for the propose of completing the electrical

circuit in the electrochemical system, which often take advantage of conductive but inert materials such as a platinum or graphite electrode to minimise the influence of the reaction at the CE [11]. The current induced to flow at the WE passes through the CE rather than the RE.

1.2.2 The Nernst equation

An electrochemical reaction refers to the process where a charge transfer occurs between the electrochemically active species and the electrode as a potential is applied on the WE [1, 2]. A simple one-electron-transfer electrochemical equilibrium reaction between *A* and *B* is considered:

$$A^{z_A}(aq) \pm e^- \leftrightharpoons B^{z_B}(aq) \tag{1.6}$$

where the z_A and z_B are the charges for species *A* and *B*.

The chemical potential, μ_j, of each species can be expressed be the gradient between its Gibbs energy (G_j) and its molar amount (N_j):

$$\mu_j = \frac{\partial G_j}{\partial N_j} \tag{1.7}$$

Thus, the chemical potential for species in solution can be rewritten as:

$$\mu_j = \mu_j^0 + \boldsymbol{RT} \ln \frac{\gamma_j c_j}{c^0} \tag{1.8}$$

where $\boldsymbol{R}$ is the gas constant, $\boldsymbol{T}$ is the temperature, μ_j^0 is the standard chemical potential, γ_j is the activity coefficient, and c^0 is the standard concentration which often takes the value of 1 $mol{\cdot}L^{-3}$.

In the case of an electrochemical reaction, the electrical potential of the solution and the electrode are further considered to give the electrochemical potential $\bar{\mu}_j$:

$$\bar{\mu}_j = \mu_j + z_j F \phi \tag{1.9}$$

where *F* is the Faraday constant.

If and when an equilibrium is reached, the net Gibbs energy of Eqn (1.6) is zero, which leads to the balance in the chemical potential:

$$\bar{\mu}_A + \bar{\mu}_{e^-} = \bar{\mu}_B \tag{1.10}$$

which, combined with Eqn (1.9), gives:

$$(\mu_A + z_A F\phi_s) + (\mu_{e^-} - F\phi_e) = (\mu_B + z_B F\phi_s) \tag{1.11}$$

Therefore, the interfacial potential difference is:

$$\phi_e - \phi_s = \frac{1}{F}(\mu_A^0 + \mu_{e^-} - \mu_B^0) + \frac{\boldsymbol{RT}}{F} \ln\left(\frac{\gamma_A c_A}{\gamma_B c_B}\right) \tag{1.12}$$

Furthermore, since the measured potential difference between WE and RE is:

$$E = (\phi_e - \phi_s) - (\phi_e^r - \phi_s^r) \tag{1.13}$$

as discussed in Eqn (1.5), combining Eqn (1.11) and Eqn (1.12) gives:

$$E = \frac{\mu_A^0 + \mu_{e^-} - \mu_B^0}{F} + \frac{\boldsymbol{RT}}{F}\ln\left(\frac{\gamma_A}{\gamma_B}\right) - (\phi_e^r - \phi_s^r) + \frac{\boldsymbol{RT}}{F} \ln\left(\frac{c_A}{c_B}\right) \tag{1.14}$$

while representing the sum of the standard values using standard potential E^0:

$$E^0 = \frac{1}{F}(\mu_A^0 + \mu_{e^-} - \mu_B^0) - (\phi_e^r - \phi_s^r) \tag{1.15}$$

and including the activity coefficients γ_A and γ_B for analyte *A* and *B*, respectively, using the standard formal potential E_f^0:

$$E_f^0 = E^0 + \frac{\boldsymbol{RT}}{F}\ln\left(\frac{\gamma_A}{\gamma_B}\right) \tag{1.16}$$

Therefore, the measurement of the potential becomes:

$$E = E_f^0 + \frac{\boldsymbol{RT}}{F}\ln\left(\frac{c_A}{c_B}\right) \tag{1.17}$$

which is a commonly used form of the Nernst equation.

1.3 Electroanalytical techniques

In electrochemical analysis, there are two major tools: amperometry and voltammetry [1, 2]. The chronoamperometric studies performed in this thesis refers to

the electrochemical analysis processes where, after applying a constant level of potential, the current on the WE is measured with respect to the reaction time. Alternatively, voltammetry utilises potential scanning over a certain range and measure the current in the meantime. In this section, these two methodologies are introduced.

1.3.1 Chronoamperometry

Considering investigating via chronoamperometry on the forward reducing reaction of Eqn (1.6), there is assumed only species *A* in the solution phase at the beginning of the chronoamperometric process. As shown in Figure 1.2(a), a constant potential E_0 is applied after t_0, which leads to a current measured at the WE. It is worth noting that the absolute value of E_0 is set to be the sufficiently large in order to resemble a diffusion-controlled electrochemical reaction by minimise any kinetic limitation. Therefore, the chronoamperometry enables insights for the diffusion to/from the electrode surface.

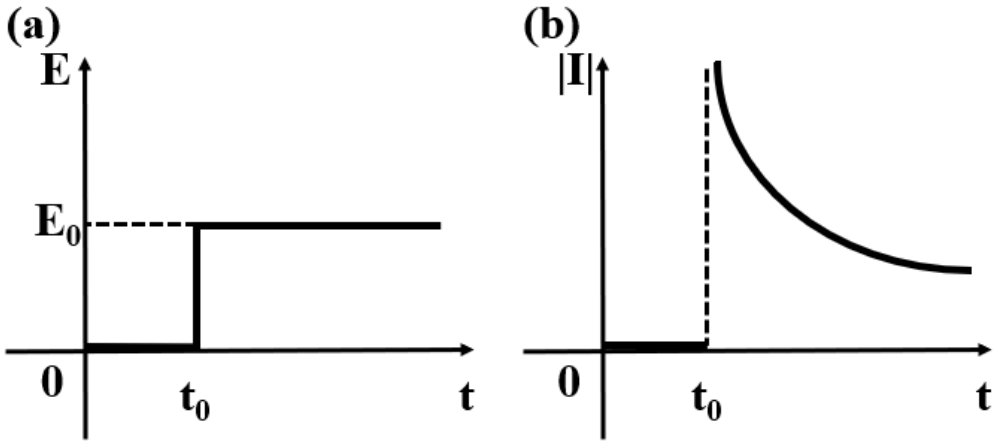


Figure 1.2: Illustrations of a typical potential applied at the electrode (a) and current response measured (b) in chronoamperometry.

Figure 1.2(b) illustrates a typical current response in chronoamperometry. The current experiences an extremely high value as the potential is initially applied to the WE, which results from the relatively high amount of analyte concentration around the electrode surface. As time proceeds, the value of current decreases rapidly due to the depletion of the analyte around the electrode surface.

For a planar macroelectrode, the chronoamperometric current follows the Cottrell equation [12] for a one-electron-transferred electrochemical reaction:

$$I = Fc^*A\sqrt{\frac{D}{\pi t}} \tag{1.17}$$

where c^* is the initial concentration of the analyte, and A is the area of the electrochemically active surface. It is worth noting that, at time beyond approximately tens of seconds, the solution is well mixed beyond the 'critical distance' δ shown in Eqn (1.4) due to the 'natural convection' - the movement resulted from density differences, which leads to a constant concentration for the bulk solution [1] and a non-zero current unlike the prediction of Eqn (1.18).

Unlike a macroelectrode, depending on the geometries of microelectrode, a steady state or quasi-steady state for the current response will be reached [13-17]. The steady/quasi-steady states regarding different electrode geometries are studied and discussed in Chapter 3 and 4.

Chronoamperometry has been well-developed and provides the basis for significant analytical tools such as the nano-impact method [18-21], where transient current spikes can be detected in presence of electrochemically active nanoparticles in the solution phase. In Chapter 5, the diffusion inside a spherical particle is studied based on the nano-impact method.

1.3.2 Cyclic voltammetry

Cyclic voltammetry is the major electroanalytical tool. In consideration of electrochemical reaction shown in Eqn (1.6) with an oxidising forward reaction, cyclic voltammetry is performed by scanning the potential over a certain range in a forward and then a reverse sweep [1, 2].

In Figure 1.3, the temporal evolution of potential applied on the electrode are

illustrated. The scanning of potential starts from a large negative level (E_{ini}) exceeding the formal potential of analyte *B* to a large positive level (E_{rev}) above the formal potential of *A* before scanning back to the negative starting level.

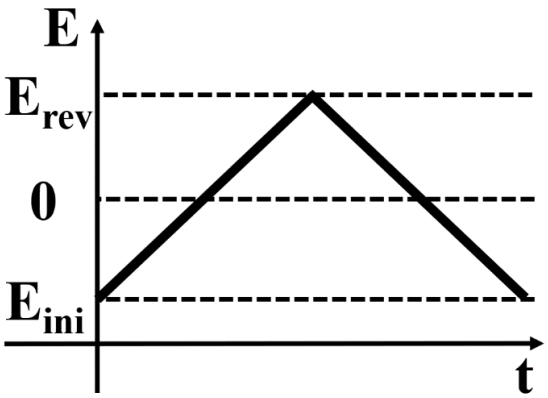


Figure 1.3: Illustrations of a typical potential applied at the electrode in cyclic voltammetry.

The cyclic voltammograms are often described as either 'reversible' or 'irreversible' depending on the relative speed of the electron transfer kinetics k_0 relative to the rate of mass transport. The size of the mass transport coefficient relative to k_0, is utilised here to classify the reversibility of an electrochemical reaction, and defined as [1]:

$$m_T = \frac{D}{\delta} \tag{1.19}$$

where δ is the diffusion layer thickness. By comparing with m_T, an electrochemical reaction is regarded as 'reversible' (for $k_0 >> m_T$) and 'irreversible' (for $k_0 << m_T$). As the scan time *t* is defined as:

$$t \sim \frac{\boldsymbol{RT}}{F\nu} \tag{1.20}$$

which, combined with Eqn (1.4) and (1.20), gives the relationship between m_T and *v*:

$$m_T \sim \sqrt{\frac{FD\nu}{\boldsymbol{RT}}} \tag{1.21}$$

Furthermore, Matsuda and Ayabe [22] introduced a parameter, Λ, to provide more detailed and experimentally feasible classification for the reversibility for an electrochemical reaction at a planar macroelectrode:

$$\Lambda = \frac{k_0}{\sqrt{FD\nu/\boldsymbol{RT}}} \tag{1.22}$$

with which the reversibility can be categorised as 'reversible':

$$\Lambda \geq 15 \; and \; \Lambda \geq 0.3\sqrt{\nu} \; (cm/s) \tag{1.23}$$

'quasi-reversible':

$$15 > \Lambda > 10^{-3} \; and \; 0.3\sqrt{\nu} > \Lambda > 2 \times 10^{-5}\sqrt{\nu} \; (cm/s) \tag{1.24}$$

, and 'irreversible':

$$\Lambda \leq 10^{-3} \; and \; \Lambda \leq 2 \times 10^{-5}\sqrt{\nu} \; \; (cm/s) \tag{1.25}$$

In practice, the reversibility of a cyclic voltammogram markedly influences the forward peak current I_p and the peak-to-peak separation ΔE_{PP} in the current-potential plot. The forward peak currents for the reversible and irreversible systems are described by the Randles-Ševčík equations [23, 24] for a one-electron process:

$$I_p = 0.446FAc^* \sqrt{\frac{FD\nu}{\boldsymbol{RT}}} \tag{1.26}$$

$$I_p = 0.496FAc^* \sqrt{\alpha} \sqrt{\frac{FD\nu}{\boldsymbol{RT}}} \tag{1.27}$$

where α is the transfer coefficient. As for the peak-to-peak separation, a measurement of 57/n *mV* at 298 *K* for the potential different between the forward and the backward peak currents is shown for the cyclic voltammogram, as k_0 increases to the range of reversible electrochemical reaction [1]. As k_0 decreases to the quasi-reversible region and the irreversible region, ΔE_{PP} increases to a larger value according to [1]:

$$\Delta E_{PP} = \frac{\boldsymbol{RT}}{\alpha F} \ln \nu + C \tag{1.28}$$

where *C* is a constant.

For the electrochemical reaction $A - e^- \rightarrow B$, only analyte *A* is usually present in the bulk solution at the beginning of a reversible cyclic voltammogram as shown in Figure 1.4(a), and no oxidation of *A* happens at relatively negative potentials. As the potential

proceeds to more positive potentials, the oxidation of *A* starts to occur. The electrode reaction starts to be fully driven when *E* is close to E_f^0. Then, the depletion of analyte around the electrode and the limitation of diffusion starts to influence the current response, which leads to the forward peak of the cyclic voltammogram before the current decay to the diffusion-limited current.

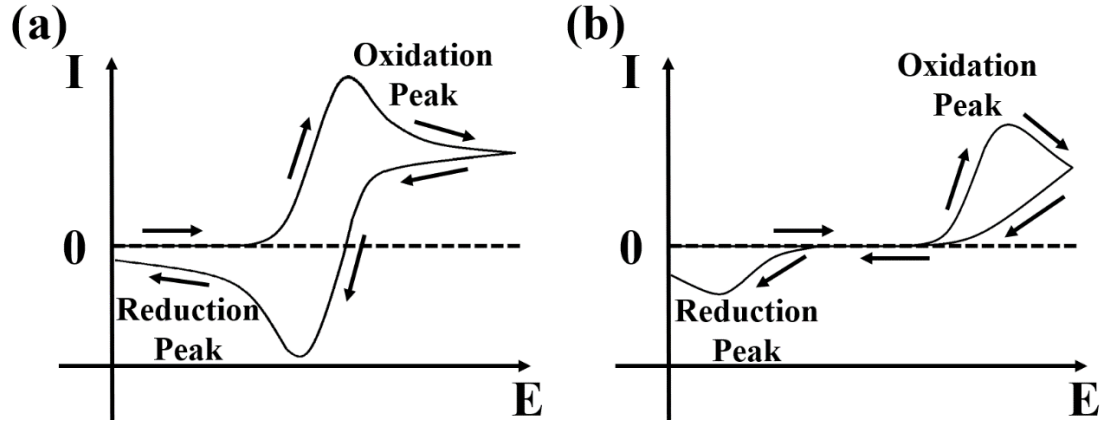


Figure 1.4: Illustrations of (a) reversible or (b) irreversible cyclic voltammetric currents.

As the potential starts to scan back to more negative levels, the current starts to move to the negative side as the reduction of species *B* takes place. Similar to the previous forward scan, the combination of electrode kinetics and diffusion of species *B* leads to the backward peak before the current decays to zero.

In terms of the irreversible voltammetry, as shown in Figure 1.4, the difference, comparing to its reversible counterpart, is that it requires larger overpotential to drive the reactions, which results in bigger ΔE_{PP}, and the values of peak currents also decreases as the electrode kinetics gets slower.

In Chapter 6, 'reversible' cyclic voltammograms, with relatively 'fast' electrode kinetics, for different electrode geometries are investigated. Cyclic voltammetry are studied in Chapter 7 for the immobilised-enzyme-mediated electrochemical reactions.

References

[1] R. G. Compton and C. E. Banks, *Understanding Voltammetry* (3rd Edition). London, World Scientific Press, **2018**.

[2] A. J. Bard and L. Faulkner, *Electrochemical Methods: Fundamentals and Applications*. John Wiley and Sons, **2001**.

[3] D. T. Gillespie and E. Seitaridou, *Simple Brownian Diffusion*. Oxford University Press, **2012**.

[4] A. Fick, *The London, Edinburgh, and Dublin Philosophical Magazine and Journal of Science*, **1855**, *10*, 30-39.

[5] J. Philibert, 'Adolf Fick and diffusion equations', in *Diffus. Solids - Past, Present Futur.*, **2006**, *249*, 1-6.

[6] C. M. A. Brett, A. M. O. Brett, *Electrochemistry: Principles, Methods, and Applications*, Oxford University Press, **1993**.

[7] F. Scholz, *Electroanalytical Methods*, Springer-Verlag Berlin Heidelberg, **2010**.

[8] A. Einstein, *Annalen der Physik*, **1905**, *322*, 549-560.

[9] D. H. Evans, K. M. O'Connell, R. A. Petersen, M. J. Kelly, *Journal of Chemical Education*, **1983**, *60*, 290.

[10] C. Amatore, A. Oleinick, I. Svir, *Analytical Chemistry*, **2008**, *80*, 7947–7956.

[11] N. Elgrishi, K. J. Rountree, B. D. McCarthy, E. S. Rountree, T. T. Eisenhart, J. L. Dempsey, *Journal of Chemical Education*, **2018**, *95*, 197–206.

[12] F. G. Cottrell, *Zeitschrift für Physikalische Chemie*, **1903**, *42*, 385.

[13] K. Aoki, J. Osteryoung, *Journal of Electroanalytical Chemistry*, **1981**, *122*, 19–35.

[14] D. Shoup, A. Szabo, *Journal of Electroanalytical Chemistry*, **1982**, *140*, 237–245.

[15] S. Coen, D. K. Cope, D. E. Tallman, *Journal of Electroanalytical Chemistry*, **1986**, *215*, 29–48.

[16] P. M. Kovach, W. L. Caudill, D. G. Peters, R. M. Wightman, *Journal of Electroanalytical Chemistry*, **1985**, *185*, 285–295.

[17] A. Szabo, D. K. Cope, D. E. Tallman, P. M. Kovach, R. M. Wightman, *Journal of Electroanalytical Chemistry*, **1987**, *217*, 417–423.

[18] K. Shimizu, K. Tschulik, and R. G. Compton, *Chem. Sci.*, **2016**, *7*, 1408-1414.

[19] L. Tian, X. Yan, and X. Chen, *ACS Catal.*, **2016**, *6*, 5441-5448.

[20] R. Tantra, *Nanomaterial Characterization: An Introduction*. Wiley VCH Verlag GmbH & Co. KGaA, **2016**.

[21] W. J. Stark *Angew. Chemie Int. Ed.*, **2011**, *50*, 1242-1258.

[22] H. Matsuda, Y. Ayabe, *Zeitschrift für Elektrochemie Berichte der Bunsengesellschaft für physikalische Chemie*, **1955**, *59*, 494–503.

[23] J. E. B. Randles, *Trans. Faraday Soc.*, **1948**, *44*, 327–338.

[24] A. Ševcík, *Collect. Czech. Chem. Commun.*, **1948**, *13*, 349–377.

Chapter 2: Electrochemical Simulations

The main investigative method used in this thesis is the simulation of electrochemical processes, such as chronoamperometry and cyclic voltammetry as introduced in the previous chapter. Therefore, it is necessary to discuss the basic concepts and theories for the electrochemical simulations used in this thesis before showing the research details and results. Readers are also referred to an introductory textbook, *Understanding Voltammetry: Simulation of Electrode Processes* [1] for further detailed guidance in electrochemical simulation.

2.1 Modelling of electrochemical systems

As discussed in the former chapter, the mass transport in the electrochemical processes of interest in this thesis is assumed to be dominated by diffusion. The most common way to tackle the modelling and simulating of diffusion processes in electrochemical systems is to solve the diffusion equation presented by Fick's Second Law introduced in the previous chapter [1]. By applying numerical methods to solve the diffusion equation, which is in the form of a second-order partial differential equation (PDE), often with a focus on the boundary conditions, the electrochemical processes can be modelled and simulated for various electrode geometries using various time and space ranges to resemble different electrochemical systems of interests [2-5]. In this section, the basic aspects of modelling an electrochemical system are introduced.

2.1.1 Diffusion equations

Following the introduction in the former chapter, Fick's Second Law presents the prediction of the temporal evolution of the species concentration according to the spatial double derivative of the analyte concentration:

$$\frac{\partial c}{\partial t} = D\nabla^2 c \tag{2.1}$$

where c is the analyte concentration at a certain space point, and t is the time. ∇ is the vector operator related to the coordinate system chosen. For example, in Cartesian coordinates, Eqn (2.1) can be rewritten as:

$$\frac{\partial c}{\partial t} = D\left(\frac{\partial^2 c}{\partial x^2} + \frac{\partial^2 c}{\partial y^2} + \frac{\partial^2 c}{\partial z^2}\right) \tag{2.2}$$

where D is the diffusion coefficient, and x, y, and z are the spatial distances in the X-, Y-, and Z-axes, respectively. In practice, the diffusion equation can also be rewritten in other coordinates, such as cylindrical or spherical coordinates which are discussed and utilised in the following chapters. To present a simple and straightforward illustration of the modelling and simulating of an electrochemical system in this section, a one-dimensional spatial system is employed first where the diffusion equation is:

$$\frac{\partial c}{\partial t} = D\left(\frac{\partial^2 c}{\partial x^2}\right) \tag{2.3}$$

The space and time grids for this electrochemical system are shown in Figure 2.1. There are n equally spaced points in the space grid and m equally spaced points in the time grid. The length of the solution phase x_{max} is set to be $\sqrt{6Dt_{max}}$ as discussed in the former chapter to prevent any influence of the outer boundary of the solution phase on the diffusive process [6].

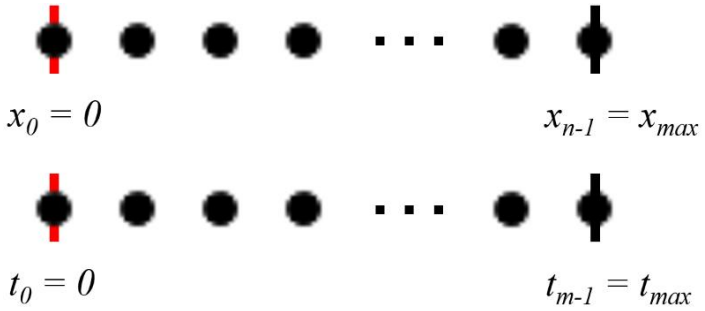


Figure 2.1: Illustrations of an electrochemical system with a uniform space grid with n space points representing the solution phase and a uniform time grid with m space points. x_0 and x_{n-1} are at the electrode and the far end of solution of the space grid, respectively. x_{max} is the length of the solution phase. t_0 and t_{m-1} are the starting and ending points of the time grid, respectively.

t_{max} is the length of the simulated period.

2.1.2 Boundary conditions

The spatial boundary conditions in the modelling are essential prerequisites in modelling any specific electrochemical process. The generic boundary conditions in this system are shown in Figure 2.2. The initial concentration of analyte *A* and *B* for all space points are set to *c** and *0*, respectively. Throughout the simulation, the concentration of analyte *A* at the electrode surface are fixed to follow the electrode kinetics *f*(*E*) for the specific electrochemical process. The outer boundary of the solution phase is set to be a no-flux boundary. In the following chapters where a number of different systems are investigated, the detailed boundary conditions are defined before the results and discussion are presented.

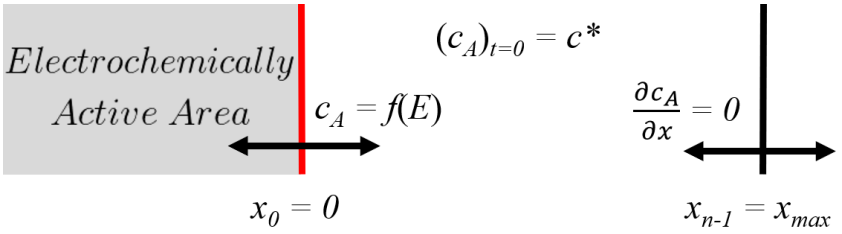


Figure 2.2: Illustration of the boundary conditions for a one-dimensional system. The red line represents the electrode surface, *f*(*E*) represents the electrode kinetics, and *c** is the initial concentration set for analyte *A*.

According to the Fick's First Law introduced in the previous chapter, the diffusive flux *j* for a species at a certain point is:

$$j = -D\frac{\partial c}{\partial x} \tag{2.4}$$

Therefore, the current I_A of analyte *A* can be calculated from the flux j_A of *A* at the surface of the electrode:

$$I_A = F\boldsymbol{A}(j_A)_{x_0} = -FD_A\left(\frac{\partial c_A}{\partial x}\right)_{x_0} \tag{2.5}$$

where *F* is the Faraday constant, and $\boldsymbol{A}$ is the electrode area, which is 1 in this case, and D_A and c_A are the diffusion coefficient and concentration for analyte *A*, respectively.

2.1.3 Dimensionless coordinates

Before using mathematical tools to discretise this model and simulate electrochemical processes, it is necessary to normalise the parameters using in the system to obtain universal applicability under different experimental conditions and insightful comparability among different electrochemical system [1]. Therefore, by introducing the following transformation from dimensional parameters to their dimensionless counterparts for any species j,

$$C_j = \frac{c_j}{c^*} \tag{2.6}$$

$$d_j = \frac{D_j}{D_A} \tag{2.7}$$

$$X = \frac{x}{\epsilon} \tag{2.8}$$

$$T = \frac{D_A t}{\epsilon^2} \tag{2.9}$$

$$\theta = \frac{F}{\boldsymbol{RT}}(E - E_f^0) \tag{2.10}$$

$$\sigma = \frac{\epsilon^2}{D_A}\frac{F}{\boldsymbol{RT}}\nu \tag{2.11}$$

where concentration c_j is normalised against the initial concentration of analyte A (c^*), the diffusion coefficient D_j is normalised against the diffusion coefficient of analyte A (D_A), and the spatial length x is normalised by a chosen length ϵ, which is normally the radius of a microdisc electrode or the width of a microband electrode. ϵ can be set to 1 in this section for the needs of this example. T is defined as the dimensionless time, θ is the dimensionless potential, F is the Faraday constant, $\boldsymbol{R}$ is the gas constant, $\boldsymbol{T}$ is the temperature, E is the dimensional potential, E_f^0 is the standard formal potential of the target redox reaction, σ is the dimensionless scan rate of the applied potential, and ν is the dimensional scan rate. Therefore, the dimensionless form of Eqn (2.3) is:

$$\frac{\partial C_j}{\partial T} = d_j\left(\frac{\partial^2 C_j}{\partial X^2}\right) \tag{2.12}$$

for species *j*, and the current calculation in Eqn (2.5) becomes:

$$I_A = \frac{F D_A c^*}{\epsilon}\left(-\frac{\partial C_A}{\partial X}\right)_{X=0} \tag{2.13}$$

The specific dimensionless parameters for other problems are defined carefully in the following chapters together with the detailed presentation of dimensionless diffusion equations and current calculations.

2.2 Solution of diffusion equations

After an essential introduction of definition and modelling, the further basis of the computational simulation of temporal evolution of the currents in diffusion processes is based on solving the diffusion equations introduced above. In this one-dimensional system, to solve Eqn (2.12), it can be realised by discretising the time and space grids and approximating the first derivative of C_j against T and the second derivative of C_j against X through the discretised grids in the light of the advances of computational methodologies and devices.

2.2.1 The finite difference method

The finite difference method (FDM) [1] is widely employed in various studies to solve the partial differential equations (PDE) in different electrochemical systems. This is due to its high time- and computing efficiency, together with the ease of implementing and manipulating the simulation codes. These enable deeper understanding of the subtle changes of the simulation systems as a single parameter or feature is varied. Therefore, all studies in this thesis utilised FDM to solve the PDEs and hence simulate various electrochemical processes. A discussion of the numerical basis of FDM on solving the diffusion equations follows.

2.2.2 Spatial derivatives

On solving Eqn (2.12), we first tackle the spatial derivative on the right-hand side. FDM approaches the derivative by discretising the grids. Thus, the first-order derivative for a space point X_i with the concentration C_i can be defined as the ratio of the variation in concentration to the variation in space:

$$\left(\frac{dC}{dX}\right)_{X_i} = \lim_{\Delta X \to 0}\left(\frac{C_{i+1} - C_i}{\Delta X}\right) \tag{2.14}$$

where, as defined before, the space grid is equally spaced, which means the spatial interval $\Delta X = X_{i+1} - X_i = X_i - X_{i-1}$.

We can approximate the derivative using the forward difference approximation:

$$\left(\frac{dC}{dX}\right)_{X_i} \approx \frac{C_{i+1} - C_i}{\Delta X} \tag{2.15}$$

The first-order derivative has three different approximation forms: the forward, the backward, and the central difference approximations [1] as shown in Figure 2.3 based on the positions and concentrations for the X_i point and its adjacent points X_{i-1} and X_{i+1}:

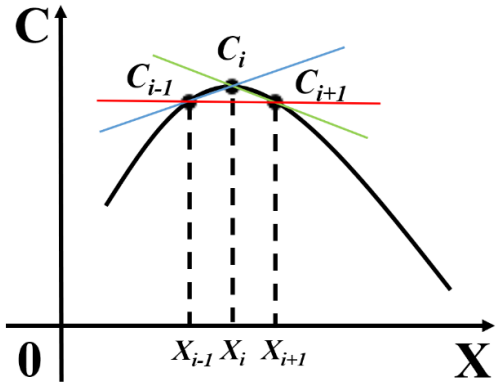


Figure 2.3: Illustrations of 3 difference approximations for the first-order spatial derivatives. The forward, backward and central differences are shown in green, blue and red lines.

The truncated error, Γ, for the forward difference approximation can be defined as:

$$\Gamma_{forward} = \left(\frac{dC}{dX}\right)_{X_i} - \frac{C_{i+1} - C_i}{\Delta X} \tag{2.16}$$

which can be further investigated by considering the Taylor Series expansion of the concentration C_{i+1}:

$$C_{i+1} = C_i + \Delta X \left(\frac{dC}{dX}\right)_{X_i} + \frac{(\Delta X)^2}{2!}\left(\frac{d^2C}{dX^2}\right)_{X_i} + \frac{(\Delta X)^3}{3!}\left(\frac{d^3C}{dX^3}\right)_{X_i} + \cdots \quad (2.17)$$

Therefore, the truncated error for the forward difference approximation can be rewritten:

$$\Gamma_{forward} = -\frac{\Delta X}{2!}\left(\frac{d^2C}{dX^2}\right)_{X_i} - \frac{(\Delta X)^2}{3!}\left(\frac{d^3C}{dX^3}\right)_{X_i} - \cdots \quad (2.18)$$

On observing Eqn (2.18), as ΔX is usually smaller than 1 by far, the first term dominates the truncated error, which can thus be written as $\Gamma_{forward} \propto \Delta X$.

Similarly, the backward difference approximation is:

$$\left(\frac{dC}{dX}\right)_{X_i} \approx \frac{C_i - C_{i-1}}{\Delta X} \quad (2.19)$$

Thus, the backward truncated error is:

$$\Gamma_{backward} = \frac{\Delta X}{2!}\left(\frac{d^2C}{dX^2}\right)_{X_i} - \frac{(\Delta X)^2}{3!}\left(\frac{d^3C}{dX^3}\right)_{X_i} + \cdots \quad (2.20)$$

which, similarly, is proportional to ΔX.

On the other hand, the central difference approximation is:

$$\left(\frac{dC}{dX}\right)_{X_i} \approx \frac{C_{i+1} - C_{i-1}}{2\Delta X} \quad (2.21)$$

where the central truncated error is the average of forward and backward truncated error:

$$\Gamma_{central} = -\frac{(\Delta X)^2}{3!}\left(\frac{d^3C}{dX^3}\right)_{X_i} - \frac{(\Delta X)^4}{5!}\left(\frac{d^5C}{dX^5}\right)_{X_i} - \cdots \quad (2.22)$$

which is instead proportional to $(\Delta X)^2$. Therefore, the central difference approximation is preferred for first-order derivative as the error is largely reduced comparing to the forward and backward difference approximations.

In term of the second-order derivative, the approximation can be realised by combining the forward and backward Taylor Series expansion of C_i:

$$C_{i+1} + C_{i-1} = 2C_i + \frac{2(\Delta X)^2}{2!}\left(\frac{d^2C}{dX^2}\right)_{X_i} + \frac{2(\Delta X)^3}{4!}\left(\frac{d^4C}{dX^4}\right)_{X_i} + \cdots \quad (2.23)$$

Therefore, the second-order derivative is:

$$\left(\frac{d^2C}{dX^2}\right)_{X_i} \approx \frac{C_{i+1} - 2C_i + C_{i-1}}{(\Delta X)^2} \tag{2.24}$$

with the truncated error:

$$\Gamma_{second} = -\frac{2(\Delta X)^2}{4!}\left(\frac{d^4C}{dX^4}\right)_{X_i} - \frac{2(\Delta X)^4}{6!}\left(\frac{d^6C}{dX^6}\right)_{X_i} - \cdots \tag{2.25}$$

which is again proportional to $(\Delta X)^2$. Therefore, this approximation is applied due to sufficiently small Γ_{second}.

2.2.3 Time Derivatives

The time derivative of the left-hand side of Eqn (2.12) is also realised by discretising the time grid. Based on the space and time grids shown in Figure 2.1, we represent the concentration at the space point *s* and the time point *k* as C_s^k. Based on a known C_s^k, the concentration of the next time point for the same space point can be obtained by the backward difference approximation:

$$\frac{\partial C}{\partial T} \approx \frac{C_s^k - C_s^{k-1}}{\Delta T} \tag{2.26}$$

which, combined with Eqn (2.24), give the discretised form of Eqn (2.12) for analyte:

$$\frac{C_s^k - C_s^{k-1}}{\Delta T} = \frac{C_{s+1} - 2C_s + C_{s-1}}{(\Delta X)^2} \tag{2.27}$$

which, depending on which time point used on the left-hand side, can be solved using one of two approaches: the explicit or implicit methods.

The explicit method uses the concentrations of the former time point to calculate the concentration of the present concentration:

$$\frac{C_s^k - C_s^{k-1}}{\Delta T} = \frac{C_{s+1}^{k-1} - 2C_s^{k-1} + C_{s-1}^{k-1}}{(\Delta X)^2} \tag{2.28}$$

which is a simple and straightforward method. However, it only shows conditional stability if $\lambda = \Delta T/(\Delta X)^2 < 0.5$ [7, 8].

The implicit method uses the concentrations of the present time point on the right-hand side of the equation:

$$\frac{C_s^k - C_s^{k-1}}{\Delta T} = \frac{C_{s+1}^k - 2C_s^k + C_{s-1}^k}{(\Delta X)^2} \tag{2.29}$$

which is more mathematically stable [1], though the only known concentration term is C_s^{k-1}. To apply the implicit method, a series of equations for the *n* space points should be extracted based on Eqn (2.29) to solve the *n* equations with unknown concentrations no more than *n*. In this thesis, the equation series are solved using the Thomas algorithm [1, 9] which will be introduced in the following section.

2.2.4 The Thomas Algorithm

Based on Eqn (2.29), the equations in the equation series can be rewritten as:

$$\alpha_s C_{s-1}^k + \beta_s C_s^k + \gamma_s C_{s+1}^k = \delta_s \tag{2.30}$$

where the coefficients are:

$$\alpha_s = -\lambda, \qquad \beta_s = 1 + 2\lambda, \qquad \gamma_s = -\lambda, \qquad \delta_s = C_s^{k-1} \tag{2.31}$$

On considering the boundary conditions shown in Figure 2.2, only the coefficients at the electrode surface and the outer boundary of the solution phase are different than the general term shown in Eqn (2.31):

$$\alpha_0 = 0, \qquad \beta_0 = 1, \qquad \gamma_0 = 0, \qquad \delta_0 = \frac{1}{1 + e^{-\theta}} \tag{2.32}$$

$$\alpha_{s-1} = 0, \qquad \beta_{s-1} = 1, \qquad \gamma_{s-1} = 0, \qquad \delta_{s-1} = 1 \tag{2.33}$$

and the set of coefficient equations can be rewritten in the form of a matrix calculation for matrix $\boldsymbol{A}$:

$$\boldsymbol{Ax} = \boldsymbol{b} \tag{2.34}$$

which, combined with Eqn (2.31), (2.32) and (2.33), gives:

$$\begin{pmatrix} \beta_0 & \gamma_0 & 0 & 0 & 0 & \cdots \\ \alpha_1 & \beta_1 & \gamma_1 & 0 & 0 & \cdots \\ 0 & \alpha_2 & \beta_2 & \gamma_2 & 0 & \cdots \\ & \ddots & \ddots & \ddots & \ddots & \\ \cdots & 0 & \alpha_{n-3} & \beta_{n-3} & \gamma_{n-3} & 0 \\ \cdots & 0 & 0 & \alpha_{n-2} & \beta_{n-2} & \gamma_{n-2} \\ \cdots & 0 & 0 & 0 & \alpha_{n-1} & \beta_{n-1} \end{pmatrix} \begin{pmatrix} C_0^k \\ C_1^k \\ C_2^k \\ \vdots \\ C_{n-3}^k \\ C_{n-2}^k \\ C_{n-1}^k \end{pmatrix} = \begin{pmatrix} C_0^{k-1} \\ C_1^{k-1} \\ C_2^{k-1} \\ \vdots \\ C_{n-3}^{k-1} \\ C_{n-2}^{k-1} \\ C_{n-1}^{k-1} \end{pmatrix} \tag{2.35}$$

where $\boldsymbol{A}$ is a tridiagonal matrix, and the matrix $\boldsymbol{x}$ is the target result for each time step. The Thomas algorithm approaches Eqn (2.35) based on the LU factorisation to decompose the matrix $\boldsymbol{A}$ into two matrices, $\boldsymbol{L}$ and $\boldsymbol{U}$:

$$\boldsymbol{A} = \begin{pmatrix} \beta_0' & 0 & 0 & 0 & 0 & \cdots \\ \alpha_1 & \beta_1' & 0 & 0 & 0 & \cdots \\ & \ddots & \ddots & \ddots & \ddots & \\ \cdots & 0 & 0 & \alpha_{n-2} & \beta_{n-2}' & 0 \\ \cdots & 0 & 0 & 0 & \alpha_{n-1} & \beta_{n-1}' \end{pmatrix} \begin{pmatrix} 1 & \gamma_0' & 0 & 0 & 0 & \cdots \\ 0 & 1 & \gamma_1' & 0 & 0 & \cdots \\ & \ddots & \ddots & \ddots & \ddots & \\ \cdots & 0 & 0 & 0 & 1 & \gamma_{n-2}' \\ \cdots & 0 & 0 & 0 & 0 & 1 \end{pmatrix} \tag{2.36}$$

where β_i' and γ_i' are modified coefficients. Thus, combined with Eqn (2.36), Eqn (2.34) can be rewritten as:

$$\boldsymbol{Ux} = \boldsymbol{L}^{-1}\boldsymbol{b} \tag{2.37}$$

Let $\boldsymbol{d} = \boldsymbol{L}^{-1}\boldsymbol{b}$, Eqn (2.37) can be rewritten as:

$$\begin{pmatrix} 1 & \gamma_0' & 0 & 0 & 0 & \cdots \\ 0 & 1 & \gamma_1' & 0 & 0 & \cdots \\ & \ddots & \ddots & \ddots & \ddots & \\ \cdots & 0 & 0 & 0 & 1 & \gamma_{n-2}' \\ \cdots & 0 & 0 & 0 & 0 & 1 \end{pmatrix} \begin{pmatrix} C_0^k \\ C_1^k \\ \vdots \\ C_{n-2}^k \\ C_{n-1}^k \end{pmatrix} = \begin{pmatrix} \delta_0' \\ \delta_1' \\ \vdots \\ \delta_{n-2}' \\ \delta_{n-1}' \end{pmatrix} \tag{2.38}$$

where δ_i' is a modified coefficient. Thus, γ_i' and δ_i' can be calculated as:

$$\gamma_i' = \begin{cases} \dfrac{\gamma_i}{\beta_i} & \text{for } i = 0 \\ \dfrac{\gamma_i}{\beta_i - \gamma_{i-1}'\alpha_i} & \text{for } i = 1, 2, \ldots, n-2 \end{cases} \tag{2.39}$$

$$\delta_i' = \begin{cases} \dfrac{\delta_i}{\beta_i} & \text{for } i = 0 \\ \dfrac{\delta_i - \delta_{i-1}'\alpha_i}{\beta_i - \gamma_{i-1}'\alpha_i} & \text{for } i = 1, 2, \ldots, n-1 \end{cases} \tag{2.40}$$

The target matrix *x* can be calculated via Eqn (2.39) and (2.40) by back substitutions:

$$C_i^k = \begin{cases} C'_{n-1} & \text{for } i = n-1 \\ \delta'_i - \gamma'_i C_{i+1}^k & \text{for } i = n-2, n-3, \dots, 0 \end{cases} \quad (2.41)$$

2.3 Simulation of electrochemical processes

After introducing the discretisation of the diffusion equations and the temporal evolution of concentrations, various electrochemical processes, such as cyclic voltammetry and chronoamperometry, can be simulated if the conditions of the electrochemical systems are known.

2.3.1 1D simulations

For the simulations of the potential step chronoamperometry for the 1D system described previously, the total simulation time T_{max} is freely chosen by the researcher. As introduced in the previous chapter, the length of the solution phase, X_{max}, is determined by T_{max}:

$$X_{max} = 6\sqrt{T_{max}} \quad (2.42)$$

and the current can be calculated by the concentration gradient at the electrode surface:

$$J = -\frac{C_1^k - C_0^k}{X_1 - X_0} \quad (2.43)$$

As for the simulations of the cyclic voltammetry for the 1D system, T_{max} depends on the initial potential $\underline{\theta_i}$, final potential θ_f, and scan rate σ:

$$T_{max} = \frac{2(\theta_f - \theta_i)}{\sigma} \quad (2.44)$$

and calculations of X_{max} and J are the same as Eqn (2.42) and (2.43).

2.3.2 Non-uniform grids

In the later chapters of this thesis, expanding time and space grids [1, 10] are adopted to reduce the simulation time. For chronoamperometry, the time and space grids can be both replaced by expanding grids. For the cyclic voltammetry, only the space grid is

typically set to be expanding because the time grid, in the cyclic voltammetry, depends on the scan rate of the potential applied, and the complexity of a cyclic voltammogram is generally higher than a chronoamperogram, where a general expanding time grid is not applicable. A typical expanding grid is a single expanding space grid:

$$X(i) = X(i-1) + dX \times \omega X^{i-1} \quad where \quad i \geq 1; X(i) \leq X_{max} \qquad (2.45)$$

where $X(i)$ is the dimensionless space length at the space grid point i as $X(0)$ is the starting space point of the simulation, dX is the dimensionless space step, ωX is the expanding factor of the space grid, and the X_{max} is the length of the space field. It is worth noting that at the last point of the whole simulation space, the length is rounded to X_{max}. Further details and the equations of the expanding grids for the corresponding systems are introduced in later chapters and Appendix.A.

The expanding grids introduce complexity to the discretised form of Eqn (2.27):

$$\frac{C_s^k - C_s^{k-1}}{\Delta T} = \frac{\frac{C_{s+1}^k - C_s^k}{\Delta X_+} - \frac{C_s^k - C_{s-1}^k}{\Delta X_-}}{\frac{1}{2}(\Delta X_+ + \Delta X_-)} \qquad (2.46)$$

where $\Delta X_+ = X_{i+1} - X_i$ and $\Delta X_- = X_i - X_{i-1}$. Thus, the coefficients in Eqn (2.31) become:

$$\alpha = -\frac{2\Delta T}{\Delta X_-^2 + \Delta X_+ \Delta X_-} \qquad (2.47)$$

$$\beta = 1 + \frac{2\Delta T}{\Delta X_-^2 + \Delta X_+ \Delta X_-} + \frac{2\Delta T}{\Delta X_+^2 + \Delta X_+ \Delta X_-} \qquad (2.48)$$

$$\gamma = -\frac{2\Delta T}{\Delta X_+^2 + \Delta X_+ \Delta X_-} \qquad (2.49)$$

2.3.3 2D simulations

In practice, 2D simulations must be used in the electrochemical systems with microdisc or microband geometries as discussed in Chapter 3. The 2D system adds another dimension to Eqn (2.12) in cylindrical coordinates or Cartesian coordinates for the microdisc or microband electrode, respectively:

$$\frac{\partial C_j}{\partial T} = d_j\left(\frac{\partial^2 C_j}{\partial R^2} + \frac{1}{R}\frac{\partial C_j}{\partial R} + \frac{\partial^2 C_j}{\partial Z^2}\right) \tag{2.50}$$

$$\frac{\partial C_j}{\partial T} = d_j\left(\frac{\partial^2 C_j}{\partial X^2} + \frac{\partial^2 C_j}{\partial Z^2}\right) \tag{2.51}$$

For example, in the simulation of a microdisc electrode, which are shown in Figure 2.4, the 2D cross-sectional illustration can be rotated around the *z*-axis to resemble the microdisc electrode.

To solve Eqn (2.49), the alternating direction implicit method (ADI method) [1, 11] is used to split the finite difference method into two individual steps, the *Z*-sweep and the *R*-sweep, which represent two implicit solution in *Z*-direction and *R*-direction in two half-time steps, $k_{0.5}$ and k. The *Z*-sweep discretisation is thus written as:

$$\begin{aligned}\frac{C_s^{k_{0.5}} - C_s^{k-1}}{0.5\Delta T} = {} & \frac{2}{\Delta R_+ + \Delta R_-}\left(\frac{C_{s+1,j}^{k-1} - C_{s,j}^{k-1}}{\Delta R_+} - \frac{C_{s,j}^{k-1} - C_{s-1,j}^{k-1}}{\Delta R_-}\right) \\ & + \frac{2}{\Delta Z_+ + \Delta Z_-}\left(\frac{C_{s,j+1}^{k_{0.5}} - C_{s,j}^{k_{0.5}}}{\Delta Z_+} - \frac{C_{s,j}^{k_{0.5}} - C_{s,j-1}^{k_{0.5}}}{\Delta Z_-}\right) \\ & + \frac{1}{R_s}\left(\frac{C_{s+1,j}^{k-1} - C_{s-1,j}^{k-1}}{\Delta R_+ + \Delta R_-}\right)\end{aligned} \tag{2.52}$$

and the *R*-sweep discretisation is:

$$\begin{aligned}\frac{C_s^{k} - C_s^{k_{0.5}}}{0.5\Delta T} = {} & \frac{2}{\Delta R_+ + \Delta R_-}\left(\frac{C_{s+1,j}^{k} - C_{s,j}^{k}}{\Delta R_+} - \frac{C_{s,j}^{k} - C_{s-1,j}^{k}}{\Delta R_-}\right) \\ & + \frac{2}{\Delta Z_+ + \Delta Z_-}\left(\frac{C_{s,j+1}^{k_{0.5}} - C_{s,j}^{k_{0.5}}}{\Delta Z_+} - \frac{C_{s,j}^{k_{0.5}} - C_{s,j-1}^{k_{0.5}}}{\Delta Z_-}\right) \\ & + \frac{1}{R_s}\left(\frac{C_{s+1,j}^{k} - C_{s-1,j}^{k}}{\Delta R_+ + \Delta R_-}\right)\end{aligned} \tag{2.53}$$

Furthermore, the current response is calculated via:

$$J = -0.5\sum_{i=1}^{n}\left[\frac{\left(C_{s,1} - C_{s,0}\right)R_s + \left(C_{s-1,1} - C_{s-1,0}\right)R_{s-1}}{Z_1 - Z_0}\right](R_i - R_{i-1}) \tag{2.54}$$

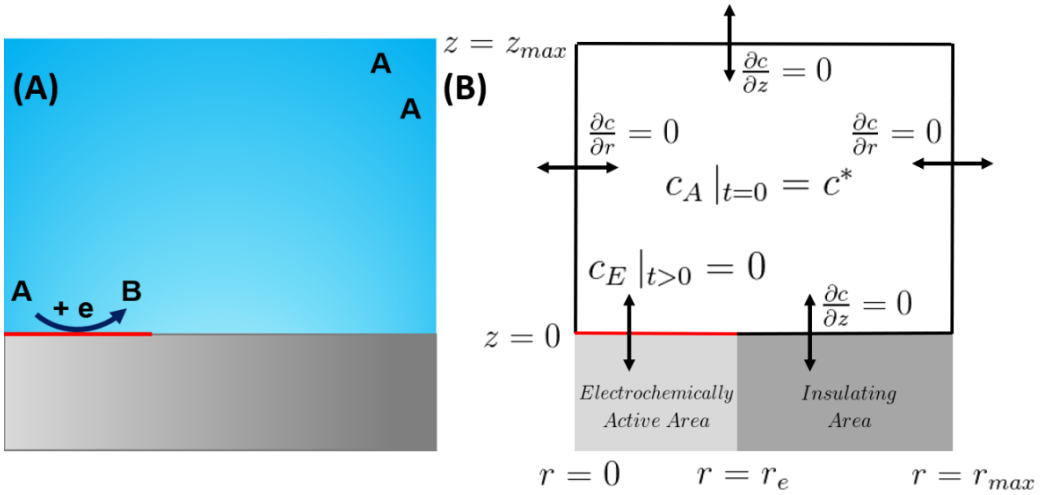


Figure 2.4: Cross-sectional illustration **(A)** and boundary conditions **(B)** of the microdisc models. $c_A|_{t=0}$ represents the concentration of analyte *A* for all of the points within the simulated space at the beginning of the simulation, c^* is the initial concentration of *A*, c_E is the concentration of *A* for points at the electrode surface, r_e is the radius of the disc, r_{max} and z_{max} are the boundaries of the simulated space in the *r*- and *z*-axis, respectively.

2.3.4 Validation and convergence studies

In the simulations, validation and convergence studies of the simulated results are essential in ensuring the correctness and reproducibility [12-14].

The validation of the simulation systems can, where possible, the comparison between the simulated results and corresponding literature or empirical equations, and the test of mass conservation. They both reflect the correctness of the simulation system, which are the prerequisites of the authenticity for the further simulated results. The calculation of the error of mass conservation is shown in Appendix.B.

The convergence studies indicate the precision of the simulated results. As discussed above, the approximations of the discretisation for the diffusion equations depend on the sizes of ΔX and ΔT, and the currents will stay at relatively constant values as ΔX and ΔT decrease to an extent. In practice, simulations involve multiple trial-and-error processes. The convergence studies are thus crucial indicators of how precise the simulated results are. In each following chapter, the validations and convergence studies for each simulation models are presented and discussed in detail.

References

[1] R. G. Compton, E. Kätelhön, E. Laborda, K. R. Ward, *Understanding Voltammetry: Simulation of Electrode Processes*, second edition, World Scientific Europe, **2020**.

[2] D. Britz, *Digital Simulation in Electrochemistry*, **2005**, *666*, Springer.

[3] H. Angerstein-Kozlowska, J. Klinger, and B. Conway, *J. Electroanal. Chem. Interf. Electrochem.*, **1977**, *75*, 45-60.

[4] J. A. Alden and R. G. Compton, *J. Phys. Chem. B*, **1997**, *101*, 8941-8954.

[5] A. J. Bard and L. Faulkner, *Electrochemical Methods: Fundamentals and Applications*. John Wiley and Sons, **2001**.

[6] I. Svir, A. Oleinick, R. Compton, *Russ. J. Electrochem.* **2003**, *39*, 160-164.

[7] K. W. Morton, *Numerical Solution of Partial Differential Equations: An Introduction*, Cambridge University Press, **2005**.

[8] G. D. Smith, *Numerical Solution of Partial Differential Equations: Finite Difference Methods*, Oxford University Press, **1985**.

[9] D. Zhou, F. Gao, E. Breaz, A. Ravey, A. Miraoui, *IEEE Transactions on Industrial Electronics*, **2018**, *65*, 7106–7118.

[10] D. J. Gavaghan, *J. Electroanal. Chem.*, **1998**, *456*, 1–12.

[11] J. Heinze, *J. Electroanal. Chem. Interf. Electrochem.*, **1981**, *124*, 73–86.

[12] E. Kätelhön, R. G. Compton, *Analyst*, **2015**, *140*, 2592–2598.

[13] E. Kätelhön, R. G. Compton, *Analyst*, **2015**, *140*, 3290–3290.

[14] E. Kätelhön, R. G. Compton, *Analyst*, **2016**, *141*, 1154–1154.

Chapter 3: The Diffusion Indicator: Comparative Chronoamperometry

This chapter introduces a new parameter, the diffusion indicator α, derived from chronoamperometric current responses. Comparative information about the temporal evolution of α values is obtained for electrodes with different geometries (spheres, discs, cylinders, and bands) to study the diffusion of an electrochemically active species from/to an electrode. The results reported in this chapter are based on a published first-author paper [1] [*Journal of Electroanalytical Chemistry*, **2020**, *866*, 114149].

3.1 Introduction

In both fundamental and analytical electrochemistry, microelectrodes are widely used and often take the form of a wide diversity of geometries including, the most common ones, spheres [2–4], discs [5–7], cylinders [8–11], and bands [12–14] as shown in Figure 3.1. The several generic and well-rehearsed advantages of microelectrodes over their macro counterparts include the access to shorter timescales, greater current densities and reduced total interfacial capacitances. The access to shorter timescales enables the measurement of faster kinetics - both heterogeneous and of coupled homogeneous reactions - as perhaps best illustrated by the fast scan (mega-Volt per second) cyclic voltammetry at microdisc electrodes pioneered by Amatore, Maisonhaute and colleagues [15, 16] and where 'faster' compares to what is seen at macroelectrodes.

Although the four microelectrode geometries illustrated in Figure 3.1 all show faster responses than macroelectrodes, they show interestingly different behaviours between themselves, which is especially noticeable in the diffusion-controlled limit of simple

Faradaic processes leading to, in the case of a microdisc or microsphere electrode, a true steady-state limiting current I_{ss}. Particularly, for the reaction $A \pm ne \rightarrow$ B, the steady-state current for a microdisc electrode is [17, 18]:

$$I_{ssD} = 4r_e nFc^* D \tag{3.1}$$

where r_e is the radius of the microdisc electrode, n is the number of electrons transferred in the electrode reaction, F is the Faraday constant, c^* is the initial concentration of the analyte A, and D is the diffusion coefficient of A.

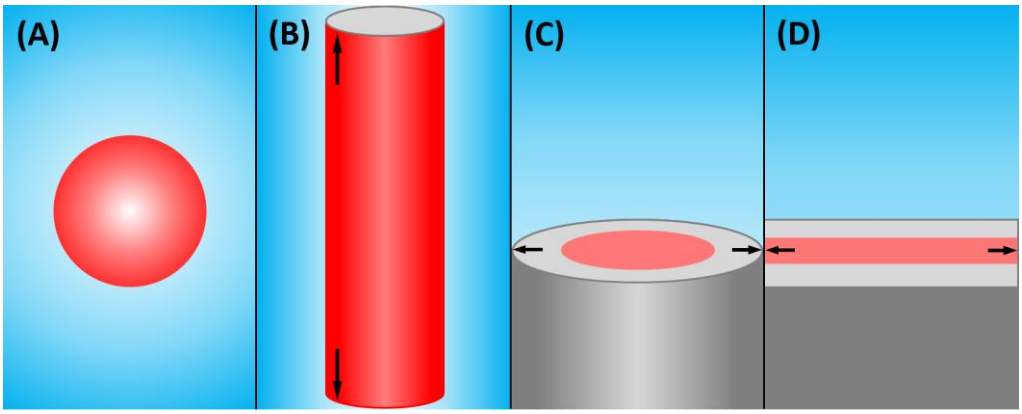


Figure 3.1: Illustrations of the electrodes studied in this work: **(A)** the microsphere electrode, **(B)** the microcylinder electrode with an infinite length, **(C)** the microdisc electrode, and **(D)** the microband electrode with an infinite length. The red areas represent the electrochemically active surfaces, the blue areas indicate the solution phase, the grey areas show the insulating surface, and the black arrows illustrate infinitely expanding areas.

Correspondingly, the steady-state current equation for a microsphere is [19]:

$$I_{sss} = 4\pi r_e nFc^* D \tag{3.2}$$

where a true steady state results from the fully convergent diffusion of A to the electrode.

However, the responses at microcylinder and microband electrodes to Faradaic processes show only quasi-steady state behaviours which feature currents decaying very slowly ultimately, in principle at least, to zero. Two well-known approximations for currents following a potential step from zero current to the diffusion-controlled electrolysis of A are, for a microcylinder of infinite length and radius r_e [20],

$$I_{qssC} = \frac{4\pi nFc^* Dl}{\ln\left(4Dt/r_e^2\right)} \tag{3.3}$$

and, for an infinitely long microband of width *w* [21],

$$I_{qssB} = \frac{2\pi nFc^{*}Dl}{\ln\left(64Dt/w^{2}\right)} \tag{3.4}$$

where *l* and l^{*} are the lengths of the cylinder and the band, respectively, and *w* is the width of the band.

The decreases of currents at long times are evident in both cases. The difference in behaviour between the quasi-steady-state electrodes from those showing true steady-state currents and fully convergent diffusion lies in the fact that the band and cylinder possess one macroscopic spatial dimension, the electrode length in each case, and this ensures that the current ultimately decays to zero under diffusion-only conditions.

In addition to comparison between the steady-state and quasi-steady state behaviours, a key question, in experimental practice, relates to how fast the electrode responses to a potential perturbation. In this chapter, we compare the chronoamperometric responses of the four electrodes of interest to a potential step from zero current to a diffusion-limited current. As a means of comparing the relative timescales and the temporal evolution of the current responses from a linear, Cottrellian, diffusion, behaviour over to a steady-state or quasi-steady state, we make use of a new approach introduced in this chapter and used in a subsequent chapter for the analysis of different types of cylindrical electrodes [22]. This approach notes that for all the electrodes of interest the short-time behaviour reflects linear diffusion and so the currents scale as:

$$I \propto t^{-0.5} \tag{3.5}$$

For the fully convergent diffusion where a steady state is established,

$$I \propto t^{0} \tag{3.6}$$

Therefore, we consider the transition from the limit of linear diffusion to that of convergent or quasi-convergent diffusion in the course of a potential step current-time transient characterised by the parameter:

$$\alpha = 2\frac{d(\log I)}{d(\log t)} + 1 \tag{3.7}$$

where the two limiting cases form the lower and upper values of α: $0 < \alpha < 1$ such that $\alpha = 0$ corresponds to linear diffusion and $\alpha = 1$ to fully convergent diffusion. We term the parameter α the "diffusion indicator" relating to the character of the diffusion.

3.2 Simulation methods

This section consists of the simulation models, the computational methods, and the dimensionless parameters used in this work.

3.2.1 Simulation models

Four simulation models for different geometries were employed as discussed above. Their currents and concentration profiles for potential step chronoamperometry were obtained and investigated. The initial concentration of the species *A* in each model is set to be c^* uniformly distributed in the simulation space before an overpotential is applied to the electrode surface, where a single-electron-transfer reduction occurs for the species *A* ($A + e^- \rightarrow$ B). The potential step chronoamperometric process in each model is assumed to be diffusion-controlled by setting a large overpotential and sufficiently high concentration of electrolyte. Therefore, the following diffusion equation can be used to describe the mass transport in the reduction process.

$$\frac{\partial c}{\partial t} = D\nabla^2 c \tag{3.8}$$

where *c* is the species concentration at a certain space point, and *t* is the time. ∇ is a vector operator related to the coordinate system chosen.

Four models are categorised into two groups, due to the similarities in their geometries: first, the microsphere electrode and the microcylinder electrode models are categorised as the 'one-dimensional' electrode models, and second, the microdisc electrode and the microband electrode models are categorised as the 'two-dimensional'

electrode models. The details for each group are introduced separately as follows.

3.2.1.1 The 'one-dimensional' electrode models

In the microsphere electrode model, due to its rotational symmetry, the model can be simplified to a one-dimensional spherical system. Therefore, ∇^2 can be simplified, and the diffusion equation of this system is:

$$\frac{\partial c}{\partial t} = D\nabla^2 c = D(\frac{\partial^2 c}{\partial r^2} + \frac{2}{r}\frac{\partial c}{\partial r}) \tag{3.9}$$

Similarly, the diffusion equation of the microcylinder model can be simplified to:

$$\frac{\partial c}{\partial t} = D\nabla^2 c = D(\frac{\partial^2 c}{\partial r^2} + \frac{1}{r}\frac{\partial c}{\partial r}) \tag{3.10}$$

due to the horizontal- and rotational symmetry in the infinite microcylinder model.

Thus, the simulation system of these two models is presented in Figure 3.2(A) which shows the one-dimensional geometries at an extremely small scale. The analyte *A* in the solution shown at the right side of the plot is illustrated in blue, and the electrode shown at the left is coloured in red, where the single-electron-transfer reduction occurs. The only difference between these two one-dimensional models is the different radial diffusion, which is respectively represented by the terms $\frac{2}{r}\frac{\partial c}{\partial r}$ and $\frac{1}{r}\frac{\partial c}{\partial r}$ in Eqn (3.9) and Eqn (3.10), during the simulated processes.

In Figure 3.2(B), the boundary conditions for the 'one-dimensional' electrode models are shown with necessary equations. In detail, the concentration of analyte *A* is set to be c^* with concentration of *B* setting to 0 before the simulation starts:

$$t = 0, r_e \le r \le r_{max}: \quad c_A = c_A^*, c_B = 0 \tag{3.11}$$

where r_{max} represent the far end of the simulation space away from the electrode, which is the sum of the electrode radius r_e and the solution space x_{sim}:

$$\begin{cases} r_{max} = r_e + x_{sim} \\ x_{sim} = 6\sqrt{Dt_{sim}} \end{cases} \tag{3.12}$$

where t_{sim} is the total simulation time. As described in the literature [23, 24], due to Brownian motion, the distance from the electrode for the concentration perturbation to occur is around: $\sqrt{|x^2|} = \sqrt{2Dt_{sim}}$. Therefore, x_{sim} is set large enough, $6\sqrt{Dt_{sim}}$, that the simulation process is independent of the far end boundary r_{max}.

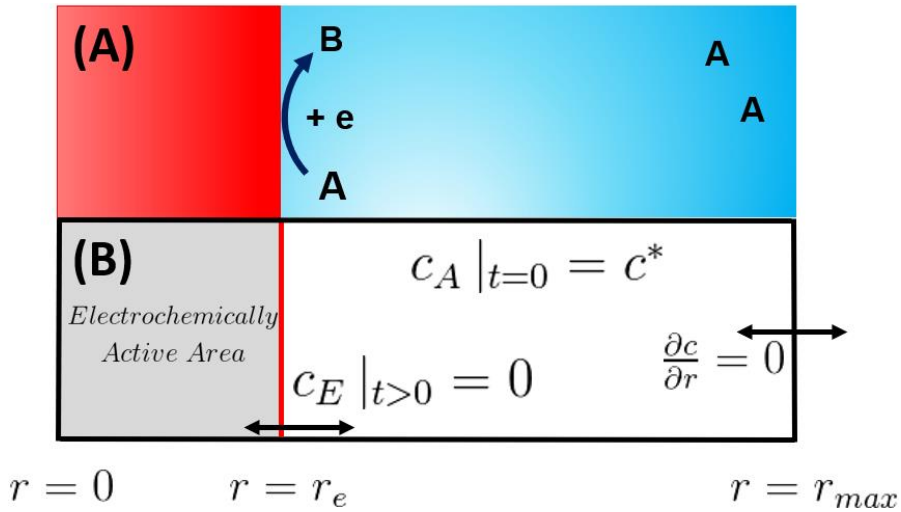


Figure 3.2: Cross-sectional illustration **(A)** and boundary conditions **(B)** of the 'one-dimensional' electrode models. $c_A|t=0$ represents the concentration of the analyte *A* for all of the points within the simulated space at the beginning of the simulation, c^* is the initially homogeneous concentration of the analyte *A*, c_E is the concentration of the analyte *A* for points at the surface of the electrochemically active area, *re* is the radius of the cylinder, and r_{max} is the boundary of the simulated space in the *r*-axis.

A no-flux boundary condition is set at the far end boundary throughout the whole simulated process while, due to the overpotential applied, the concentration of *A* on the electrodes surface ($r = r_e$) is set to 0 as the simulation starts:

$$\begin{cases} t > 0, r = r_{max}: & \dfrac{\partial c}{\partial r} = 0 \\ t > 0, r = r_e: & c_A = 0 \end{cases} \tag{3.13}$$

According to Fick's first law and Faraday's law, the current responses in two electrode models in this section as:

$$\begin{cases} I_S = Fj_S \quad \text{where} \quad j_S = -4\pi r_e^2 D \left.\dfrac{\partial c_A}{\partial r}\right|_{r=r_e} \\ I_C = Fj_C \quad \text{where} \quad j_C = -2\pi l r_e D \left.\dfrac{\partial c_A}{\partial r}\right|_{r=r_e} \end{cases} \tag{3.14}$$

where I_s and I_c are the current responses for the microsphere electrode model and the microcylinder electrode model, respectively, j_s and j_c are the fluxes of the analyte A for the microsphere electrode model and the microcylinder electrode model, respectively.

3.2.1.2 The 'two-dimensional' electrode models

Similarly, due to the rotational symmetry, the microdisc model can be simplified to a two-dimensional spherical system, and the diffusion equation of this system is:

$$\frac{\partial c}{\partial t} = D\nabla^2 c = D\left(\frac{\partial^2 c}{\partial r^2} + \frac{1}{r}\frac{\partial c}{\partial r} + \frac{\partial^2 c}{\partial z^2}\right) \tag{3.15}$$

and the diffusion equation for the microband electrode model can be simplified, according to the vertical symmetry, to:

$$\frac{\partial c}{\partial t} = D\nabla^2 c = D\left(\frac{\partial^2 c}{\partial x^2} + \frac{\partial^2 c}{\partial z^2}\right) \tag{3.16}$$

as shown in Figure 3.3(A).

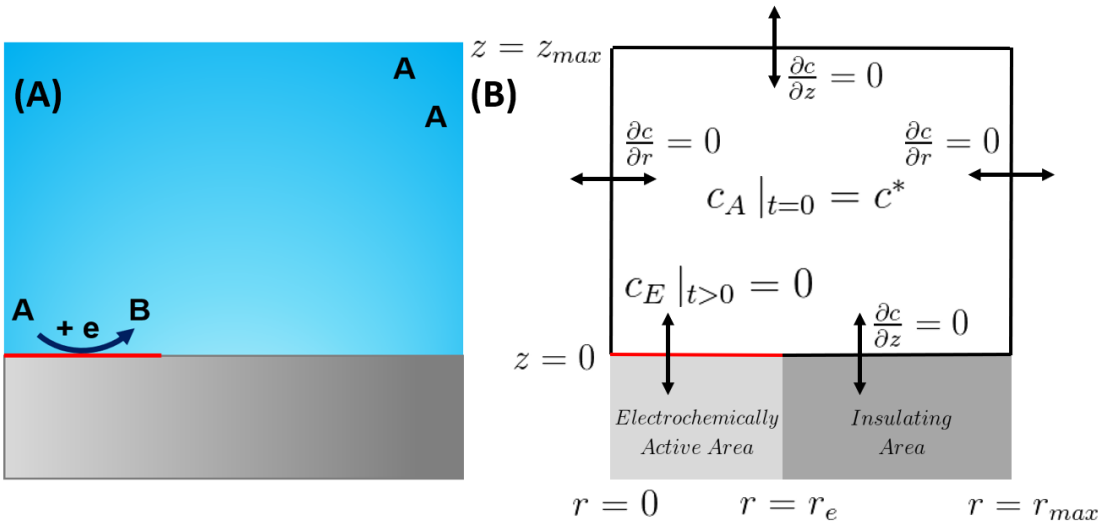


Figure 3.3: Cross-sectional illustration (A) and boundary conditions (B) of the 'two-dimensional' electrode models. z_{max} is the boundary of the simulated space in the z-axis.

The boundary conditions for the 'two-dimensional' electrode models are set as shown in Figure 3.3(A). Firstly, the concentrations of species A and B within the simulation spaces are set to c^* and 0, respectively, at the beginning of the simulations:

$$t = 0, 0 \le r \le r_{max}, 0 \le z \le z_{max}: \quad c_A = c_A^*, c_B = 0 \tag{3.17}$$

For $t > 0$, the concentration of A for the space points at the electrode surface are set

to 0 according to the overpotential applied:

$$t > 0, 0 \le r \le r_e, z = 0: \quad c_A = 0 \tag{3.18}$$

and the rest of the boundaries are set to be no-flux boundaries:

$$\begin{cases} t > 0, r = 0, 0 \le z \le z_{max}: & \dfrac{\partial c}{\partial r} = 0 \\ t > 0, r = r_{max}, 0 \le z \le z_{max}: & \dfrac{\partial c}{\partial r} = 0 \\ t > 0, r_e \le r \le r_{max}, z = 0: & \dfrac{\partial c}{\partial z} = 0 \\ t > 0, 0 \le r \le r_{max}, z = z_{max}: & \dfrac{\partial c}{\partial z} = 0 \end{cases} \tag{3.19}$$

where the simulation space x_{sim} is also determined by the simulation time:

$$\begin{cases} r_{max} = r_e + x_{sim} \\ z_{max} = x_{sim} \\ x_{sim} = 6\sqrt{D t_{sim}} \end{cases} \tag{3.20}$$

Thus, the current responses can be calculated according to the fluxes of species *A* at the electrode surface:

$$\begin{cases} I_D = F j_D \quad \text{where} \quad j_D = -2\pi D \displaystyle\int_0^{r_e} \left.\frac{\partial c_A}{\partial z}\right|_{z=0} r dr \\ I_B = F j_B \quad \text{where} \quad j_B = -2 l^* D \displaystyle\int_0^{r_e} \left.\frac{\partial c_A}{\partial z}\right|_{z=0} dr \end{cases} \tag{3.21}$$

3.2.2 Dimensionless parameters

Dimensionless parameters are introduced as shown in Table 3.1 to present the analytical and simulation results in a simple and universal way.

Table 3.1: Conversion of dimensional parameters to dimensionless ones where r_r is the reference length of respective models, ***R*** is the Universal Gas Constant, and ***T*** is the temperature.

Dimensionless Parameters	Conversions
Concentration of species j	$C_j = \dfrac{c_j}{c^*}$
Diffusion coefficient of species j	$d_j = \dfrac{D_j}{D}$
Radial distance	$R = \dfrac{r}{r_r}$

Axial distance	$Z = \frac{z}{r_r}$
Time	$T = \frac{Dt}{r_r^2}$
Potential	$\theta = \frac{F}{\boldsymbol{RT}}(E - E_f^0)$
Current	$J = \frac{I}{Fr_r Dc^*}$

Thus, the diffusion equations Eqn (3.9), Eqn (3.10), Eqn (3.15), and Eqn (3.16) can be transformed into their dimensionless counterparts:

$$\begin{cases} \dfrac{\partial C_j}{\partial T} = d_j\left(\dfrac{\partial^2 C_j}{\partial R^2} + \dfrac{2}{R}\dfrac{\partial C_j}{\partial R}\right) \\ \dfrac{\partial C_j}{\partial T} = d_j\left(\dfrac{\partial^2 C_j}{\partial R^2} + \dfrac{1}{R}\dfrac{\partial C_j}{\partial R}\right) \\ \dfrac{\partial C_j}{\partial T} = d_j\left(\dfrac{\partial^2 C_j}{\partial R^2} + \dfrac{1}{R}\dfrac{\partial C_j}{\partial R} + \dfrac{\partial^2 C_j}{\partial Z^2}\right) \\ \dfrac{\partial C_j}{\partial T} = d_j\left(\dfrac{\partial^2 C_j}{\partial X^2} + \dfrac{\partial^2 C_j}{\partial Z^2}\right) \end{cases} \tag{3.22}$$

where C_j and d_j are dimensionless concentration and diffusion coefficient for species j.

Therefore, the dimensionless current responses for the four models are:

$$\begin{cases} J_S = -4\pi d_A \left.\dfrac{\partial C_A}{\partial R}\right|_{R=1} \\ J_C = -2\pi L d_A \left.\dfrac{\partial C_A}{\partial R}\right|_{r=1} \\ J_D = -2\pi d_A \displaystyle\int_0^1 \left.\frac{\partial C_A}{\partial Z}\right|_{Z=0} R\,dR \\ J_B = -2L^* d_A \displaystyle\int_0^1 \left.\frac{\partial C_A}{\partial Z}\right|_{Z=0} dR \end{cases} \tag{3.23}$$

where L and L^* are the dimensionless lengths for the cylinder and the band. Additionally, the parameter α can be calculated using dimensionless current J and time T:

$$\alpha = 2\frac{d(\log J)}{d(\log T)} + 1 \tag{3.24}$$

3.2.3 Expanding simulation grids

For all models, there is an expanding time grid, as defined in Appendix.A, employed in each simulation. For the microsphere and microcylinder electrode, there is a single

expanding space grid beyond the electrode surface. For the microdisc and microband electrode, there is a double expanding grid for the electrode surface, and there is a single expanding grid for each of the axes (*X* axis, *R* axis) beyond the electrode surface.

3.2.4 Computational Methods

Simulation models were developed in *C++*, and the simulation results were processed via *Python* using the *NumPy* and *matplotlib* libraries. The diffusion equations were solved via matrices via the finite difference approach together with the alternating direction implicit (ADI) method [25–27]. Please refer to the textbook [24] for more details. Testing and validation [28–30] were performed including studies of error of mass conservation and convergence, which are shown in the Appendices.

3.3 Theoretical analyses

Based on several well-known literature analytical and empirical equations for the chronoamperometric responses, we derived the α values for microsphere, microcylinder, microdisc, and microband electrodes in this section.

3.3.1 Microsphere electrode

The analytical expression of chronoamperometric current response of a hemispherical electrode is [31]:

$$I = FADc^* \left(\frac{1}{\sqrt{D\pi t}} + \frac{1}{r_e} \right) \tag{3.25}$$

for which the dimensionless current *J* is:

$$J = 2\pi \left(\frac{1}{\sqrt{\pi T}} + 1 \right) \tag{3.26}$$

The expression for the diffusion indicator α is:

$$\alpha = 2 \frac{d \log J}{d \log T} + 1 = 2T \frac{d \ln J}{dT} + 1 \tag{3.27}$$

Thus, combined with Eqn (3.26), the temporal evolution of α for the hemispherical

electrode can be expressed by:

$$\alpha = -\frac{1}{1+\sqrt{\pi T}} + 1 \qquad (3.28)$$

3.3.2 Microdisc electrode

As reported by Shoup et al [18], an empirical expression for the chronoamperometric current response at a microdisc electrode based on fitting to simulations is:

$$I = 4Fr_eDc^*\{0.7854 + 0.8863\left(\frac{4Dt}{r_e^2}\right)^{-0.5} + 0.2146\exp\left[-0.7823\left(\frac{4Dt}{r_e^2}\right)^{-0.5}\right]\} \qquad (3.29)$$

where r_e is the disc radius. The error of this equation was reported [18] to be less than 0.6% for all times. In dimensionless form this becomes:

$$J = 3.1416 + 1.7726T^{-0.5} + 0.8584\exp(-0.3912T^{-0.5}) \qquad (3.30)$$

which, combined with Eqn (1.27), gives the temporal evolution of α for the microdisc:

$$\alpha = \frac{-1.7726T^{-0.5} + 0.3358T^{-0.5}\exp(-0.3912T^{-0.5})}{3.1416 + 1.7726T^{-0.5} + 0.8584\exp(-0.3912T^{-0.5})} + 1 \qquad (3.31)$$

3.3.3 Microcylinder electrode

The cylindrical electrode model discussed in this section refers to a cylinder with an infinite length. Therefore, only the side of the cylinder is considered. As reported by Szabo et al [21], an empirical expression for the chronoamperometric current at a microcylinder electrode of radius r_e is:

$$I = FDc^*l\left(\frac{e^{-0.1\sqrt{\pi T}}}{\sqrt{\pi T}} + \frac{1}{\ln[(4e^{-\gamma}T)^{0.5} + e^{5/3}]}\right) \qquad (3.32)$$

where Υ is a constant which equals to 0.5772..., and the error of this equation is less than 1.3% for all times [21]. The dimensionless current J can be expressed as:

$$J = L\left(\frac{e^{-0.1\sqrt{\pi T}}}{\sqrt{\pi T}} + \frac{1}{\ln[(4e^{-\gamma}T)^{0.5} + e^{5/3}]}\right) \qquad (3.33)$$

which, combined with Eqn (3.27), give the temporal evolution of α for the microband:

$$\alpha = -\frac{\left(\frac{1}{10}+\frac{1}{\sqrt{\pi T}}\right)e^{-0.1\sqrt{\pi T}}+\frac{2e^{-0.5\gamma T^{0.5}}}{(2e^{-0.5\gamma T^{0.5}}+e^{5/3})\{\ln[2e^{-0.5\gamma T^{0.5}}+e^{5/3}]\}^2}}{\frac{e^{-0.1\sqrt{\pi T}}}{\sqrt{\pi T}}+\frac{1}{\ln[2e^{-0.5\gamma T^{0.5}}+e^{5/3}]}}+1 \quad (3.34)$$

3.3.4 Microband electrode

In this section, the length of the microband is considered to be infinite, which means only the diffusion from/to the side of the microband is considered. The reference length is set to the width of the band w_e (rather than r_e). As reported by Aoki et al. [32], an approximation for the chronoamperometric current of a microband electrode is:

$$I = FDc^{*}l\,[\frac{1}{\sqrt{\pi T}}+0.97-1.1\exp(\frac{-9.9}{|\ln(12.37T)|})] \quad (3.35)$$

where the error of this equation was reported [32] to be less than 0.8% for $\log_{10}T \leq 8$. The dimensionless current J is:

$$J = L[\frac{1}{\sqrt{\pi T}}+0.97-1.1\exp(\frac{-9.9}{|\ln(12.37T)|})] \quad (3.36)$$

Hence, temporal evolution of α for microband electrode, according to Eqn (3.27), is:

$$\begin{cases}\alpha = \dfrac{-\frac{1}{\sqrt{\pi T}}\pm\frac{21.78}{(\ln 12.37T)^2}\exp(\frac{-9.9}{|\ln(12.37T)|})}{\frac{1}{\sqrt{\pi T}}+0.97-1.1\exp(\frac{-9.9}{|\ln(12.37T)|})}+1 \\ \pm \rightarrow \begin{cases}+ & when \quad \ln(12.37T) < 0 \\ - & when \quad \ln(12.37T) \geq 0\end{cases}\end{cases} \quad (3.37)$$

3.4 Results and discussion

The curves and trends for the currents and α values are discussed for the four electrodes with different geometries based on the literature analytical and empirical equations for their chronoamperometric current responses introduced in the previous section. Moreover, simulations for these four models are performed and concentration profiles are extracted at different timescales ($\log_{10}$T = −2, 0, 2, 4) to obtain more information about the diffusion of the analyte *A* to the different electrode geometries.

3.4.1 Literature analytical and empirical equations

First, we validated the authenticity of the literature analytical and empirical equations through comparing them (Eqn (3.25), Eqn (3.29), Eqn (3.32), Eqn (3.35)) to the steady-state and quasi-steady-state currents (Eqn (3.1) to Eqn (3.4)) mentioned in the Introduction for these four electrodes as shown in Figure 3.4 presented as dimensionless current responses normalised by the surface areas of different electrodes, J/a with $\log_{10}$ − $\log_{10}$ scales over a dimensionless time range from $-6 \leq \log_{10}T \leq 6$. We found that the four equations for the current responses chosen follow the steady-state and quasi-steady-state current equations at long timescales.

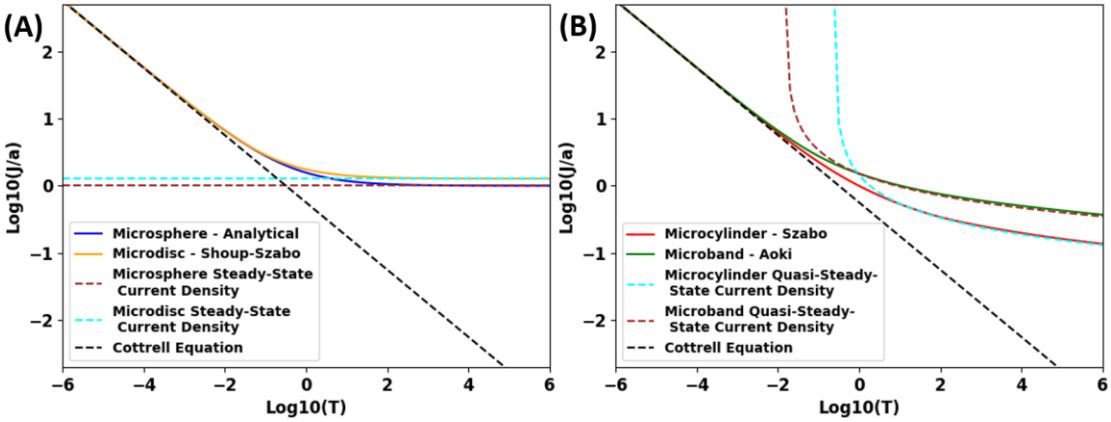


Figure 3.4: Literature analytical and empirical equations chosen for electrode models investigated in this work compared with the steady-state currents **(A)** and quasi-steady-state currents **(B)** for the corresponding geometries.

Hence, we present the current densities J/a, as shown in Figure 3.5(A), to compare the trends of currents between four electrodes. The currents for four electrodes follow the Cottrell equation when $\log_{10}T < -2$. As time proceeds, four currents start to deviate from the Cottrell equation when $\log_{10}T \geq -2$, at different rates, approaching their steady- or quasi-steady states when $\log_{10}T \geq 2$ as shown in Figure 3.4. Specifically, the steady-state current density for the microdisc electrode is larger than that for the microsphere electrode at long timescales. Moreover, the quasi-steady-state current density for the microband electrode is larger compared to that for the microcylinder electrode.

We further present the temporal evolutions of α values in Figure 3.5(B) to obtain a straightforward but sensitive illustration of the character of diffusion towards electrodes with different geometries. The deviation from the linear, Cottrellian, diffusion for all four electrodes starts even before $\log_{10}T = -4$. The α values of the microdisc electrode and microsphere electrode stay at almost identical values as that for the microband electrode until the α value for the microdisc electrode start to approach the convergent diffusion limit faster than the other two electrodes at $\log_{10}T = -2$, and the α value for the microsphere electrode starts to deviate from that for the microband electrode just after $\log_{10}T = -1$. We note that the timescales for the α values for the microdisc electrode and microsphere electrode to reach the convergent diffusion limit are similar ($\log_{10}T \approx 4$) despite the fact that the α value for the microdisc electrode is generally larger than the α value for the microsphere electrode over the range $-2 \leq \log_{10}T \leq 4$. However, the α values for the microcylinder electrode and the microband electrode do not reach the convergent diffusion limit within the simulated period, reflecting the quasi-steady-state responses of these two electrodes. Larger α values are noted for the microband electrode than the microcylinder electrode over the range $-4 \leq \log_{10}T \leq 6$.

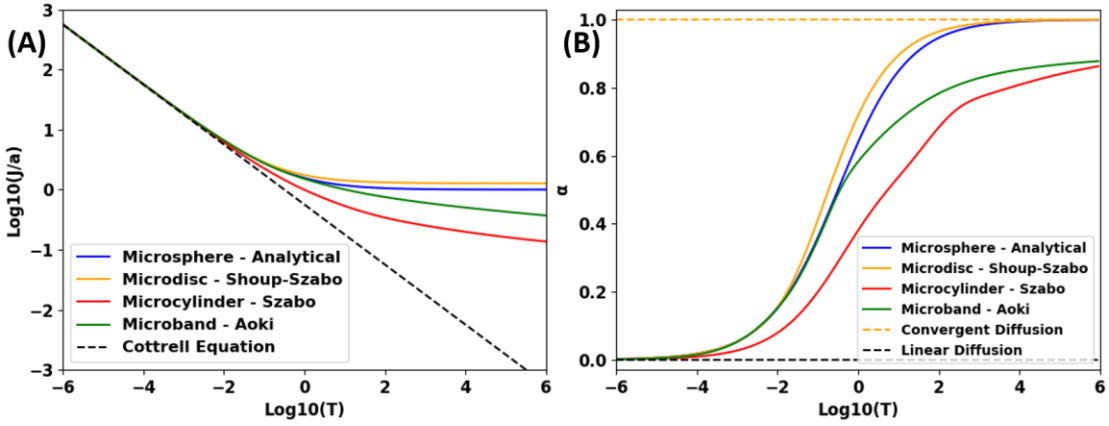


Figure 3.5: Temporal evolution of the current densities J/a **(A)** and α values **(B)** for four different electrode geometries: microsphere (blue), microdisc (orange), microcylinder (red), microband (green). The limits of Cottrellian diffusion (linear diffusion, black), and convergent diffusion (yellow) are shown at $\alpha = 0$ and 1, respectively.

3.4.2 Simulated concentration profiles

In the following sections, the concentration profiles are extracted at different timescales from simulation results for these four electrode models, we comparatively discuss the character of the diffusion on the α values.

First, the simulations were validated by testing the errors of mass conservation, as defined in Appendix.B, and the convergence studies by keeping all but one simulation parameters constant and ensuring low errors of mass conservation and trivial variations in voltammograms. Appropriate parameter sets were obtained for different models shown in Table 3.2. Studies of errors of mass conservation and convergence for the microsphere electrode model, the microdisc electrode model, the microcylinder electrode model and the microband electrode model, as shown in Figure 3.6 to 3.9, were performed by keeping the values of all but one parameter constant (dX, dT, ωX, and ωT) and varying the latter in the simulations.

Table 3.2: Dimensionless parameter sets for simulation models

Dimensionless Parameters	Microsphere	Microdisc	Microcylinder	Microband
Potential, θ	-50	-50	-50	-50
Initial concentration, C^*	1	1	1	1
Diffusion coefficient, d	1	1	1	1
Reference distance	$R_f = 1$	$R_f = 1$	$R_f = 1$	$W_f = 1$
Simulation time, T	10^6	10^6	10^6	10^6
Space step, dX	10^{-4}	10^{-4}	10^{-4}	10^{-4}
Space expand factor, wX	1.05	1.05	1.05	1.05
Time step, dT	10^{-8}	10^{-9}	10^{-8}	10^{-9}
Time expand factor, wT	1.001	1.001	1.001	1.0001

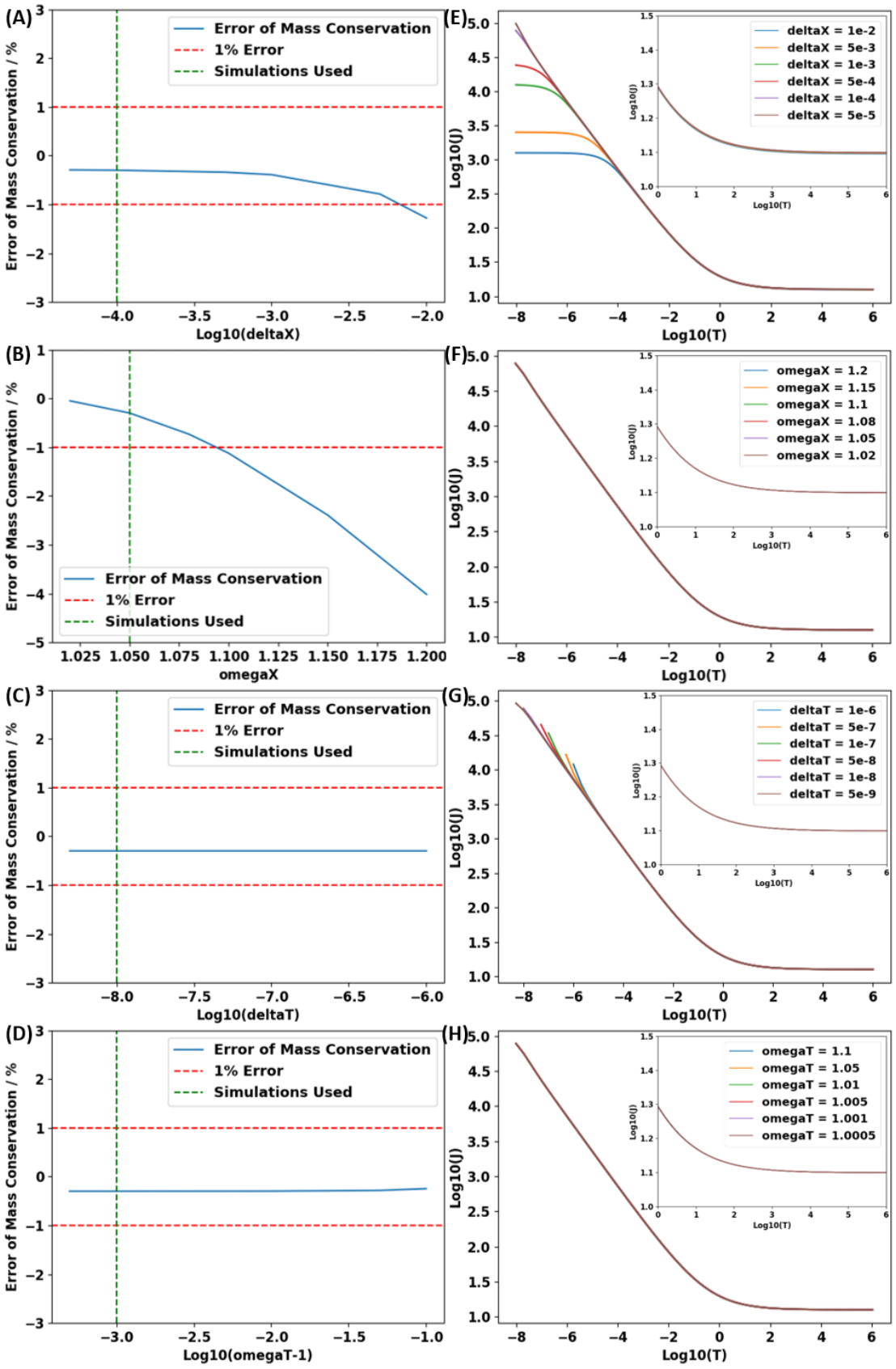


Figure 3.6: Errors of mass conservation **(A-D)** and current responses **(E-H)** for the microsphere electrode model varying dX, dT, ωX, and ωT.

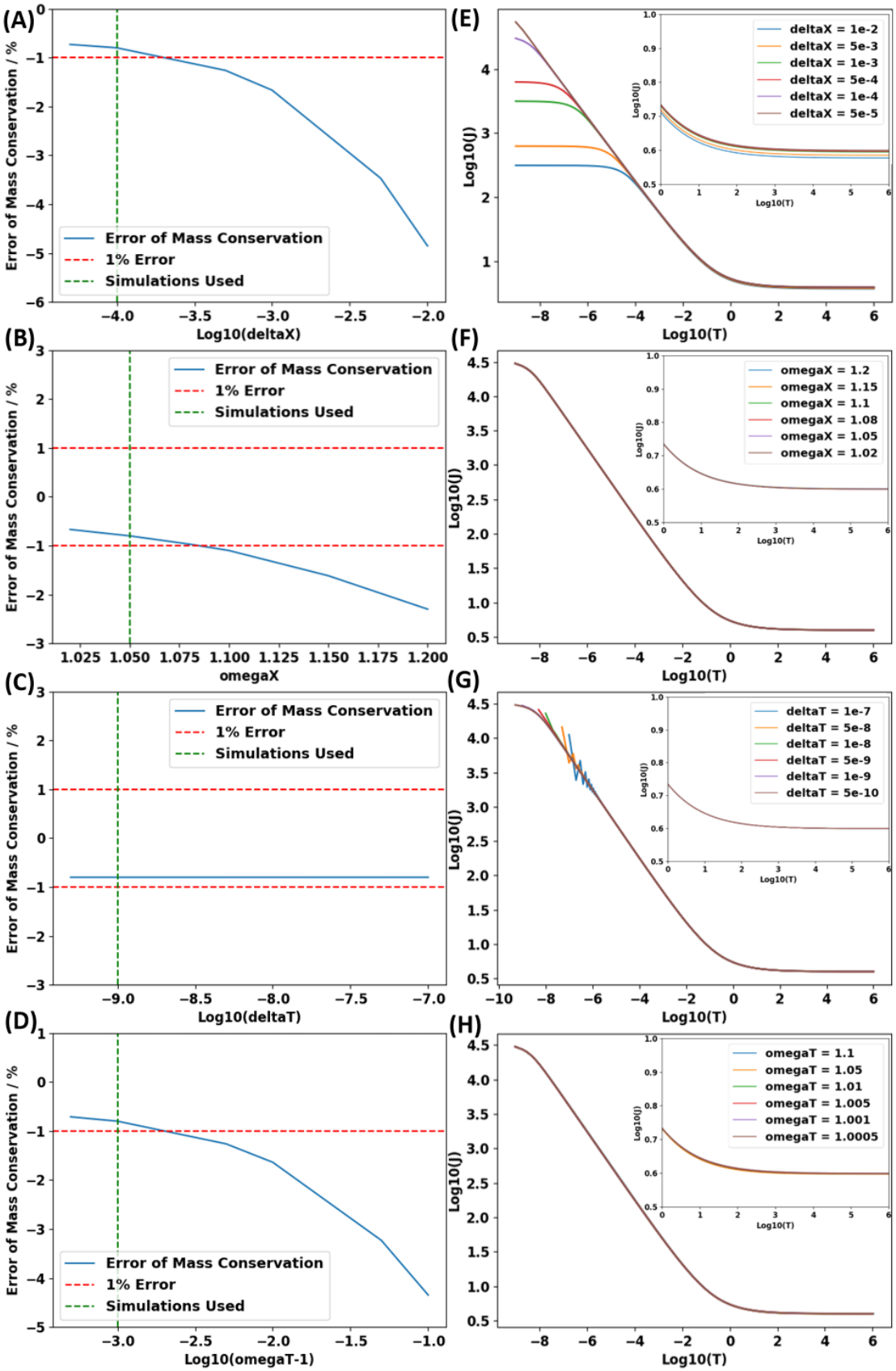


Figure 3.7: Errors of mass conservation **(A-D)** and current responses **(E-H)** for the microdisc electrode model varying dX, dT, ωX, and ωT.

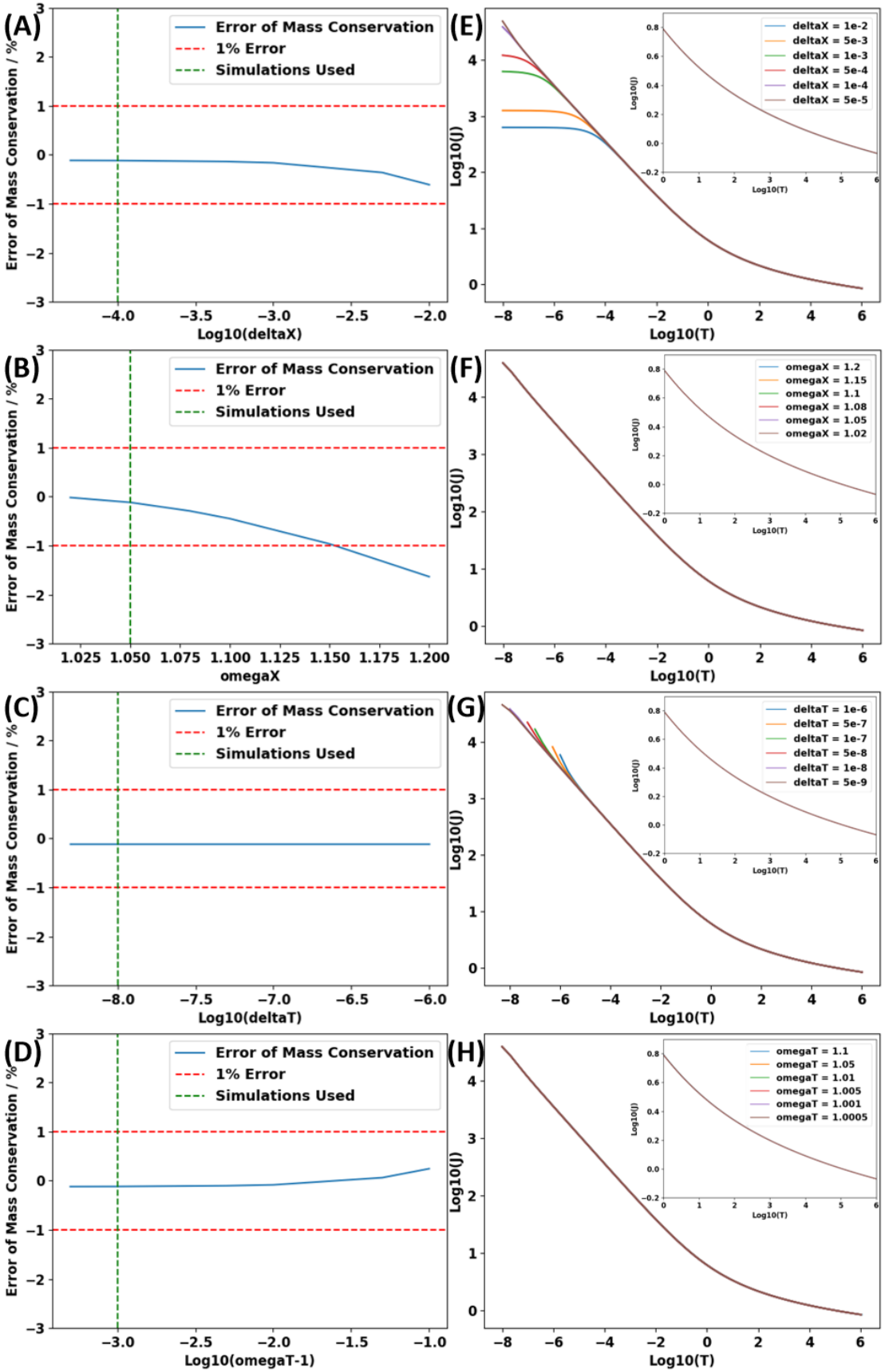


Figure 3.8: Errors of mass conservation **(A-D)** and current responses **(E-H)** for the microcylinder electrode model varying dX, dT, ωX, and ωT.

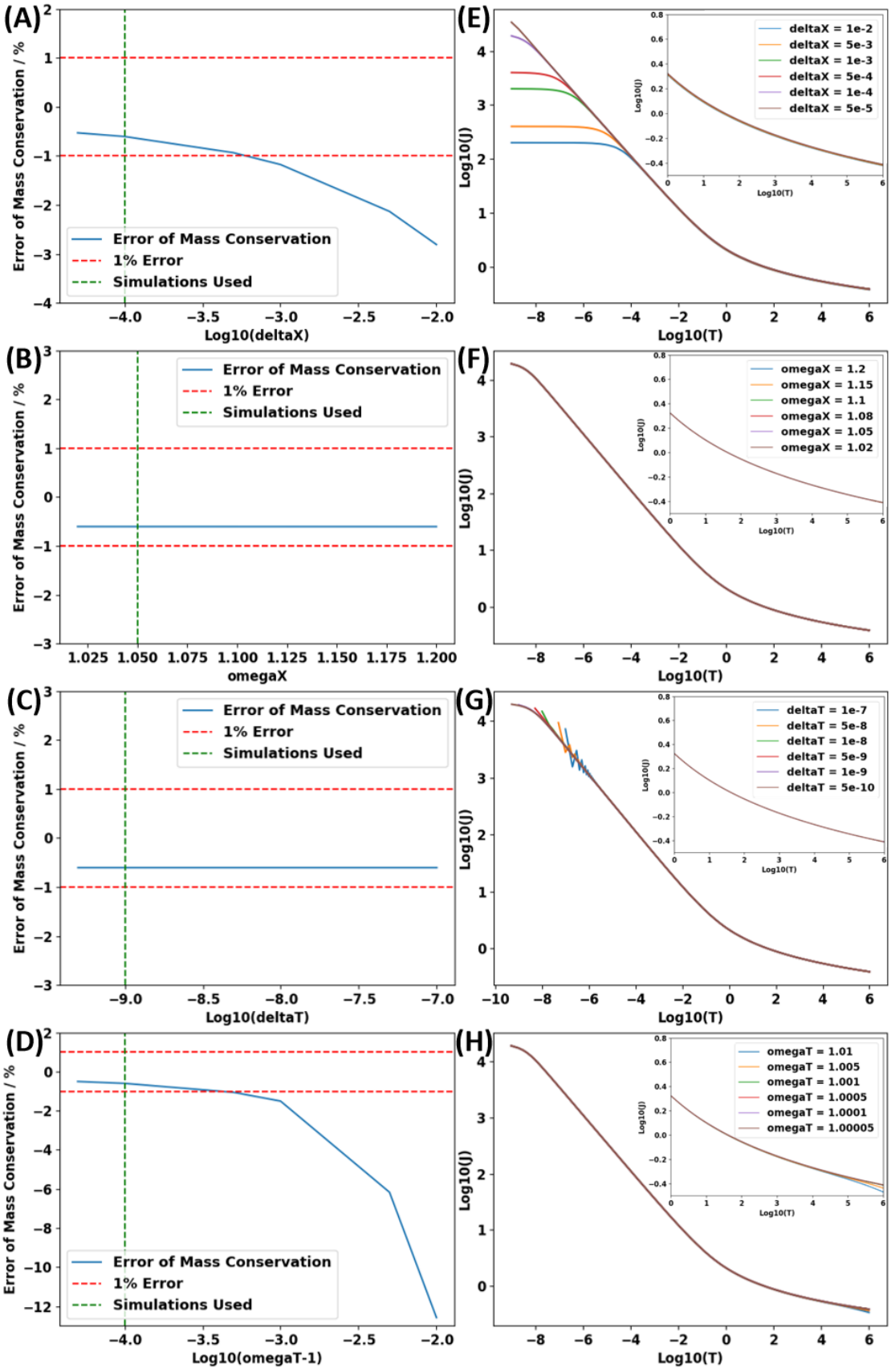


Figure 3.9: Errors of mass conservation **(A-D)** and current responses **(E-H)** for the microband electrode model varying dX, dT, ωX, and ωT.

As we observe in Figure 3.6 to 3.9, the parameter sets used for the simulations shows convergence because not only the the errors of mass conservation at the parameter sets stay at a very low level (below 1%), but also when a more precise parameter is chosen (for example, dX decreases from 10^{-8} to 5×10^{19}), the errors of mass conservation experience a decreased variation comparing to a less precise parameter chosen. The plots of currents also show that choosing a more precise parameter give trivial changes in the current responses. Therefore, we can assert that the set of parameters chosen is 'converged' before the simulation results are analysed and interpreted.

3.4.2.1 The 'one-dimensional' electrode models

The concentration profiles near the electrode surfaces for the 'two-dimensional' electrodes, i.e. the microsphere and the microcylinder electrodes, are shown in Figure 3.10(A-D) and 3.10(E-H), respectively, at $\log_{10}T = -2, 0, 2, 4$. The plots take the form of dimensionless concentration as a function of the dimensionless radial coordinate R. Figure 3.10(A) and 3.10(E) show that the depleted area of the analyte A around the electrode surface for the microcylinder electrode is obviously larger than that for the microsphere electrode at $\log_{10}T = -2$. As time evolves, the depleted areas increase for both models, and the depleted area for the microcylinder electrode stays larger than that for the microsphere electrode across the entire timescale show in Figure 3.10.

Combined with the fact that, after $\log_{10} T = -4$, the current density and the α values for the microsphere electrode are larger than those for the microcylinder electrode once they start to deviate from the Cottrell equation, as shown in Figure 3.5, we can assert that there is a huge difference in the diffusion towards these two electrodes as soon as their current responses deviate from the Cottrell equation. This is due to the three-dimensional radial diffusion from/to the microsphere electrode resulting in a larger diffusion source, and hence larger current density and α values. In contrast the two-

dimensional radial diffusion from/to the microcylinder electrode is less effective.

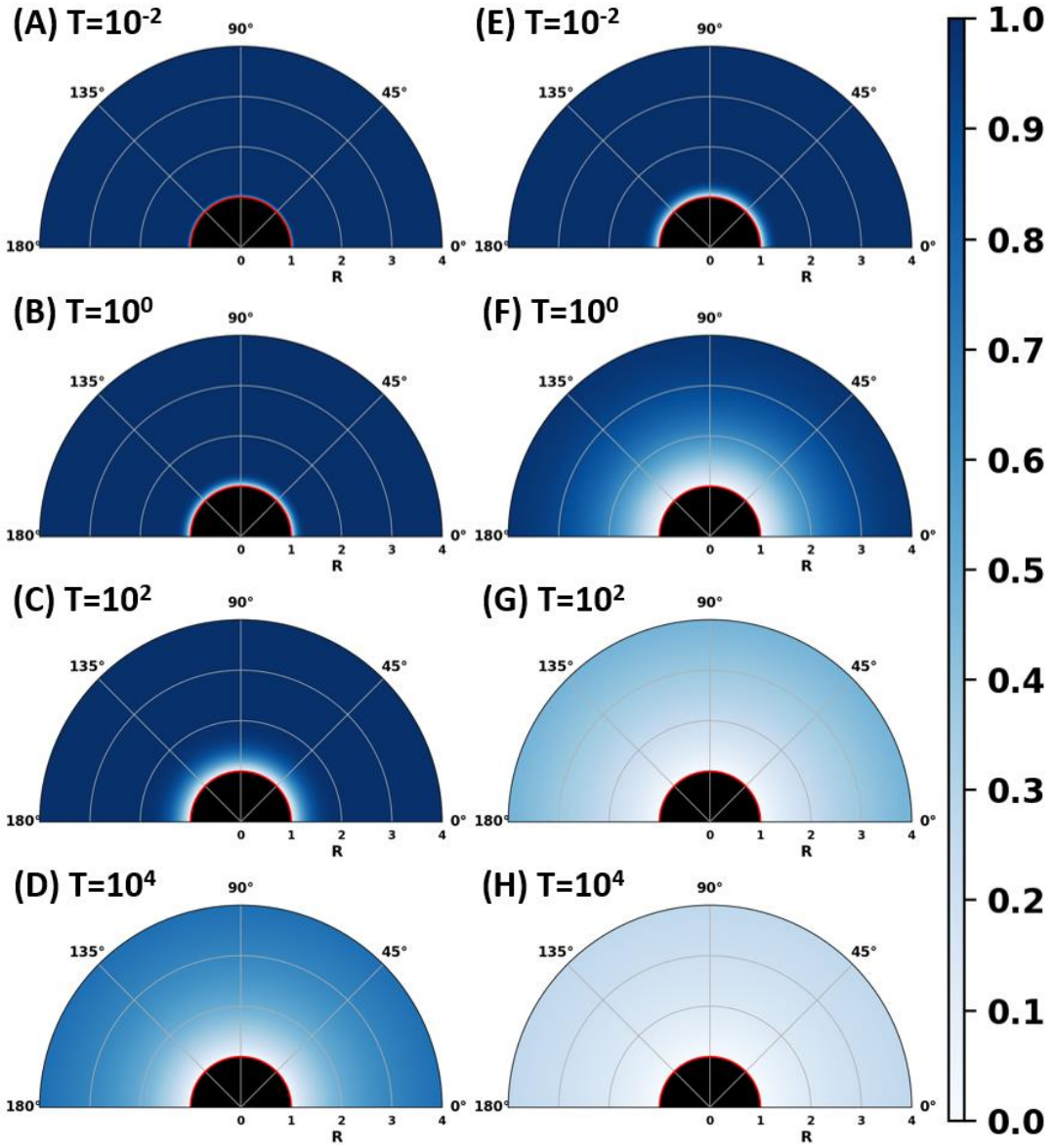


Figure 3.10: Concentration profiles extracted for the microsphere electrode **(A-D)** and the microcylinder electrode **(E-H)** at $\log_{10} T = -2, 0, 2, 4$ from top to bottom.

3.4.2.2 The 'two-dimensional' electrode models

The concentration profiles, in (*R, Z*) space, near the electrode surfaces for the 'two-dimensional' electrodes, i.e. the microdisc and the microband electrodes, are shown in Figure 3.11(A-D) and 3.11(E-H), respectively, at $\log_{10}T = -2, 0, 2, 4$. As shown in Figure 3.11(A) and 3.11(E), the depleted areas of the analyte *A* around the electrode surfaces for the microdisc electrode and the microband electrode are almost identical at $\log_{10}T = -2$. As time continues, however, the depleted areas increase for both models,

but the depleted area for the microcylinder electrode grows faster than that for the microdisc electrode shown in Figure 3.11.

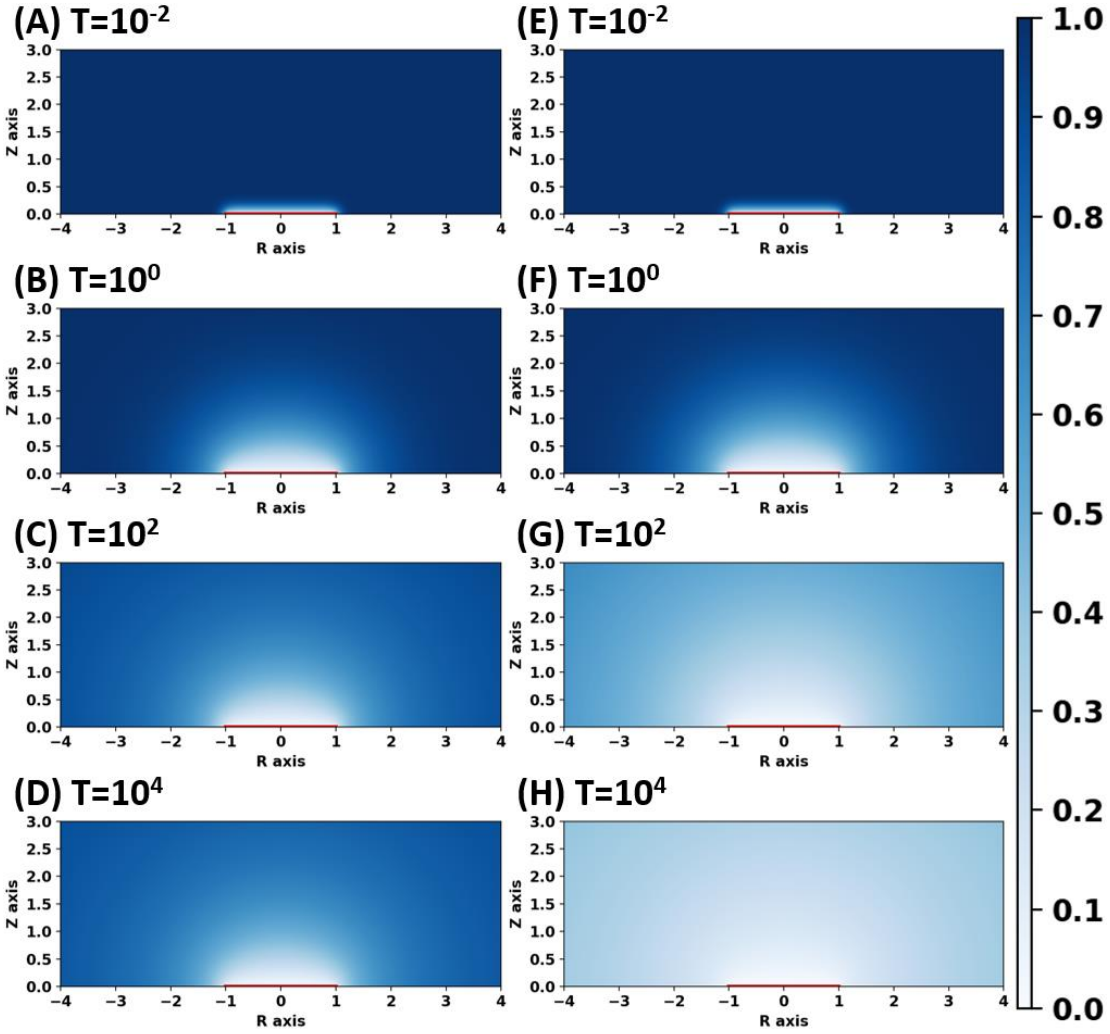


Figure 3.11: Concentration profiles extracted for the microdisc electrode **(A-D)** and the microband electrode **(E-H)** at $\log_{10} T = -2, 0, 2, 4$ from top to bottom.

These findings echo the curves for the currents and α values for these two electrodes in Figure 3.5. At $\log_{10}T = -2$, there is no obvious difference in the plots of currents and α values. For $\log_{10}T > -2$, the α values for the microband increases less rapidly than that for the microdisc electrode. This is caused by the additional radial diffusion for the microdisc electrode.

Of the four electrodes, two - the microsphere and the microdisc electrodes - reach a true steady state. The timescales at which this happens are very similar although the edge diffusion at the microdisc electrode can be seen to give rise to a slightly more

rapid response. A similar effect explains the significantly different timescales of the microcylinder and microband electrode responses.

3.5 Conclusions

In this chapter, we introduced a new parameter, the diffusion indicator α and applied this parameter to derive expressions for α from literature analytical and empirical equations for four different electrode geometries. With the help of concentration profiles extracted from the simulations, comparison of the current densities and the α values between the electrodes of interests showed the different contributions of planar and convergent/divergent diffusion in the different geometries. This newly introduced parameter α has a high sensitivity when investigating the diffusion phenomena whilst is simple and straightforward to use and analyse.

References

[1] H. Le, R. G. Compton, *Journal of Electroanalytical Chemistry*, **2020**, *866*, 114149.

[2] L. Bieniasz, J. González, Á. Molina, E. Laborda, *Electrochimica Acta* **2010**, *56*, 543–552.

[3] Y. Liu, H. Cai, H. Li, *Journal of Manufacturing Processes* **2015**, *17*, 162–170.

[4] S. Li, C. Peng, Y. Liu, K. Wang, H. Kong, Z. Wei, *The International Journal of Advanced Manufacturing Technology* **2019**, 1–9.

[5] I. B. Svir, A. I. Oleinick, *Journal of Electroanalytical Chemistry* **2001**, *499*, 30–38.

[6] S. Eloul, R. G. Compton, *ChemElectroChem* **2014**, *1*, 917–924.

[7] S. Eloul, E. Kätelhön, C. Batchelor-McAuley, K. Tschulik, R. G. Compton, *Journal of Electroanalytical Chemistry* **2015**, *755*, 136–142.

[8] K. Ngamchuea, C. Lin, C. Batchelor-McAuley, R. G. Compton, *Analytical Chemistry* **2017**, *89*, 3780–3786.

[9] L. Chen, C. Lin, R. G. Compton, *Physical Chemistry Chemical Physics.* **2018**, *20*, 15795–15806.

[10] C. Zhang, N. Driver, Q. Tian, W. Jiang, H. Liu, *Journal of Biomedical Materials Research - Part A*, **2018**, *106*, 1887–1895.

[11] D. Li, C. Batchelor-McAuley, L. Chen, R. G. Compton, *Physical Chemistry Chemical Physics*, **2019**, *21*, 9969–9974.

[12] D. H. Craston, C. P. Jones, D. E. Williams, N. E. Murr, *Talanta* **1991**, *38*, 17–26.

[13] J. A. Alden, R. G. Compton, *Journal of Electroanalytical Chemistry* **1996**, *404*, 27–35.

[14] L. Authier, C. Grossiord, P. Brossier, B. Limoges, *Analytical Chemistry* **2001**, *73*, 4450–4456.

[15] C. Amatore, E. Maisonhaute, G. Simonneau, *Electrochemistry Communications* **2000**, *2*, 81–84.

[16] C. Amatore, E. Maisonhaute, G. Simonneau, *Journal of Electroanalytical Chemistry* **2000**, *486*, 141–155.

[17] K. Aoki, J. Osteryoung, *Journal of Electroanalytical Chemistry* **1981**, *122*, 19–35.

[18] D. Shoup, A. Szabo, *Journal of Electroanalytical Chemistry* **1982**, *140*, 237–245.

[19] S. Coen, D. K. Cope, D. E. Tallman, *Journal of Electroanalytical Chemistry* **1986**, *215*, 29–48.

[20] P. M. Kovach, W. L. Caudill, D. G. Peters, R. M. Wightman, *Journal of Electroanalytical Chemistry* **1985**, *185*, 285–295.

[21] A. Szabo, D. K. Cope, D. E. Tallman, P. M. Kovach, R. M. Wightman, *Journal of Electroanalytical Chemistry* **1987**, *217*, 417–423.

[22] H. Le, E. Kätelhön, R. G. Compton, *Journal of Electroanalytical Chemistry* **2019**, *855*, 113602.

[23] I. B. Svir, A. I. Oleinick, R. G. Compton, *Russian Journal of Electrochemistry* **2003**, *39*, 160–164.

[24] R. G. Compton, E. Laborda, K. R. Ward, *Understanding Voltammetry: Simulation of Electrode Processes*, Imperial College Press, **2013**.

[25] D. Peaceman, H. Rachford, Jr., *Journal of the Society for Industrial and Applied Mathematics* **1955**, *3*, 28–41.

[26] J. Heinze, *Journal of Electroanalytical Chemistry and Interfacial Electrochemistry*, **1981**, *124*, 73–86.

[27] J. A. Alden, R. G. Compton, *The Journal of Physical Chemistry B* **1997**, *101*, 8941–8954.

[28] E. Kätelhön, R. G. Compton, *Analyst* **2015**, *140*, 2592–2598.

[29] E. Kätelhön, R. G. Compton, *Analyst* **2015**, *140*, 3290–3290.

[30] E. Kätelhön, R. G. Compton, *Analyst* **2016**, *141*, 1154–1154.

[31] R. G. Compton, C. E. Banks, *Understanding Voltammetry*, Third, World Scientific Press, **2018**.

[32] K. Aoki, K. Tokuda, H. Matsuda, *Journal of Electroanalytical Chemistry* **1987**, *230*, 61–67.

Chapter 4: The Diffusion Indicator: Microcylinder and Microring Electrodes

In this chapter the diffusion indicator α introduced in the previous chapter is further applied to characterise several different microcylinder and microring electrodes. Contrasting time scales of diffusive fluxes from different spatial locations are revealed and discussed. Moreover, the applicability of the Aoki equation [1] [*Journal of Electroanalytical Chemistry*, **1985**, *186*, 79] to the chronoamperometric currents for various cylinder-like models is explored and assessed. The results reported in this chapter are based on a published first-author paper [2] [*Journal of Electroanalytical Chemistry*, **2019**, *855*, 113602].

4.1 Introduction

As introduced in previous chapters, microelectrodes are essential to the electrochemical studies of mass transport, reaction mechanisms and voltammetry as reviewed in the literature [3–9]. In particular, diffusion can be readily studied through microcylinder electrodes and microwire electrodes [1, 10–33] because of the ease of fabrication and utilisation of the electrodes. From the theoretical perspective, the studies of diffusive fluxes towards microcylinder electrodes by Aoki et al [1] and Szabo et al [12] reported two approximate equations in 1985 and 1987, respectively, to describe the chronoamperometric current towards an infinitely long cylindrical electrode. In 2009, Fang et al [19] proposed a different approximate equation which features a simpler form.

In the following years, there were more simulation studies of more complex cylinder-like systems. Ferrigno et al [17] reported, in 1997, the numerical simulations of a

‘protruding microdisc’ model and discussed the influence of the protruding cylinder-like part of the electrode on the total current. Dickinson et al [18] presented simulations of ‘top-only’ and ‘side-only’ cylindrical electrode models with only the top or the side of the cylinder being electrochemical active, respectively, and further reported the analysis of the partial derivative of current with respect to time in $\log_{10}$ scales, on which basis we develop the diffusion indicator α in this chapter. Britz et al [21] reported a comparison between the chronoamperometric currents at an infinitely long cylindrical electrode and a capped cylindrical electrode in 2010 and discuss the (quasi-) steady-state currents in these two models with respect to the length of the cylindrical electrode. Bieniasz has additionally presented studies [22–24] to provide various simulation methods for cylindrical electrodes.

In this chapter, we apply the previously introduced diffusion indicator α, and use it to analyse simulated chronoamperometric data of cylinder-like electrode models. In addition, we include an analysis of a microring model to further discuss and give insight to diffusion from/to different spatial locations surrounding the electrodes.

4.2 Theoretical methods

In this section, we present the theoretical models to be studied in detail followed by the introduction of the dimensionless parameters, the simulation grids, and the computational methods used in this chapter.

4.2.1 Simulation models

In this chapter we simulate the chronoamperometric processes based on a cylindrical wire electrode geometry considering two different situations as presented in Figure 4.1 ① and ②. The first model, the ‘annular band’ electrode model, is an infinite cylinder featuring an electrochemically active area in the shape of an annular band on a

cylindrical insulating surface. The second model is a normal cylinder electrode, the 'full cylinder' electrode model, with two variations of this model: the 'side-active-only cylinder' electrode model, and the 'end-active-only cylinder' electrode model, where only the side or the end of the cylinder, respectively, is set to be electrochemically active. We further model the chronoamperometry in an electrode geometry where a ring-shape electrode is embedded on a surface, the 'embedded ring' electrode model, as shown in Figure 4.1 ③, which is explained and analysed later in this chapter.

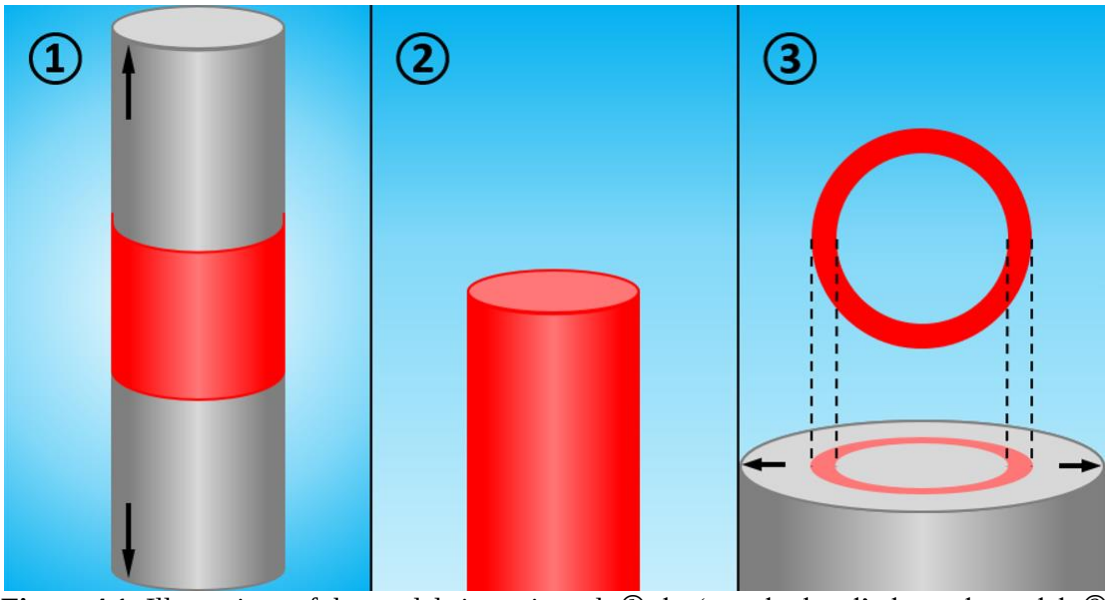


Figure 4.1: Illustrations of the models investigated: ① the 'annular band' electrode model, ② the cylinder electrode model, ③ the 'embedded ring' electrode model. The black arrows in the figures represent infinitely expanding insulating areas.

In all models, the initial concentration of the analyte A is set to be c^* uniformly before the reaction starts. After applying a sufficiently large overpotential ('potential step chronoamperometry') at the electrode surfaces, A is reduced at the solution-electrode interface where a single-electron-transfer reaction $A + e^- \rightarrow B$ occurs. Assuming a sufficiently large overpotential at the electrode and sufficient electrolyte concentration, the reaction of analyte is considered to be diffusion-controlled. By varying the sizes of the electrode surfaces, the time evolution of the currents and the concentration profiles are recorded and subsequently investigated.

4.2.1.1 The ‘annular band’ electrode model

First, the ‘annular band’ electrode model is illustrated in Figure 4.2 ① which consists of an infinitely long insulating cylinder with radius r_e in a solution of the analyte A and an electrochemically active area with length l_e. The grey area is insulated, the red area is the electrode surface, and the blue area is the solution of analyte A.

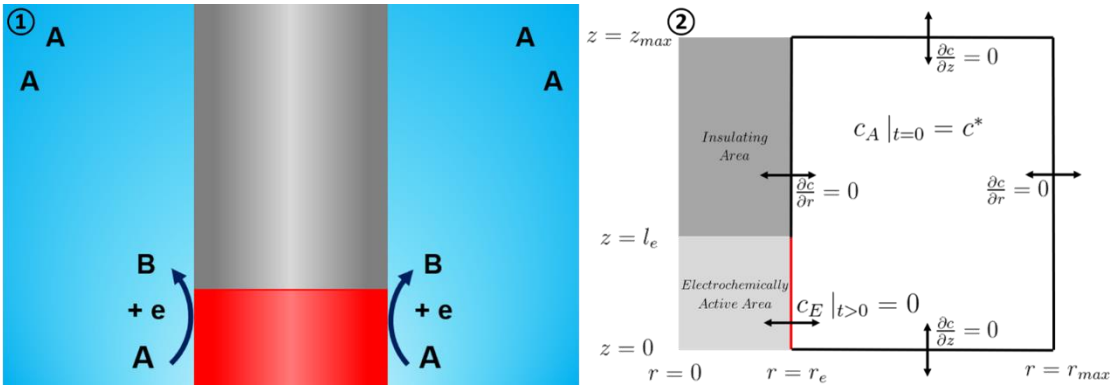


Figure 4.2: Cross-sectional illustration (①) and boundary conditions (②) of the ‘annular band’ electrode model. c is the concentration of analyte A, c_A is the concentration of A for all of the points in the model, c^* is the initially uniform concentration of A, c_E is the concentration of A for points at the surface of the electrochemically active area, r_{max} and z_{max} are the boundaries of the simulated space in the z- and r-axis, l_e is the length of the annular band in the z-axis.

This model is in cylindrical coordinates (r, z, ϕ), where r is the radial distance, z is the axial distance, and ϕ is the angle around the z-axis of the plane set by the r-axis and the z-axis. The mass transport here can be described by the diffusion equation:

$$\frac{\partial c}{\partial t} = D\nabla^2 c = D\left(\frac{\partial^2 c}{\partial r^2} + \frac{1}{r}\frac{\partial c}{\partial r} + \frac{\partial^2 c}{\partial z^2} + \frac{1}{r^2}\frac{\partial^2 c}{\partial \phi^2}\right) \quad (4.1)$$

which, due to the rotational symmetry around the z-axis in this model, a simplification of this model from a three-dimensional coordinate system (r, z, ϕ) to a two-dimensional coordinate system (r, z) was made and the diffusion equation for this model, and all following models, can be simplified to:

$$\frac{\partial c}{\partial t} = D\nabla^2 c = D\left(\frac{\partial^2 c}{\partial r^2} + \frac{1}{r}\frac{\partial c}{\partial r} + \frac{\partial^2 c}{\partial z^2}\right) \quad (4.2)$$

The boundary conditions for this model are presented in Figure 4.2 ②. The initial concentration of A in solution is set to c^*:

$$t = 0, r_e \le r \le r_{max}, 0 \le z \le z_{max}: \quad c = c^* \tag{4.3}$$

For t > 0, the concentration of A at the electrode surface is set to 0 corresponding to the large potential step applied at t = 0:

$$t > 0, r = r_e, 0 \le z \le l_e: \quad c = 0 \tag{4.4}$$

No-flux boundaries are set everywhere else:

$$\begin{cases} t > 0, r = r_e, l_e \le z \le z_{max}: & \dfrac{\partial c}{\partial r} = 0 \\ t > 0, r = r_{max}, 0 \le z \le z_{max}: & \dfrac{\partial c}{\partial r} = 0 \\ t > 0, 0 \le r \le r_{max}, z = 0: & \dfrac{\partial c}{\partial z} = 0 \\ t > 0, 0 \le r \le r_{max}, z = z_{max}: & \dfrac{\partial c}{\partial z} = 0 \end{cases} \tag{4.5}$$

where the simulation space depends on the total simulation time t_{sim}:

$$\begin{cases} r_{max} = r_e + x_{sim} \\ z_{max} = l_e + x_{sim} \\ x_{sim} = 6\sqrt{D t_{sim}} \end{cases} \tag{4.6}$$

where the x_{sim} is set in a way that the simulation space is large enough, as discussed in the previous chapter, so that concentration changes at the electrode are not affected by the boundaries at the far ends [34].

Following Fick's first law and Faraday's law, the current responses for the 'annular band' electrode model can be calculated as:

$$I_s = F j_s \quad \text{where} \quad j_s = -2\pi D \int_0^{l_e} \left.\frac{\partial c}{\partial r}\right|_{r=r_e} r_e dz \tag{4.7}$$

where I_s is the current to the side of the cylinder, F is the Faraday constant, and j_s is the flux of the analyte A to the side of the cylinder.

4.2.1.2 The cylinder electrode models

As shown in Figure 4.3 ①, the 'full cylinder' electrode model, with the radius r_e and the length of the cylinder l_e, resembles a wire electrode as commonly used in experiments. To investigate the electrochemical reactions at the side and the end of the

cylinder electrode, we introduced two additional limiting models, the 'side-active- only cylinder' electrode model, and the 'end-active-only cylinder' electrode model, where the side or the end, respectively, are set electrochemically active while keeping other model parameters unchanged, shown in Figure 4.3 ② and ③.

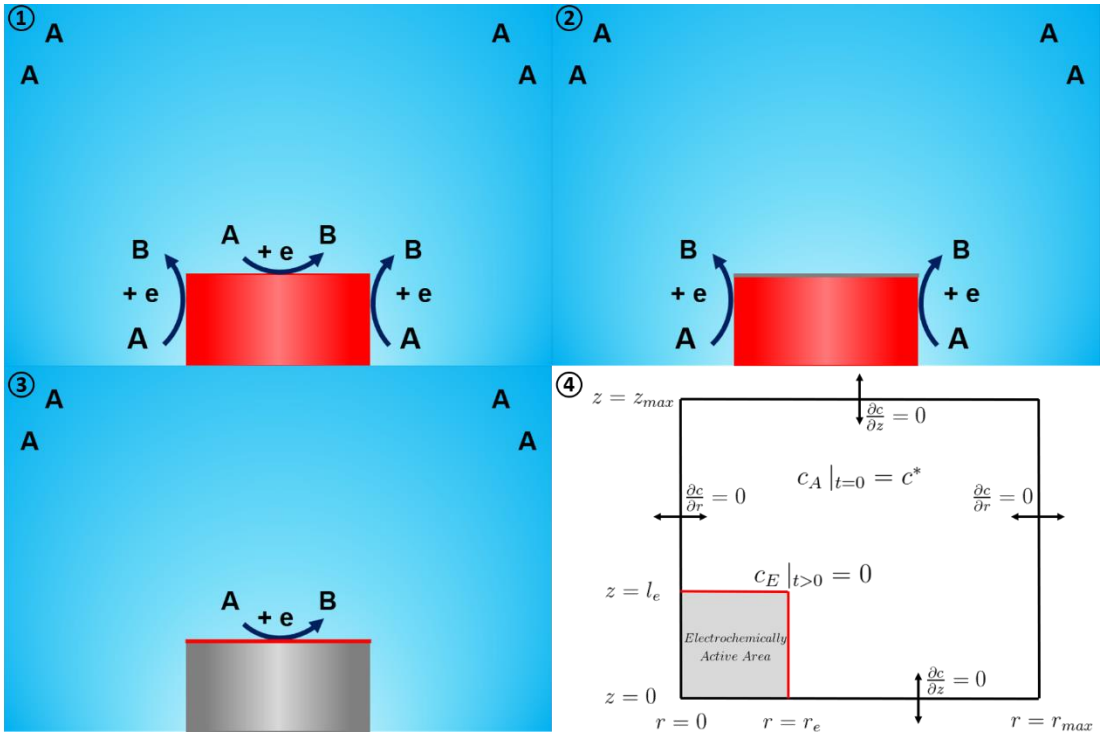


Figure 4.3: Cross-sectional illustrations of 3 electrode models: the 'full cylinder' electrode model (①), the 'side-active-only cylinder' electrode model (②), and the 'end-active-only cylinder' electrode model (③); boundary conditions (④) of these three models.

In all cylinder electrode models, the diffusion equation can be expressed by Eqn (4.2). The only difference amongst these three models is the difference in sizes of electrode surface areas and the associated boundary conditions. The latter, shown in Figure 4.3 ④, can be illustrated using a single figure with different sizes of the electrochemically active boundaries and no-flux boundaries. The initial concentration for all of the points in the simulations of these three models is also set as c^* as in Eqn (4.3) except that the points within the electrode are excluded from the simulations and the concentration for those points are set to be 0 at t = 0:

$$t = 0, 0 \le r \le r_e, 0 \le z \le l_e: \quad c = 0 \tag{4.8}$$

No-flux boundaries are set similarly to Eqn (4.5). The differences in the boundary conditions among the cylinder electrode models and compared with the 'annular band' electrode model are as following: For the 'full cylinder' electrode model:

$$\begin{cases} t > 0, r = r_e, 0 \le z \le l_e: & c = 0 \\ t > 0, 0 \le r \le r_e, z = l_e: & c = 0 \end{cases} \tag{4.9}$$

For the 'side-active-only cylinder' electrode model:

$$\begin{cases} t > 0, r = r_e, 0 \le z \le l_e: & c = 0 \\ t > 0, 0 \le r \le r_e, z = l_e: & \dfrac{\partial c}{\partial z} = 0 \end{cases} \tag{4.10}$$

For the 'end-active-only cylinder' electrode model:

$$\begin{cases} t > 0, r = r_e, 0 \le z \le l_e: & \dfrac{\partial c}{\partial r} = 0 \\ t > 0, 0 \le r \le r_e, z = l_e: & c = 0 \end{cases} \tag{4.11}$$

where the simulation space is:

$$\begin{cases} r_{max} = r_e + x_{sim} \\ z_{max} = l_e + x_{sim} \\ x_{sim} = 6\sqrt{D t_{sim}} \end{cases} \tag{4.12}$$

There are two means of current calculation, i.e. the currents towards the side and the end of the cylinder. For the current towards the side of the cylinder, the calculation follows Eqn (4.7). The current towards the end of the cylinder can be calculated as:

$$\begin{cases} I_s = F j_s \quad \text{where} \quad j_s = -2\pi D \displaystyle\int_0^{l_e} \left.\frac{\partial c}{\partial r}\right|_{r=r_e} r_e dz \\ I_e = F j_e \quad \text{where} \quad j_e = -2\pi D \displaystyle\int_0^{r_e} \left.\frac{\partial c}{\partial z}\right|_{z=l_e} r dr \\ I_t = I_s + I_e \end{cases} \tag{4.13}$$

where I_e and j_e are the current and the flux of A to the end of the cylinder, and the total current I_t for the 'full cylinder' model is the sum of the current towards the side I_s and the end I_e of the electrode. The current responses in the 'side-active-only cylinder' model and the 'end-active-only cylinder' model are I_s and I_e, respectively.[1] We will

[1] We note that the simulations for these three models are separate. For example, I_s in the 'full cylinder' model is different from the I_s in the 'side-active-only cylinder' electrode model.

later investigate in the different diffusion fields the effects on these three models with different electrode geometries by varying the length l_e for a constant r_e.

4.2.1.3 The 'embedded ring' electrode model

As presented in Figure 4.4 ①, this model features an electrochemically active ring area enclosing an insulating circular area and surrounded by an infinite, flat, insulating area. The diffusion equation adopted in this model is Eqn (4.2).

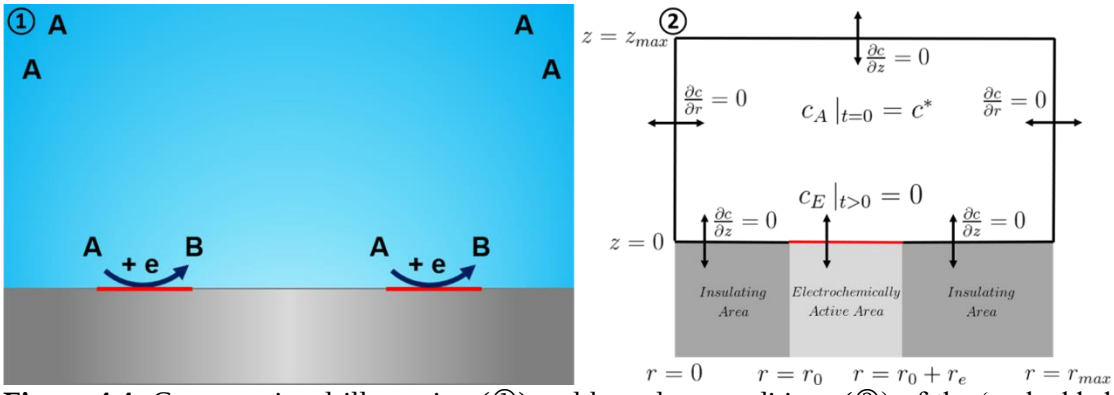


Figure 4.4: Cross-sectional illustration (①) and boundary conditions (②) of the 'embedded ring' electrode model. r_0 is the radius of the insulating area and the inner radius of the ring area, r_e is the width of the ring area.

The boundary conditions can be found in Figure 4.4 ②, where the outer radius of the ring area is the sum of the radius of the insulating area r_0 and the width of the ring area r_e. The initial concentration of all points and the no-flux boundaries are set as in Eqn (4.3) and Eqn (4.5). On the surface where the electrochemically active ring embedded, the boundary conditions are:

$$\begin{cases} t > 0, 0 \le r < r_0, z = 0: & \dfrac{\partial c}{\partial r} = 0 \\ t > 0, r_0 \le r \le r_0 + r_e, z = 0: & c = 0 \\ t > 0, r_0 + r_e < r \le r_{max}, z = 0: & \dfrac{\partial c}{\partial r} = 0 \end{cases} \tag{4.14}$$

where the simulation space is:

$$\begin{cases} r_{max} = r_0 + r_e + x_{sim} \\ z_{max} = x_{sim} \\ x_{sim} = 6\sqrt{D t_{sim}} \end{cases} \tag{4.15}$$

The current can be calculated as:

$$I_r = Fj_r \quad \text{where} \quad j_r = -2\pi D \int_{r_0}^{r_0+r_e} \left.\frac{\partial c}{\partial z}\right|_{z=0} r dr \tag{4.16}$$

where I_r is the current, and j_r is the flux of the analyte A.

4.2.2 Dimensionless parameters

Similar to the approach in the previous chapter, the dimensional simulated results were converted to their dimensional counterparts to present the results in a simple and universal way which also enables a straightforward comparison between different experimental systems. The conversions are shown in Table 4.1.

Table 4.1: Conversion of dimensional parameters to dimensionless ones where r_r is the reference length of respective model, R is the Universal Gas Constant, and T is the temperature.

Dimensionless Parameters	Conversions
Concentration of species j	$C_j = \frac{c_j}{c^*}$
Diffusion coefficient of species j	$d_j = \frac{D_j}{D}$
Radial distance	$R = \frac{r}{r_r}$
Axial distance	$Z = \frac{z}{r_r}$
Time	$T = \frac{Dt}{r_r^2}$
Potential	$\theta = \frac{F}{\boldsymbol{RT}}(E - E_f^0)$
Current	$J = \frac{I}{Fr_r Dc^*}$

Thus, the diffusion equation, Eqn (4.2), can be rewritten in its dimensionless form:

$$\frac{\partial C}{\partial T} = d_A\left(\frac{\partial^2 C}{\partial R^2} + \frac{1}{R}\frac{\partial C}{\partial R} + \frac{\partial^2 C}{\partial Z^2}\right) \tag{4.17}$$

where C and d_A are the dimensionless concentration and diffusion coefficient of the analyte A, respectively, as defined in Table 4.1. The dimensionless currents, converted from Eqn (4.7), Eqn (4.13), and Eqn (4.16), are:

$$J_s = -2\pi d_A \int_0^{L_e} \left.\frac{\partial C}{\partial R}\right|_{R=1} dZ \tag{4.18}$$

$$\begin{cases} J_s = -2\pi d_A \int_0^{L_e} \left.\frac{\partial C}{\partial R}\right|_{R=1} dZ \\ J_e = -2\pi d_A \int_0^{1} \left.\frac{\partial C}{\partial Z}\right|_{Z=L_e} RdR \\ J_t = J_s + J_e \end{cases} \tag{4.19}$$

$$J_r = -2\pi d_A \int_1^{1+R_e} \left.\frac{\partial C}{\partial Z}\right|_{Z=0} RdR \tag{4.20}$$

where L_e is the dimensionless length of the electrode, and R_e is the dimensionless width of the electrochemically active area.

4.2.3 Expanding simulation grids

For each model in this chapter, there is an expanding time grid, as defined in Appendix.A, employed in every simulation model. For the 'annular band' electrode model, the simulation space points in the Z-axis consist of a double-expanding space grid and a single-expanding space grid shown in Figure 4.5. There is a single-expanding space grid in the R-axis. Furthermore, as shown in Figure 4.6, there are both a double-expanding grid and a single-expanding grid in the Z- and R-axis for the cylinder models. Finally, there are two double-expanding grids and one single-expanding grid in the R-axis as shown in Figure 4.7, whilst there is a single-expanding grid in the Z-axis for the 'embedded ring' electrode model.

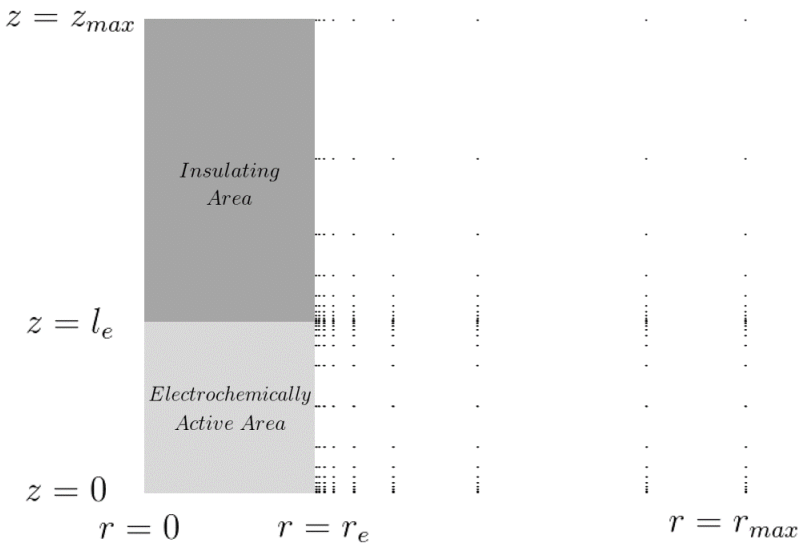


Figure 4.5: Cross-sectional illustration of the simulation space points for the 'annular band'

electrode model. r_{max} and z_{max} are the boundaries of the simulated space in the z- and r-axis, l_e is the length of the annular band in the z-axis.

4.2.4 Computational methods

Customised simulation software was developed in C++ for all of the models reported in this chapter. Following the finite difference approach, we discretise partial differential equations for solution via matrix equations. The alternating direction

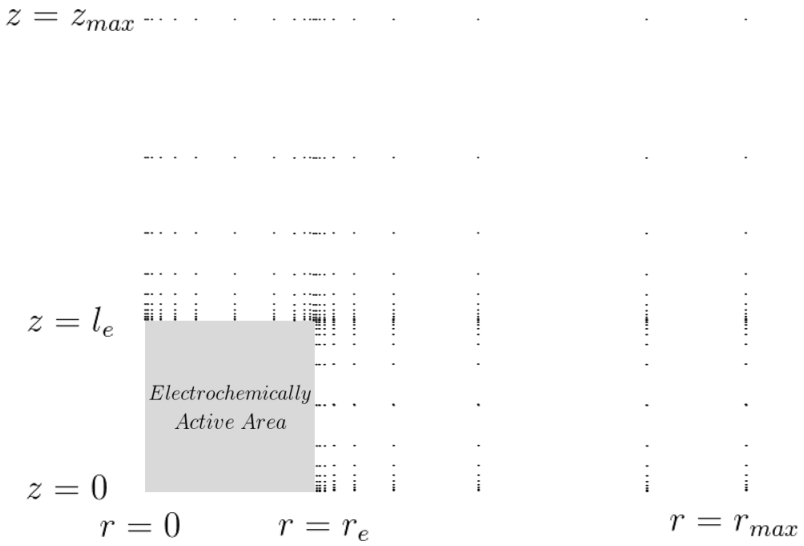


Figure 4.6: Cross-sectional illustration of the simulation space points for the 'full cylinder' electrode model, the 'side-active-only cylinder' electrode model, and the 'end-active-only cylinder' electrode model. r_e is the radius of the electrode.

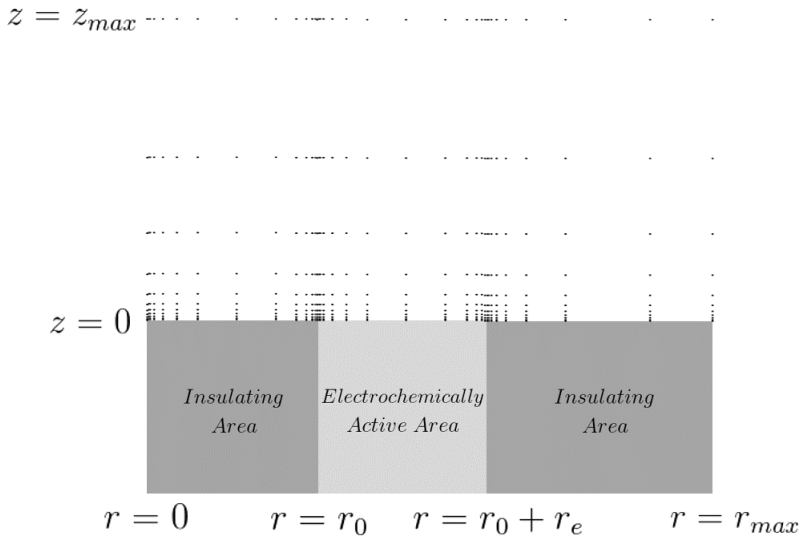


Figure 4.7: Cross-sectional illustration of the simulation space points for the 'embedded ring' electrode model. r_0 is the radius of the insulating area and the inner radius of the ring area, r_e is the width of the ring area.

implicit (ADI) method [35–37] is used to convert the resulting systems of linear equations to tri-diagonal matrix equations that can be solved via the Thomas algorithm [38]. OpenMP is used for the parallel computing and results are processed and visualised via Python scripts using the NumPy and matplotlib libraries. An expanding time grid is implemented for all models for better accuracy at short time scales. Further details can be found in the textbook [34].

4.3 Results and discussion

The following section reports and discusses simulation results for different models in the order in which the respective systems were introduced. The 'annular band' electrode model, the 'full cylinder' electrode model, the 'side-active-only cylinder' electrode model, and the 'end-active-only cylinder' electrode model are addressed first and the diffusion towards the side and the end of a cylindrical electrode are analysed. Subsequently, the 'embedded ring' electrode model is discussed to further investigate and enlighten related diffusion processes and to establish analogies among the models.

For clarity in the following discussion, first, we note that the derivation and definition of the diffusion indicator α, which is applied in this chapter, are mentioned in the previous chapter. Second, different zones are termed as shown in Figure 4.8.

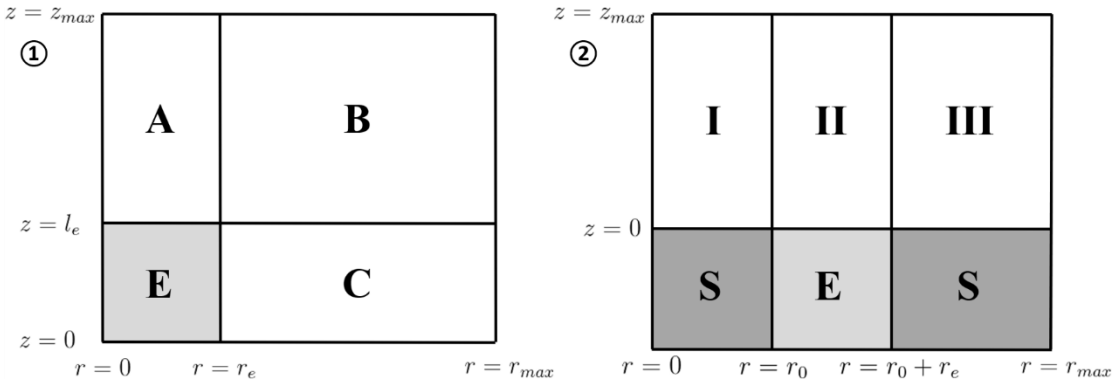


Figure 4.8: Different zones in the 'annular band' electrode model, the cylinder models (①) and the 'embedded ring' model (②).

In the 'annular band' electrode model, the zones *A* and *E* are the insulating body of

the cylinder on which the electrode is mounted and the electrode, respectively, while the zones *B* and *C* are in solution. For the cylinder electrode models, the zone *E* is the electrode and the zones *A, B* and *C* are in solution. In the 'embedded ring' electrode model, the zones *E* and *S* are the electrode and the insulating substrate, respectively, while the zones *I, II,* and *III* are in solution.

4.3.1 Testing numerical simulations

The rigorous and careful testing and validation [39] of all of the models built are essential. Thus, the comprehensive tests are employed first including convergence studies and studies of error of mass conservation. All models are tested in convergence studies and through the error of mass conservation by varying the space step *dX*, time step *dT*, space expanding factor ωX, and time expanding factor ωT in the simulations. Appropriate parameter sets were obtained for different models shown in Table 4.2 by varying the four parameters (*dX*, *dT*, ωX, and ωT).

Table 4.2: Dimensionless parameter sets for simulation models

Dimensionless Parameters	The 'Annular Band' Model	Cylinder Models	The 'Embedded Ring' Model
Potential, θ	-50	-50	-50
Initial concentration, C^*	1	1	1
Diffusion coefficient, *d*	1	1	1
Reference distance, R_0	$R_f = 1$	$R_f = 1$	$R_f = 1$
Simulation time, *T*	10^6	10^6	10^6
Space step, *dX*	10^{-4}	5×10^{-5}	10^{-5}
Space expand factor, *wX*	1.03	1.03	1.05
Time step, *dT*	5×10^{-9}	10^{-11}	10^{-11}
Time expand factor, *wT*	1.0001	1.00005	1.0001

The errors of mass conservation, defined in Appendix.B, calculated for each of the simulation model of different L (or R_e) from 0.1 to 1000 remain under 1% for the 'annular band' electrode model and the 'embedded ring' electrode model as shown in Figure 4.9. Moreover, the errors of mass conversions of different L are below 2% for the cylinder electrode models. Therefore, the errors of mass conversions for all models are considered to be trivial which ensures the authenticity of the simulation models.

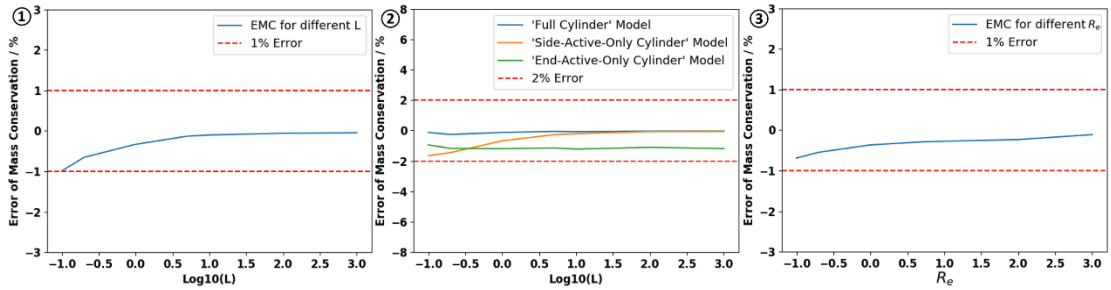


Figure 4.9: Errors of mass conservation calculated for different L (or R_e) from 0.1 to 1000 for: ① the 'annular band' electrode model; ② the 'full cylinder' electrode model, the 'side-active-only cylinder' electrode model, and the 'end-active-only cylinder' electrode model; ③ the 'embedded ring' electrode model.

The current responses and the errors of the mass conservation for each model in this chapter are obtained to ensure convergence in following sections, where the values of all but one parameter are kept constant (dX, dT, ωX, and ωT), and the latter is varied.

4.3.1.1 Testing the 'annular band' electrode model

First, we performed the tests of errors of mass conservation and the convergence studies for the 'annular band' electrode model for two L (0.1 and 1000). The errors of mass conservation for different test simulations, varying each one of the simulation parameters stated in previous sections, are shown in Figure 4.10. Apart from test simulations varying dT, the errors of mass conservation of the simulations varying the other three parameters decrease as those parameters decrease. When these simulation parameters were decreased to an extent, the errors of mass conservation remain on a lower level (below 1%). When varying dT, the errors are small throughout.

The convergence studies for the ‘annular band’ electrode model are shown in Figure 4.11. As the simulation parameters decrease to a sufficient extent, the curves of the current responses remain at similar levels. Thus, combined with the tests of the errors of mass conservation, the set of parameters chosen previously is considered ‘converged’ before the simulation results are analysed and interpreted.

4.3.1.2 Testing the cylinder electrode models

Second, we performed the tests of errors of mass conservation and the convergence studies for the ‘full cylinder’ electrode model, the ‘side-active-only cylinder’ electrode model, and the ‘end-active-only cylinder’ electrode model for two L (0.1 and 1000). The errors of mass conservation for different test simulations, varying each one of the simulation parameters stated in previous sections, are shown in Figure 4.12. Similarly, we ensure that the errors of mass conservation for the simulation results analysed and discussed in later sections for all models remain on a low level (below 2%).

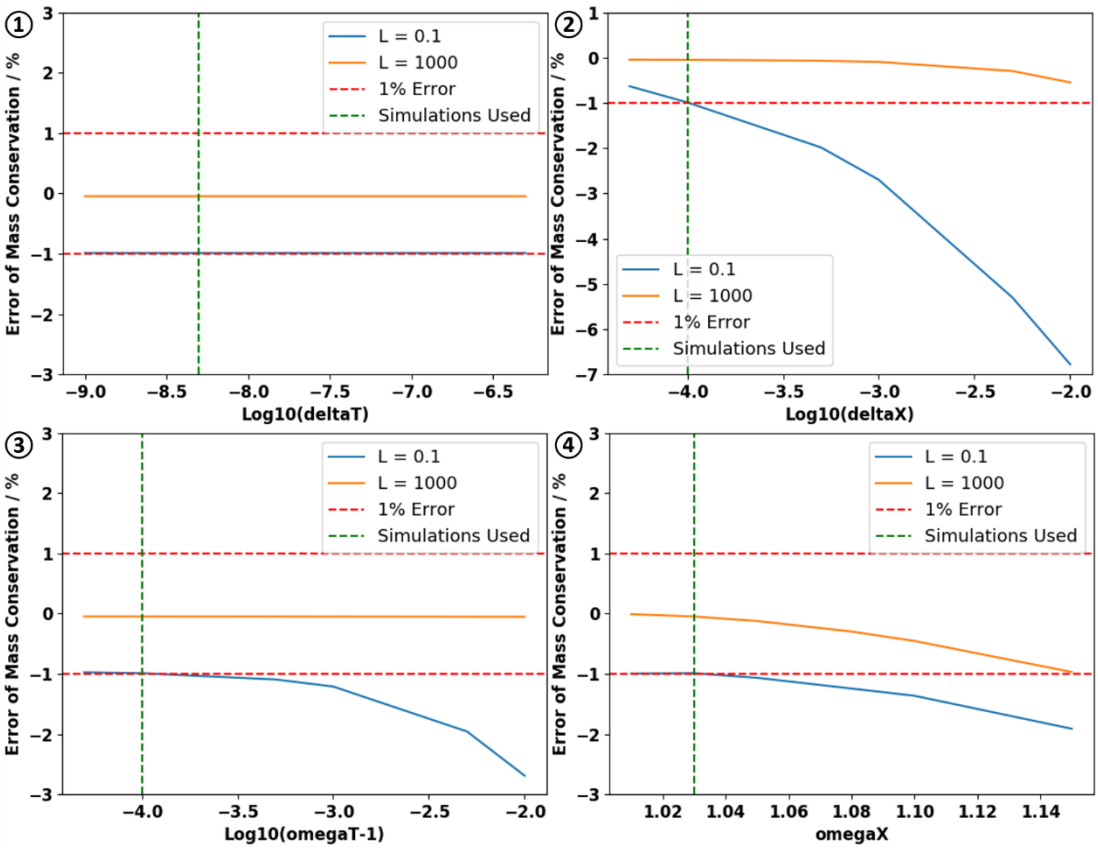


Figure 4.10: Errors of mass conservation calculated for L = 0.1 and 1000 for the ‘annular band’

electrode model varying: ① dT; ② dX; ③ ωT; ④ ωX.

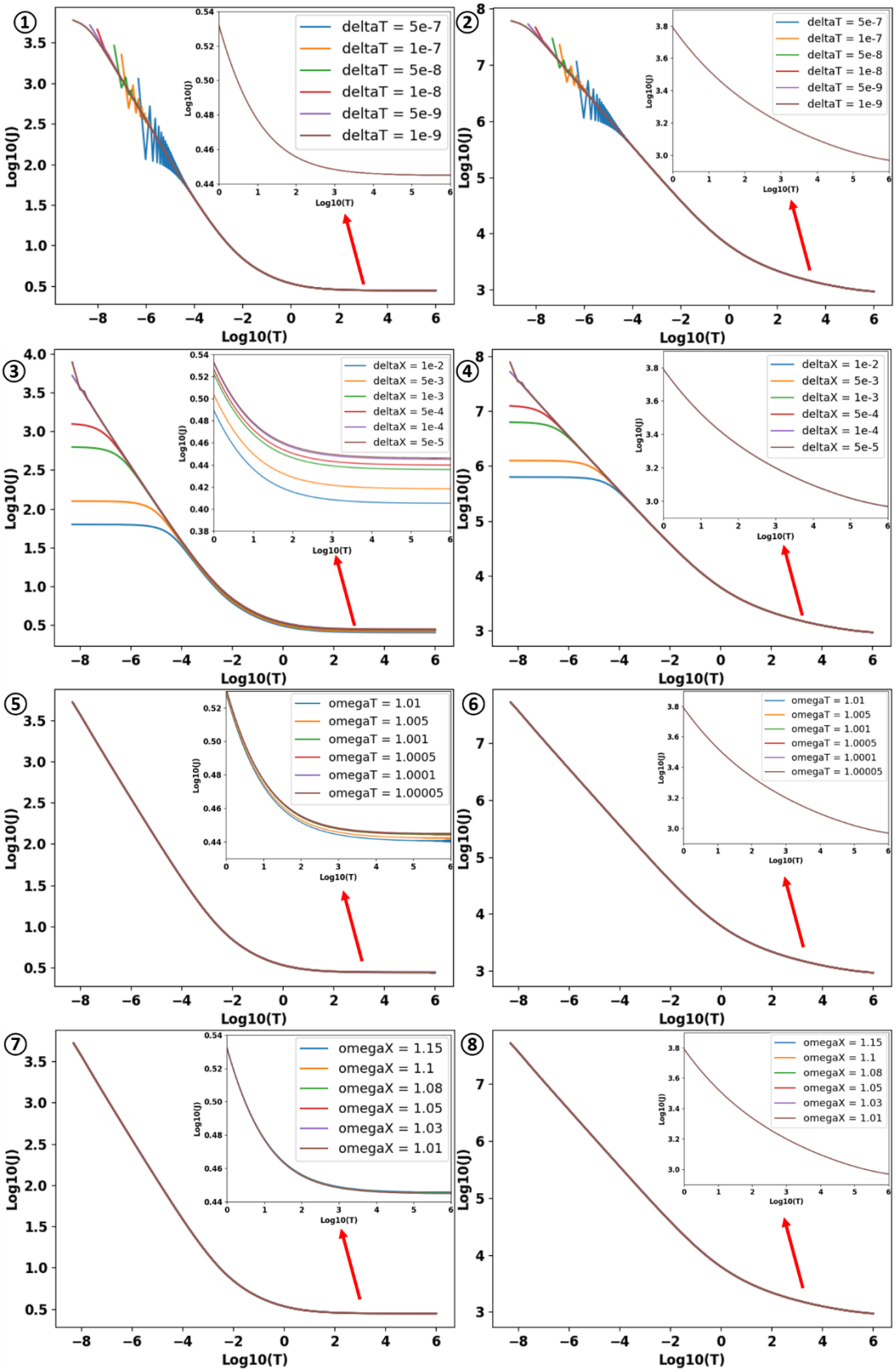


Figure 4.11: Current responses of test simulations for L = 0.1 (left) and 1000 (right) for the 'annular band' electrode model varying: dT: ①②; dX: ③④; ωT: ⑤⑥; ωX: ⑦⑧.

The convergence studies for the 'full cylinder' electrode model, the 'side-active only cylinder' electrode model, and the 'end-active-only cylinder' electrode model are shown in Figure 4.13, Figure 4.14, Figure 4.15, and Figure 4.16. As the simulation parameters decrease sufficiently, the curves of current responses remain at similar levels. Thus, combined with the tests of the errors of mass conservation, the set of parameters chosen is deemed 'converged'.

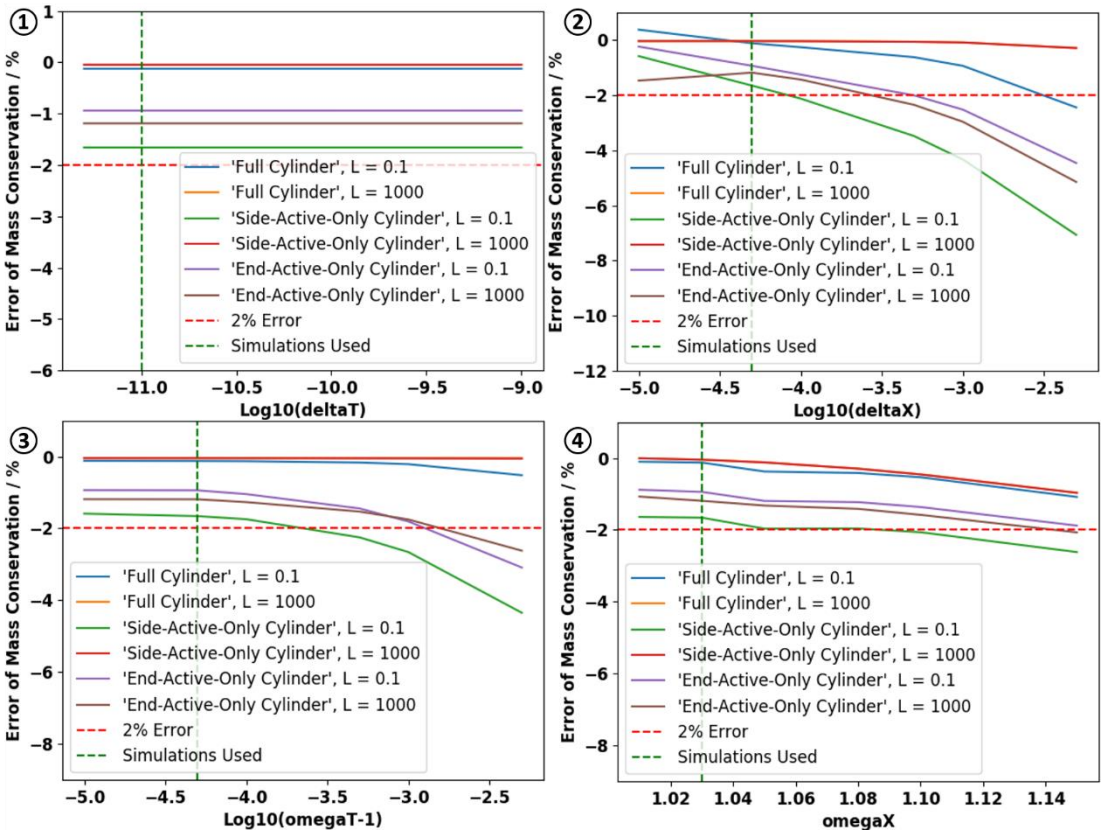


Figure 4.12: Errors of mass conservation calculated for L = 0.1 and 1000 for the 'full cylinder' electrode model, the 'side-active-only cylinder' electrode model, and the 'end-active-only cylinder' electrode model varying: ① dT; ② dX; ③ ωT; ④ ωX.

4.3.1.3 Testing the 'annular band' electrode model

Finally, we performed the tests of errors of mass conservation and the convergence studies for the 'embedded ring' electrode model for two L (0.1 and 1000). The errors of mass conservation for different test simulations, varying one of the simulation parameters stated in previous sections, are shown in Figure 4.17. Similarly, we ensure that the errors of mass conservation for the simulation results analysed and discussed

in later sections for all models remain on a low level (below 2%).

Moreover, the convergence studies for the 'embedded ring' electrode model are shown in Figure 4.18. As simulation parameters decrease to sufficiently small values, the variation in the curves of currents becomes trivial. Thus, combined with the tests of errors of mass conservation, this set of parameters is deemed 'converged'.

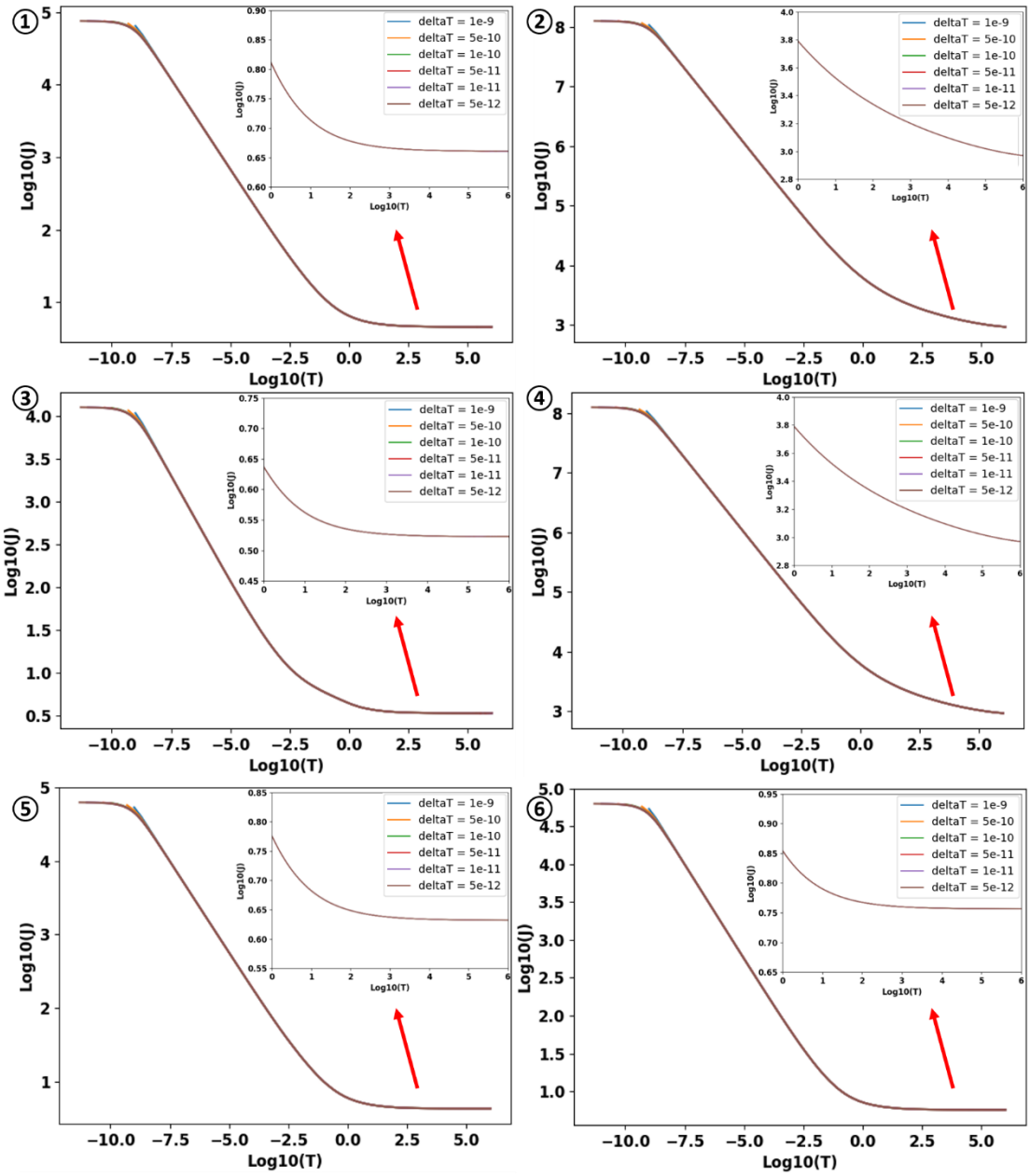


Figure 4.13: Current responses of test simulations for L = 0.1 (left) and 1000 (right) varying *dT* for: ①② the 'full cylinder' electrode model; ③④ the 'side-active-only cylinder' electrode model; ⑤⑥ the 'end-active-only cylinder' electrode model.

4.3.2 The ‘annular band’ electrode model

Simulations for different sizes of the electrochemically active area in this model were computed as the dimensionless length L of the cylinder was varied while the radius was kept constant and set to a reference length r_r as defined in the dimensionless coordinates. The temporal evolution of the dimensionless currents J for four

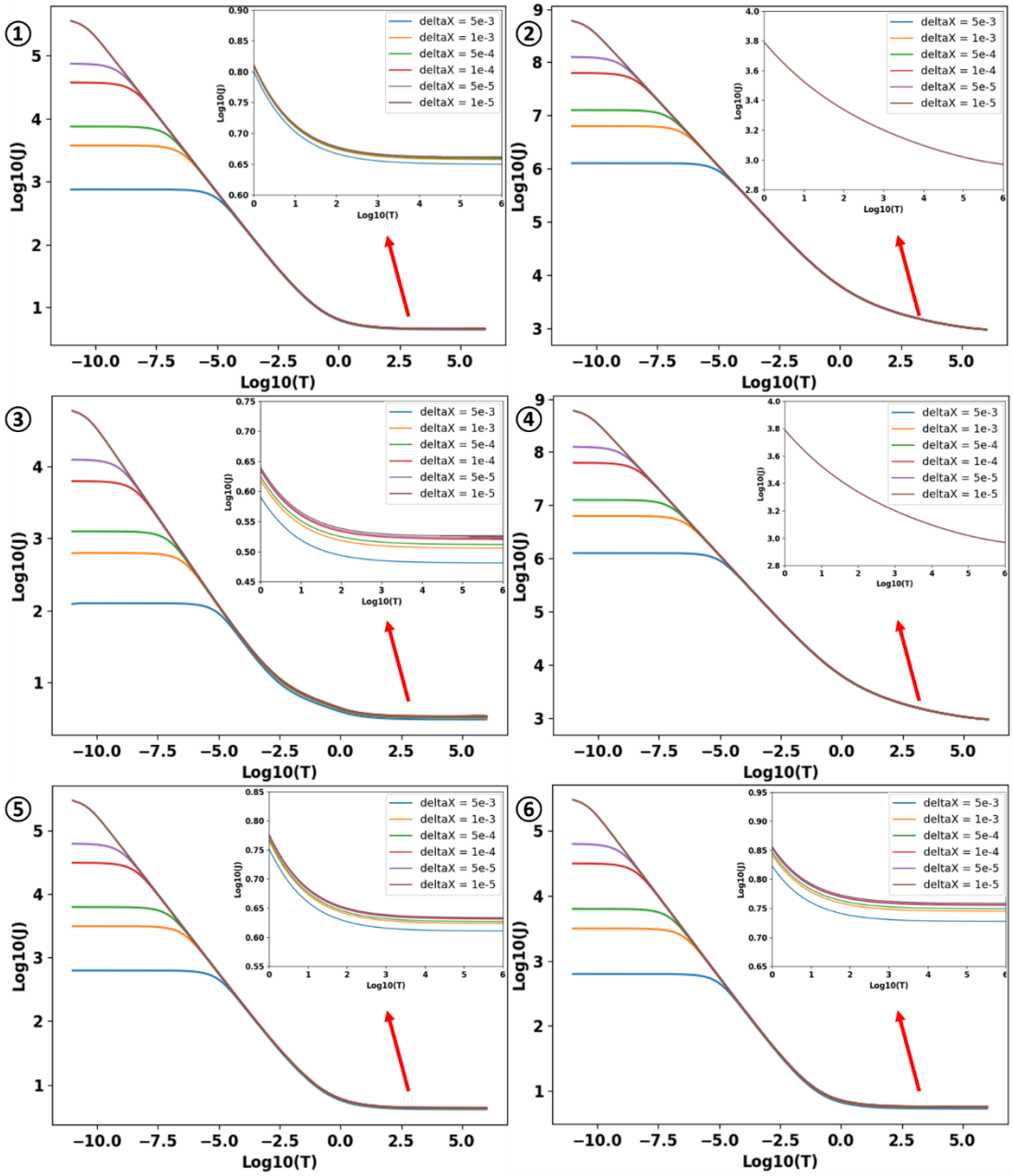


Figure 4.14: Current responses of test simulations for L = 0.1 (left) and 1000 (right) varying *dX* for: ①② the ‘full cylinder’ electrode model; ③④ the ‘side-active-only cylinder’ electrode model; ⑤⑥ the ‘end-active-only cylinder’ electrode model.

representative simulations normalised by the lengths L is shown in Figure 4.19 ① noting the $\log_{10}$ scales. As stated previously, the diffusion indicator α was applied here, and the α values of the currents for different L are shown in 4.19 ②.

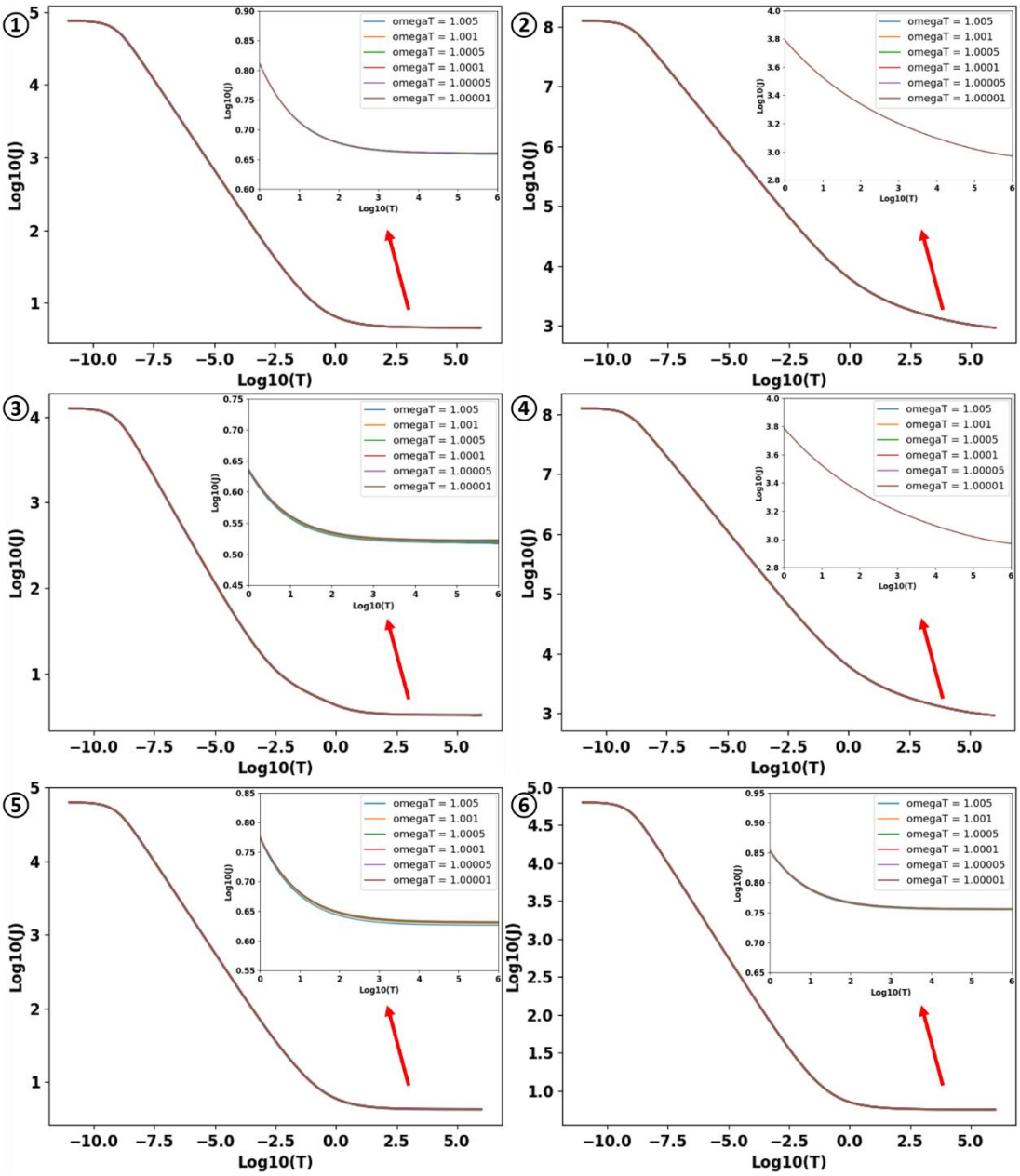


Figure 4.15: Current responses of test simulations for L = 0.1 (left) and 1000 (right) varying ωT for: ①② the 'full cylinder' electrode model; ③④ the 'side-active-only cylinder' electrode model; ⑤⑥ the 'end-active-only cylinder' electrode model.

We compared the simulated currents for the 'annular band' model with the Cottrell Equation and two equations describing the chronoamperometric current for an infinitely long cylinder electrode. The first one was reported by Aoki et al. [1], Eqn (4.21):

$$\begin{cases} I_A = \dfrac{FDc^*}{r_e} f(T) \\ f(T) = \dfrac{1}{\sqrt{\pi T}} + 0.422 - 0.0675 \log_{10} T \pm 0.0058(\log_{10} T - 1.47)^2 \\ \pm \rightarrow \begin{cases} + & when \quad \log_{10} T \geq 1.47 \\ - & when \quad \log_{10} T < 1.47 \end{cases} \end{cases} \quad (4.21)$$

where I_A is the current, D is the diffusion coefficient of the analyte, c^* is the initial concentration of the analyte, T is the dimensionless time, and r_e is the radius of the electrode. The error of this equation was reported [1] to be less than 1% for $\log_{10}T \leq 6$.

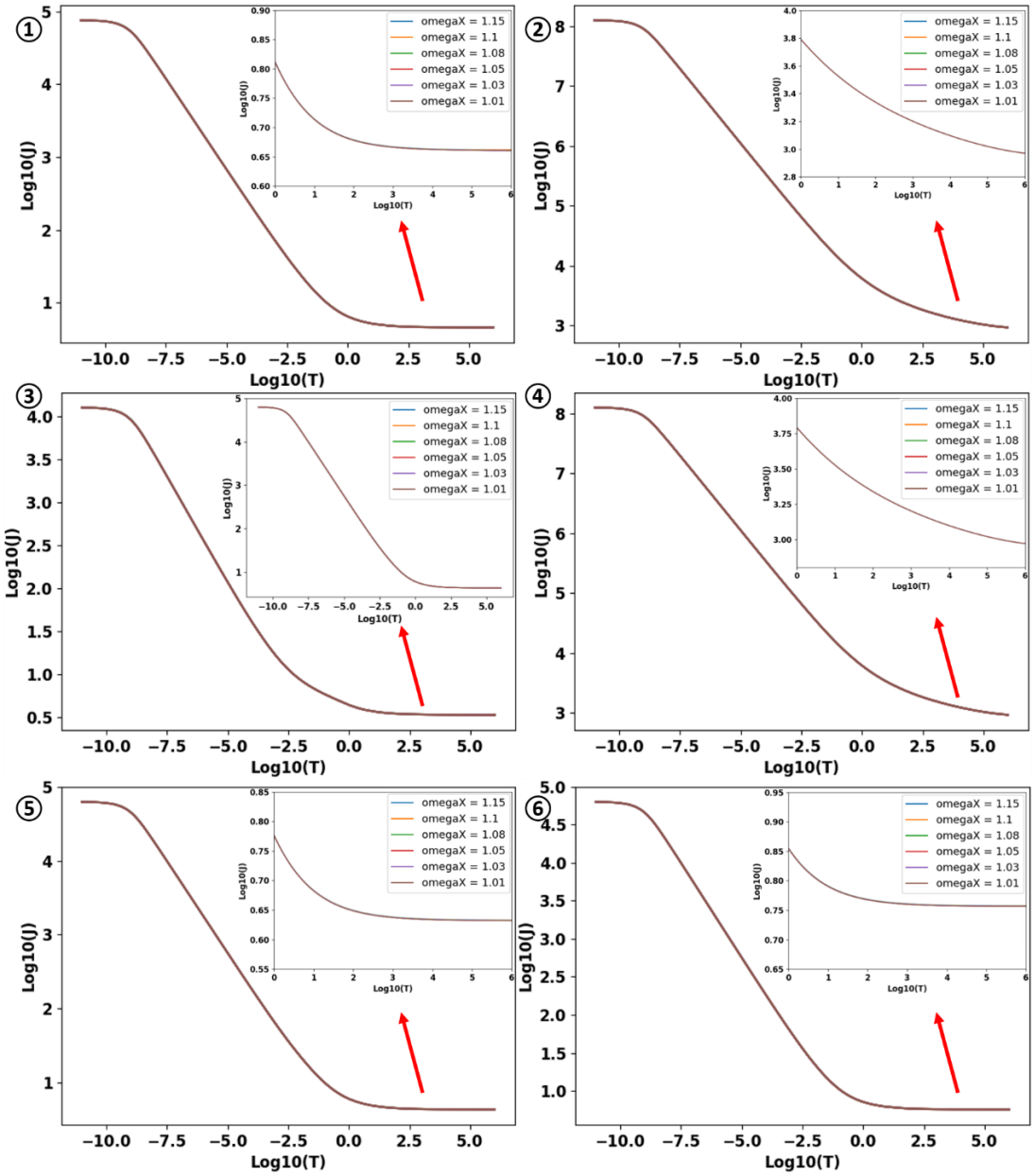


Figure 4.16: Current responses of test simulations for L = 0.1 (left) and 1000 (right) varying ωX for: ①② the 'full cylinder' electrode model; ③④ the 'side-active-only cylinder' electrode model; ⑤⑥ the 'end-active-only cylinder' electrode model.

The second equation was reported by Szabo et al. [12], Eqn (4.22):

$$\begin{cases} I_{Sz} = \pi F D c^* l \cdot f(T) \\ f(T) = \dfrac{e^{-\sqrt{\pi T}/10}}{\sqrt{\pi T}} + \dfrac{1}{\ln\left[\sqrt{4Te^{-\gamma}} + e^{5/3}\right]} \end{cases} \tag{4.22}$$

where I_{Sz} is the current, Υ (= 0.5772...) is the Euler's Constant, and l is the length of the electrode. The error of this equation was reported [12] to be less than 1.3% for all times.

The simulated currents normalised be the length L of the electrode are shown in Figure 4.19 ①. We found that the normalised currents, the Aoki equation and the Szabo equation follow the Cottrell equation at short time scales. As time proceeds, all simulated currents, the Aoki equation and the Szabo equation start to converge to a (quasi-) steady state. For the simulated currents, the longer is the length of the electrochemically active area, the later does the current converge to a quasi-steady state, the smaller is the dimensionless quasi-steady state current, and the closer the current transient converges to the Aoki equation and the Szabo equation.

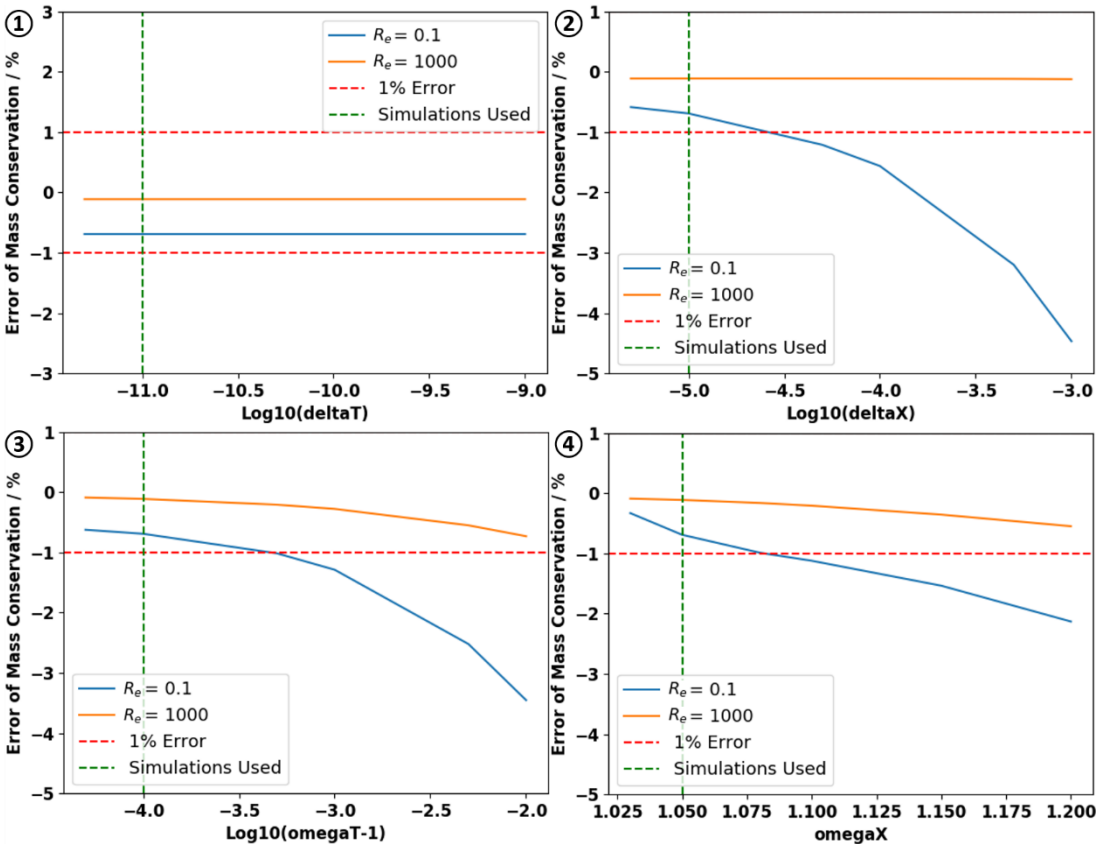


Figure 4.17: Errors of mass conservation calculated for L = 0.1 and 1000 for the 'embedded

ring' electrode model varying: ① dT; ② dX; ③ ωT; ④ ωX.

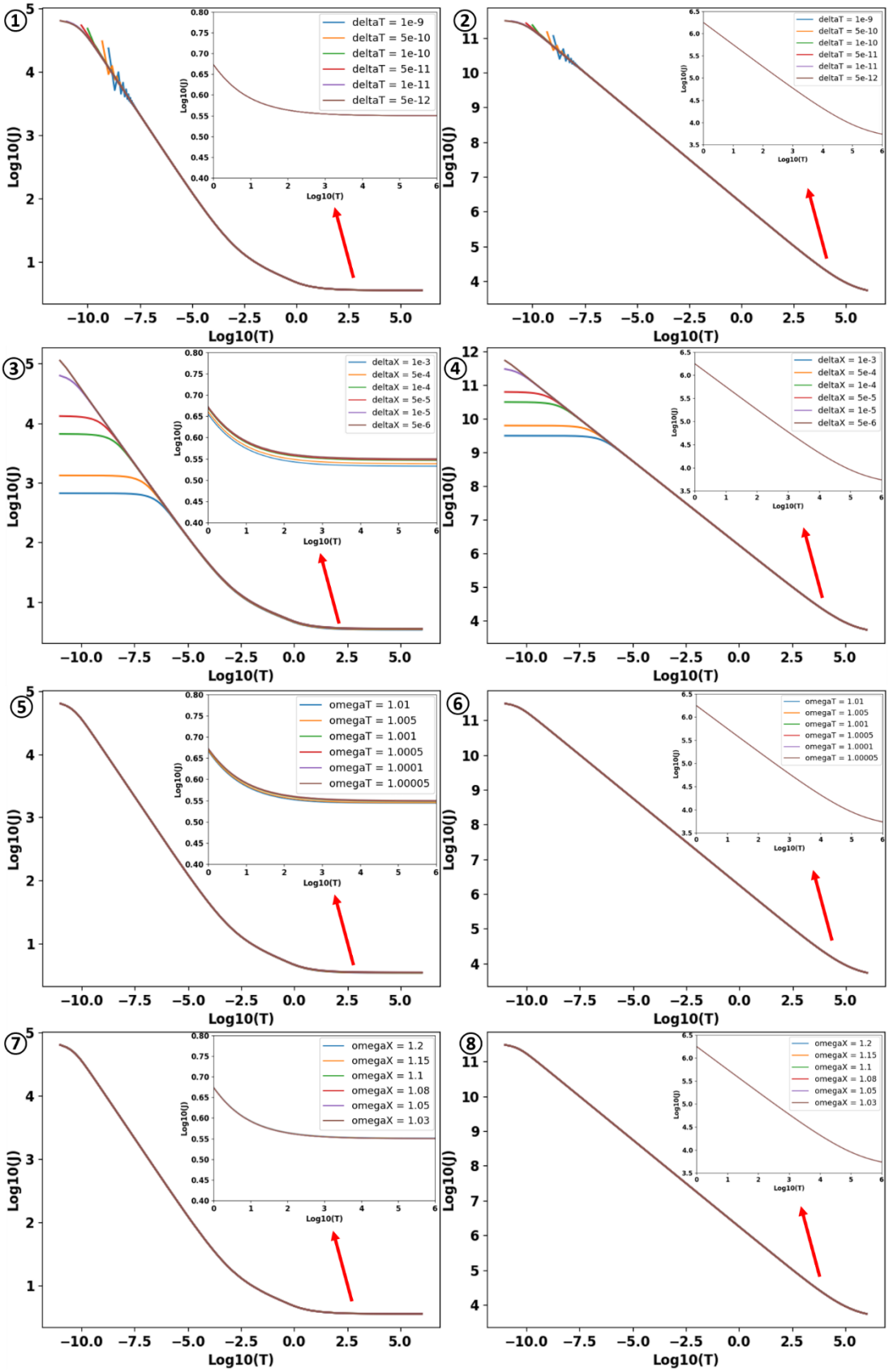


Figure 4.18: Current responses of test simulations for L = 0.1 (left) and 1000 (right) for the 'embedded ring' electrode model varying: dT: ①②; dX: ③④; ωT: ⑤⑥; ωX: ⑦⑧.

The α values of all the simulated currents are illustrated in Figure 4.19 ② together with the Aoki equation and the Szabo equation. The α values echo previous findings that the mass transport is characterised by linear diffusion at short time scales and convergent diffusion in the long-time limit with a transition in between. The curves of the simulated current for electrodes of longer L converge to a quasi-steady state later and are closer to α curves of the Aoki equation and the Szabo equation. These observations reflect that the radial mass transport from the diffusion zone *B* contributes proportionally less to the overall current at longer L.

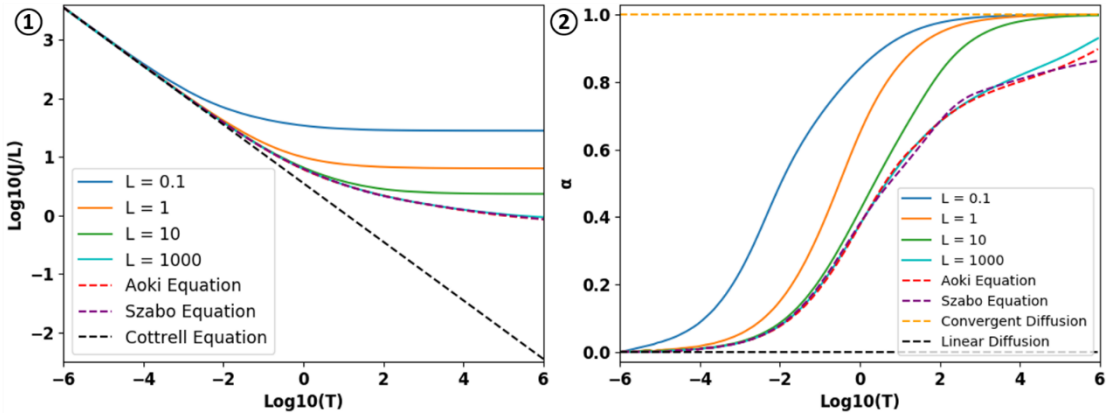


Figure 4.19: Normalised currents (①) and α values (②) for the 'annular band' model for different L compared with the Cottrell equation, the Aoki equation, and the Szabo equation. Simulated currents are solid lines: L = 0.1 (blue), L = 1 (orange), L = 10 (green), and L = 1000 (cyan). Literature equations are dashed lines: the Aoki equation (red), the Szabo equation (purple), the Cottrell equation (linear diffusion, black), and convergent diffusion (yellow).

Moreover, as shown in Figure 4.20, as L increases further, the two approximate equations perform well in the time range between $\log_{10}T = -6$ and $\log_{10}T = 6$ as the percentage differences between the simulated currents, the Aoki equation and the Szabo equation are smaller than 1.2% in the simulated time ranges. The percentage differences are close to the errors reported by Aoki et al. [1] and Szabo et al. [12].

As illustrated in Figure 4.21, the normalised currents simulated for the 'annular band' electrode model for different L are shown in comparison with the Aoki equation and the Szabo equation. Together with Figure 4.19 and Figure 4.21, we find that although

the difference between the Aoki equation and the Szabo equation are small, the Aoki equation describes the temporal evolution of simulated currents better in terms of α for longer L, especially in the time range of $\log_{10}T \leq 4$. Thus, we will focus on the comparison between the simulated currents towards the side of the cylinder and the Aoki equation in the following sections.

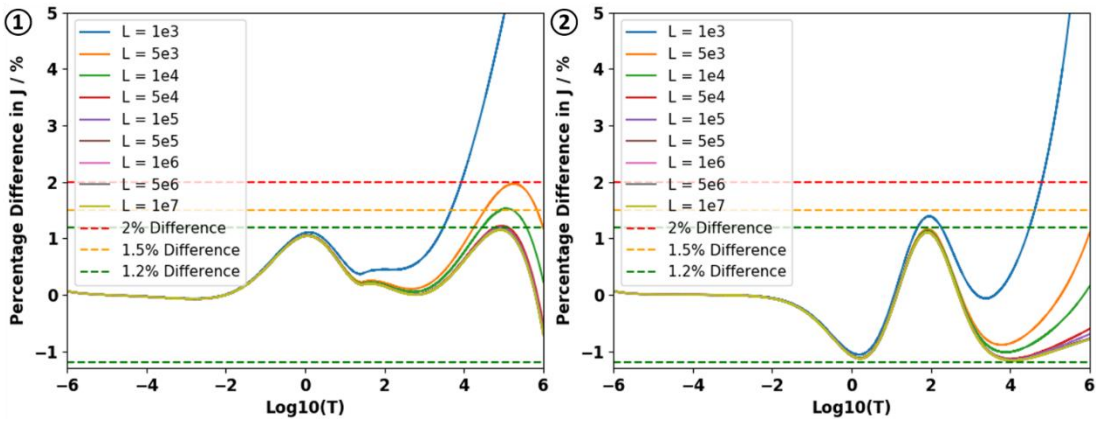


Figure 4.20: Percentage differences between simulated currents for the 'annular band' model for different L compared with the Aoki equation and the Szabo equation (① and ②, respectively). Simulated currents (solid lines): from L = 1e3 (blue) to L = 1e7 (yellow-green). Constant percentage differences (dashed lines): 1.2% (green), 1.5% (yellow), and 2.0% (red).

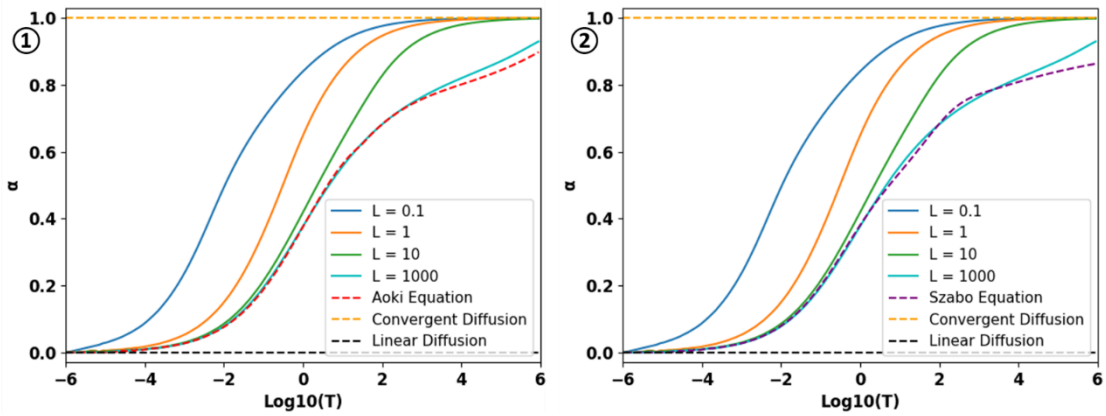


Figure 4.21: α for the simulated currents for the 'annular band' electrode model for different L compared with the Aoki equation and the Szabo equation (① and ②, respectively). Simulated currents are solid lines: L = 0.1 (blue), L = 1 (orange), L = 10 (green), and L = 1000 (cyan). Literature equations are dashed lines: the Aoki equation (red), the Szabo equation (purple), the Cottrell equation (linear diffusion, black), and convergent diffusion (yellow).

4.3.3 The cylinder electrode models

This section presents results for the ‘full cylinder’ electrode model, the ‘side-active-only cylinder’ electrode model, and the ‘end-active-only cylinder’ electrode model.

4.3.3.1 The ‘full cylinder’ electrode model

First, the simulated chronoamperograms and corresponding plots of α values for L = 0.1, 1, 10, 1000 for the ‘full cylinder’ electrode model are shown in Figure 4.22. In each plot the currents to the side, J_s, and to the end of the cylinder, J_e, are evaluated separately and summed up to give the total current J_t.

In Figure 4.22 ①③⑤⑦, for shorter L, J_e is higher than J_s. As L increases, J_e remains at a similar level, J_s increases, and J_s contributes proportionally more to J_t. Whilst many transients in the plots of currents in Figure 4.22 look superficially similar, the diffusion indicator α can be used to sensitively identify subtle differences in the transients and to track the origins of them to different parts of the electrode via comparison with the contributions from the end and side plotted in isolation.

Thus, the temporal evolutions of the α values of J_t, J_s and J_e are shown in Figure 4.22 ②④⑥⑧, where the α values shown start from 0 at short time scales and asymptote to 1 in the long-time limit. Specifically, at short L, e.g. L = 0.1, the α value for J_s begins the transition from 0 to 1 earlier than those for J_t and J_e while the α values for J_t are closer to those for J_e. With increasing L, the α values for J_s begin the transition later while the differences between the α values of J_t and J_s decrease. In extreme cases, as shown in Figure 4.22, the plots of against $\log_{10}T$ show interesting stepped behaviours with two contributions, each with a characteristic ‘time constant’. Each ‘step’ is associated with a diffusion to or from a physically different part of the electrode.

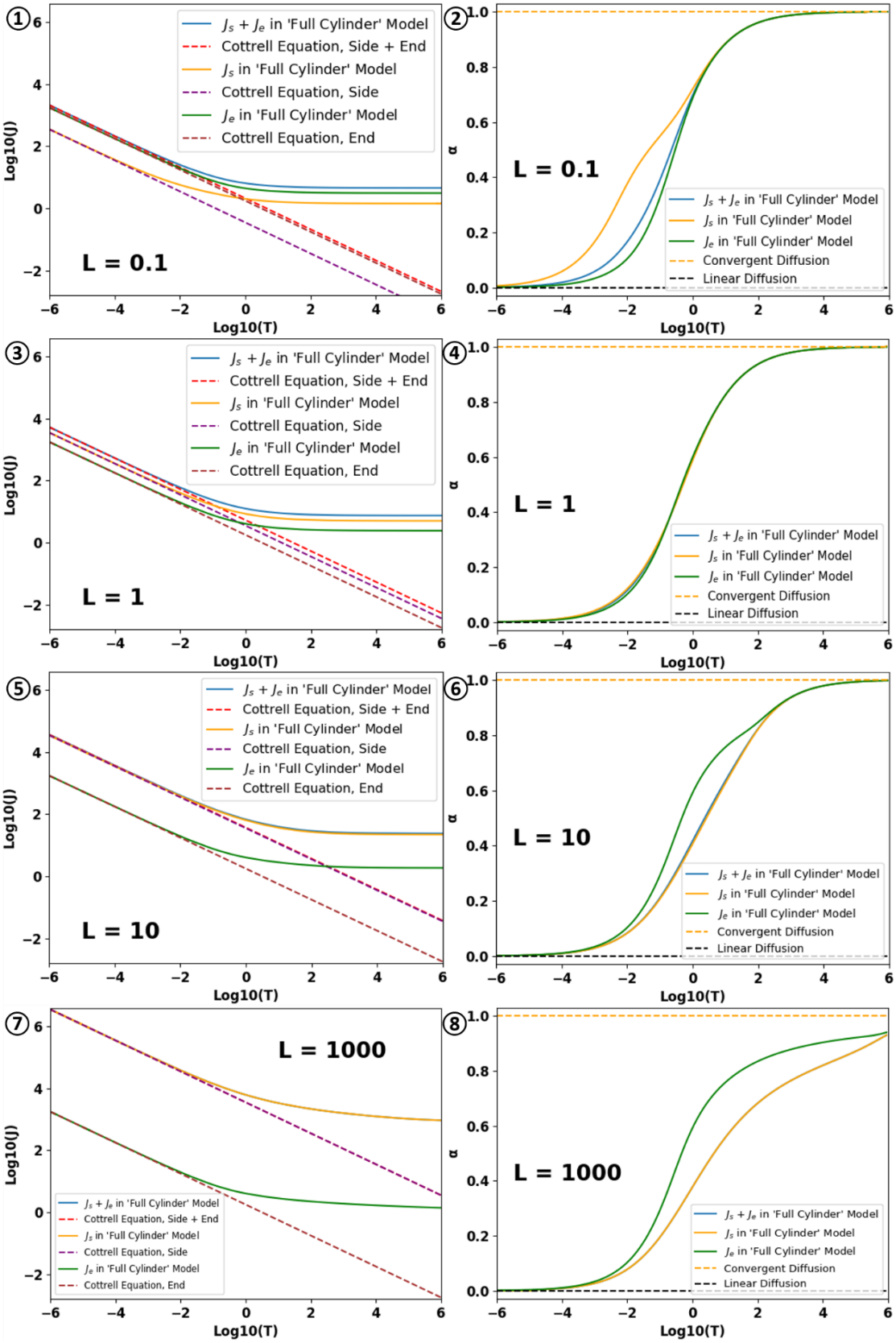


Figure 4.22: Currents (left) and α values (right) for the 'full cylinder' electrode model for different L. Simulated currents are solid lines: J_t (J_s+J_e, blue), J_s (orange), and J_e (green). Literature equations are dashed lines: the Cottrell equation for corresponding areas (red, purple, and brown), linear diffusion (black) and convergent diffusion (orange).

Further insights into the diffusion mechanisms prevalent in the chronoamperograms are provided by the plots of α. For L = 0.1, the α value for J_s begins the transition at around $\log_{10}T = -5$ while that for J_e begins at around $\log_{10}T = -4$. This observation can be assigned to the fact that the diffusion from the diffusion zone *B* contributes proportionally more to J_s at these time scales. The slope of the α values for J_s decreases around $\log_{10}T = -1$, from which we infer that there is a flux of analyte from the zones *C* and *B* towards the partially depleted zone *A*. When L = 1, the shapes of the α plots for J_s and J_e are similar, which shows that the diffusion mechanisms of the end and the side are similar for L = 1 though the area of the end is twice as big as that of the side which leads to different magnitudes of currents for J_s and J_e. For longer L, the α value of J_s increases more slowly to convergent diffusion which can be assigned to the proportionally smaller mass transport from zones *A* and *B* to the side of the cylinder. Furthermore, the α value of J_e increases more slowly for $\log_{10}T \geq 0$ due to the competition from the side. Finally, since J_t is the sum of J_s and J_e, the α values of J_t are closer to those of J_e when L is small. If L is long, e.g. L = 1000, the contribution from J_s is so large that we hardly see any difference between J_t and J_s in the α values.

Thus, the parameter L is shown to control a huge impact on the diffusion mechanisms to both the side and the end of a cylinder electrode. However, the analysis of J_t, J_s and J_e in the 'full cylinder' electrode model is not sufficient to provide an exhaustively understanding about the diffusion mechanisms for the side and the end of the cylinder separately. In the following sections, the comparison between the 'full cylinder' electrode model and the 'side-active-only cylinder' electrode model and the 'end-active-only cylinder' electrode model is made to provide further details.

4.3.3.2 Currents at the side of a cylinder

We performed further simulations for equal L for both the 'side-active-only cylinder'

electrode model and the ‘end-active-only cylinder’ electrode model then compared the J_s and J_e with simulated and other models and equations presented below. In terms of J_s, we compare currents and α values for J_s for the ‘side-active-only cylinder’ electrode model with J_s for the ‘full cylinder’ electrode model, J_s for the ‘annular band’ electrode model, the Cottrell equation, and the Aoki equation for various L = 0.1, 1, 10, 1000 in Figure 4.23.

As shown in Figure 4.23, the currents towards the side of the cylinder and their α values for three models and the Aoki equation show the trends from linear-diffusion-controlled electrochemical processes at the short-time scales to quasi-steady states at the long-time scales, analogous to these trends illustrated in former sections.

Furthermore, there are some stepped behaviours showing in the α plots which will be discussed later in this section.

In the current plots in Figure 4.23, for shorter L, the quasi-steady-state currents for J_s of these three models are in the order as, from high to low, J_s for the ‘side-active-only cylinder’ electrode model, J_s for the ‘annular band’ electrode model, J_s for the ‘full cylinder’ electrode model. The quasi-steady-state current of J_s for the ‘side-active-only cylinder’ electrode model is higher than that for the ‘annular band’ electrode model, which can be assigned to additional diffusion for the diffusion zone *A*. The quasi-steady-state current of J_s for the ‘full cylinder’ electrode model is lower than those for the previous two models, which we assign to the competition with the end of the cylinder. As L increases, the magnitude relationship of simulated currents remains the same while the simulated currents decrease and approach to the Aoki equation. We infer that the decline in simulated currents as L increases may be caused by the proportionally less contribution of the diffusion zone *A* and *B* to the overall mass transport towards the side of the cylinder.

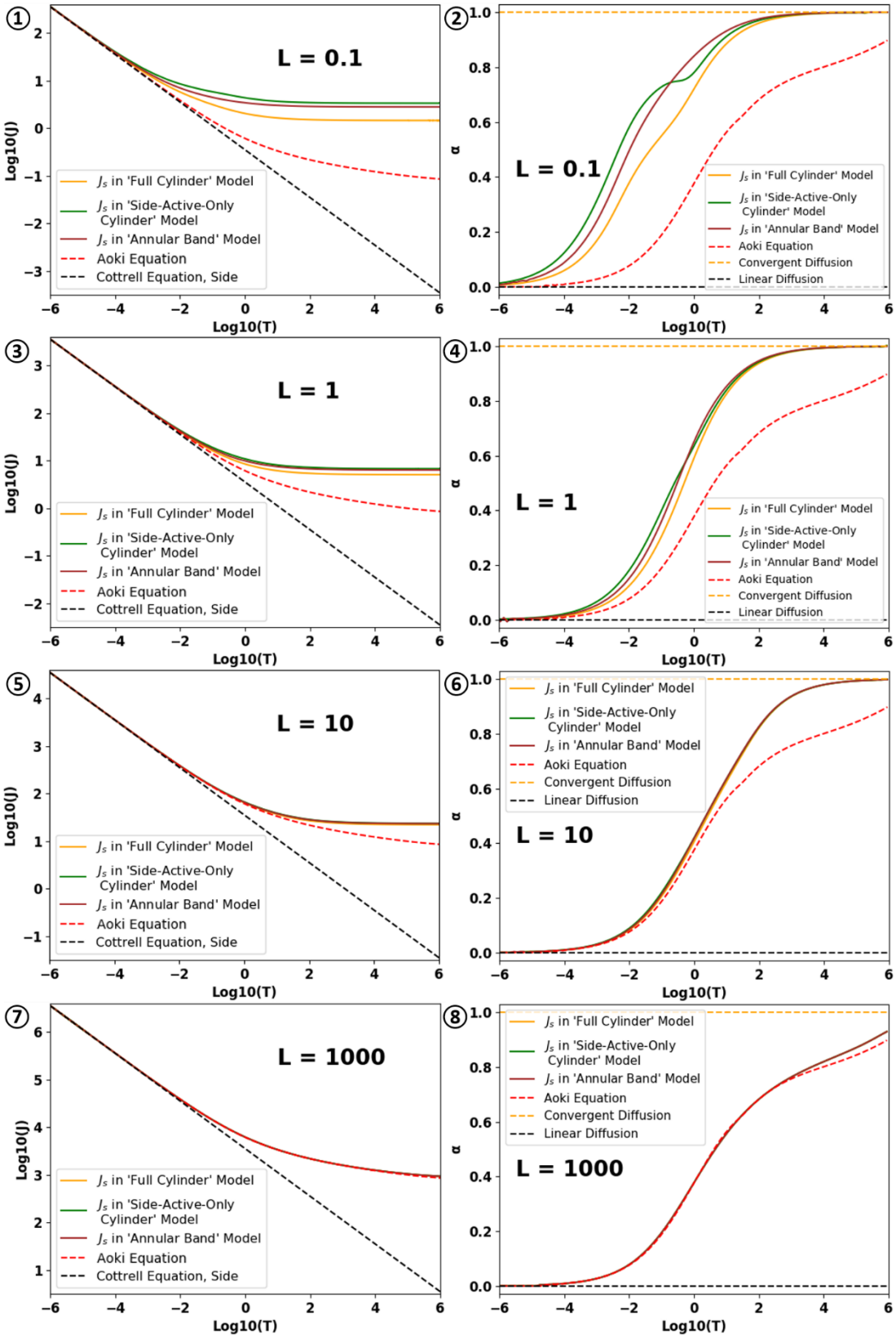


Figure 4.23: Currents (left) and α values (right) for the 'side-active-only cylinder' electrode model for different L compared with those of previous models and literature equations. Simulated currents are solid lines: J_s in 'full cylinder' model (orange), Js in 'side-active-only cylinder' model (green), and J_s in 'annular band' model (brown). Literature equations are

dashed lines: the Aoki equation (red), the Cottrell equation (linear diffusion, black), and convergent diffusion (yellow).

In the α plots in Figure 4.23, for $\log_{10}T < -2$, the slopes of the α plots for the three models are in the same sequence, from high to low, as the magnitude of their corresponding simulated currents, which we assign to the contribution from diffusion zone *A* for the 'side-active-only cylinder' electrode model and the competition from the end of the cylinder for the 'full cylinder' electrode mode. However, for $-2 \leq \log10\ T < 0$, the α plots for J_s for the 'side-active-only cylinder' electrode model and the 'full cylinder' electrode model show stepped behaviours. The slopes of the α plots for these two models decrease for $-2 \leq \log10\ T < 0$, which we assign to the mass transport from zones *C* and *B* to zone *A*. By comparing the plots and the diffusion zones for these three models, the stepped behaviours in the α plots of J_s for the 'side-active-only cylinder' electrode model and the 'full cylinder' electrode model is caused by the diffusion from zone *A*; two contributions of diffusion with two different 'time constants' can, therefore, only be assigned to the mass transport from zone *A*, and the mass transport from zone *B* and zone *C* combined. As L increases, decreasing proportional contribution from the zones *A* and *B* to the side of the cylinder results in the approach of the α plots to the Aoki equation which echo the observations in the current plots.

4.3.3.3 Currents at the end of a cylinder

We further compared the current responses and the α values of J_e for the 'end-active-only cylinder' electrode model with those of J_e for the 'full cylinder' electrode model, and the Cottrell equation and the Shoup-Szabo equation in Figure 4.24.

In Figure 4.24 ①③⑤⑦, for shorter L, e.g. L = 0.1, the steady-state current for J_e in the 'end-active-only cylinder' electrode model is higher than that in the 'full cylinder' electrode model while the steady-state current calculated via Shoup-Szabo equation is lower than the two simulated steady-state currents. As L increases, the steady state

current for J_e in the ‘full cylinder’ electrode model drops dramatically while that for the ‘end-active-only cylinder’ electrode model increases slightly.

In Figure 4.24 ②④⑥⑧, the α values of simulated currents and current calculated by the Shoup-Szabo equation start from linear diffusion at the short time scales to convergent diffusion at the long-time scales. For the shorter L, the α plot for J_e in the ‘end-active-only cylinder’ electrode model tends to converge to steady state earlier than that for the ‘full cylinder’ electrode model while the approach of the Shoup-Szabo equation to 1 is slower than those for J_e in the ‘end-active-only cylinder’ electrode model and J_e in the ‘full cylinder’ electrode model, which we assign to the contributions from the diffusion zone *C*. Consistent with the slower approach convergent diffusion for J_s in both models for $\log_{10}T \geq -2$ shown in previous sections, the approach of the α plot for J_e for both models is faster than the microdisc electrode without zone *C*. As L increases, the stepped behaviours in both models shows that there is an increase of mass transport to the end of the cylinder in the ‘end-active-only cylinder’ electrode model while there is a decrease of mass transport in the ‘full cylinder’ electrode model, which we infer that for longer L the diffusion from zone *C* contributes to J_e in the ‘end-active-only cylinder’ electrode model more while the competition from the side of the cylinder increases for the ‘full cylinder’ electrode model, which results in larger differences in both the currents plots and the α plots between the two models.

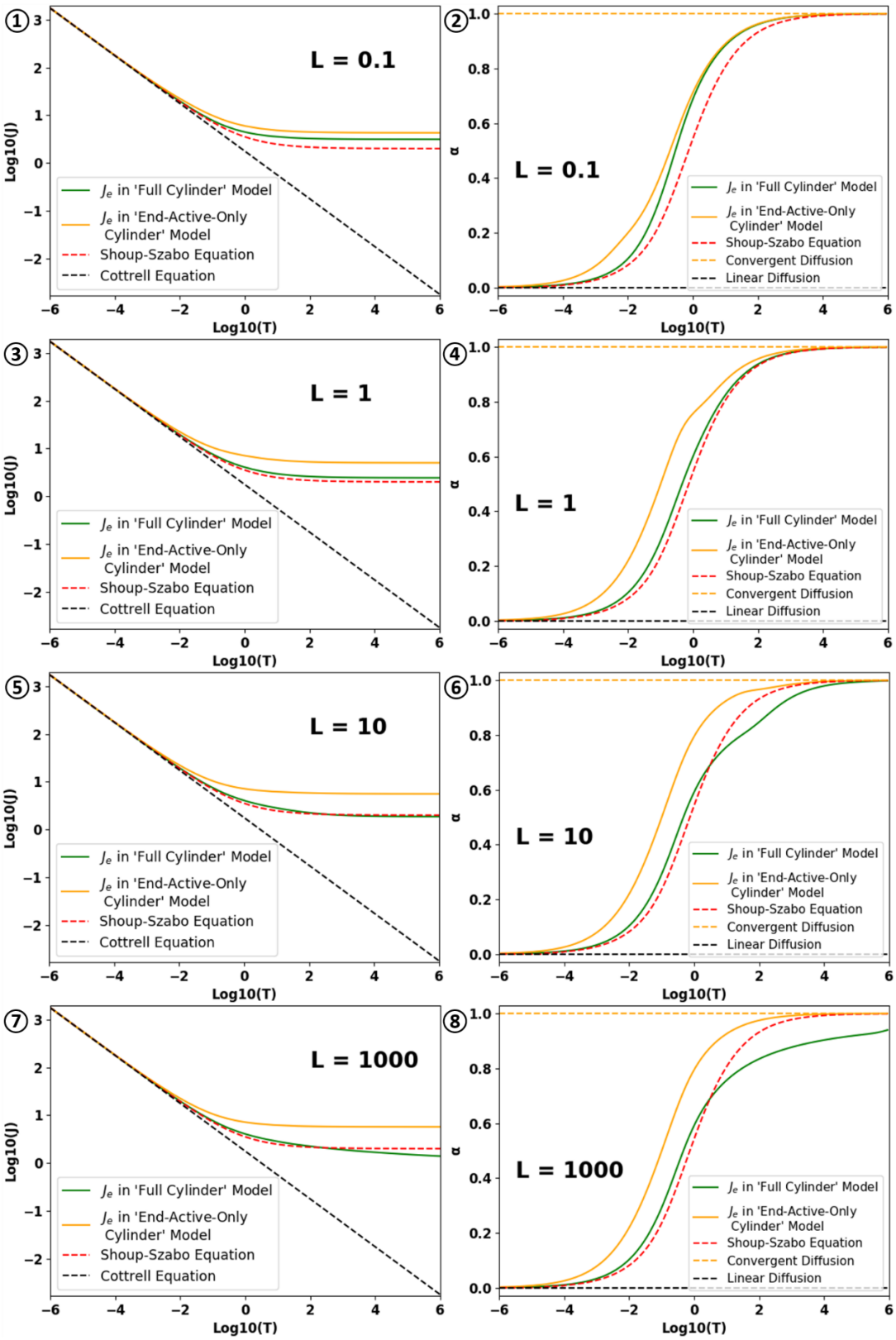


Figure 4.24: Currents (left) and the α values (right) for the 'end-active-only cylinder' electrode model for different L compared with those of previous models and literature equations. Simulated currents are solid lines: J_e in 'full cylinder' model (green), and J_e in 'side-active-only cylinder' model (orange). Literature equations are dashed lines: the Shoup-Szabo equation (red), the Cottrell equation (linear diffusion, black), and convergent diffusion (yellow).

4.3.4 The 'embedded ring' electrode model

We have presented in previous sections that, for shorter L, e.g. L = 0.1, the rates of evolutions of the α plots for J_s in the 'full cylinder' electrode model and J_s in the 'side-active-only cylinder' electrode model 'slow' down for $-2 \leq \log_{10}T < 0$ due to the diffusive flux from the zone *C* to the zones *B* and *A*. If L is even smaller, the electrochemically active area which approaches a band-shape for the 'side-active-only cylinder' electrode model that tends to resemble a ring-shaped electrode on an insulating surface as zone *C* decreases. Therefore, we investigate the 'embedded ring' electrode model to further study the observations in previous models. In this model, we simulated this ring-like model for varying widths R_e. The simulated currents are then normalised by the areas of the electrodes:

$$J_{Nr} = J_r/a \quad \text{where} \quad a = \pi(R_e^2 - 1^2) \tag{4.23}$$

where J_{Nr} is the normalised current for the 'embedded ring' electrode model, a is the area of the ring-shaped electrode.

As shown in Figure 4.25, the current densities towards the embedded ring and their values also show the trends from linear-diffusion-controlled electrochemical processes at the short-time scales to quasi-steady states at the long-time scales. The larger is the area of the ring-shaped electrode, the longer it takes the current to approach to the steady state. For shorter R_e, e.g. $R_e = 0.1$, there is a drop in the approach rate for the α plot at $-2 \leq \log_{10}T < 0$, which we assign to the depletion of diffusion zone *I*. As R_e increases, the drop-in approach rate decreases due to the smaller influence of zone *I* on the total current. Considering the similarities in the diffusion zones of models shown in Figure 4.8, these observations reflect the stepped behaviours are resulted from the different 'time constants' for the diffusion from zones *A* (*I*) and other zones. Furthermore, the stepped behaviours are more obvious when the zone *A* (*I*) is larger.

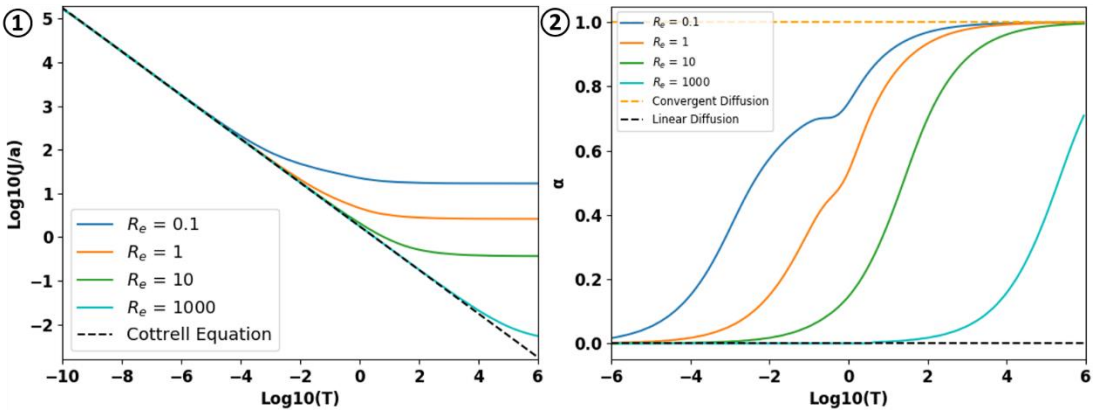


Figure 4.25: Normalised currents (①) and the α values (②) for the 'embedded ring' electrode model for R_e = 0.1, 1, 10, 1000 compared with the Cottrell equation. Simulated currents are solid lines: R_e = 0.1 (blue), R_e = 1 (orange), R_e = 10 (green), and R_e = 1000 (cyan). Literature equations are dashed lines: the Cottrell equation (linear diffusion, black), and convergent diffusion (yellow).

4.3.5 Physical insights

We reported in previous sections that when L increases, J_s in the 'annular band' electrode model, the 'side-active-only cylinder' electrode model, and the 'full cylinder' electrode model approach the Aoki equation. Therefore, beyond a certain value of L, we can use the Aoki equation to predict the chronoamperometric currents in all three models. Thus, we compared, in this section, the simulated currents with the Aoki equation for $-6 \leq \log_{10}T \leq 6$ and obtain the percentage differences, which are shown in Figure 4.26. The percentage differences compared with the Aoki equation in all three models are small due to little influence of the zones *A* and *B*, and the electrochemically active area at the end of the cylinder when L is large. Thus, a case study is presented here for the typical experimental parameters shown in Table 4.3. By converting the dimensionless results into their dimensional counterparts, we produce a set of dimensional simulated results that can be used by experimentalists to obtain an insight of how the simulations relate to experiments. Shown in Figure 4.26 is a second x-axis showing the dimensional lengths of which the largest percentage differences between the simulated currents and the currents predicted by the Aoki equation $-6 \leq \log_{10}T \leq 6$.

It is worth noting that when $L = 5 \times 10^3$ (l = 17.5mm), where l is the dimensional length of the cylinders, the largest percentage difference between the simulated currents and the currents predicted by the Aoki equation for the 'annular band' electrode model, the 'full cylinder' electrode model and the 'side-active-only cylinder' electrode model are, respectively, 1.966%, 1.972%, and 1.978%. Therefore, if l is longer than 17.5mm when the radius is 3.5μm, the largest percentage errors between simulated currents from three models and the Aoki equation are less than 2% for 1.225×10^{-8} s ≤ t ≤ 1.225×10^4 s.

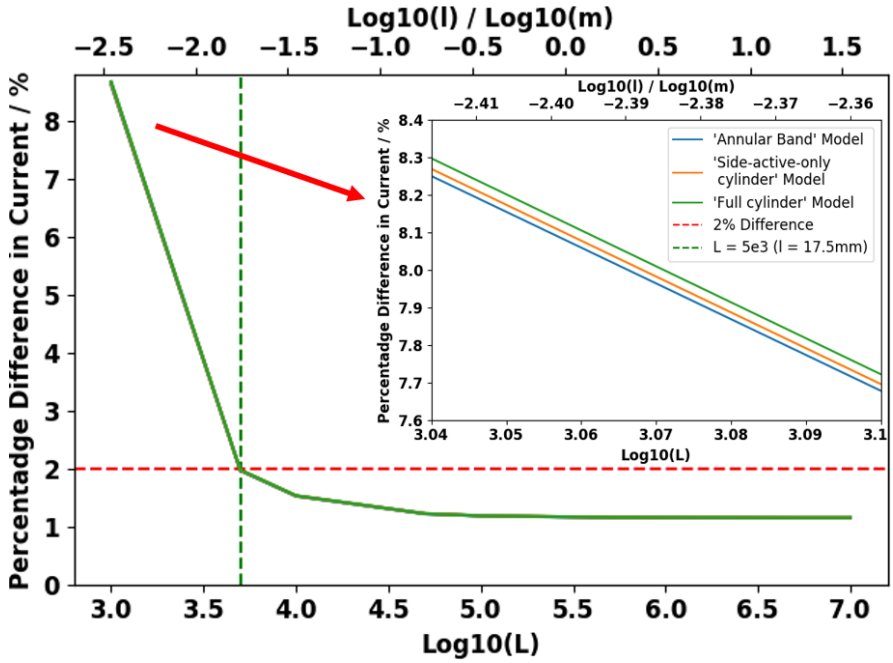


Figure 4.26: Percentage differences in currents between simulated currents in the 'annular band' electrode model, the 'side-active-only cylinder' electrode model, and the 'full cylinder' electrode model compared with the Aoki equation. The percentage differences are solid lines: the 'annular band' electrode model (blue), the 'side-active-only cylinder' electrode model (orange), and the 'full cylinder' electrode model (green). Some reference values are dashed lines: 2% (red), and $L = 5 \times 10^3$ (l = 17.5mm) (green).

Table 4.3: Value of dimensional parameters commonly used in microelectrode chronoamperometric experiments [26, 28]

Dimensional Parameters	Value
Electrode radius, r_e	3.5 μm
Analyte initial concentration, c^*	10^{-9} m^2/s
Diffusion coefficient, D	1 mM

4.4 Conclusions

This chapter took advantages of the diffusion indicator α introduced in the previous chapter to characterise diffusion and analyse the extents of linear and convergent diffusion in chronoamperometric measurements for the cylinder-like models and the 'embedded ring' electrode model. The roles of different parts of the electrode surface and different diffusion zones are thus identified and discussed, in particular, the 'top' and 'side' of the cylinder can show different responses with different time scales leading to 'stepped' chronoamperometry. This chapter further determines the conditions under which the Aoki equation can be used to predict chronoamperometric currents for cylinder-like models. We find that if the length of the cylinder is at least 5000 times longer than the radius, the percentage differences at different times between the simulated current and the Aoki equation are less than 2%, that is for instance, if the length of the cylinder is longer than 17.5mm when the radius is 3.5μm.

References

[1] K. Aoki, K. Honda, K. Tokuda, H. Matsuda, *Journal of Electroanalytical Chemistry* **1985**, *186*, 79–86.

[2] H. Le, E. Kätelhön, R. G. Compton, *Journal of Electroanalytical Chemistry* **2019**, *855*, 113602.

[3] K. Aoki, *Electroanalysis* **1993**, *5*, 627–639.

[4] J. Heinze, *Angewandte Chemie International Edition in English* **1993**, *32*, 1268–1288.

[5] R. J. Forster, *Chem. Soc. Rev.* **1994**, *23*, 289–297.

[6] R. J. C. Brown, D. J. L. Brett, *Microchimica Acta* **2009**, *164*, 337–344.

[7] D. Tallman, *Journal of Solid State Electrochemistry* **2011**, *15*, 1703–1710.

[8] K. J. Aoki, C. Zhang, J. Chen, T. Nishiumi, *Journal of Electroanalytical Chemistry* **2013**, *706*, 40–47.

[9] K. J. Aoki, J. Chen, *Faraday Discussions* **2018**, *210*, 219–234.

[10] P. M. Kovach, W. L. Caudill, D. G. Peters, R. M. Wightman, *Journal of Electroanalytical Chemistry* **1985**, *185*, 285–295.

[11] C. Amatore, M. Deakin, M. Wightman, *Journal of Electroanalytical Chemistry* **1986**, *206*, 23–36.

[12] A. Szabo, D. K. Cope, D. E. Tallman, P. M. Kovach, R. M. Wightman, *Journal of Electroanalytical Chemistry* **1987**, *217*, 417–423.

[13] K. Aoki, H. Kaneko, *Journal of Electroanalytical Chemistry* **1988**, *247*, 17–27.

[14] S. Singleton, J. O'Dea, J. Osteryoung, *Analytical Chemistry* **1989**, *61*, 1211–1215.

[15] B. Seddon, H. Girault, M. Eddowes, W. Peng, Z. Zhao, *Journal of the Chemical Society Faraday Transactions* **1991**, *87*, 2603–2606.

[16] W. Peng, E. Wang, *Analytical Chemistry* **1993**, *65*, 2719–2723.

[17] R. Ferrigno, P. Brevet, H. Girault, *Electrochimica Acta* **1997**, *42*, 1895–1903.

[18] E. J. F. Dickinson, I. Streeter, R. G. Compton, *The Journal of Physical Chemistry C* **2008**, *112*, 11637–11644.

[19] Y.-M. Fang, J.-J. Sun, G.-N. Chen, *ChemPhysChem* **2009**, *10*, 2393–2396.

[20] E. Rivero, P. Granados, F. Rivera, M. Cruz, I. González, *Chemical Engineering Science* **2010**, *65*, 3042–3049.

[21] D. Britz, O. Østerby, J. Strutwolf, *Electrochimica Acta* **2010**, *55*, 5629–5635.

[22] L. K. Bieniasz, *Electrochimica Acta* **2011**, *56*, 6982–6988.

[23] L. K. Bieniasz, *Journal of Electroanalytical Chemistry* **2011**, *662*, 371–378.

[24] L. K. Bieniasz, *Journal of Electroanalytical Chemistry* **2012**, *674*, 38–47.

[25] S. J. Percival, B. Zhang, *The Journal of Physical Chemistry C* **2013**, *117*, 13928–13935.

[26] J. Ellison, C. Batchelor-McAuley, K. Tschulik, R. G. Compton, *Sensors and Actuators B: Chemical* **2014**, *200*, 47–52.

[27] J. Li, Q. Fang, F. Liu, Y. Liu, *Journal of Power Sources* **2014**, *272*, 121–127.

[28] C. Batchelor-McAuley, J. Ellison, K. Tschulik, P. L. Hurst, R. Boldt, R. G. Compton, *Analyst* **2015**, *140*, 5048–5054.

[29] J. Chakraborty, C. P. Please, A. Goriely, S. J. Chapman, *International Journal of Solids and Structures* **2015**, *54*, 66–81.

[30] H. R. Moazami, S. S. H. Davarani, J. Mohammadi, S. Nojavan, M. Abrari, *Analytica Chimica Acta* **2015**, *891*, 151–159.

[31] A. Molina, J. González, E. Laborda, R. Compton, *Journal of Electroanalytical Chemistry* **2015**, *756*, 1–21.

[32] S. Eloul, E. Kätelhön, C. Batchelor-McAuley, K. Tschulik, R. G. Compton, *Journal of Electroanalytical Chemistry* **2015**, *755*, 136–142.

[33] K. Ngamchuea, C. Lin, C. Batchelor-McAuley, R. G. Compton, *Analytical Chemistry* **2017**, *89*, 3780–3786.

[34] R. G. Compton, E. Laborda, K. R. Ward, *Understanding Voltammetry: Simulation of Electrode Processes*, Imperial College Press, **2013**.

[35] D. Peaceman, H. Rachford, Jr., *Journal of the Society for Industrial and Applied Mathematics* **1955**, *3*, 28–41.

[36] J. Heinze, *Journal of Electroanalytical Chemistry and Interfacial Electrochemistry* **1981**,

124, 73–86.

[37] J. A. Alden, R. G. Compton, *The Journal of Physical Chemistry B* **1997**, *101*, 8941–8954.

[38] W. H. Press, S. A. Teukolsky, W. T. Vetterling, B. P. Flannery, *Numerical Recipes: The Art of Scientific Computing (Third Edition)*, Cambridge University Press, **2007**.

[39] E. Kätelhön, R. G. Compton, *Analyst* **2015**, *140*, 2592–2598.

Chapter 5: Single-entity Electrochemistry: Diffusion inside a Particle

This chapter presents the simulated processes of the diffusion-limited depletion of an analyte inside a nanoparticle which is initially doped with this analyte and, upon impact at the electrode, may deform, adsorb, and react. Two different theoretical models are illustrated and compared before discussing the key physical quantities, such as the contact area between the particle and electrode, which can be extracted from experimental data in favourable cases. In addition, we present a dimensional analysis of the theoretical model simplifying the analysis of experimental data by reducing the number of required fitting parameters. The results reported in this chapter are based on a published first-author paper [1] [*Electrochimica Acta*, **2019**, *298*, 778-787].

5.1 Introduction

Recent progress in nanoparticle electrochemistry has enabled the detection of individual nanoparticles and the characterisation of nanoparticle populations as reviewed [2–11]. The nano-impact technique is strikingly simple and straightforward where an electrode is set in contact with a solution of analyte nanoparticles and its potential biased versus the solution potential. By virtue of Brownian motion, individual nanoparticles may then reach the electrode where they may either react due to their intrinsic electrochemical properties or mediate a reaction between the electrode and species present in the solution. Throughout the experiment, individual nanoparticle reactions are monitored via the electrode current and provide valuable insights into the properties of the investigated solution. The rate of individual ‘nano-impacts’ can be measured to determine the particle concentration and, in many cases, the size

distribution [12–14] of a nanoparticle population can be measured by simple integration of the overall charge transferred per spike. This technique has advanced to allow exciting insights into reaction mechanisms from inference of the progress of the reaction of an individual nanoparticle as reflected in the electrode current-time response.

The analysis of spike shapes was further explored theoretically [15] to extract the information beyond particle concentrations and size distributions from experimental data. Various methods have been validated and used for the analysis of diverse experiments including the study of the electro-doping [16] processes in individual nanoparticles, lithium de-insertion [17] processes in battery materials, the characterisation of the electro-dissolution [18] of individual silver nanoparticles, the detection of viruses via antibodies [19], the label-free detection of living bacteria [20] and an analysis of activity fluctuations of individual enzymes [21] near an electrode.

Previously, Nafion polymers have been modified with redox-functional ions such as methyl viologen dication (MV^{2+}) [22, 23] and Tris(2,2'-bipyridyl)dichlororuthenium dication ($Ru(bpy)_3^{2+}$) [24–26] to realise applications such as the catalysis of oxalate oxidation[24]. Literature recently reported further experimental work on the diffusion of MV^{2+} in MV^{2+}-doped 'soft' Nafion particles [27] and the application of such nanoparticles in the electro-catalytic reduction of oxygen [28]. The contact areas of these 'soft' particles with the electrode herein play a significant role in the electrochemical reaction as shown in studies of the contact resistance and -area [29, 30] while related physiochemical processes still remain to be explored.

In this chapter, we introduce, investigate, and contrast two different mathematical models for diffusive depletion processes of analyte inside nanoparticles resulting from impacts on an electrode to establish the theoretical basis of the nano-impact experiments based on MV^{2+}-doped Nafion particles and to enable a more

comprehensive analysis of related experimental data. Furthermore, quantities that can be extracted from experimental data are identified and practical fitting parameters for data analysis are presented.

5.2 Theoretical models

This chapter presents two simulation models for the previously discussed reaction of individual nanoparticles in impact electrochemistry. Both models describe the diffusive depletion processes of an analyte within an individual polymer particle after its impact on the electrode surface where the particle is adsorbed and the analyte reacts.

Before the nanoparticle arrives stochastically via Brownian motion and its transient adsorption at the electrode, the particle is assumed to be spherical with radius r_0 and to contain a homogeneous concentration of a species A^+. After the particle arrives at the electrode, A^+ is reduced at the electrode-particle interface held at a sufficiently negative over-potential to drive the single-electron-transfer reaction $A^+ + e^- \rightarrow B$[2]. The simulated time interval begins with the arrival of the particle at the electrode and ends with the complete reduction of A^+ before the particle either leaves the electrode or remains adsorbed. An illustration of the process can be found in Figure 5.1.

A spike-shaped current signal can be measured while A^+ is reduced to B during the nano-impact process. Assuming the particle remains electro-neutral at all time, the reduction is modelled in terms of either a slow charge hopping process within the particle alongside a fast ion exchange at its surface or rate-determining ion diffusion inside the particle. In the latter case, the electro-neutrality is realised by the diffusion of a negative ion species X^- from within the particle into the solution (Eqn (5.1)) or the diffusion of a positive ion species M^+ from the solution into the particle (Eqn (5.2)).

[2] We note that the reduction of A^+ to B has been chosen exemplarily and the model can be easily altered to describe other reactions.

$$A^+X^-_{particle} + e^- \rightarrow B + X^-_{solution} \quad (5.1)$$

$$A^+X^- + M^+_{solution} + e^- \rightarrow BX^-M^+_{particle} \quad (5.2)$$

Both mechanisms can be represented by equivalent mathematical models, as illustrated below, enabling a wide range of possible applications of the presented theory.

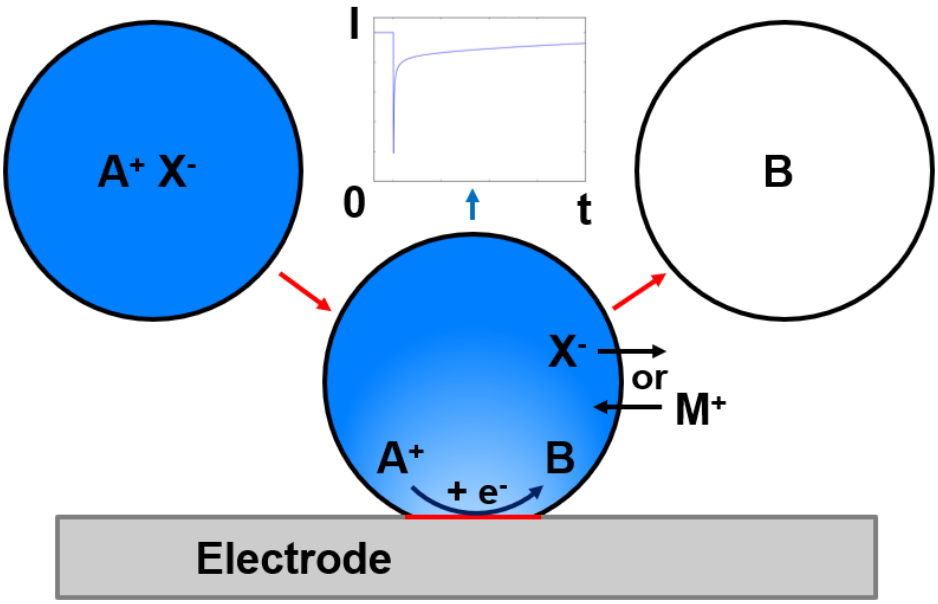


Figure 5.1: Cross-sectional illustration of the simulated nano-impact process in both theoretical models. The inset schematically describes the chronoamperometric current measured at the electrode during the reaction.

Four further assumptions are made: First, the electrode is assumed to be held at a large over-potential to ensure fast reaction kinetics limited only by the diffusive mass transport of charge carriers towards the electrode. Second, the X^- and M^+ species do not participate in any reaction. Third, there is sufficient electrolyte in the solution to enable the facile ion insertion and de-insertion accompanied with Eqn (5.1) or Eqn (5.2). And fourth, the ion insertion or de-insertion rate of X^- or M^+ is fast enough to not be the rate-determining step.

In the following sections, we compare and contrast the 'truncated-sphere' and the 'undeformed-sphere' models differing in the considered particle geometries following the impact at the electrode surface. It is worth noting that the mass transport in this model is assumed to be dominated by diffusion. As discussed in Chapter 1, since the

depletion of the species within the particles are rapid, convection has a negligible impact on the experimental data in this system. However, attention should be paid in the fitting of experimental results with simulated currents as migration could influence the experimental current responses at very short timescales.

5.2.1 The 'truncated-sphere' model

First, the 'truncated-sphere' model assumes that, after the adsorption of the formerly spherical particle at the electrode surface, the particle deforms into a truncated sphere as shown in Figure 5.2.

The particle radius after the adsorption of the particle at the electrode surface is instantaneously adjusted to r_1 in a way that the particle volume and the initial uniform concentration c^* of the analyte remain unchanged for different contact areas, r_e:

$$\begin{cases} \frac{\partial c}{\partial r} = 0 V_p = \int_{V_p} dV = V_p^{init} = \text{const.} \\ c^* = c^{*,\,init} = \text{const.} \end{cases} \tag{5.3}$$

where V_p is the particle volume, $\int_{Vp}$ is the integration over the volume of the particle, and the superscript *init* indicates volumes and concentrations before the deformation. Thus, the total amount of analyte in a particle is conserved during the deformation.

In addition, as shown in Figure 5.2, the contact area between the particle and the electrode features the shape of a planar circle of radius r_e (shown in red) where the reaction exclusively takes place.

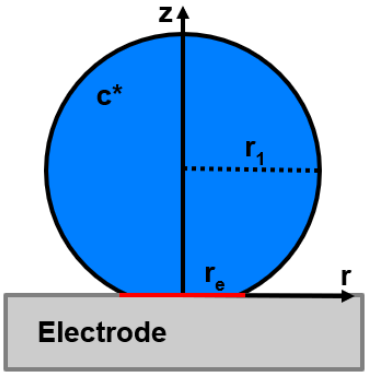


Figure 5.2: Cross-sectional illustration of the 'truncated-sphere' model for the depletion of A^+

within a truncated sphere. c^* is the initial uniform concentration of the analyte inside the particle, r_1 is the radius of the particle after the adsorption at the electrode surface, and r_e is the radius of the contact area with the electrode.

The simulation process is modelled using cylindrical coordinates (r, z, ϕ), where r is the radial distance, z is the axial distance, and ϕ is the angle of the plane formed by the r-axis and the z-axis rotating around the z-axis. Since, due to the rotational symmetry of the system with respect to the z-axis, the concentration at a specific point in r and z is independent of the angle ϕ, we simplify the three-dimensional coordinate system (r, z, ϕ) to a two-dimensional coordinate system (r, z). The diffusion equation can hence be simplified to:

$$\frac{\partial c}{\partial t} = D\nabla^2 c = D\left(\frac{\partial^2 c}{\partial r^2} + \frac{1}{r}\frac{\partial c}{\partial r} + \frac{\partial^2 c}{\partial z^2}\right) \tag{5.4}$$

where *c* and *D* are the concentration and diffusion coefficient of A^+ inside the particle.

The boundary conditions for this model are shown in Figure 5.3. By assuming a sufficiently large negative over-potential applied at the electrode, we ensure that the concentration of A^+ can be approximated to zero at all time and the rate of charge transfer is hence diffusion-controlled. No-flux boundaries are set everywhere else, obstructing any release of the analyte into solution during the impact. Following Fick's first law, the current at the electrode can be calculated as:

$$I = Fj \quad \text{where} \quad j = -2\pi D \int_0^{r_e} \left.\frac{\partial c}{\partial z}\right|_{z=0} r dr \tag{5.5}$$

where n is the number of the electron transferred in the reaction, F is the Faraday Constant, and j is the flux of the analyte.

5.2.2 The 'undeformed-sphere' model

Second, in the 'undeformed-sphere' model, the particle shape remains spherical upon the impact and adsorption. Thus, the contact area between the particle and the electrode is considered as curved, as shown in red in Figure 5.4. In analogy with the previous

model, the A^+ reacts only at this interface and is confined to the volume of the particle throughout the impact.

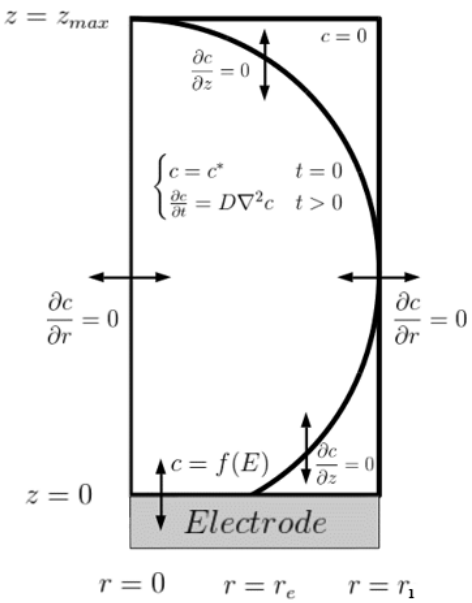


Figure 5.3: Boundary conditions in the truncated-sphere model. z_{max} is the upper boundary of the simulated space in z for r = 0 and is implicitly set through the choice of r_1 and r_e. f(E) represents the boundary condition at the electrode surface which, here, is equivalent to c = 0 at a the large over-potential applied.

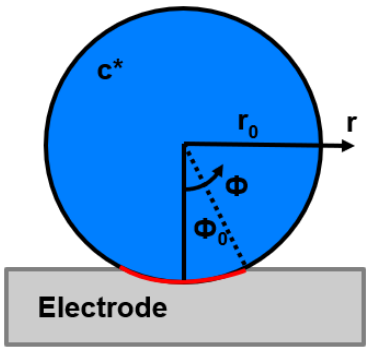


Figure 5.4: Cross-sectional illustration of the 'undeformed-sphere' model. c^* indicates the initial concentration of A^+, Φ_0 defines the contact area (red), and r_0 is the radius of the particle.

In contrary to the previous model, the diffusion of A^+ inside the particle for this model is simulated in spherical coordinates (r, Φ, ϕ), where r is the radial distance, Φ is the polar angle, and ϕ is the zenith angle. According to the symmetry of the system with respect to the zenith, only the concentration distribution in r and Φ are taken into consideration as the concentration is invariant with respect to the zenith angle ϕ. Thus, the diffusion equation for this model is:

$$\frac{\partial c}{\partial t} = D\nabla^2 c = D\left(\frac{\partial^2 c}{\partial r^2} + \frac{2}{r}\frac{\partial c}{\partial r} + \frac{1}{r^2}\frac{\partial^2 c}{\partial \Phi^2} + \frac{1}{r^2 \tan\Phi}\frac{\partial c}{\partial \Phi}\right) \quad (5.6)$$

As shown in the Figure 5.5, a large electrode over-potential is assumed at the electrode so that the concentration of A^+ is set to zero at the electrode surface, and no-flux boundaries are set everywhere else to prevent any release of the analyte into the solution surrounding the particle.

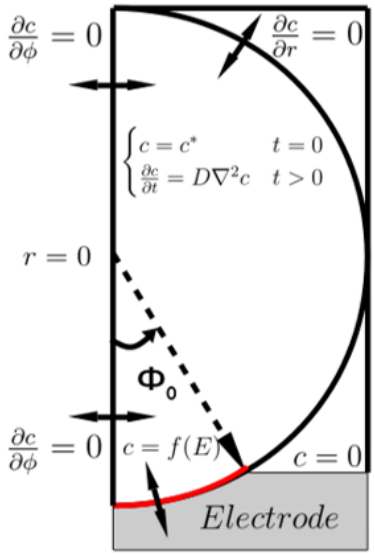


Figure 5.5: Boundary conditions in the undeformed-sphere model. f(E) represents the boundary condition at the electrode surface which, here, is equivalent to c = 0 at a the large over-potential applied.

The total current across the contact area can be calculated based on Fick's first law:

$$I = nFD\frac{\partial}{\partial t}\left(2\pi \int c\, r\, sin\Phi\, dr d\Phi\right) \quad (5.7)$$

5.2.3 Dimensionless parameters

As shown in Table 5.1, the dimensional parameters are converted to their dimensionless counterparts later in this chapter for simplicity of presentation and to enable an easier comparison with experimental data. In the 'truncated-sphere' model, since the particle volume and the overall amount of A^+ inside the particle are conserved during the deformation process, see Eqn (5.3), the dimensionless particle radius R_1 is a function of the contact area and $R_1 \geq 1$. In contrast and as the particle is not deformed

in the ‘undeformed-sphere’ model, $R_0 = 1$ is independent of the contact angle Φ_0.

Table 5.1: Conversion of dimensional parameters to dimensionless ones where r_0 is the radius of the spherical particle throughout the entire simulation for the ‘truncated-’ and the ‘undeformed-sphere’ model, respectively, f_c is the dimensional frequency which is defined as 1/t , F is the Faraday Constant, **R** is the Universal Gas Constant, and **T** is the temperature.

Dimensionless Parameters	Conversions
Concentration of species j	$C_j = \frac{c_j}{c^*}$
Diffusion coefficient of species j	$d_j = \frac{D_j}{D}$
Radial distance	$R = \frac{r}{r_0}$
Axial distance	$Z = \frac{z}{r_0}$
Time	$T = \frac{Dt}{r_0^2}$
Frequency	$F_c = \frac{r_0^2 f_c}{D}$
Potential	$\theta = \frac{F}{\boldsymbol{RT}}(E - E_f^0)$
Current	$J = \frac{I}{F r_0 D c^*}$

5.2.4 Computational methods

The partial differential equations for the two models are solved via two different finite difference approaches. For the ‘truncated-sphere’ model, custom code was developed in C++ which makes use of the alternating direction implicit (ADI) method [31–33] to simplify the resulting systems of linear equations to tri-diagonal matrix equations which are then solved via the Thomas algorithm [34]. Results are visualised via Python scripts using the *NumPy* and *matplotlib* libraries. The ‘undeformed-sphere’ model was realized and visualised in *MATLAB R2018a* where the ADI method was adopted to solve the matrix system. An expanding time grid is used to for both models for better accuracy at short time scales, as defined in Appendix.A. Further details can be found in the textbook [35] by Compton et al.

5.3 Results and discussion

This section is divided into four parts. We first discuss the testing and validating of the simulations. Second, we focus on the truncated-sphere model and discuss the simulation results with respect to concentration profiles, electrode current, and impact analogue signal processing in a typical experimental set-up on the measurement. Third, we compare both theoretical models and, finally, we conduct a dimensional analysis to establish two useful fitting parameters for the analysis of experimental data.

5.3.1 Testing numerical simulations

We recognise the importance of testing and validation of models [36–38] and have carried out comprehensive tests including convergence studies and the studies of mass conservation. By varying the radius step dR, time step dT, and time expanding factor ωT in the simulations, an appropriate parameter set was obtained as shown in Table 5.2.

Table 5.2: Dimensionless parameter sets for both models

Dimensionless Parameters	Microsphere
Potential, θ	-50
Initial concentration, C^*	1
Diffusion coefficient, d	1
Reference distance, R_0	1
Simulation time, T	16
Radius step, dR	10^{-3}
Time step, dT	10^{-7}
Time expand factor, wT	1.01

The current responses and the errors of the mass conservation, as defined in Appendix.B, for different simulations are obtained to ensure convergence by keeping the values of all but one parameter constant (dR, dT and ωT) and varying the latter. Thus, the testing and validating for both models are presented as following.

5.3.1.1 Testing the 'truncated-sphere' model

Convergence studies and tests of the errors of mass conservation for the 'truncated-sphere' model are performed for two limiting contact areas (Ar = 0.5, 2.0) and for varied radius step dR, time step dT, and time expanding factor ωT.

Varying dR: Current responses are plotted on the left of Figure 5.6 for simulations for six different radius step widths (dR = 0.03 − 0.001). As discussed previously, the current responses at short time scales are of no experimental relevance and are affected by intrinsic limitations of the finite difference method. Thus, we focus on the data shown in the inset, where we can see that if the dR values are decreased to 0.001, the current responses converge. Analogously, the errors of mass conservation, plotted in the right-hand side graphs of Figure 5.6, calculated for the simulation of the same dR vary little and remain at a low level.

Varying dT: Current responses and the errors of mass conservation are plotted in Figure 5.7 for six different time steps (dT = 5×10^{-5} − 1×10^{-7}). While the errors of the mass conservation for these simulations, shown in the right graphs of Figure 5.7, remain at an almost invariant low level, the behaviours of the current responses are different. For a small dR, such as dR = 0.001 in this case, dT must be kept to a low level, as otherwise there is a convergence problem that manifests in an oscillating current response. When dT is decreased to a certain level, the current response converges to a certain value as shown in the left-hand side graphs of Figure 5.7.

Varying ωT: Current responses and the errors of mass conservation are plotted in Figure 5.8 for five different ωT = 1.01 − 1.001. As we can see, ωT has only little influence on the current responses while the errors of the mass conservation remain at a low level.

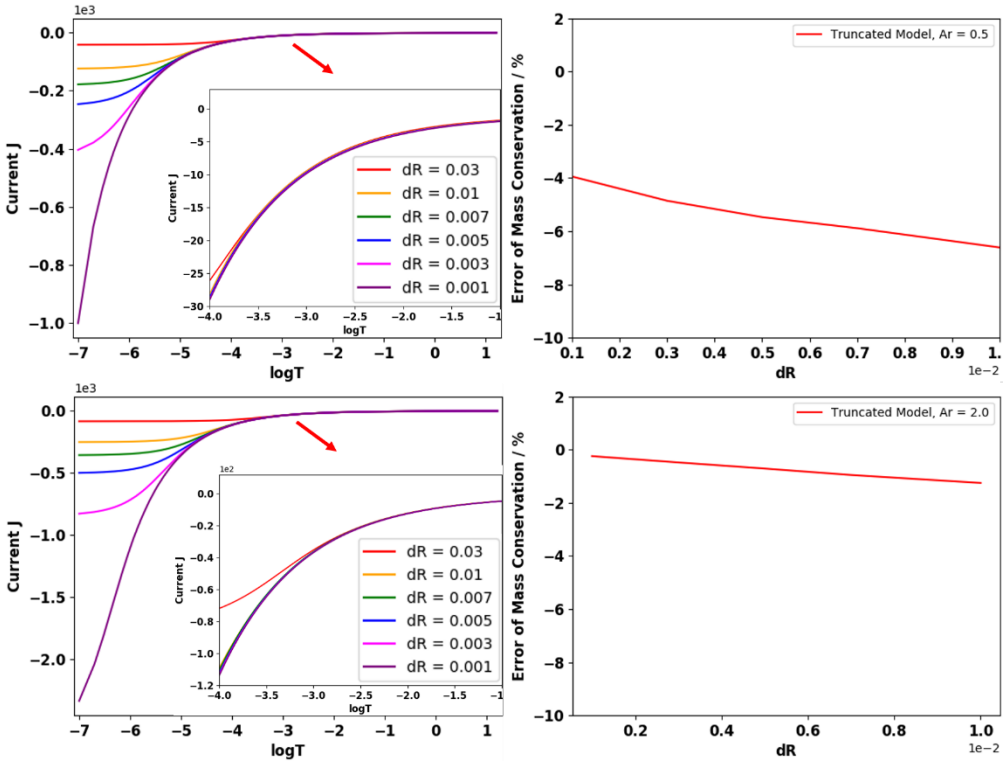


Figure 5.6: Current responses (left) and error of mass conservation (right) calculated for the contact areas Ar = 0.5 (top), Ar = 2.0 (bottom) for the dimensionless parameter dR in the 'truncated-sphere' model.

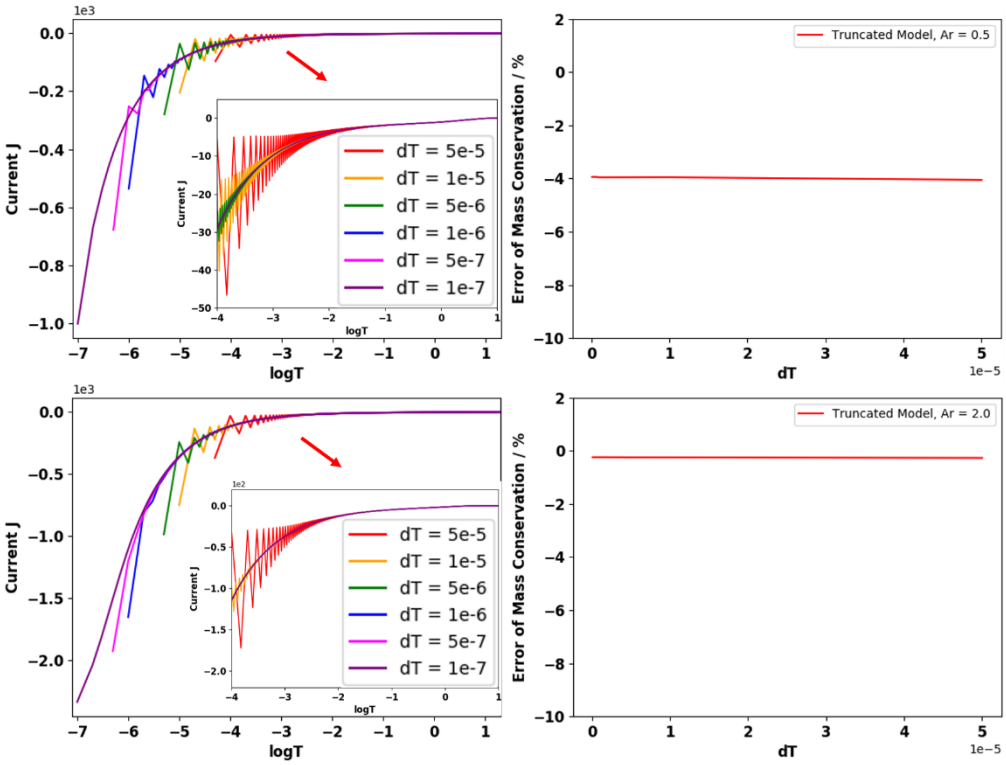


Figure 5.7: Current responses (left) and errors of mass conservation (right) for the contact areas Ar = 0.5 (top), Ar = 2.0 (bottom) for the dimensionless parameter dT in the 'truncated-sphere' model.

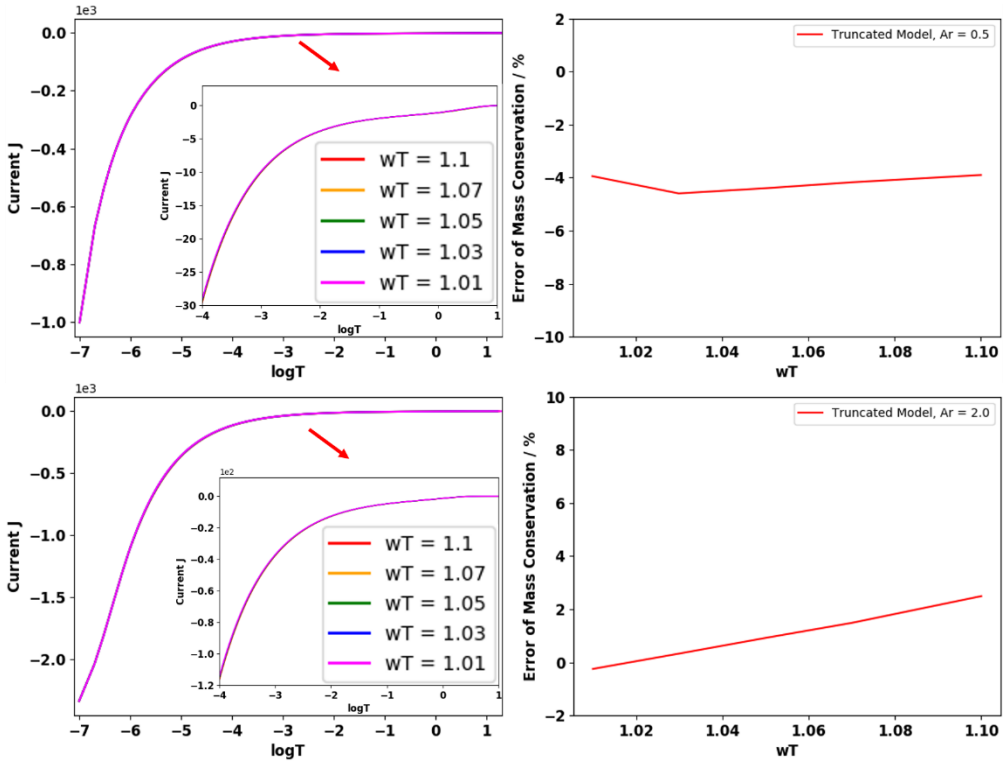


Figure 5.8: Current responses (left) and errors of mass conservation (right) for the contact areas Ar = 0.5 (top), Ar = 2.0 (bottom) for the dimensionless parameter time step expanding factor ωT in the 'truncated-sphere' model.

5.3.1.2 Testing the 'undeformed-sphere' model

Similar to the model above, the convergence studies and the tests of the errors of mass conservation for the 'undeformed-sphere' model are performed for two contact areas (Ar = 0.5, 2.0) and for varied dR, dT and ωT.

Varying dR: The current responses are plotted on the left hand side of Figure 5.9 for simulations for five different radius step widths (dR = 0.01 − 0.001). Similar to the reports in the previous section, we can see in the left-hand side graphs that if the dR are decreased to 0.001, the current responses converge to certain values. Simultaneously, the errors of mass conservation, plotted on the right of Figure 5.9, are small.

Varying dT: The current responses and the errors of mass conservation are plotted in Figure 5.10 for six different time steps (dT = 5×10^{-5} − 1×10^{-7}). As in the previous section, dT must be kept low for convergent results as, otherwise, the current response oscillates. When dT is decreased to a certain level, the current response converges to a

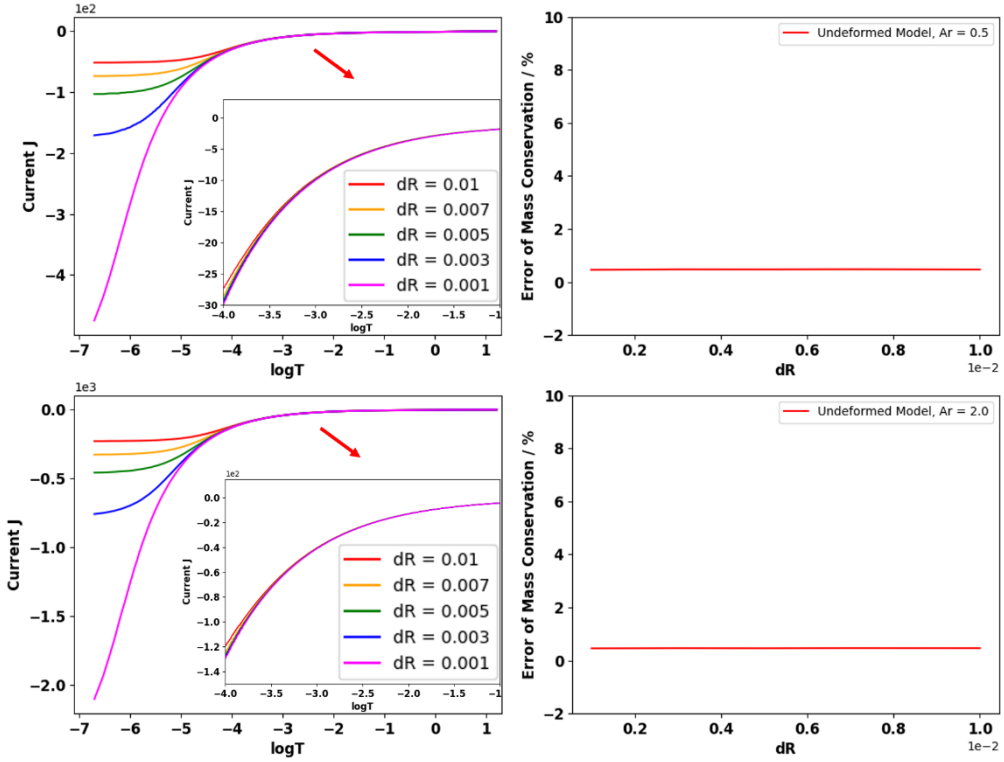


Figure 5.9: Current responses (left) and errors of mass conservation (right) for the contact areas Ar = 0.5 (top), Ar = 2.0 (bottom) for varied dimensionless parameter dR in the 'undeformed-sphere' model.

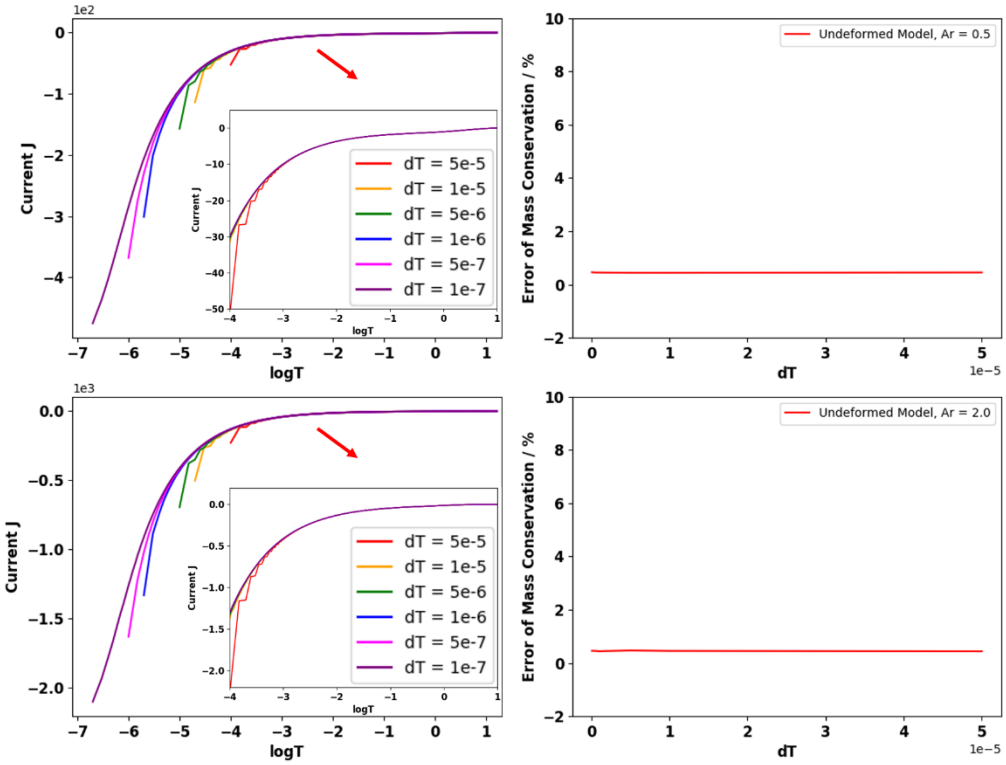


Figure 5.10: Current responses (left) and errors of mass conservation (right) for the contact areas Ar = 0.5 (top), Ar = 2.0 (bottom) for the dimensionless parameter dT in the 'undeformed-sphere' model.

near constant value. The errors of the mass conservation are small throughout.

Varying ωT: The current responses and the errors of mass conservation are plotted in Figure 5.11 for five different ωT = 1.01 − 1.001. As we can see, the time grid expanding factor ωT has only little influence on the current responses while the errors of the mass conservation decrease when ωT decreases.

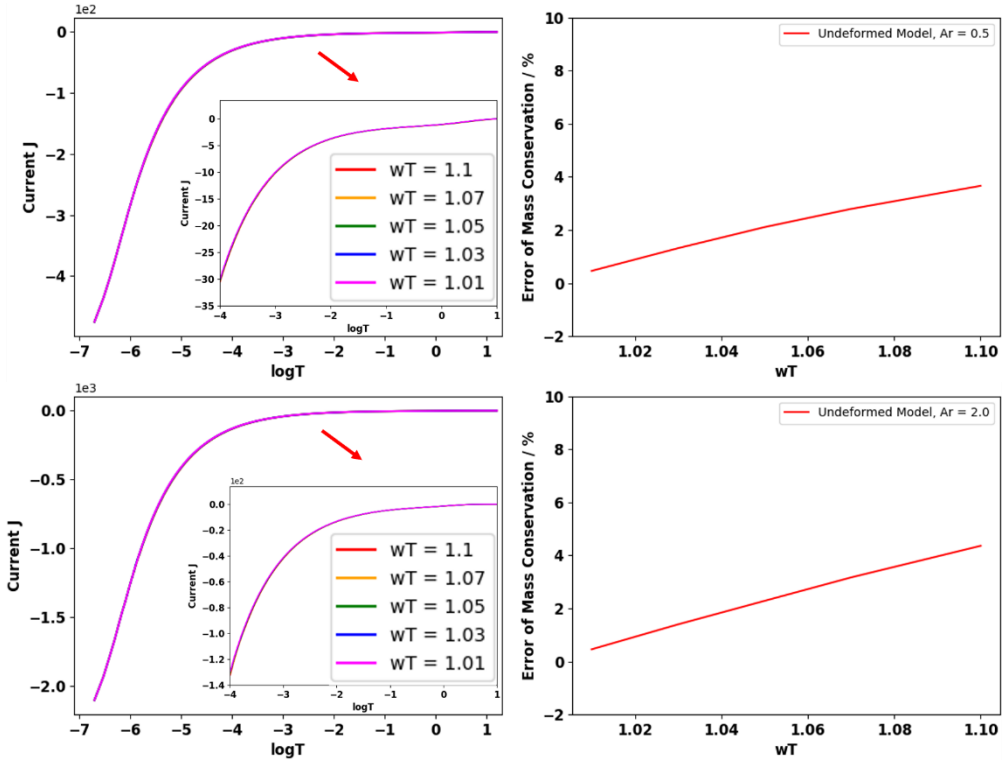


Figure 5.11: Current responses (left) and errors of mass conservation (right) for the contact areas Ar = 0.5 (top), Ar = 2.0 (bottom) for the dimensionless parameter ωT in the 'undeformed-sphere' model.

5.3.2 The 'truncated-sphere' model

By varying the size of contact area between the electrode and the sphere, a series of simulations is performed for the 'truncated-sphere' model and the concentration profiles of A^+ are investigated as shown Figure 5.12. There is a significant dependency of the temporal evolution of the depletion on the size of the contact area. For large contact areas the analyte depletion progresses much faster than for smaller areas. At the time T = 1, for instance, about 70% of the initial mass has been consumed for a

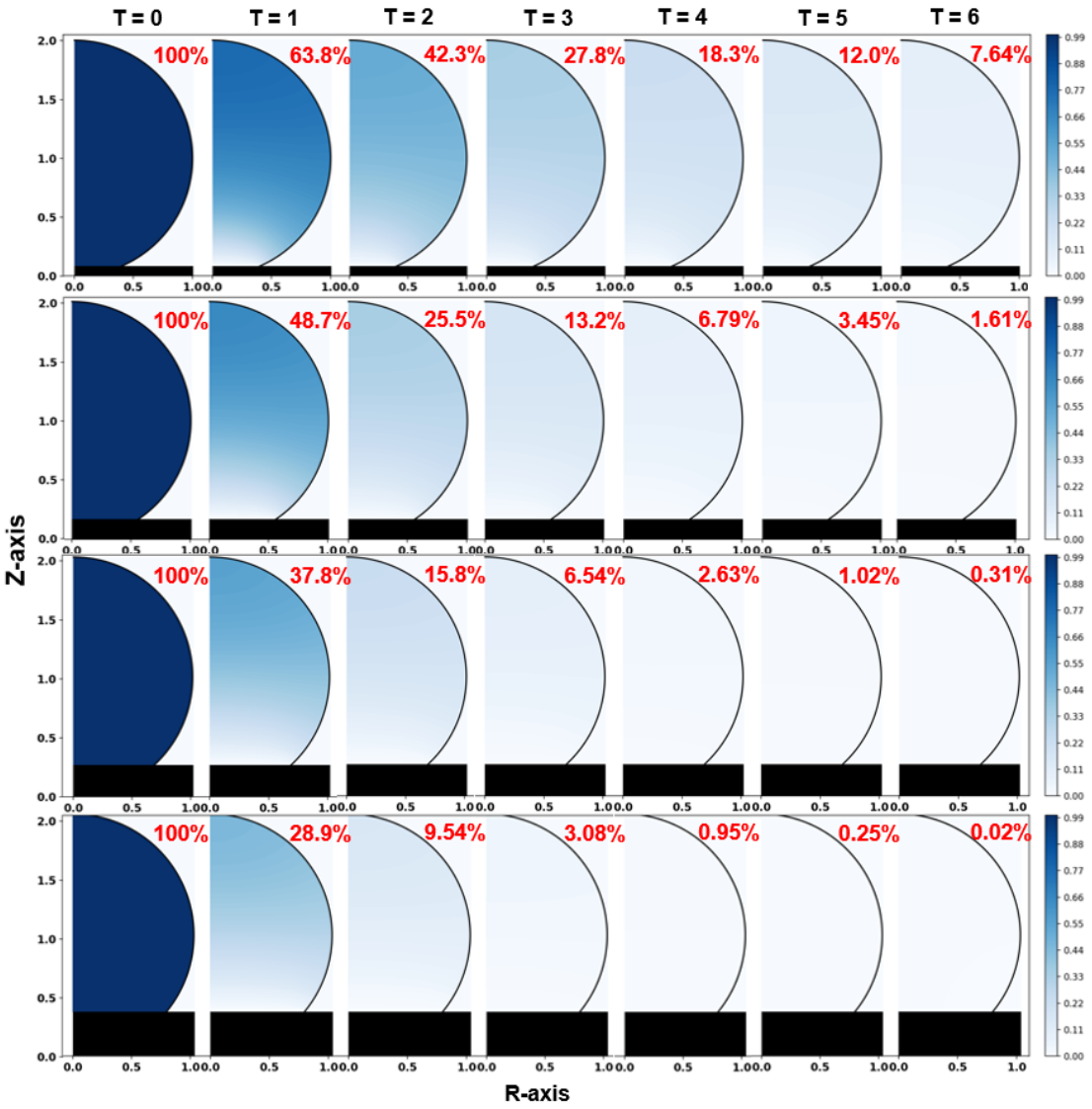


Figure 5.12: Temporal evolution of the concentration profiles simulated for four different contact areas. Plots are arranged in a way that the time increases from the left to the right while the contact area increases from the top to the bottom and simulations for Ar = 0.5, 1.0, 1.5, 2.0 are depicted. The values plotted as red insets indicate percentage of the initial mass remaining in the particle at the respective simulated time.

contact area of 2 while only about 35% has been consumed at the same time for a contact area of 0.5. This large difference suggests that the contact area might be inferred from the current transient measured at the electrode.

We further analyse the temporal evolution of the current alongside the mass remaining within the particle in Figure 5.13. The data shown confirms the strong dependency of the current response on the contact area anticipated on the basis of

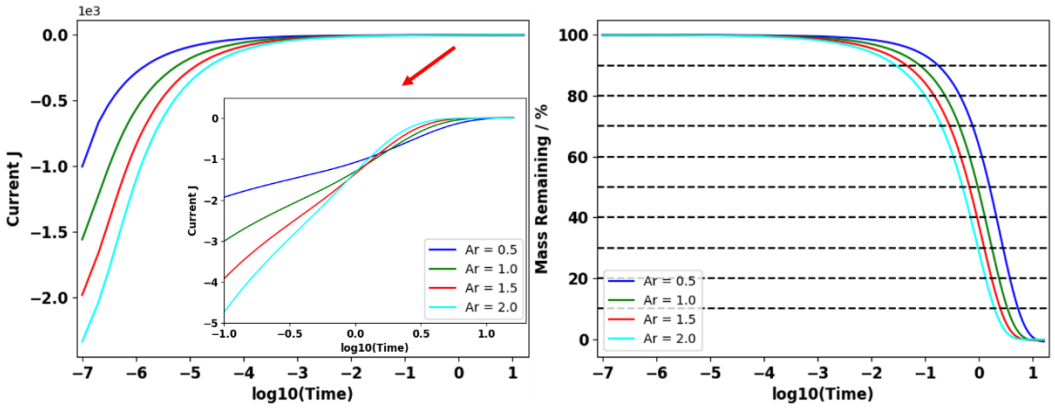


Figure 5.13: Temporal evolution of the electrode current (left) and the mass remaining within the particle (right) in the 'truncated-sphere' model.

Figure 5.12: The larger is the contact area, the greater[3] is the current at short times after the impact and the faster the depletion progresses. Despite the initial greater current for greater contact areas, the current response simulated for smaller contact areas exceeds the response calculated for larger contact areas at long time scales. This can be understood considering that the overall amount of analyte inside the particle remains unchanged with different contact areas and an initial lower current hence necessarily results in a larger current at long time scales.

To further rationalise the simulated current responses, we compare the modelled data with the Cottrell equation [39] which describes the temporal evolution of the current I at large overpotentials in one-dimensional chronoamperometry. In its dimensional form[4], Cottrell equation is given by:

$$I = nFAc^* \sqrt{\frac{D}{\pi t}} \tag{5.8}$$

where n is the number of electrons transferred, F is the Faraday Constant, A is the area of the electrode, c^* is the initial concentration of the analyte, D is the diffusion coefficient, and t is the time. We note that the simulated current in the 'truncated-sphere'

[3] We note that for very short time scales, the simulated geometry resembles a one-dimensional geometry, i.e. $I \propto t^{-0.5}$ and hence $I \rightarrow \infty$ for $t \rightarrow 0$. As infinite current cannot be modelled via the finite difference method, the simulated data for very short time scales can only be of a qualitative nature.
[4] The dimensionless form representation is: $J = \sin^2(\Phi_0)/2(\pi T)^{0.5}$.

model differs from the Cottrell model as it is not exclusively limited by linear diffusion. However, at short-time scales, when radial diffusion does not have a large influence on the mass transport towards the electrode, the simulated current is expected to converge to reproduce the Cottrell equation.

The current evolutions calculated for two different contact areas (Ar = 0.5, 1.0) are compared in Figure 5.14 where the x-axis depicts $T^{-0.5}$ and hence the regions ① to ④ and ⑤ to ⑧ are reached in ascending order with time, i.e. ① → ② → and so forth, and ⑤ → ⑥ → and so forth. A direct comparison between the simulated currents and Cottrell equation reveals that at short times, in the regions ② and ⑥, the simulated currents approach the Cottrell equation as the geometry resembles the one-dimensional diffusion case as modelled by Cottrell. In the regions ③ and ⑦, radial diffusion additionally contributes to the current which then exceeds the corresponding value of the Cottrell equation. At the end of the simulated time, ④ and ⑧, the current drops to zero due to the limited amount of analyte within the particle which is now entirely consumed. At very short times ① and ⑤ we find a deviation between the simulated data and the Cottrell equation which results from intrinsic limitations of the finite differences method and can be understood along the lines of the footnote in Section 5.3.2.

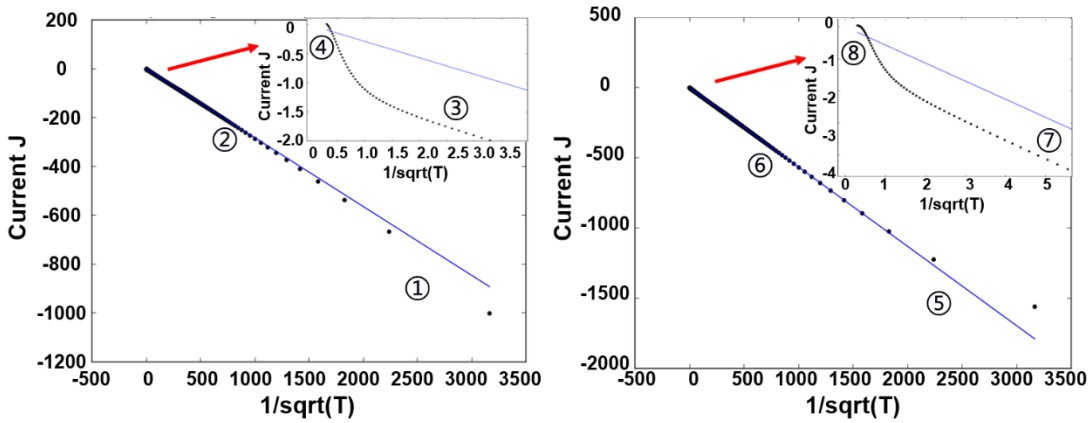


Figure 5.14: Comparison between Cottrell equation and our simulation results for different Ar, Ar = 0.5 and Ar = 1. Cottrell equation and simulation results are depicted in blue and black, respectively.

We though note that the time scale at which we observe these artefacts is of no experimental relevance as illustrated below in the discussion of the experimental signal processing.

In literature [16], it was shown that the shapes of current spikes measured in impact electrochemistry often reflect more the signal processing characteristics of the potentiostat than the temporal evolution of the actual charge process at the electrode surface. In order to compare the simulated currents with an experimental data, the signal transfer function of the potentiostat - for many experiments a simple low-pass filter - must hence be included in the simulation. To this end, we apply a digital first-order low-pass filter to the simulated current to model bandwidth limitations of the potentiostat. The key parameter is herein the filter's cut-off frequency which is a measure for the signal bandwidth. If the frequency of a spectral signal component is larger than the cut-off frequency, the contribution of this component to the output signal is attenuated whereas other signal components experience only small changes in terms of their contribution. In addition, despite of no relevance in this work, we note the cut-off frequency has an influence on the phase shift of the individual spectral components.

As shown in Figure 5.15, we compare the current evolutions before and after the application of digital filter for different contact areas Ar = 0.5, 1.0, 1.5, 2.0 and a dimensionless cut-off frequency of 100. The x-axes on the left and right depict the dimensionless time T and $\log_{10}$T, respectively, while the same data is shown. In the figure we find that immediately after impact all currents are attenuated significantly while in the following filtered currents slightly exceed their unfiltered equivalents before, finally, both converge to the same value. Prior literature has shown that for this type of filter, the overall charge transferred, i.e. the integral of the current, is conserved [9]. The above discussed intrinsic inaccuracy of our simulations at very short time

scales is hence of negligible practical relevance for the shape of the spike after the filtering. Most notably, the current response significantly depends on the contact area even after the filter and, in the context of this theoretical model, can hence be used to extract the contact area as well as the degree of the particle deformation from experimental data.

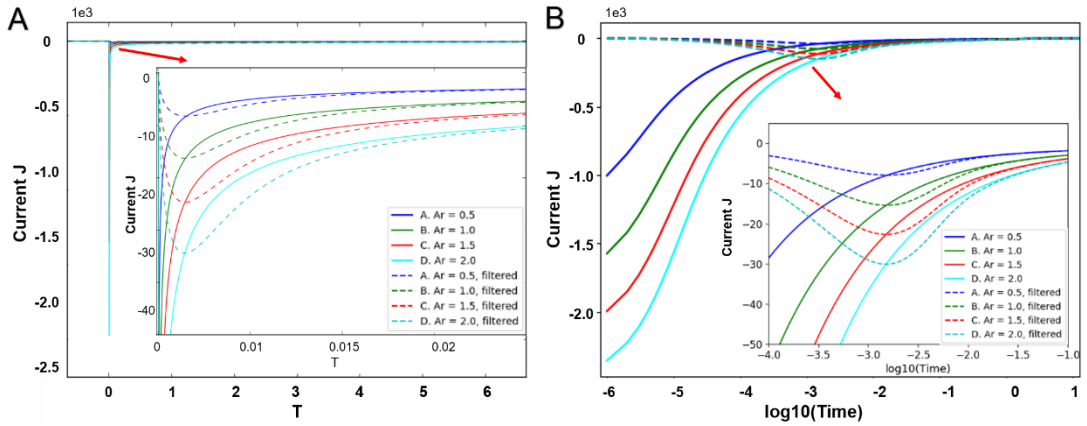


Figure 5.15: Evolution of the current response before and after a digital filter operated at a dimensionless cut-off frequency of 100. Different contact areas are investigated and, for clarity, the same data is plotted versus both T and $\log_{10}$T.

To further investigate the influence of the cut-off frequency, the current transients before and after filtering are compared for different dimensionless cut-off frequencies, F_c = 25, 50, 100, 150, 200, when the contact area is set to be 1. From the Figure 5.16, we can see that when the cut-off frequency is set to a low value, the signal is masked by the filter and only little information can be retained as higher-bandwidth features are attenuated. In contrast and at higher cut-off frequencies, the potentiostat is less limiting, though experimentally the signal may be masked by other sources of noise so that the cut-off frequency needs to be chosen carefully to sufficiently suppress external noise while still retaining spectral information of interest.

5.3.3 Comparison between two models

We consider four different cases as shown in Figure 5.17 in the comparison between two models used. The red and green areas represent the contact areas simulated for the

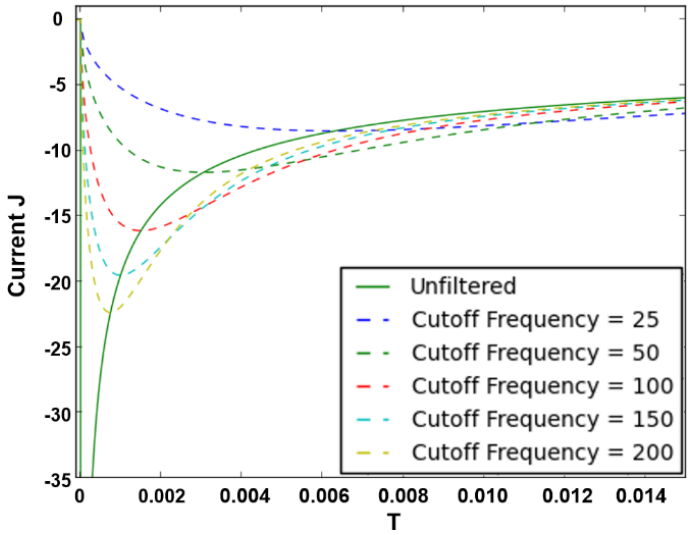


Figure 5.16: Current evolutions before and after filtering evaluated for different cut-off frequencies and a contact area of 1.

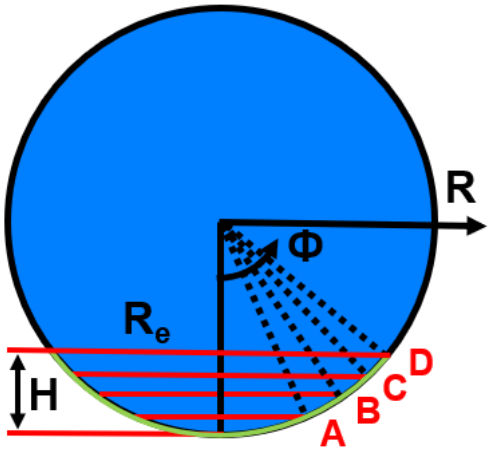


Figure 5.17: Comparison of different simulated contact areas for two models. Red and green areas show the 'truncated-' and the 'undeformed-sphere' model, respectively.

'truncated-' and the 'undeformed-sphere' model, respectively. The angles Φ_0, which define the contact areas in both models, feature identical values in corresponding simulations for both models. Currents are evaluated for four different angles Φ_0, $\sin\Phi_0$ = 0.399, 0.561, 0.679, 0.774, which are labelled A, B, C, and D in the Figure 5.17 and correspond to the above four surface areas Ar = 0.5, 1.0, 1.5, 2.0 in the 'truncated-sphere' model. As discussed above, the total volume of the particles remains unchanged for different angles and particle radii R_1 of deformed particles in the 'truncated-sphere' model hence increase accordingly as the particle is deformed upon the impact.

The dimensionless contact areas can be calculated from the angle Φ_0 for the

'truncated-sphere' model:

$$Ar = \pi R_e^2 = \pi R_1^2 sin^2\Phi_0 \quad (5.9)$$

and the 'deformed-sphere' model:

$$Ar = 2\pi R_0 H \quad \text{where} \quad H = R_0(1 - cos\Phi_0) \quad (5.10)$$

The temporal evolutions of the current for both models are compared in Figure 5.18 where we find that the smaller is the contact angle, the smaller is the difference in the current response. This can be rationalised considering that for small contact angles $\Phi \rightarrow 0$ both models converge to the same geometry. We further observe very similar current responses at intermediate- and long timescales despite clear differences at the short timescales. The latter however do not feature any experimental relevance in the light of the bandwidth limitations imposed experimentally and can therefore be neglected. To illustrate this, Figure 5.19 additionally contrasts the same current signals after the signal filtering which feature significant similarities at all time scales. When analysing experimental data it is hence not possible to distinguish between the two theoretical models solely on the basis of the spike shape which leaves us with the convenience of a choosing one of the two models for the estimation of the contact area angle Φ_0 from experimental data in favourable cases where the values of the below introduced fitting parameters can be determined with sufficient accuracy.

5.3.4 Dimensional analysis and fitting parameters

In both theoretical models discussed in this chapter, four different fitting parameters must be considered when comparing measured dimensional currents with simulated data: The diffusion coefficient D of the analyte A^+, the radius of the particle r_0 before the impact and adsorption[5], the concentration c^* of the analyte within the particle, and

[5] For polymer particles, we note that as the material may adsorb water and swell in solution [40, 41], the real values of r_0 and c^* are therefore difficult to determine in solution.

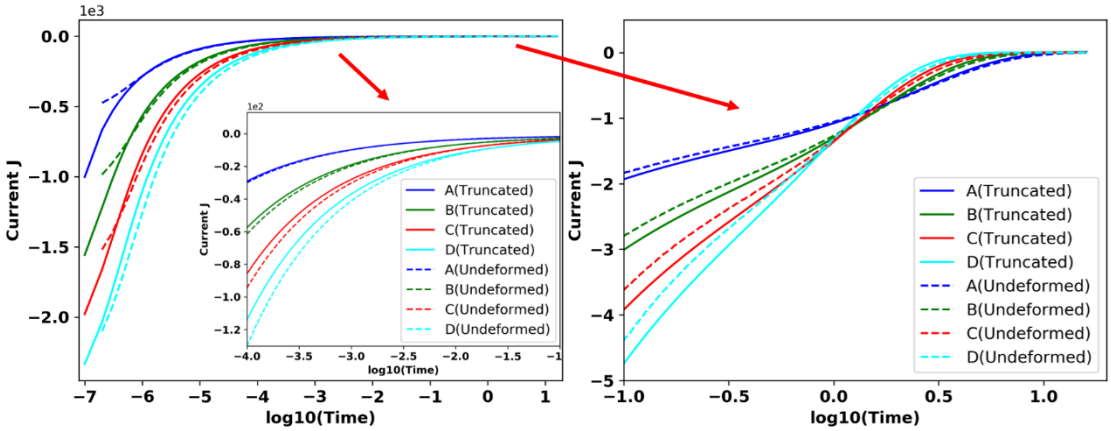


Figure 5.18: Comparison of the temporal evolutions of the current responses in the 'truncated-' and the 'undeformed-sphere' models evaluated for different Ar.

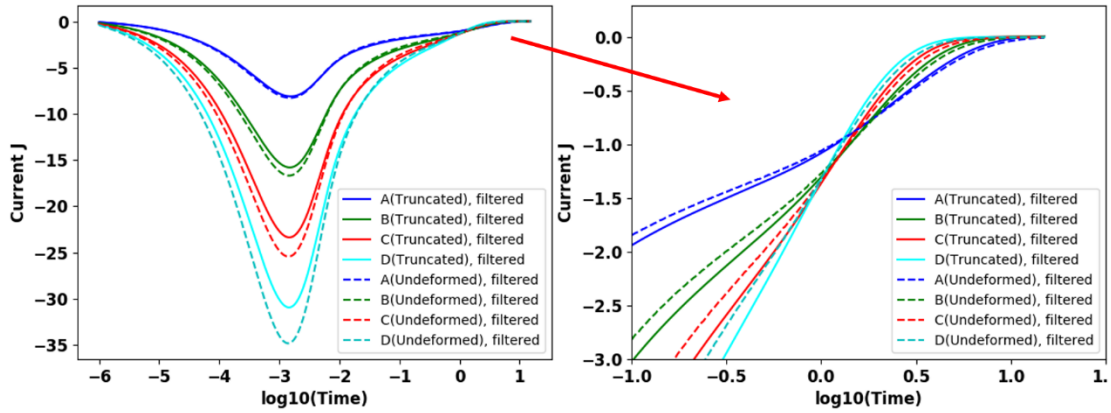


Figure 5.19: Comparison of the current responses found in the 'truncated-' and the 'undeformed-sphere' models when evaluated for different Ar after signal filtering at a dimensionless cut-off frequency of 100.

the contact area angle Φ_0. The large number of parameters obviously complicates the comparison with experimental data where exact values may be unknown. It is therefore desirable to reduce the number of parameters as well as to use quantities that are more accessible from experimental data. To this end, this section conducts a dimensionless analysis to establish a set of less and more convenient parameters for the theoretical modelling. First, we consider the relation between the dimensional current and the dimensionless current as provided in Table 5.1:

$$I = Fr_0 Dc^* J \tag{5.11}$$

The dimensionless currents calculated on the basis of Fick's first law can be written using this transformation:

$$J_t = \left.\frac{\partial C_t}{\partial Z}\right|_{Z=0,R<R_e} \tag{5.12}$$

$$J_f = \left.\frac{\partial C_f}{\partial R}\right|_{R=1,\Phi<\Phi_0} \tag{5.13}$$

where J_t and J_f are for the 'truncated-' and 'undeformed-sphere' model, respectively.

We further obtain the partial differential equation for the temporal evolution of dimensionless concentration from Fick's second law based on the transformations given in Table 5.1:

$$\frac{\partial C}{\partial T} = \nabla_{R,Z}^2 C \tag{5.14}$$

Analogously, we transform the boundary conditions defined in Figure 5.3 and Figure 5.5, namely no-flux boundaries of the form:

$$\vec{n} \cdot \nabla_{R,Z} C = 0 \tag{5.15}$$

where $\vec{n}$ is the normal vector of the respective boundary, and most notably set the dimensionless concentration at the electrode to 0:

$$C_t = 0|_{Z=0,R<R_e} \tag{5.16}$$

$$C_f = 0|_{R=1,\Phi<\Phi_0} \tag{5.17}$$

The above Eqn (5.12) to Eqn (5.17) represent a complete definition of the theoretical models solved in this work.

A closer investigation reveals that the dimensionless currents in both models solely depend on two parameters:

$$J_t = f_t(T, R_e) \tag{5.18}$$

$$J_f = f_t(T, \Phi_0) \tag{5.19}$$

For the 'truncated-sphere' model, we can further express R_e as a function of R_1 and Φ_0:

$$R_e = R_1 sin\Phi_0 \tag{5.20}$$

where R_1 is the particle radius following the deformation in the 'truncated-sphere'

model. Since, in this model, we can calculate the dimensionless volume of a particle before and after the adsorption:

$$V_0 = \frac{4}{3}\pi R_0^3 \tag{5.21}$$

$$V_1 = \frac{\pi}{3}(3R_1 - H)H^2 \tag{5.22}$$

where H is the height of the missing cap of the truncated sphere as defined in Figure 5.17, we express the dimensionless R_e as a function of Φ_0:

$$R_e = \sqrt[3]{\frac{R_0^3 sin^3\Phi_0}{2 - 3cos\Phi_0 + cos^3\Phi_0}} = \sqrt[3]{\frac{sin^3\Phi_0}{2 - 3cos\Phi_0 + cos^3\Phi_0}} \tag{5.23}$$

Currents in both models, Eqn (5.18) and Eqn (5.19), can hence be expressed in the form:

$$J = f(T, \Phi_0) \tag{5.24}$$

Substituting the definition of the dimensionless time:

$$T = \frac{Dt}{r_0^2} \tag{5.25}$$

and Eqn (5.11), the dimensional current can be written:

$$I = Fr_0 Dc^* f\left(t \cdot \frac{D}{r_0^2}, \Phi_0\right) \tag{5.26}$$

where the shape of the current transient is solely defined by only two parameters, $D/(r_0)^2$ and Φ_0, and an additional proportionality factor, r_0Dc^*. To further simplify this factor, we write the overall charge of all analyte Q within the particle as:

$$Q = c^* FV \tag{5.27}$$

where V is the total dimensional volume of the particle before the impact which can be calculated by:

$$V = \frac{4}{3}\pi r_0^3 \tag{5.28}$$

Substitution of Eqn (5.27) and Eqn (5.28) simplifies Eqn (5.26) to:

$$I = \frac{r_0 DQ}{V} f\left(t \cdot \frac{D}{r_0^2}, \Phi_0\right) = \frac{3}{4\pi} \cdot \frac{D}{r_0^2} \cdot Q \cdot f\left(t \cdot \frac{D}{r_0^2}, \Phi_0\right) \qquad (5.29)$$

which features three parameters, $D/(r_0)^2$, Φ_0, and the overall charge Q which is readily available from the integration of the respective current spike. The above dimensional analysis hence reduces the number of fitting parameters from four to three, one of which is directly accessible from the experimental data. There are hence only two parameters left that must be fitted simultaneously for the comparison of experimental currents with simulated data.

5.4 Conclusions

In this chapter, we investigate the diffusion-controlled electrochemical depletion of an analyte inside a 'soft' nanoparticle adsorption at an electrode. Two theoretical models are introduced and differ in the assumed particle shape upon adsorption. Simulated electrode currents are rationalised and discussed in the light of bandwidth limitations that are typically imposed by experimental measurement set-ups. Our analysis reveals that, in cases where simulated data can be fitted to experimental data with sufficient accuracy, the size of the contact area between the particle and the electrode can be extracted from experimental data while the deformation of the particle hardly affects the measured current transients. In addition, we present a dimensional analysis to reduce the number of fitting parameters in both theoretical models.

References

[1] H. Le, C. Lin, E. Kätelhön, R. G. Compton, *Electrochimica Acta*, **2019**, *298*, 778–787.

[2] W. Cheng, R. G. Compton, *TrAC Trends in Analytical Chemistry*, **2014**, *58*, 79–89.

[3] M. Pumera, *ACS Nano* **2014**, *8*, 7555–7558.

[4] C. Batchelor-McAuley, E. Kätelhön, E. O. Barnes, R. G. Compton, E. Laborda, A. Molina, *ChemistryOpen* **2015**, *4*, 224–260.

[5] P. H. Robbs, N. V. Rees, *Physical Chemistry Chemical Physics* **2016**, *18*, 24812–24819.

[6] M. V. Mirkin, T. Sun, Y. Yu, M. Zhou, *Accounts of Chemical Research* **2016**, *49*, 2328–2335.

[7] Y. Wang, X. Shan, N. Tao, *Faraday Discussions* **2016**, *193*, 9–39.

[8] E. N. Saw, M. Kratz, K. Tschulik, *Nano Research* **2017**, *10*, 3680–3689.

[9] S. V. Sokolov, S. Eloul, E. Kätelhön, C. Batchelor-McAuley, R. G. Compton, *Physical Chemistry Chemical Physics* **2017**, *19*, 28–43.

[10] K. J. Stevenson, K. Tschulik, *Current Opinion in Electrochemistry* **2017**, *6*, 38–45.

[11] L. K. Allerston, N. V. Rees, *Current Opinion in Electrochemistry* **2018**, *10*, 31–36.

[12] Y. G. Zhou, N. V. Rees, R. G. Compton, *Angewandte Chemie International Edition* **2011**, *50*, 4219–4221.

[13] Y. G. Zhou, N. V. Rees, J. Pillay, R. Tshikhudo, S. Vilakazi, R. G. Compton, *Chemical Communications* **2012**, *48*, 224–226.

[14] H. S. Toh, R. G. Compton, *ChemistryOpen* **2014**, *4*, 261–263.

[15] E. Kätelhön, E. E. L. Tanner, C. Batchelor-McAuley, R. G. Compton, *Electrochimica Acta* **2016**, *199*, 297–304.

[16] E. Kätelhön, A. Feng, W. Cheng, S. Eloul, C. Batchelor-McAuley, R. G. Compton, *The Journal of Physical Chemistry C* **2016**, *120*, 17029–17034.

[17] G. Zampardi, C. Batchelor-McAuley, E. Kätelhön, R. G. Compton, *Angewandte Chemie International Edition* **2017**, *56*, 641–644.

[18] K. J. Krause, F. Brings, J. Schnitker, E. Kätelhön, P. Rinklin, D. Mayer, R. G. Compton,

S. G. Lemay, A. Offenhäusser, B. Wolfrum, *Chemistry – A European Journal* **2017**, *23*, 4638–4643.

[19] J. E. Dick, A. T. Hilterbrand, A. Boika, J. W. Upton, A. J. Bard, *Proceedings of the National Academy of Sciences* **2015**, *112*, 5303–5308.

[20] J. Y. Lee, B. .-K. Kim, M. Kang, J. H. Park, *Scientific Reports* **2016**, *6*, 30022.

[21] C. Lin, L. Sepunaru, E. Kätelhön, R. G. Compton, *The Journal of Physical Chemistry Letters* **2018**, *9*, 2814–2817.

[22] J. G. Gaudiello, P. K. Ghosh, A. J. Bard, *Journal of the American Chemical Society* **1985**, *107*, 3027–3032.

[23] R. J. Mortimer, J. L. Dillingham, *Journal of the Electrochemical Society* **1997**, *144*, 1549–1553.

[24] I. Rubinstein, A. J. Bard, *Journal of the American Chemical Society* **1981**, *103*, 5007–5013.

[25] C. R. Martin, I. Rubinstein, A. J. Bard, *Journal of the American Chemical Society* **1982**, *104*, 4817–4824.

[26] D. A. Buttry, F. C. Anson, *Journal of the American Chemical Society* **1982**, *104*, 4824–4829.

[27] H. Yang, X. Li, C. Batchelor-McAuley, S. V. Sokolov, R. G. Compton, *Physical Chemistry Chemical Physics* **2018**, *20*, 682–689.

[28] L. Chen, C. Lin, R. G. Compton, *Physical Chemistry Chemical Physics* **2018**, *20*, 15795–15806.

[29] X. Li, C. Batchelor-McAuley, L. Shao, S. V. Sokolov, N. P. Young, R. G. Compton, *The Journal of Physical Chemistry Letters* **2017**, *8*, 507–511.

[30] A. Krittayavathananon, X. Li, S. V. Sokolov, C. Batchelor-McAuley, M. Sawangphruk, R. G. Compton, *Applied Materials Today* **2018**, *10*, 122–126.

[31] D. Peaceman, H. Rachford, Jr., *Journal of the Society for Industrial and Applied Mathematics* **1955**, *3*, 28–41.

[32] J. Heinze, *Journal of Electroanalytical Chemistry and Interfacial Electrochemistry* **1981**, *124*, 73–86.

[33] J. A. Alden, R. G. Compton, *The Journal of Physical Chemistry B* **1997**, *101*, 8941–8954.

[34] W. H. Press, S. A. Teukolsky, W. T. Vetterling, B. P. Flannery, *Numerical Recipes: The Art of Scientific Computing (Third Edition)*, Cambridge University Press, **2007**.

[35] R. G. Compton, E. Laborda, K. R. Ward, *Understanding Voltammetry: Simulation of Electrode Processes*, Imperial College Press, **2013**.

[36] E. Kätelhön, R. G. Compton, *Analyst* **2015**, *140*, 2592–2598.

[37] E. Kätelhön, R. G. Compton, *Analyst* **2015**, *140*, 3290–3290.

[38] E. Kätelhön, R. G. Compton, *Analyst* **2016**, *141*, 1154–1154.

[39] F. G. Cottrell, *Zeitschrift für Physikalische Chemie* **1903**, *42*, 385.

[40] G. Gebel, P. Aldebert, M. Pineri, *Polymer* **1993**, *34*, 333–339.

[41] M. H. Eikerling, P. Berg, *Soft Matter* **2011**, *7*, 5976–5990.

Chapter 6: Reversible Cyclic Voltammetry at Cylindrical Electrodes

This chapter investigates the cyclic voltammetry of a reversible one-electron-transfer using finite difference simulations at three different electrode models: an 'infinitely long cylinder' electrode featuring a cylindrical electrode with an infinite length, an 'annular band' electrode, whose band-shape electrochemically active area is located around an infinitely long insulating cylinder, and a 'full cylinder' electrode which resembles the microwire electrodes widely used in electrochemical experiments with both side and end active. Following the simulation of the infinitely long cylindrical electrode, a polynomial equation is subsequently produced and introduced to describe the forward peak potentials at different scan rates. Based on further simulations of the other two electrodes above, we find if the lengths of the latter are greater than ~10^4 times the radius of the cylinders, the electrochemical reversible cyclic voltammetry of them can be well described by the 'infinitely long cylinder' model with the errors of less than 1%. The results reported in this chapter are based on a published first-author paper [1] [*Journal of Electroanalytical Chemistry*, **2020**, *859*, 113865].

6.1 Introduction

Microelectrodes are wildly used [2–7] to investigate electrochemical reactions and mass-transport processes through voltammetry. Microcylinder electrodes, often in the forms of microwire electrodes, are frequently used [8–21] due to their advantages including, but not limited to, their low cost and ease of fabrication. Microcylinder electrodes show different voltammetric behaviours from microdisc [22–24] and hemisphere electrodes [25–27] as they have one micro dimension (the radius) and one

macro dimension (the length), which leads to quasi-steady state voltammetry rather than a true steady state under slow voltage scan rate conditions [2, 3, 28]. The quasi-steady state gives rise to vestigial back peaks in cyclic voltammetry which can have mechanistic value. Furthermore, the increased electrode area enables microwire electrodes to play an essential role in diverse research areas including environmental sensors [29–31], medical diagnosis [32–34], and nano-impact studies [14, 35–37].

There are various theoretical studies [38–40] modelling the current responses of infinitely long cylindrical electrodes as illustrated in Figure 6.1.

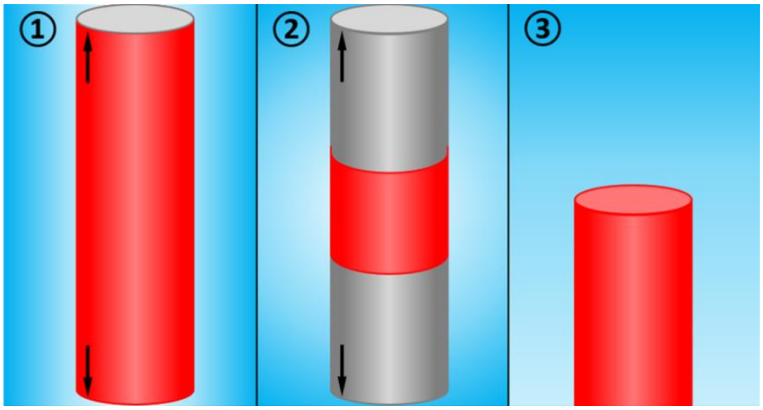


Figure 6.1: Illustrations of the models investigated: ① the 'infinitely long cylinder' electrode model, ② the 'annular band' electrode model, ③ the 'full cylinder' electrode model. The black arrows in the figures represent infinitely expanding areas.

However, in experimental research utilising microcylinder electrodes, an infinite length of the microcylinder is obviously impossible to realise. The question then arises as to how long either an annular band or a cylinder with an electrochemically active end must be in order that the one-dimensional approximation is valid. Thus, building on our recent work [41] and Chapter 4 on chronoamperometric current responses of realistic cylinder electrode models identifying finite length effects and the contributions from the disk-like cylinder 'end', this chapter presents studies of simulated cyclic voltammetric currents using the geometries shown in Figure 6.1. The conditions under which an infinitely long cylindrical electrode model can describe the two other cylinder-like electrodes are clarified.

6.2 Theory and simulation

In this section, we introduce the theoretical models, the expanding grids, the dimensionless parameters, and the computational methods used in this chapter. Please refer to chapter 4 and a recent work [41] for all details beyond the below summary.

6.2.1 Theoretical models

The cyclic voltammetry of a single-electron-transfer reaction is studied in this chapter as shown in Eqn (6.1), at the three different cylinder-like electrode geometries shown in Figure 6.1.

$$A + e^- \rightleftharpoons B \tag{6.1}$$

First, the 'infinitely long cylinder' electrode model is an infinite cylinder with the electrochemically active area at the side of the cylinder. Second, the 'annular band' electrode model features the electrochemically active area of length *l* at the side of an infinitely long insulating cylinder. Finally, the third model is the 'full cylinder' electrode model with the side and the end of the cylinder being electrochemically active. Beyond the electrode surface in the simulation models, the initial concentrations c_A^* of the analyte *A* are assumed homogeneous before an overpotential is applied, and the initial concentration of *B* is set to zero in all simulated space. Assuming a sufficiently high electrolyte concentration, the mass transport is considered exclusively to be diffusion and can be described by the diffusion equation, which is shown in Eqn (6.2) in cylindrical coordinates (r, z, ϕ):

$$\frac{\partial c}{\partial t} = D\nabla^2 c = D\left(\frac{\partial^2 c}{\partial r^2} + \frac{1}{r}\frac{\partial c}{\partial r} + \frac{\partial^2 c}{\partial z^2} + \frac{1}{r^2}\frac{\partial^2 c}{\partial \phi^2}\right) \tag{6.2}$$

where *c* is the concentration of any species at a certain point, *t* is the time, *D* is the diffusion coefficient of *A*, *r* is the radial distance, *z* is the axial distance, and ϕ is the angle around the *z*-axis of the plane set by the *r*-axis and the *z*-axis. In the 'infinitely

long cylinder' electrode model, the horizontal symmetry and rotational symmetry for the *z*-axis result in the independence of the concentration of the axial distance *z* and the angle ϕ. Therefore, this system can be modelled using a one-dimensional coordinate system (*r*), and Eqn (6.2) can be simplified to:

$$\frac{\partial c}{\partial t} = D\nabla^2 c = D(\frac{\partial^2 c}{\partial r^2} + \frac{1}{r}\frac{\partial c}{\partial r}) \tag{6.3}$$

Similarly, the rotational symmetries around the *z*-axes in the 'annular band' electrode model and the 'full cylinder' electrode model lead to the simplification of Eqn (6.2) can be simplified to:

$$\frac{\partial c}{\partial t} = D\nabla^2 c = D(\frac{\partial^2 c}{\partial r^2} + \frac{1}{r}\frac{\partial c}{\partial r} + \frac{\partial^2 c}{\partial z^2}) \tag{6.4}$$

In all simulations, the current responses and the concentration profiles are recorded and analysed for varied lengths of the electrochemically active areas. The electrode process at the electrochemically active areas is described by the Nernst equation:

$$E = E^0_{A/B} + \frac{RT}{F}\ln\left(\frac{c^0_A}{c^0_B}\right) \tag{6.5}$$

where *E* is the electrode potential, $E^0_{A/B}$ is the formal potential of the *A/B* redox reaction, ***R*** is the Universal Gas Constant, ***T*** is the temperature, *F* is the Faraday constant, and c^0_A and c^0_B are the concentration of *A* and *B*, respectively, at the electrode surface. In the cyclic voltammetric simulations, *E* are applied to the electrochemically active areas in a constantly varying way shown in Eqn (6.6):

$$E(t) = \begin{cases} E(t_0) - \nu t & where \quad t < \dfrac{t_{sim}}{2} \\ E\left(\dfrac{t_{sim}}{2}\right) + \nu\left(t - \dfrac{t_{sim}}{2}\right) & where \quad t \geq \dfrac{t_{sim}}{2} \end{cases} \tag{6.6}$$

where $E(t)$ is the potential applied at *t* time point, $E(t_0)$ is the initial potential applied at the beginning of the simulation, t_{sim} is the total simulation time, and ν is the scan rate of the potential applied.

6.2.1.1 The 'infinitely long cylinder' electrode model

The radius of the infinitely long cylinder is r_e, as shown in ① in Figure 6.2, while the electrochemically active area is shown in red, and the analyte *A* is shown in blue.

As shown in ② in Figure 6.2, the boundary conditions for the simulation are presented setting the initial concentration of *A* to c_A^* and that of *B* to zero:

$$t = 0, r_e \le r \le r_{max}: \quad c_A = c_A^*, c_B = 0 \tag{6.7}$$

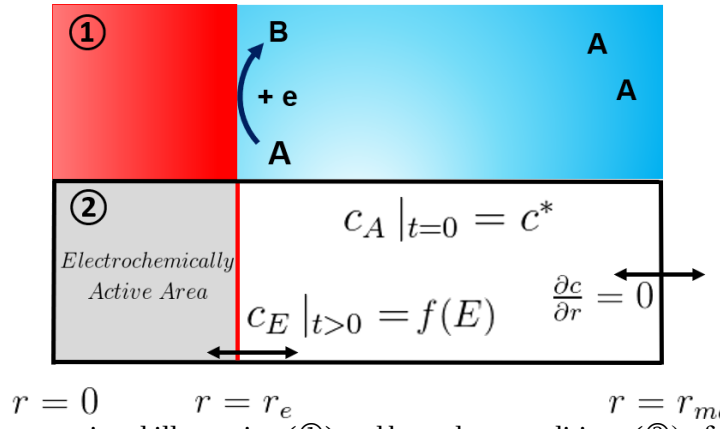


Figure 6.2: Cross-sectional illustration (①) and boundary conditions (②) of the 'infinitely long cylinder' electrode model. *c* is the concentration of any species, c_A is the concentration of analyte *A* for all of the points within the simulated space, c_A^* is the initially homogeneous concentration of *A*, c_E is the concentration of *A* for points at the electrode surface, r_e is the radius of the cylinder, and r_{max} is the boundary of the simulated space in the *r*-axis.

As the reaction starts, the concentration variation at the electrode surface follows the Nernst equilibrium. No-flux boundaries are set at the far end of the simulated space:

$$t > 0, r = r_{max}: \quad \frac{\partial c}{\partial r} = 0 \tag{6.8}$$

with the simulated space being a function of the total simulation time t_{sim}:

$$\begin{cases} r_{max} = r_e + x_{sim} \\ x_{sim} = 6\sqrt{D t_{sim}} \end{cases} \tag{6.9}$$

where x_{sim} is large enough to enable the concentration changes at the electrode surface to be independent on the boundary at the far end [42].

We can calculate the current responses, following Fick's first law and Faraday's law, in the 'infinitely long cylinder' electrode model as:

$$I_{ILC} = Fj_{ILC} \quad where \quad j_{ILC} = -2\pi l_e r_e D \frac{\partial c_A}{\partial r}|_{r=r_e} \tag{6.10}$$

where I_{ILC} is the current, j_{ILC} is the flux of the analyte *A*, and l_e is the length of the cylinder if we only extract a fragment of the infinitely long cylinder.

6.2.1.2 The 'annular band' electrode model

This model, as shown in Figure ① in Figure 6.3, features the electrochemically active area with the radius r_e and length l_e. The area shown in grey is the insulating area.

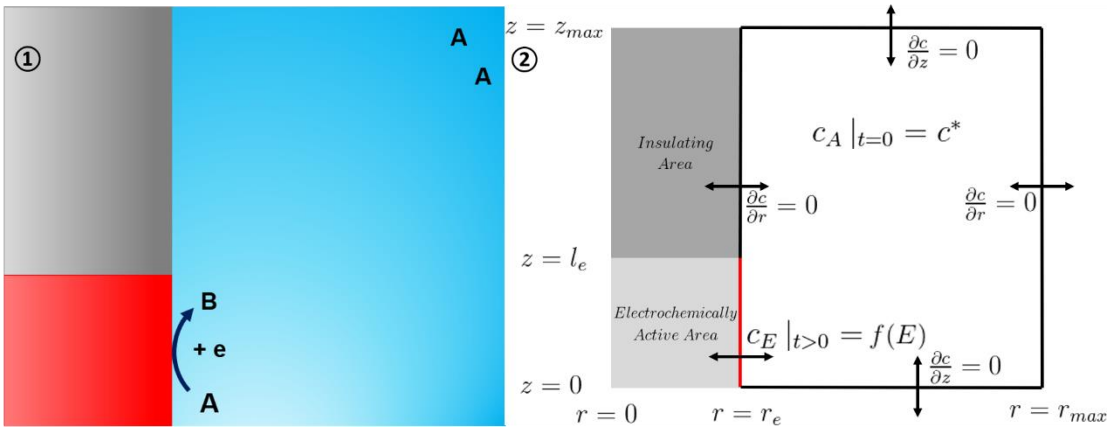


Figure 6.3: Cross-sectional illustration (①) and boundary conditions (②) of the 'annular band' electrode model adapted from a plot in a recent work [41]. z_{max} is the boundary of the simulated space in the *z*-axis, and l_e is the length of the annular band in the *z*-axis.

The boundary conditions for the simulation are shown in ② in Figure 6.3. Before applying the potential, the initial concentrations of *A* and *B* are set to c_A^* and zero:

$$t = 0, r_e \le r \le r_{max}, 0 \le z \le z_{max}: \quad c_A = c_A^*, c_B = 0 \tag{6.11}$$

As the cyclic voltammetry starts, the boundary conditions at the electrochemically active area and everywhere else correspond to the Nernst equilibrium and the no-flux limits, respectively. The no-flux boundaries are:

$$\begin{cases} t > 0, r = r_e, l_e \le z \le z_{max}: & \dfrac{\partial c}{\partial r} = 0 \\ t > 0, r = r_{max}, 0 \le z \le z_{max}: & \dfrac{\partial c}{\partial r} = 0 \\ t > 0, 0 \le r \le r_{max}, z = 0: & \dfrac{\partial c}{\partial z} = 0 \\ t > 0, 0 \le r \le r_{max}, z = z_{max}: & \dfrac{\partial c}{\partial z} = 0 \end{cases} \tag{6.12}$$

where the simulation spaces and their corresponding simulation time t_{sim} are:

$$\begin{cases} r_{max} = r_e + x_{sim} \\ z_{max} = l_e + x_{sim} \\ x_{sim} = 6\sqrt{Dt_{sim}} \end{cases} \tag{6.13}$$

Similar to the previous model, we can calculate the current responses of *A* for the 'annular band' electrode model as:

$$I_{AB} = Fj_{AB} \quad where \quad j_{AB} = -2\pi r_e D \int_0^{l_e} \frac{\partial c_A}{\partial r} |_{r=r_e} \, dz \tag{6.14}$$

6.2.1.3 The 'full cylinder' electrode model

As shown in Figure ① of Figure 6.4, the side and the end of cylinder in this model are electrochemically active. This model aims to model the microcylinder, or microwire, electrode, which is commonly used in experiments. In this system, diffusion equation is also expressed by Eqn (6.4).

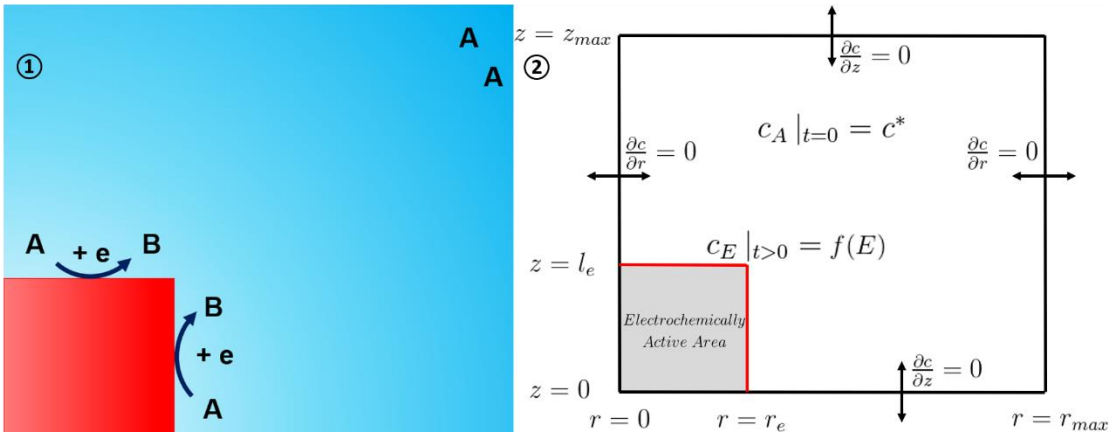


Figure 6.4: Cross-sectional illustration (①) and boundary conditions (②) of the 'full cylinder' electrode model adapted from a plot in a recent work [41].

The boundary conditions, shown in Figure ② in Figure 6.4, demonstrate the modelling details. The concentrations of *A* and *B* for all of the points in the simulations are initially set as c_A^* and zero:

$$t = 0, 0 \le r \le r_e, 0 \le z < l_e: \quad c_A = c_A^*, c_B = 0 \tag{6.15}$$

The boundary conditions for the electrochemically active areas follows the Nernst equilibrium. No-flux boundaries are set similarly to Eqn (6.12):

$$\begin{cases} t > 0, r = r_e, 0 \le z \le l_e: & c = 0 \\ t > 0, z = l_e, 0 \le r \le r_e: & c = 0 \end{cases} \tag{6.16}$$

where the simulation space is:

$$\begin{cases} r_{max} = r_e + x_{sim} \\ z_{max} = l_e + x_{sim} \\ x_{sim} = 6\sqrt{Dt_{sim}} \end{cases} \tag{6.17}$$

The fluxes and currents of *A* towards the side and end of the cylinder are calculated separately before summed up to the total fluxes j_{FC} and the total currents I_{FC} of *A*:

$$\begin{cases} I_s = Fj_s \quad where \quad j_s = -2\pi r_e D \int_0^{l_e} \frac{\partial c_A}{\partial r} |_{r=r_e} \, dz \\ I_e = Fj_e \quad where \quad j_e = -2\pi D \int_0^{r_e} \frac{\partial c_A}{\partial z} |_{z=l_e} \, rdr \\ j_{FC} = j_s + j_e \\ I_{FC} = I_s + I_e \end{cases} \tag{6.18}$$

where I_e is the current to the end of the cylinder, j_e is the flux of the analyte *A* to the end of the cylinder, and the total current I_{FC} is the sum of the current towards the side I_s and the end I_e of the electrode.

6.2.2 Dimensionless parameters

Here we present the dimensionless parameters used in this chapter to enable a simple and universal presentation of the simulation results. By adopting dimensionless forms, comparison between different experimental systems can be more straightforward. The transformations are shown in Table 6.1, where σ and v are the dimensional and dimensionless form of the scan rate of the potential applied.

The dimensionless diffusion equations Eqn (6.3) and Eqn (6.4) can be rewritten as:

$$\begin{gathered} \frac{\partial C_j}{\partial T} = d_j \left(\frac{\partial^2 C_j}{\partial R^2} + \frac{1}{R} \frac{\partial C_j}{\partial R} \right) \\ \frac{\partial C_j}{\partial T} = d_j \left(\frac{\partial^2 C_j}{\partial R^2} + \frac{1}{R} \frac{\partial C_j}{\partial R} + \frac{\partial^2 C_j}{\partial Z^2} \right) \end{gathered} \tag{6.19}$$

where C_j is the dimensionless concentration of the species *j*, and d_j is the dimensionless diffusion coefficient of the species *j*, as defined in Table 6.1. Furthermore, the current

Table 6.1: Transformation of dimensional parameters to dimensionless parameters where r_r is the reference length of the respective model.

Dimensionless Parameters	Conversions
Concentration of species j	$C_j = \frac{c_j}{c^*}$
Diffusion coefficient of species j	$d_j = \frac{D_j}{D}$
Radial distance	$R = \frac{r}{r_r}$
Axial distance	$Z = \frac{z}{r_r}$
Cylinder length	$L = \frac{l}{r_r}$
Time	$T = \frac{Dt}{r_r^2}$
Potential	$\theta = \frac{F}{\boldsymbol{RT}}(E - E_f^0)$
Scan rate	$\sigma = \frac{r_r^2 F}{\boldsymbol{DRT}}\nu$
Current	$J = \frac{I}{Fr_r Dc^*}$

calculations Eqn (6.10), Eqn (6.14), and Eqn (6.18) can be rewritten as:

$$J_{ILC} = -2\pi L_e d_A \frac{\partial C_A}{\partial R}\,|_{R=1} \tag{6.20}$$

$$J_{AB} = -2\pi d_A \int_0^{l_e} \frac{\partial C_A}{\partial R}\,|_{R=1}\, dZ \tag{6.21}$$

$$\begin{cases} J_s = -2\pi d_A \int_0^{L_e} \frac{\partial C_A}{\partial R}\,|_{R=1}\, dZ \\ J_e = -2\pi d_A \int_0^{1} \frac{\partial C_A}{\partial Z}\,|_{Z=L_e}\, RdR \\ J_{FC} = J_s + J_e \end{cases} \tag{6.22}$$

where L_e is the dimensionless length of the electrode.

6.2.3 Simulation grids

Expanding space grids are implemented in all simulation models. For the 'infinitely long cylinder' electrode model, the one-dimensional simulated space features a single expanding space grid shown in Figure 6.5, as defined in Appendix.A. Furthermore, for

the ‘annular band’ electrode model, the simulation space grids in the *z*-axis consist of a double-expanding space grid and a single-expanding space grid shown in Figure 6.6, and there is a single-expanding space grid in the *r*-axis. Finally, as shown in Figure 6.7, there are both a double-expanding grid and a single-expanding grid in the *z*- and *r*-axis for the ‘full cylinder’ electrode model. For all models in this chapter, equally spaced θ grids were employed, which also means equally spaced time grids.



Figure 6.5: Cross-sectional illustration of simulation space points for the ‘infinitely long cylinder’ electrode model. r_e is the radius of the electrode, r_{max} is the boundary of simulation space in the *r*-axis, the red line represents the electrochemically active surface of the electrode.

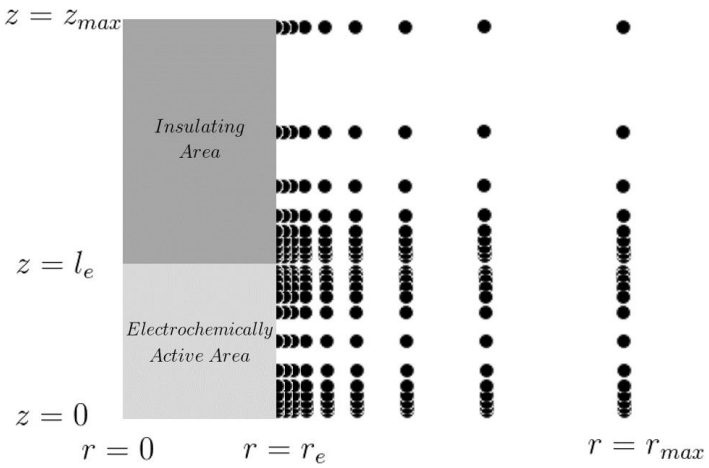


Figure 6.6: Cross-sectional illustration of the simulation space points for the ‘annular band’ electrode model. l_e is the length of the annular band in the *z*-axis, z_{max} is the boundary of the simulated space in the *z*-axis.

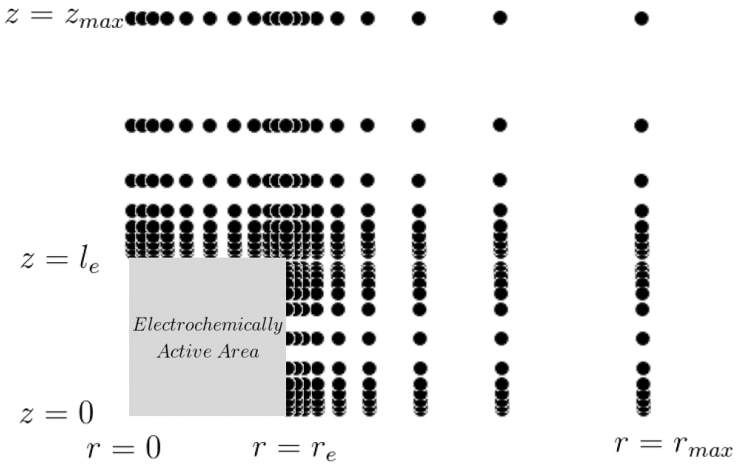


Figure 6.7: Cross-sectional illustration of the simulation space points for the ‘full cylinder’ electrode model.

6.2.4 Computational methods

Customised simulation codes were developed in *C++* for the simulation models shown in previous sections. The partial differential equations in this chapter are solved via matrix equations using the finite difference approach. Specifically, the alternating direction implicit (ADI) method [43–45] is used to solve the corresponding matrix system. Data is processed and visualised via *Python* scripts using the *NumPy* and *matplotlib* libraries. Please refer to the textbook [42] and Chapter 4 for more details.

6.3 Results and discussion

In this section, after showing the numerical testing and validating results for the simulation models, we discuss the results for different models. The 'infinitely long cylinder' electrode model is addressed first to develop empirical equations for the peak separation (ΔE_{pp}) and forward peak currents (I_p) for a reversible electrochemical reaction. The 'annular band' electrode model and 'full cylinder' electrode model are discussed subsequently to compare between the cylinder-like models and to further investigate how long a microcylinder should be for its cyclic voltammetric currents to be described accurately by the 'infinitely long cylinder' electrode model.

6.3.1 Testing numerical simulations

Testing and validation methods [46] are employed and reported below including convergence studies and studies of error of mass conservation by varying the potential step dθ, space step dX, and space expanding factor ωX in the simulations while setting some of the physical parameters constant. Appropriate parameter sets were obtained for different models shown in Table 6.2 and Table 6.3 by varying the three parameters ($d\theta$, dX, and ωX) at two extreme values of scan rates chosen ($\theta = 10^{-5}, 10^{5}$).

The forward peak potentials, forward peak currents and the errors of the mass

conservation, as defined in Appendix.B, for different simulations are obtained to ensure convergence by keeping the values of all but one parameter constant ($d\theta$, dX, and ωX) and varying the latter as presented below.

Table 6.2: Dimensionless parameter sets for the 'infinitely long cylinder' model

Dimensionless Parameters	The 'Infinitely Long Cylinder' Model	
Potential, θ	30 to -30	
Initial concentration, C^*	1	
Diffusion coefficient, d	1	
Radius, R_0	1	
Scan rate, σ	10^{5}	10^{-5}
Space step, dX	10^{-5}	10^{-2}
Space expand factor, wX	1.0003	1.000001
Potential step, $d\theta$	10^{-3}	10^{-2}

Table 6.3: Dimensionless parameter sets for the 'annular band' model and 'full cylinder' model

Dimensionless Parameters	The 'Annular Band' Model		The 'Full Cylinder' Model	
Potential, θ	30 to -30		30 to -30	
Initial concentration, C^*	1		1	
Diffusion coefficient, d	1		1	
Radius, R_0	1		1	
Scan rate, σ	10^{5}	10^{-5}	10^{5}	10^{-5}
Space step, dX	5×10^{-6}	5×10^{-6}	3×10^{-5}	3×10^{-3}
Space expand factor, wX	1.08	1.08	1.08	1.08
Potential step, $d\theta$	10^{-3}	10^{-3}	2×10^{-4}	10^{-2}
Length (L) range	10^{-1} to 10^{1}	10^{3} to 10^{5}	10^{-1} to 10^{2}	10^{3} to 10^{5}

6.3.1.1 Testing the 'infinitely long cylinder' electrode model

We performed the convergence studies and tests of the errors of mass conservation for the 'infinitely long cylinder' electrode model for different scan rates ($10^{-5} \leq \sigma \leq 10^{5}$

with the interval $\log_{10}\Delta\sigma = 1$), two of which are shown in this section ($\sigma = 10^{-5}$, 10^{5}).

The errors of mass conservation for different simulations varying one of the simulation parameters above are shown in Figure 6.8. The errors of mass conservation of simulation with the previous stated parameter sets are kept at a lower level (below 1%). When further decreasing the simulation parameters, the errors do not vary much.

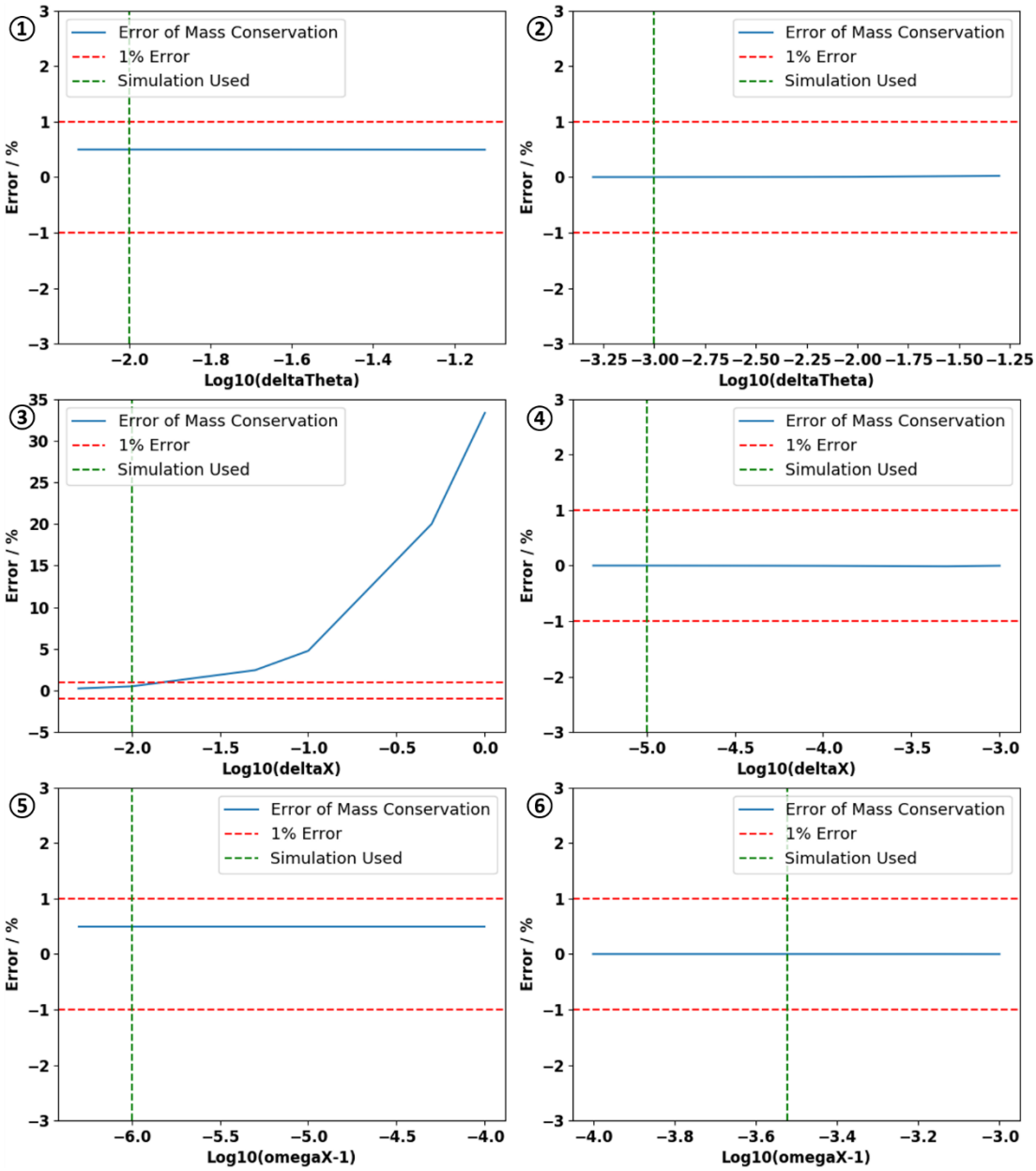


Figure 6.8: Errors of mass conservation calculated for $\sigma = 10^{-5}$ (left) and $\sigma = 10^{5}$ (right) for the 'infinitely long cylinder' electrode model for simulations varying: $d\theta$: ①②; dX: ③④; ωX: ⑤⑥.

As shown in Figure 6.9 and 6.10, as the corresponding parameters decreases to an extent, the forward peak potential and forward peak current of voltammogram remain

at similar levels. Based on the test of errors of mass conservation and the convergence studies of the current responses, the sets of parameters chosen in this section is considered as 'converged' before the simulation results are analysed and interpreted.

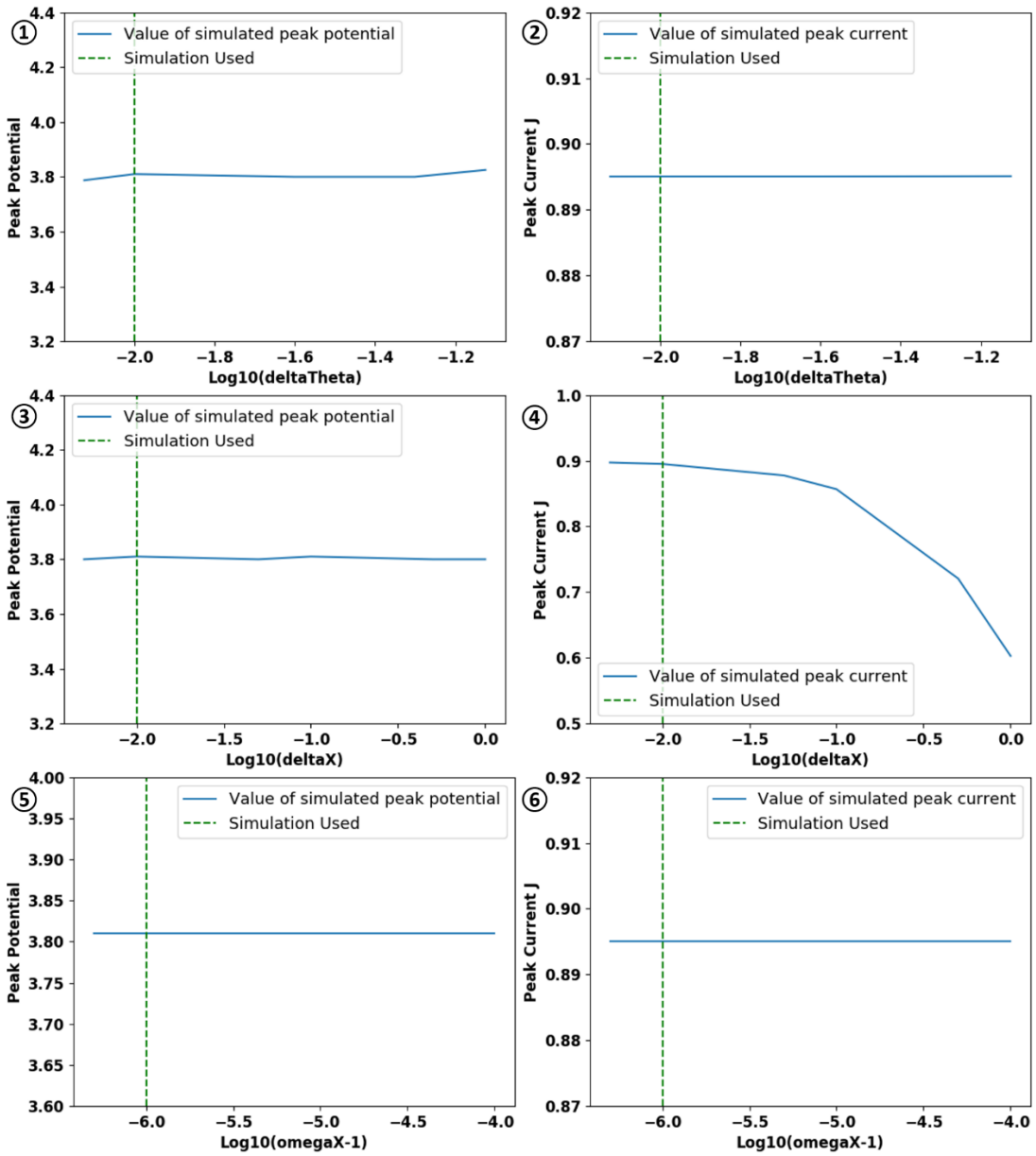


Figure 6.9: Peak potentials (left) and peak currents (right) of current responses for test simulations for the 'infinitely long cylinder' electrode model for $\sigma = 10^{-5}$ varying: $d\theta$: ①②; dX: ③④; ωX: ⑤⑥.

After the convergence studies and test of mass conservation, the parameters of individual scan rates are selected. The errors of mass conservation, in Figure 6.11, calculated for the simulations of different scan rate σ from 10^{-5} to 10^{5} using corresponding parameter sets remain under 1% for the 'infinitely long cylinder' models.

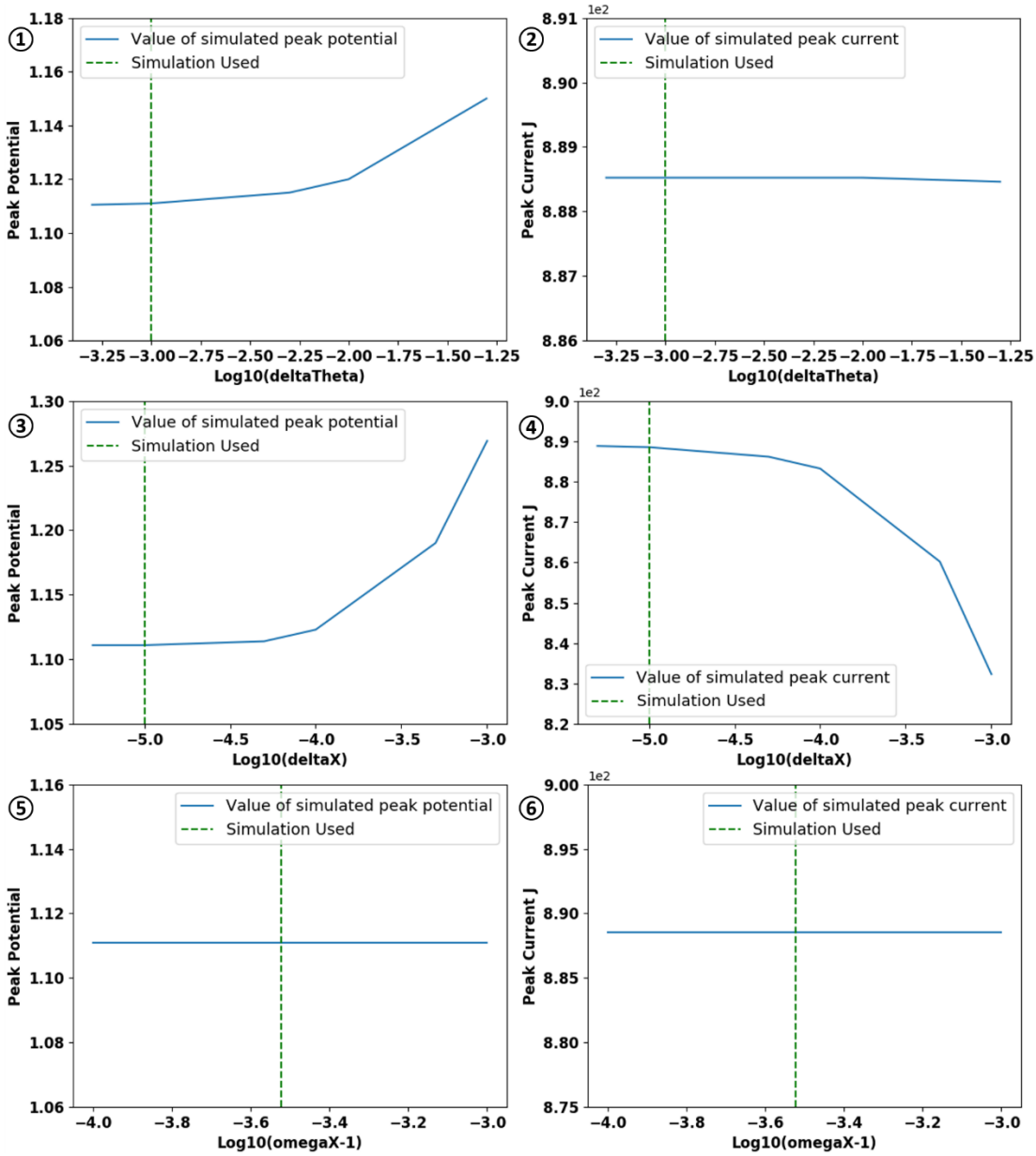


Figure 6.10: Peak potentials (left) and peak currents (right) of current responses for test simulations for the 'infinitely long cylinder' electrode model for $\sigma = 10^5$ varying: $d\theta$: ①②; dX: ③④; ωX: ⑤⑥.

6.3.1.2 Testing the 'annular band' electrode model

We further performed the convergence studies and tests of mass conservation for the 'annular band' electrode model at corresponding L ranges for different scan rates ($\sigma = 10^{-5}, 10^0, 10^5$), two of which are shown in this section ($\sigma = 10^{-5}, 10^5$).

For the two extreme scan rates chosen in this section, the corresponding L range are shown in Table 6.3. The errors of mass conservation for different test simulations

varying one of the simulation parameters stated above are shown in Figure 6.12. The errors of mass conservation of simulation with the previous stated parameter sets are kept at a lower level (below 1%). When further decreasing the simulation parameters, the errors do not vary much.

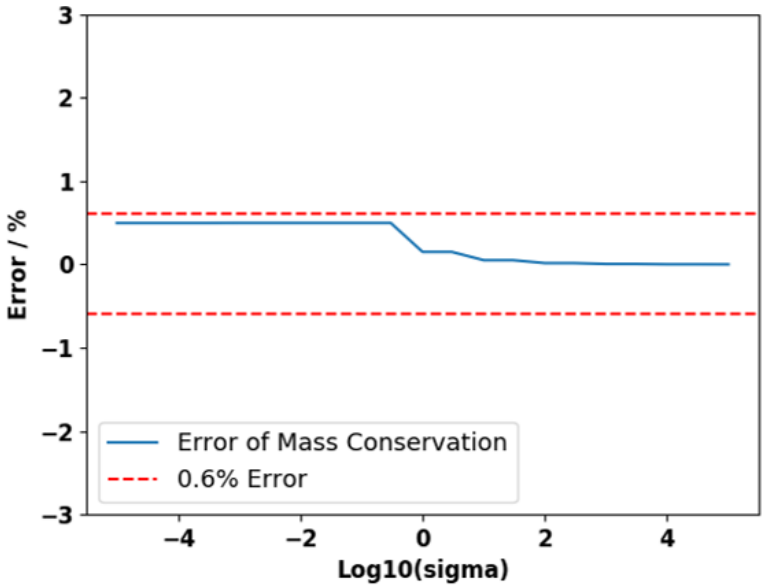


Figure 6.11: Errors of mass conservation calculated for different scan rate σ from 10^{-5} to 10^{5} for the 'infinitely long cylinder' electrode model.

As shown in Figure 6.13 to 6.16, as the chosen parameters decreases to an extent, the forward peak potential and forward peak current of the voltammogram remain at similar levels. Based on the test of errors of mass conservation and the convergence studies of the current responses, the sets of parameters chosen in this section is considered as 'converged' before the simulation results are analysed and interpreted.

After the convergence studies and the test of mass conservation, the parameters of individual scan rates are selected. As shown in Figure 6.17, the errors of mass conservation calculated for the simulations of corresponding L using selected parameter sets at different scan rate $\sigma = 10^{-5}$, 10^{0}, 10^{5} remain under 1% for the 'annular band' electrode models.

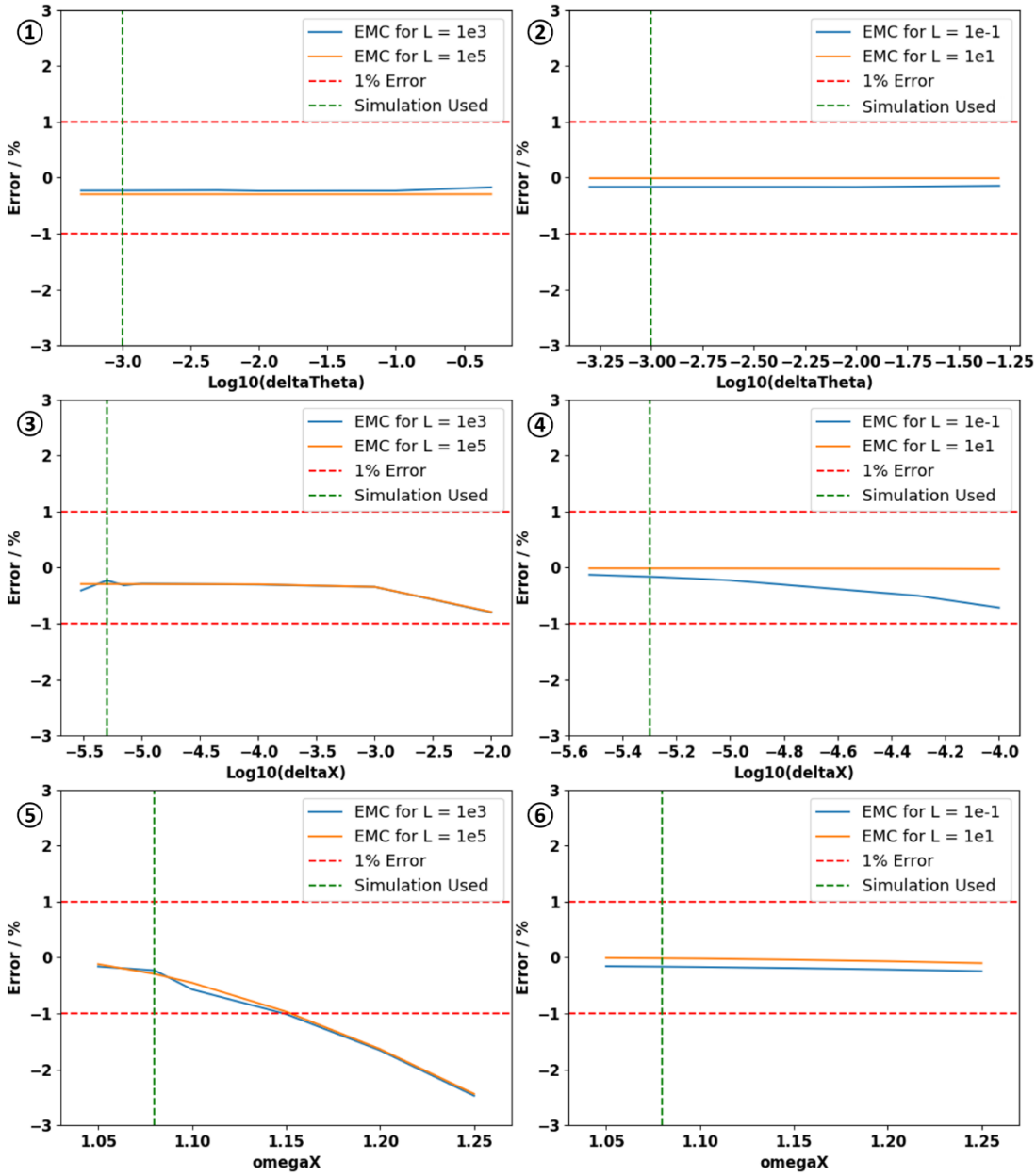


Figure 6.12: Errors of mass conservation calculated for $\sigma = 10^{-5}$ (left) and $\sigma = 10^{5}$ (right) for the 'annular band' electrode model for simulations varying: $d\theta$: ①②; dX: ③④; ωX: ⑤⑥.

6.3.1.3 Testing the 'full cylinder' electrode model

Last, we performed the convergence studies and tests of mass conservation for the 'full cylinder' electrode model at corresponding L ranges for different scan rates ($\sigma = 10^{-5}, 10^{0}, 10^{5}$), two of which are shown in this section ($\sigma = 10^{-5}, 10^{5}$).

For the two extreme scan rates chosen in this section, the corresponding L range are shown in Table 6.3. The errors of mass conservation for different test simulations varying one of the simulation parameters stated above are shown in Figure 6.18. The

errors of mass conservation of simulation with the previous stated parameter sets are kept at a lower level (below 1%). When further decreasing the simulation parameters, the errors do not vary much.

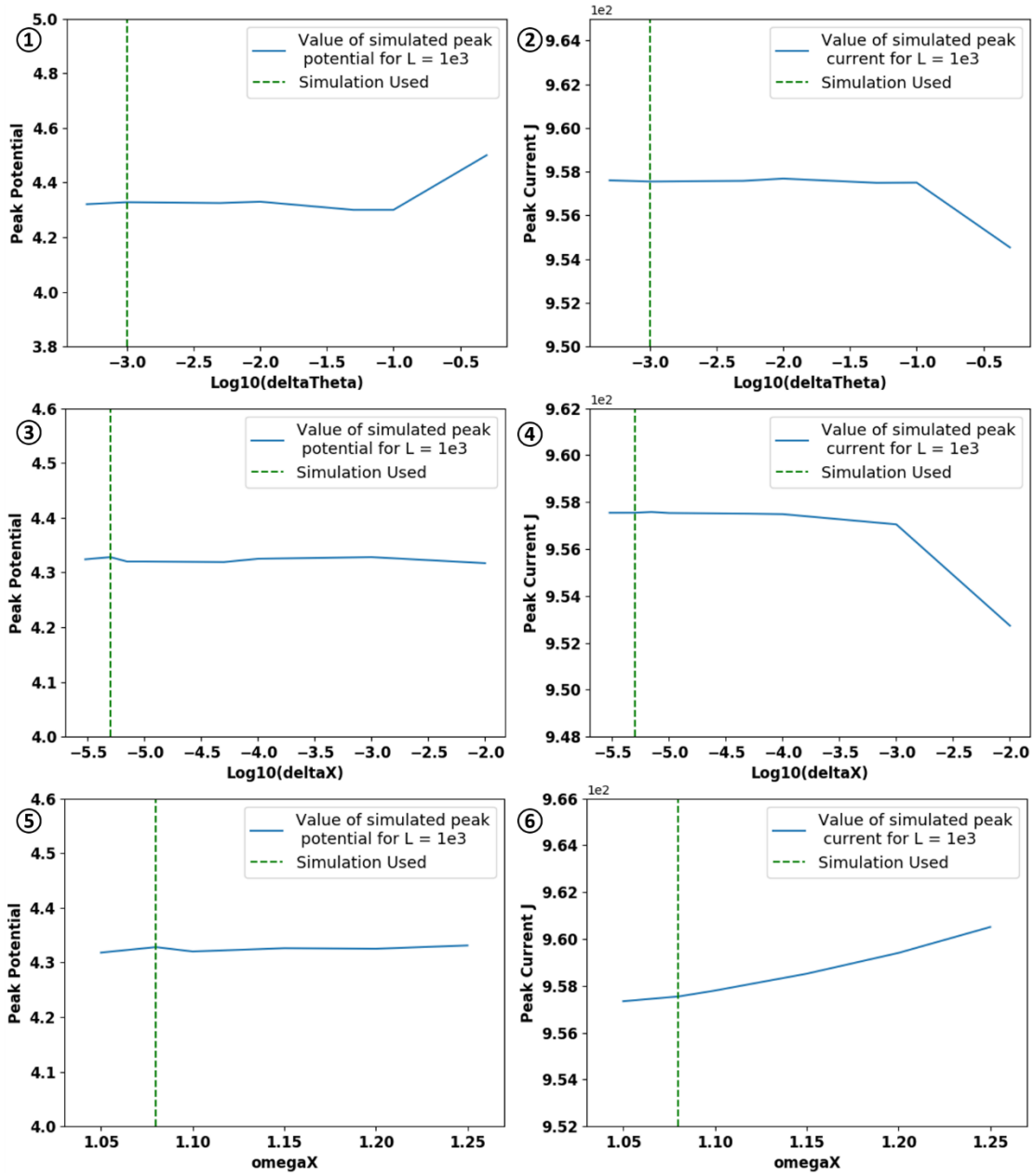


Figure 6.13: Peak potentials (left) and peak currents (right) of current responses for test simulations for the 'annular band' electrode model for $L = 10^3$ and $\sigma = 10^{-5}$ varying: $d\theta$: ①②; dX: ③④; ωX: ⑤⑥.

As shown in Figure 6.19 to 6.22, as the chosen parameters decreases to an extent, the forward peak potential and the forward peak current of the voltammogram remain at similar levels. Based on the test of errors of mass conservation and the convergence

studies of the current responses, the sets of parameters chosen in this section is considered as 'converged' before the simulation results are analysed and interpreted.

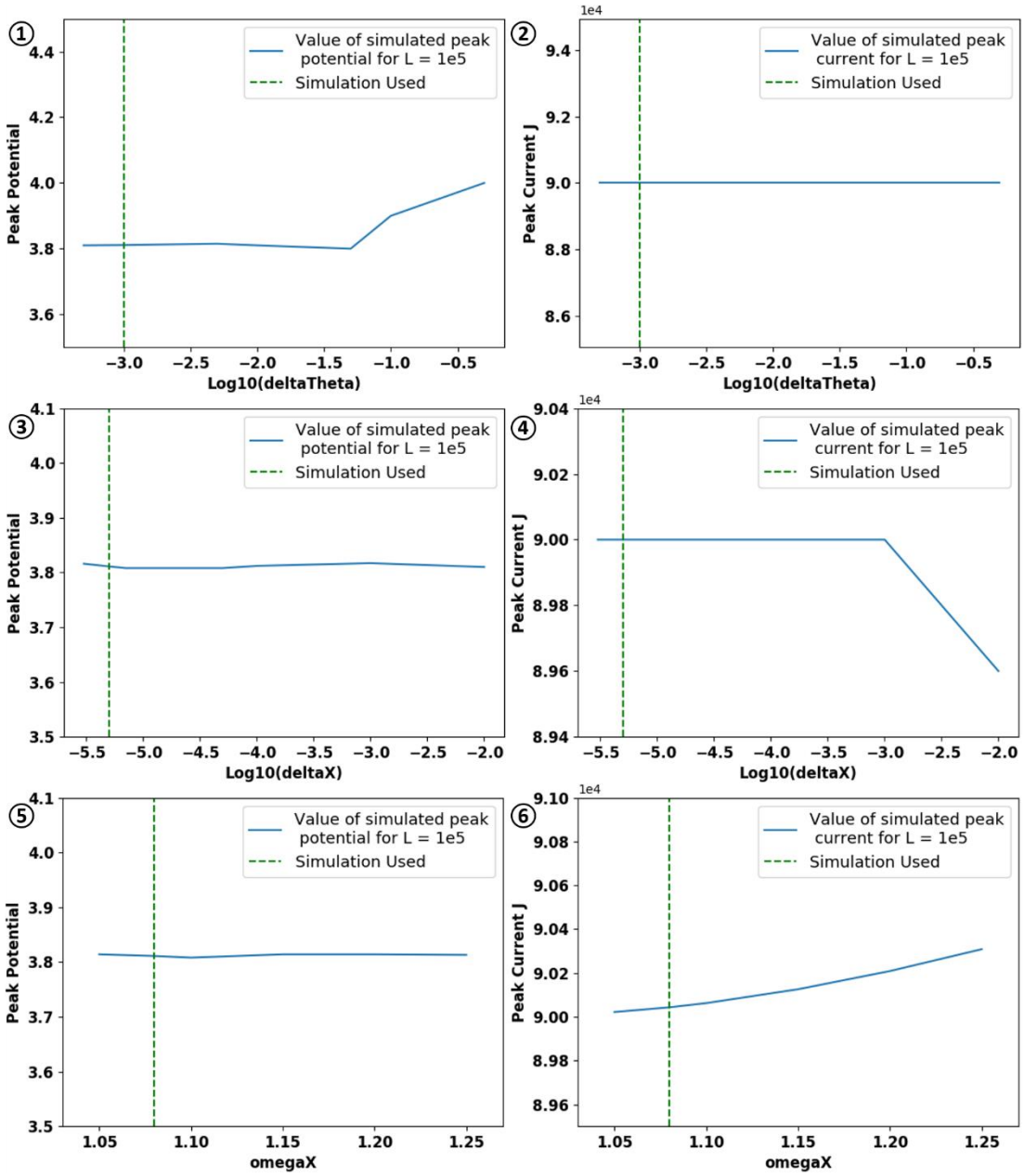


Figure 6.14: Peak potentials (left) and peak currents (right) of current responses for test simulations for the 'annular band' electrode model for $L = 10^5$ and $\sigma = 10^{-5}$ varying: $d\theta$: ①②; dX: ③④; ωX: ⑤⑥.

After the convergence studies and the test of mass conservation, the parameters of each scan rates are selected. In Figure 6.23, the errors of mass conservation calculated for the simulations of corresponding L using selected parameter sets at different scan rate $\sigma = 10^{-5}$, 10^0, 10^5 remain under 1% for the 'full cylinder' electrode models.

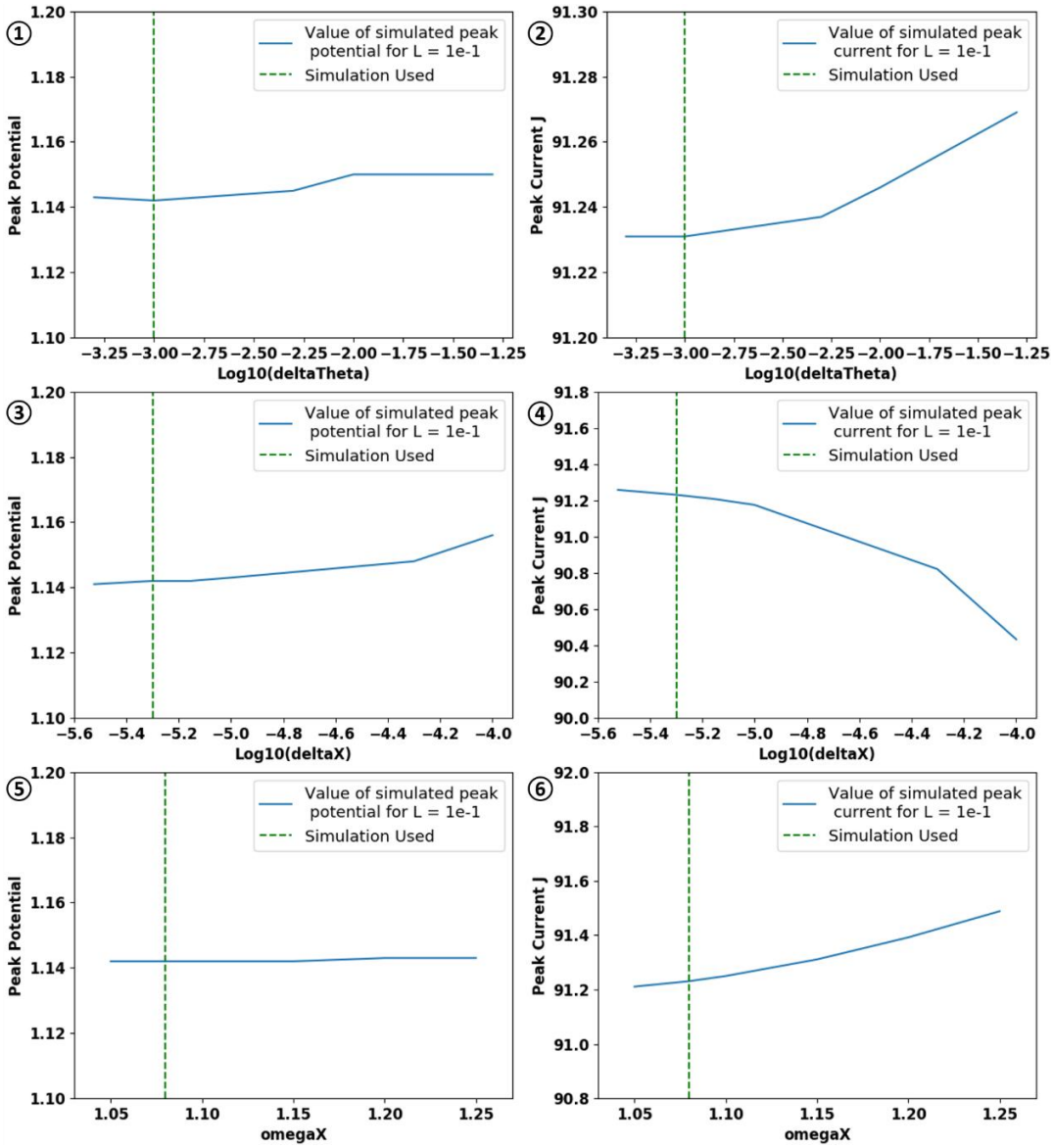


Figure 6.15: Peak potentials (left) and peak currents (right) of current responses for test simulations for the 'annular band' electrode model for $L = 10^{-1}$ and $\sigma = 10^5$ varying: $d\theta$: ①②; dX: ③④; ωX: ⑤⑥.

6.3.2 The 'infinitely long cylinder' electrode model

Simulations were computed for different scan rates ($10^{-5} \leq \sigma \leq 10^5$ with interval $\log_{10}\Delta\sigma = 1$) for the 'infinitely long cylinder' model. At high scan rates, ΔE_{pp} and I_p in the cyclic voltammetric currents for an infinitely long cylinder can be described by [47]:

$$\begin{cases} \Delta E_{pp} = 2.218\dfrac{\boldsymbol{RT}}{F} \\ I_p = -0.446FAc_A^*\sqrt{\dfrac{FD\nu}{\boldsymbol{RT}}} \end{cases} \tag{6.23}$$

where A is the size of the electrochemically active area of the electrode. At low scan rates, two empirical equations [38] have been reported by Aoki et al to describe the forward peak potentials E_{fpp} and forward peak currents I_p:

$$\begin{cases} log_{10}(p) = \dfrac{-E_{fpp}^4 - 40}{100} + \dfrac{2.75}{E_{fpp}^4 - 1.41} \\ I_p = \dfrac{Fc_A^* D(0.446p + 0.335p^{0.15})}{r} \\ p = \sqrt{\dfrac{Fr^2\nu}{\boldsymbol{RT}D}} \end{cases} \tag{6.24}$$

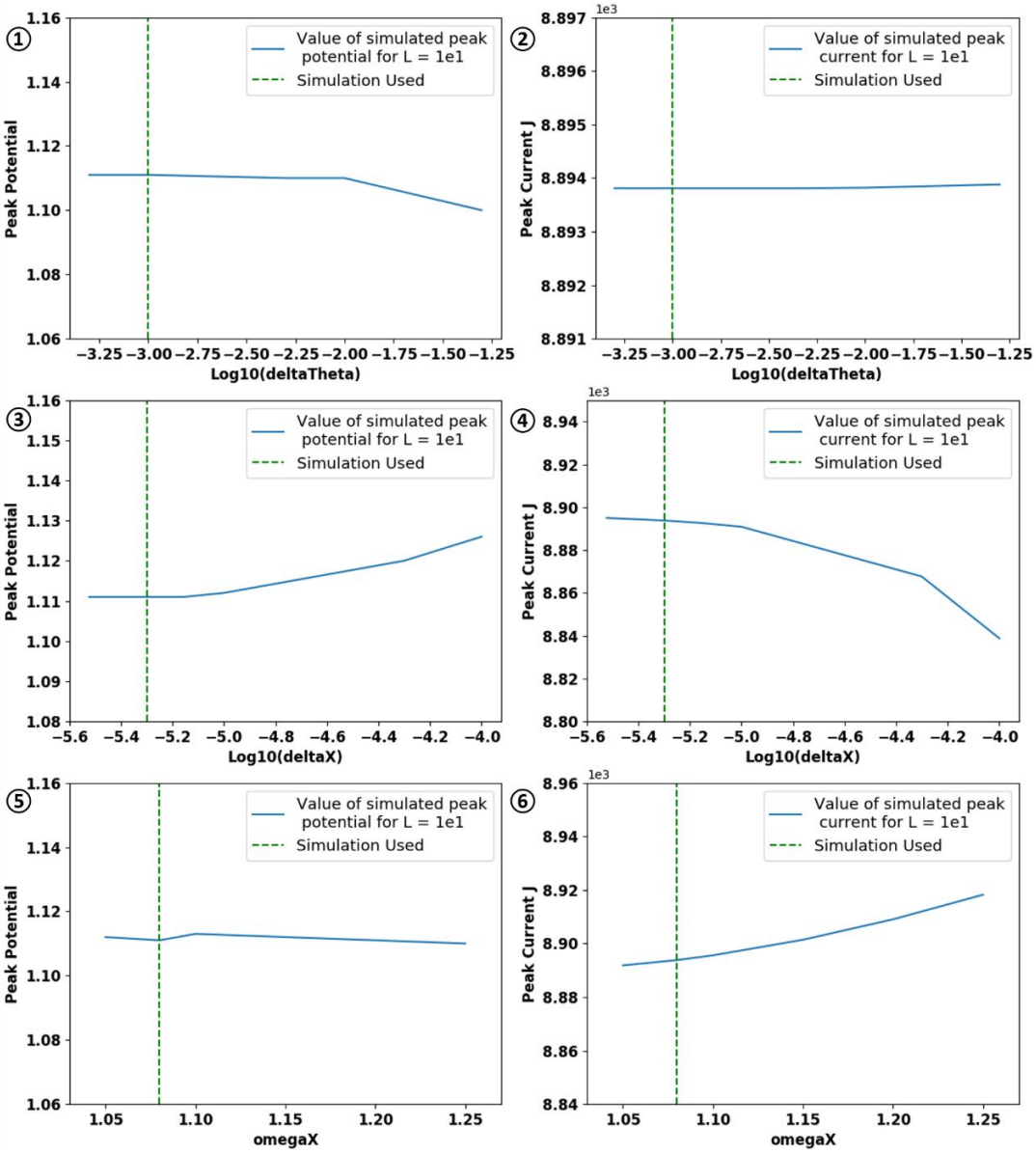


Figure 6.16: Peak potentials (left) and peak currents (right) of current responses for test simulations for the 'annular band' electrode model for $L = 10^1$ and $\sigma = 10^5$ varying: $d\theta$: ①②; dX: ③④; ωX: ⑤⑥.

where the percentage errors of the empirical equation for E_{fpp} are reported to be less than 0.17 as a dimensionless value, which is 4mV at 298K, for $\log_{10}(p) < -2$. The errors of the empirical equation for I_p are reported [38] to be less than 2% for any p.

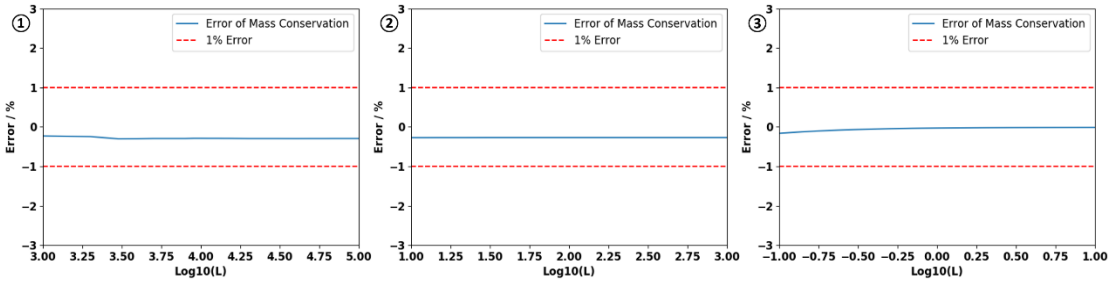


Figure 6.17: Errors of mass conservation calculated for the simulations of corresponding L at different scan rate $\sigma = 10^{-5}$ (①), 10^{0} (②), 10^{5} (③) for the 'annular band' electrode model.

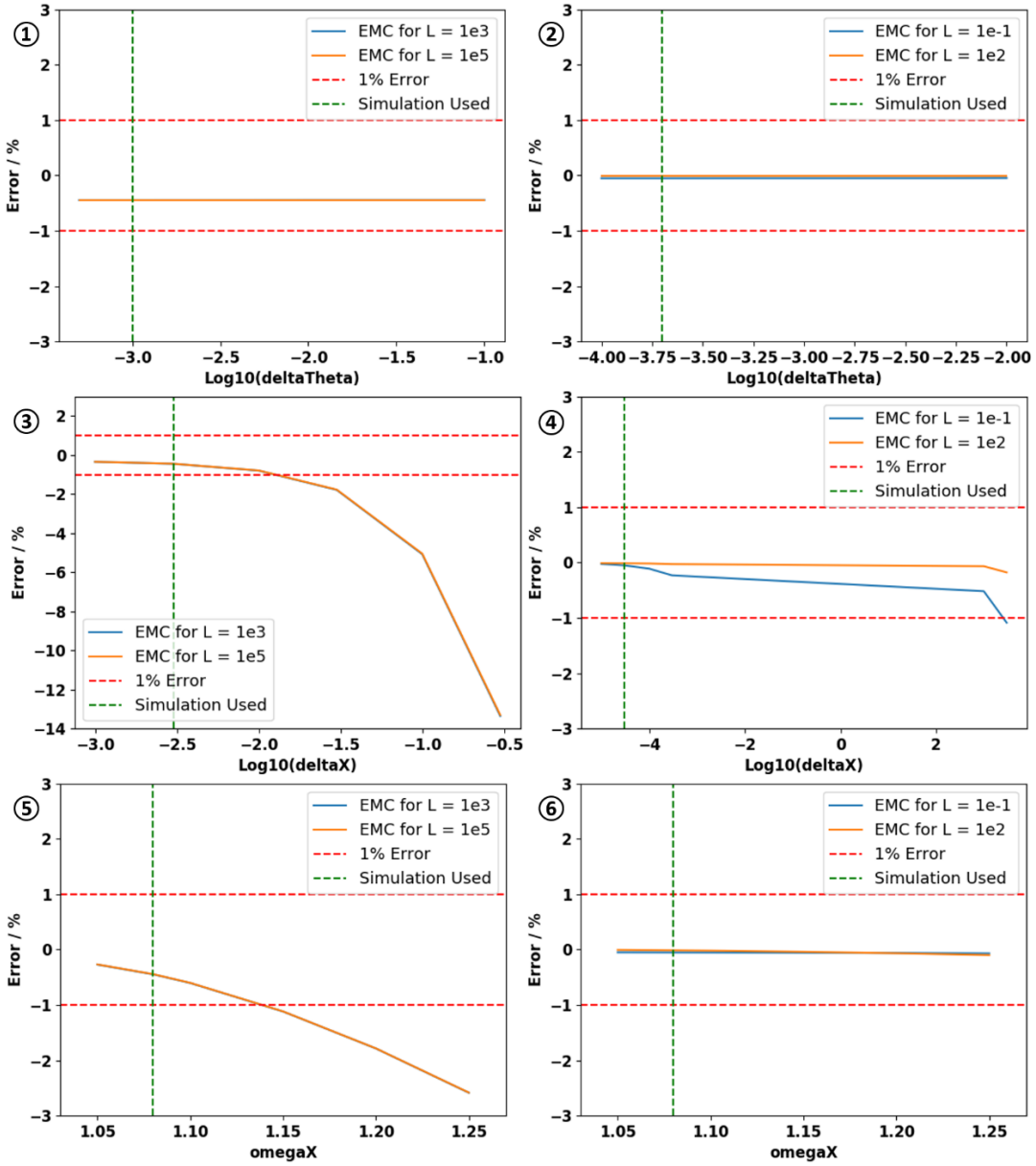


Figure 6.18: Errors of mass conservation calculated for $\sigma = 10^{-5}$ (left) and $\sigma = 10^{5}$ (right) for the 'full cylinder' electrode model for simulations varying: $d\theta$: ①②; dX: ③④; ωX: ⑤⑥.

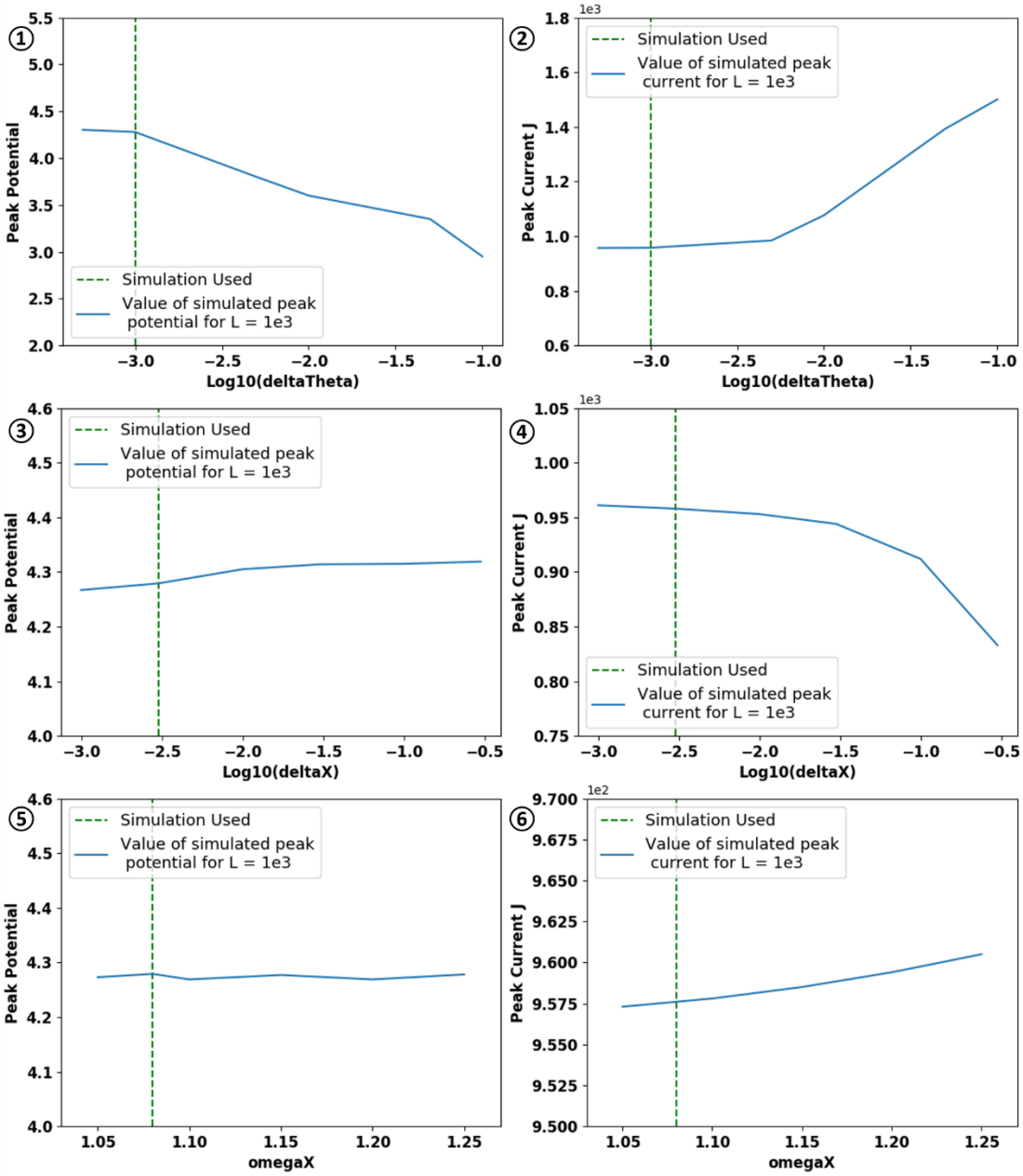


Figure 6.19: Peak potentials (left) and peak currents (right) of current responses for test simulations for the 'full cylinder' electrode model for $L = 10^3$ and $\sigma = 10^{-5}$ varying: $d\theta$: ①②; dX: ③④; ωX: ⑤⑥.

As shown in ① and ② in Figure 6.24, the simulated dimensionless forward peak position θ_{fpp} and dimensionless forward peak current J_p are plotted compared with the empirical equations introduced previously. In ① in Figure 6.24, the Aoki equation for θ_{fpp} [38] can describe the simulated θ_{fpp} for $\log_{10}(p) < -2$. However, for large scan rates, there is an increased difference between the Aoki equation for θ_{fpp} and the simulated θ_{fpp} as the scan rate increases. To describe the θ_{fpp} over a wider range of scan rates, we

performed the fitting using polynomial equations to the simulated θ_{fpp}. The best fitting equations are shown with 5th, 6th and 7th order polynomial fittings in Eqn (6.25):

$$\begin{cases} 5th\ order: & \theta_{fpp} = -0.007374x^5 - 0.01784x^4 + 0.1022x^3 + 0.2187x^2 \\ & \quad - 0.8928x\ +\ 1.767 \\ 6th\ order: & \theta_{fpp} = 0.003786x^6 - 0.007406x^5 - 0.05259x^4 + 0.1024x^3 \\ & \quad +0.2964x^2 - 0.8931x + 1.742 \\ 7th\ order: & \theta_{fpp} = 0.001118x^7 + 0.003777x^6 - 0.01944x^5 - 0.05252x^4 \\ & \quad +0.1387x^3 + 0.2963x^2 - 0.9198x + 1.742 \\ x = log_{10}(p) \end{cases} \quad (6.25)$$

where the errors of the best fitting polynomial equation for 5th-, 6th- and 7th orders are 3.5%, 1.6%, and 1.2%, respectively, comparing the corresponding simulated θ_{fpp}.

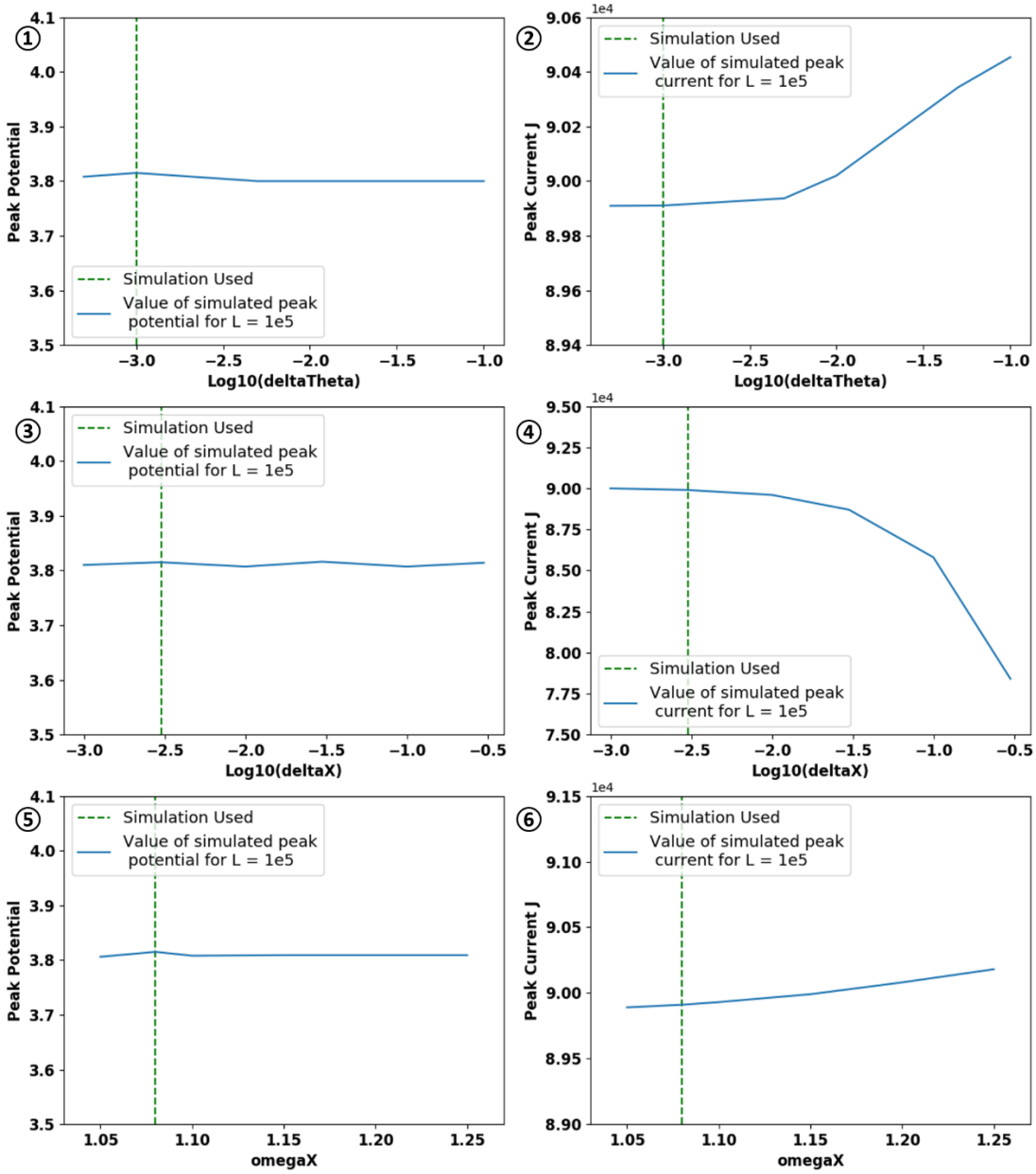


Figure 6.20: Peak potentials (left) and peak currents (right) of current responses for test

simulations for the 'full cylinder' electrode model for $L = 10^5$ and $\sigma = 10^{-5}$ varying: $d\theta$: ①②; dX: ③④; ωX: ⑤⑥.

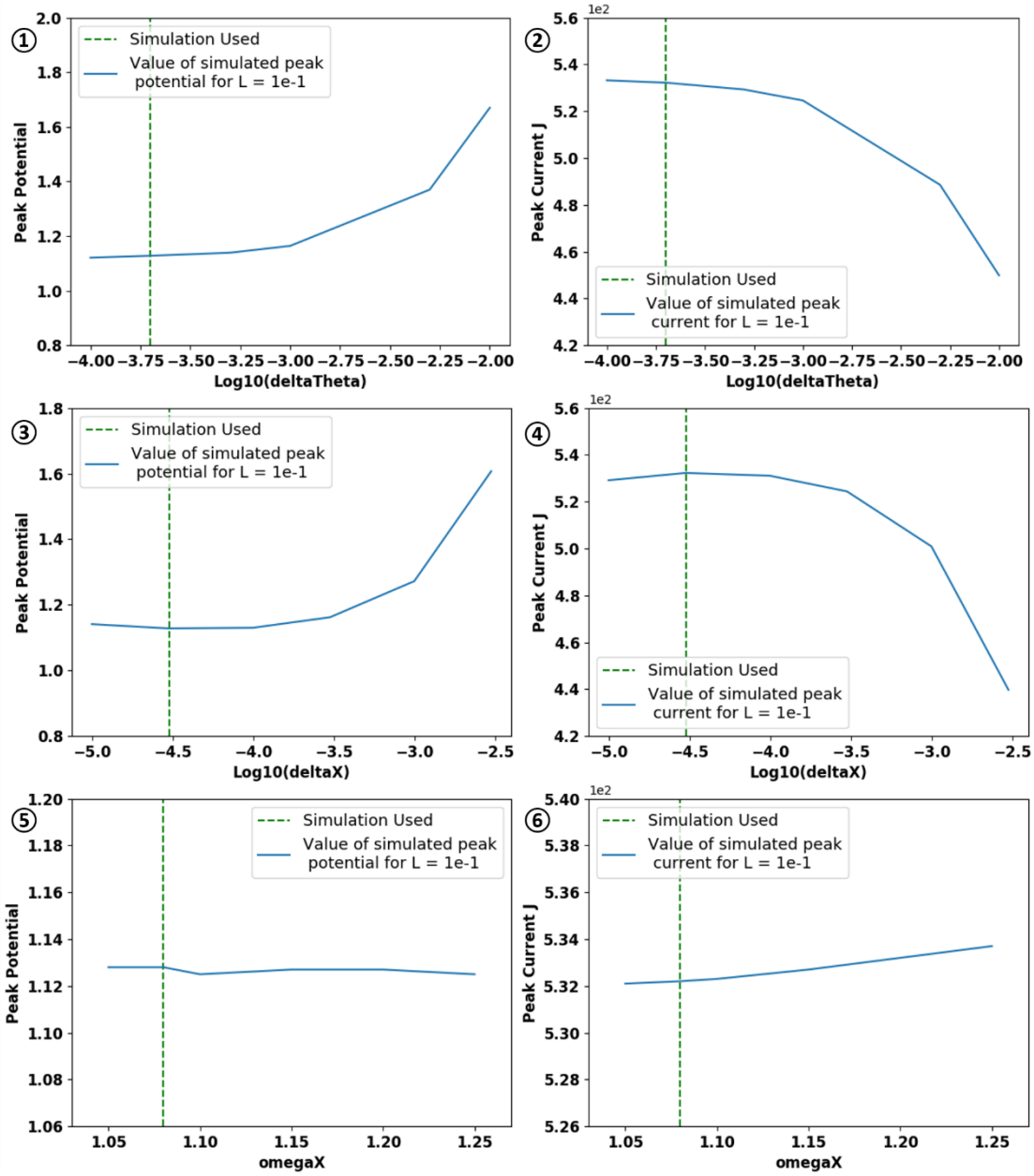


Figure 6.21: Peak potentials (left) and peak currents (right) of current responses for test simulations for the 'full cylinder' electrode model for $L = 10^{-1}$ and $\sigma = 10^5$ varying: $d\theta$: ①②; dX: ③④; ωX: ⑤⑥.

In terms of comparing the dimensionless forward peaks of the simulated current responses to the empirical equation, as shown in ② in Figure 6.24, the Aoki equation for J_p showed adequate capability in describing simulated J_p. Furthermore, at high scan rates, simulated J_p and the Aoki equation for J_p approach the Randles-Ševčík equation.

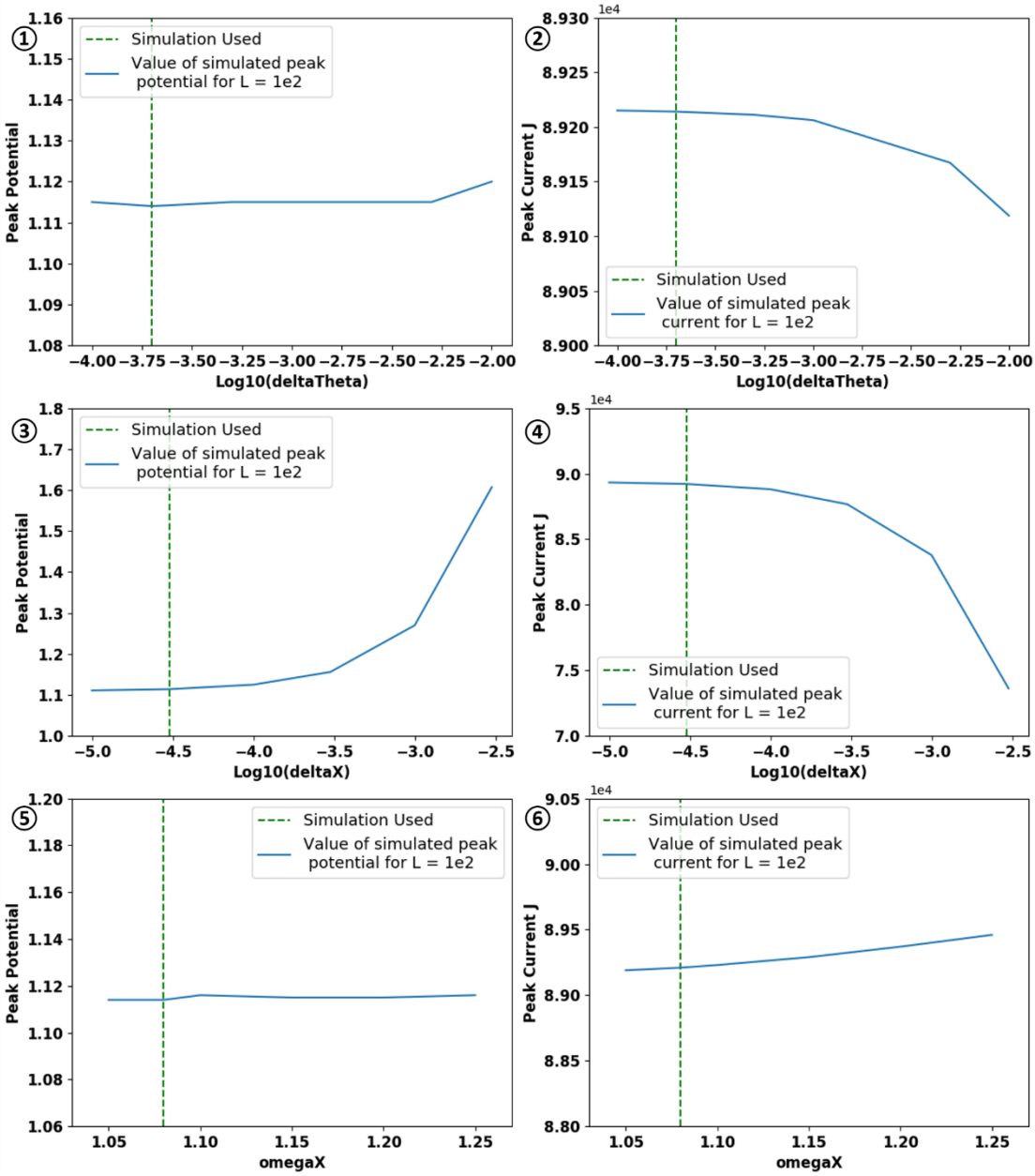


Figure 6.22: Peak potentials (left) and peak currents (right) of current responses for test simulations for the 'full cylinder' electrode model for $L = 10^2$ and $\sigma = 10^5$ varying: $d\theta$: ①②; dX: ③④; ωX: ⑤⑥.

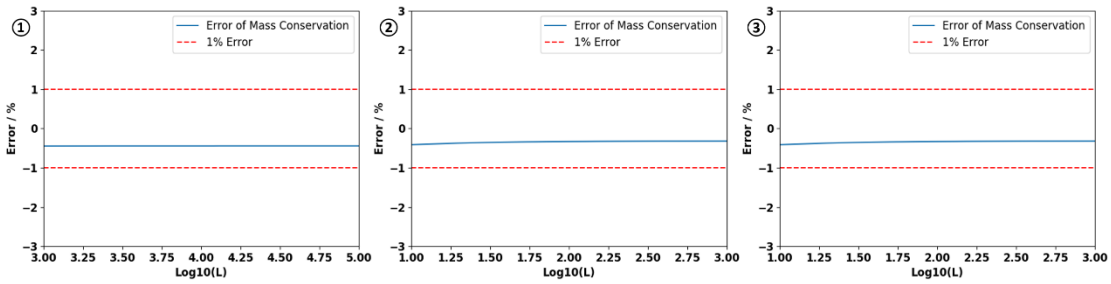


Figure 6.23: Errors of mass conservation calculated for the simulations of corresponding L at different scan rate $\sigma = 10^{-5}$ (①), 10^0 (②), 10^5 (③) for the 'full cylinder' electrode model.

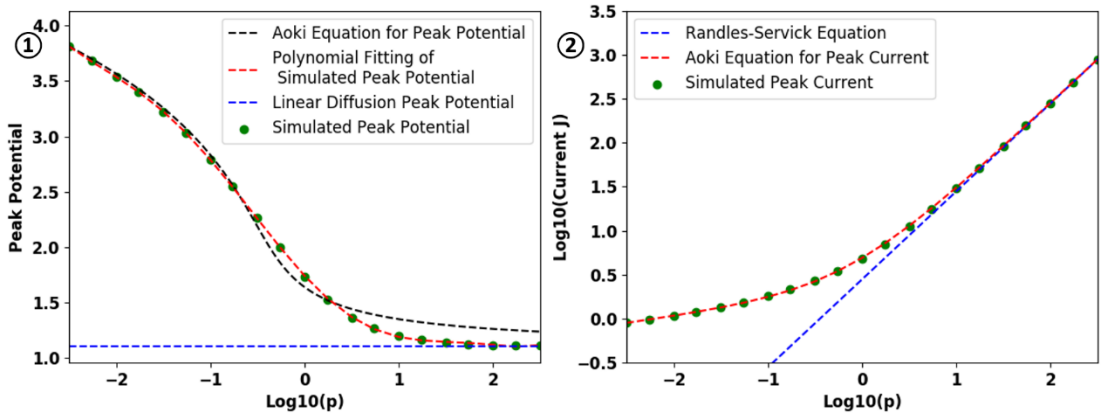


Figure 6.24: Comparison of the simulated forward peak potentials (①) and forward peak currents (②) and the corresponding empirical equations. ① The simulated forward peak potentials (green dots) are compared with the Aoki equation for the forward peak potentials (black), the polynomial fitting of the simulated forward peak potentials (red), and the theoretical forward peak potential for linear diffusion (blue). ② The simulated forward peak currents (green) are compared with the Randles-Ševčík equation (blue) and the Aoki equation for the forward peak current(red).

6.3.3 Determining minimum values of *L*

In simulations of the 'annular band' electrode model and 'full cylinder' electrode model, as *L* increases, the simulated current responses will converge to the simulated current response of the 'infinitely long cylinder' electrode model at the same scan rate.

In order to determine the minimum value of *L* where the differences between the forward peak potentials and forward peak currents of the simulated currents for the 'annular band' electrode model and 'full cylinder' electrode model and those for the 'infinitely long cylinder' electrode model are less than 1%, two series of simulations varying the lengths *L* of the cylinders for these two models were performed.

As shown in Figure 6.25 and 6.26, the differences between the forward peak potentials and forward peak currents for corresponding compared models and those for the 'infinitely long cylinder' model decreases as *L* increases. Minimum values of *L* where the differences of simulated currents between corresponding models are less than 1% can be therefore extracted from the plots and shown in the following sections.

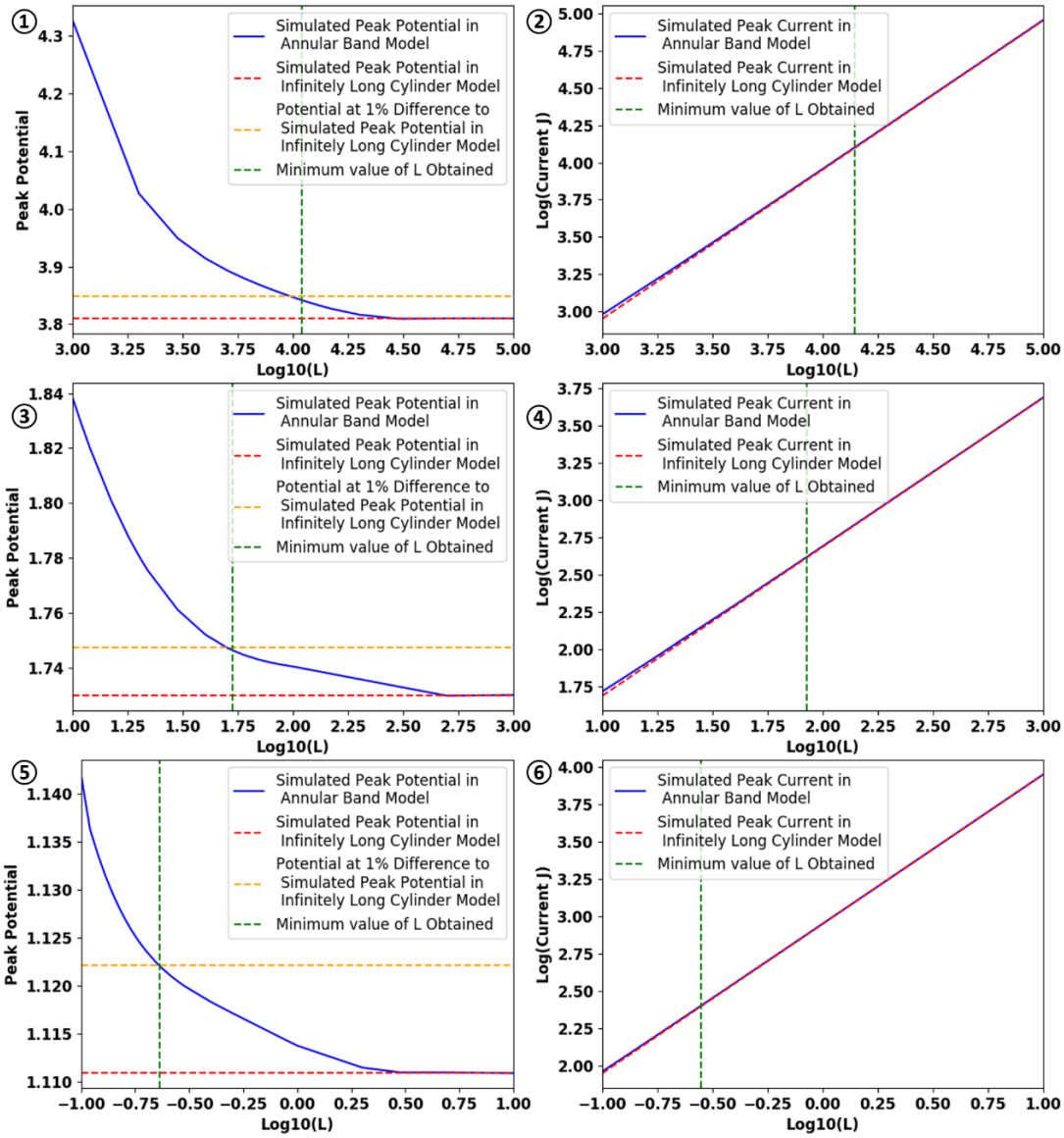


Figure 6.25: Simulated dimensionless forward peak potential (left) and forward peak position (right) varying L at different scan rate $\sigma = 10^5$ (①②) , 10^0 (③④) , 10^5 (⑤⑥) for the 'annular band' electrode model comparing to the corresponding simulated results for the 'infinitely long cylinder' electrode model. The green dashed lines show the minimum values of L chosen for the differences between simulated current responses of two models less than 1%.

6.3.4 The 'annular band' electrode model

Various simulations for different lengths L of the electrochemically active area were computed at three different scan rates: $\sigma = 10^{-5}$, 10^0, 10^5.

As shown in Figure 6.27, the minimum value of lengths L, where the differences between the simulated results for forward peak potentials and forward peak currents for this model and those for the infinitely long cylinder model are less than 1%, are plotted

at different scan rates. Figure 6.27 shows that when the scan rates σ increases, the minimum value of L for the cyclic voltammograms from this model to resemble those for the infinitely long cylinder model at $\log_{10}$ scale decreases almost linearly with the $\log_{10}\sigma$. We infer that this is because the increased σ results in reduce of diffusion layer which gives the additional diffusion field near the insulating areas a smaller impact.

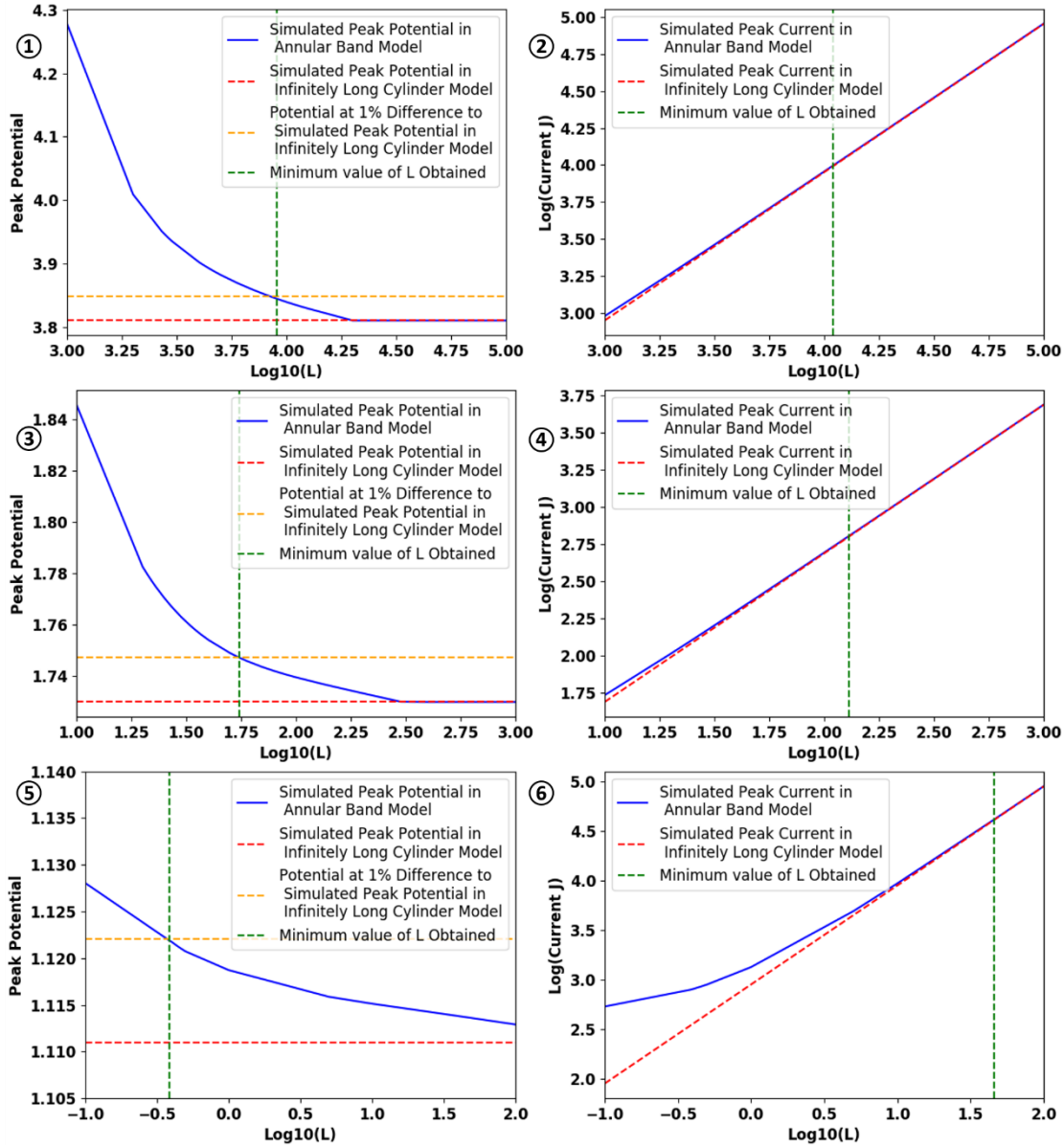


Figure 6.26: Simulated dimensionless forward peak potential (left) and forward peak position (right) varying L at different scan rate $\sigma = 10^5$ (①②), 10^0 (③④), 10^5 (⑤⑥) for the 'full cylinder' electrode model comparing to the corresponding simulated results for the 'infinitely long cylinder' electrode model. The green dashed lines show the minimum values of L chosen for the differences between simulated current responses of two models less than 1%.

Therefore, the minimum value of L is smaller when the σ increases. It is noticeable that the minimum value of L for the peak currents are higher than those for forward peak potentials, which suggested the forward peak current is a more sensitive indicator comparing to the forward peak potential in the 'annular band' electrode model.

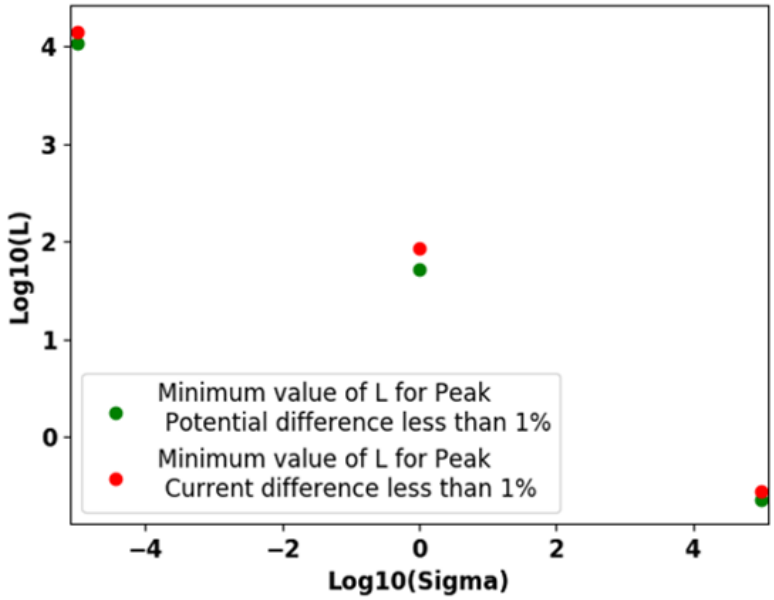


Figure 6.27: The minimum value of lengths L where the differences between the simulated results for peak potentials and forward peak currents for the 'annular band' model and those for the infinitely long cylinder model are less than 1%.

A set of typical experimental parameters, shown in Table 6.4, is used to convert the dimensionless current responses into their dimensional counterparts to present an experimental perspective.

Table 6.4: A dimensional parameter set based on the commonly used conditions in microelectrode experiments [14, 15]

Dimensional Parameters	Value
Electrode radius, r_e	3.5 μm
Analyte initial concentration, c^*	10^{-9} m^2/s
Diffusion coefficient, D	1 mM

The minimum value of L for the corresponding differences less than 1% are also provided in Table 6.5. Overall, if the value of L is greater than $L = 1.4 \times 10^4$ (l = 49mm when the radius is 3.5μm), where l is the dimensional length of the cylinders, for the

'annular band' electrode model, the percentage differences between forward peak potential and forward peak current for the 'annular band' electrode model and those for the 'infinitely long cylinder' electrode model are less than 1% for dimensional scan rate in the range from 2.1×10^{-5}v/s to 2.1×10^{5}v/s for the parameters shown in Table 6.4.

Table 6.5: The minimum value of lengths L and their dimensional counterparts where the differences between the simulated results for peak potentials and forward peak currents for the 'annular band' model and those for the infinitely long cylinder model are less than 1%.

σ	v (V/s)	L for E_{fpp}	l for E_{fpp} (mm)	L for I_p	l for I_p (mm)
10^{-5}	2.1×10^{-5}	1.1×10^{4}	3.9×10^{1}	1.4×10^{4}	4.9×10^{1}
10^{0}	2.1	5.3×10^{1}	1.9×10^{-1}	8.5×10^{1}	3.0×10^{-1}
10^{5}	2.1×10^{5}	2.3×10^{-1}	8.1×10^{-4}	2.8×10^{-1}	9.8×10^{-4}

6.3.5 The 'full cylinder' electrode model

Similarly, corresponding simulations were computed for various lengths L of the electrochemically active area at three different scan rates: $\sigma = 10^{-5}, 10^{0}, 10^{5}$ for the 'full cylinder' electrode model.

As shown in Figure 6.28, the minimum value of lengths L, where the differences between the simulated results for peak potentials and forward peak currents for this model and those for the infinitely long cylinder model are less than 1%, are plotted at different scan rates. Figure 6.28 shows that when the scan rates σ increases, the minimum value of L for the cyclic voltammograms of this model resembling those for the 'infinitely long cylinder' electrode model decreases. However, at high σ, the minimum value of L for the peak currents is much higher than that in the 'annular band' electrode model. We assign this difference to the contribution from the top of the cylinder electrode: at high σ, the peak current is much higher than the peak current in the infinitely long cylinder model because the electrochemical reaction at the top of the cylinder contribute to a large amount of the total current responses, which results in

larger minimum value of L.

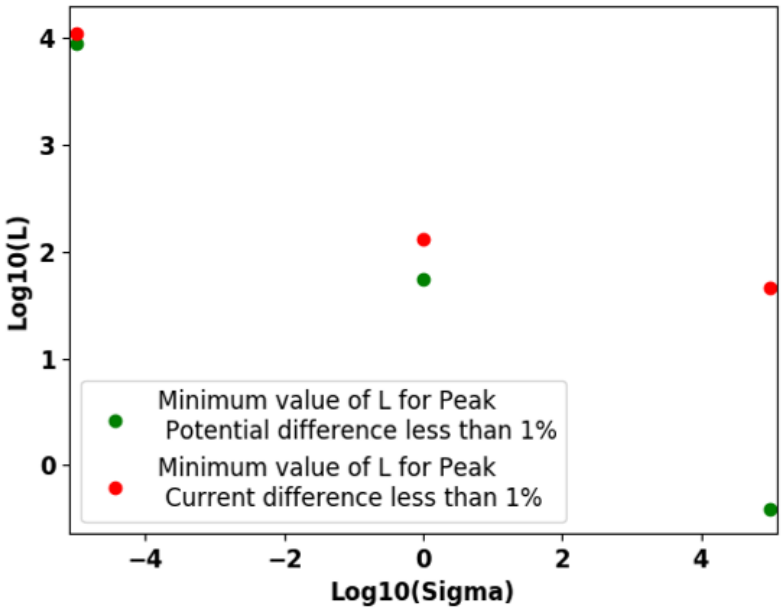


Figure 6.28: The minimum value of lengths L where the differences between the simulated results for peak potentials and forward peak currents for the 'full cylinder' model and those for the infinitely long cylinder model are less than 1%.

The minimum value of L for the corresponding differences less than 1% are also provided in Table 6.6. Overall, if the value of L is greater than $L = 1.1 \times 10^4$ (l = 39mm when the radius is 3.5μm) for the 'full cylinder' electrode model, the percentage differences between forward peak potential and forward peak current for the 'full cylinder' model and those for the infinitely long cylinder model are less than 1% for dimensional scan rate in the range from 2.1×10^{-5}v/s to 2.1×10^{5}v/s for the parameters shown in Table 6.4.

Table 6.6: The minimum value of lengths L and their dimensional counterparts where the differences between the simulated results for peak potentials and forward peak currents for the 'full cylinder' model and those for the infinitely long cylinder model are less than 1%.

σ	v (V/s)	L for E_{fpp}	l for E_{fpp} (mm)	L for I_p	l for I_p (mm)
10^{-5}	2.1×10^{-5}	9.0×10^{3}	3.2×10^{1}	1.1×10^{4}	3.9×10^{1}
10^{0}	2.1	5.5×10^{1}	1.9×10^{-1}	1.3×10^{2}	4.6×10^{-1}
10^{5}	2.1×10^{5}	3.9×10^{-1}	1.4×10^{-3}	4.6	1.6×10^{-1}

6.4 Conclusions

This chapter produced and presented a polynomial empirical equation to describe the cyclic voltammetric currents at infinitely long cylindrical electrodes for reversible electrochemical reactions. By comparing the simulated peak potentials and peak currents for two cylinder-like electrode models with the simulated results for the infinitely long cylinder model, we find that if the length of the cylinder is at least 1.4×10^4 times and 1.1×10^4 times longer than the radius for the 'annular band' electrode model and the 'full cylinder' electrode model, respectively, the percentage differences between the simulated cyclic voltammograms for the infinitely long cylinder model and the simulated results for the 'annular band' electrode model and the 'full cylinder' electrode model are less than 1% for scan rates σ in the range from 2.1×10^{-5} V/s to 2.1×10^5 $V \cdot s^{-1}$, that is for instance, if the length of the cylinder is longer than 49mm and 39mm, respectively, when the radius is 3.5μm and the diffusion coefficient is $10^{-9} m^2 \cdot s^{-1}$.

References

[1] H. Le, E. Kätelhön, R. G. Compton, *Journal of Electroanalytical Chemistry* **2020**, *859*, 113865.

[2] K. Aoki, *Electroanalysis* **1993**, *5*, 627–639.

[3] J. Heinze, *Angewandte Chemie International Edition in English* **1993**, *32*, 1268–1288.

[4] R. J. Forster, *Chem. Soc. Rev.* **1994**, *23*, 289–297.

[5] R. J. C. Brown, D. J. L. Brett, *Microchimica Acta* **2009**, *164*, 337–344.

[6] D. Tallman, *Journal of Solid State Electrochemistry* **2011**, *15*, 1703–1710.

[7] K. J. Aoki, C. Zhang, J. Chen, T. Nishiumi, *Journal of Electroanalytical Chemistry* **2013**, *706*, 40–47.

[8] P. M. Kovach, W. L. Caudill, D. G. Peters, R. M. Wightman, *Journal of Electroanalytical Chemistry* **1985**, *185*, 285–295.

[9] K. Aoki, H. Kaneko, *Journal of Electroanalytical Chemistry* **1988**, *247*, 17–27.

[10] S. Singleton, J. O'Dea, J. Osteryoung, *Analytical Chemistry* **1989**, *61*, 1211–1215.

[11] R. Ferrigno, P. Brevet, H. Girault, *Electrochimica Acta* **1997**, *42*, 1895–1903.

[12] D. Britz, O. Østerby, J. Strutwolf, *Electrochimica Acta* **2010**, *55*, 5629–5635.

[13] S. J. Percival, B. Zhang, *The Journal of Physical Chemistry C* **2013**, *117*, 13928–13935.

[14] J. Ellison, C. Batchelor-McAuley, K. Tschulik, R. G. Compton, *Sensors and Actuators B: Chemical* **2014**, *200*, 47–52.

[15] C. Batchelor-McAuley, J. Ellison, K. Tschulik, P. L. Hurst, R. Boldt, R. G. Compton, *Analyst* **2015**, *140*, 5048–5054.

[16] A. Molina, J. González, E. Laborda, R. Compton, *Journal of Electroanalytical Chemistry* **2015**, *756*, 1–21.

[17] S. Eloul, E. Kätelhön, C. Batchelor-McAuley, K. Tschulik, R. G. Compton, *Journal of Electroanalytical Chemistry* **2015**, *755*, 136–142.

[18] K. Ngamchuea, C. Lin, C. Batchelor-McAuley, R. G. Compton, *Analytical Chemistry* **2017**, *89*, 3780–3786.

[19] L. Chen, C. Lin, R. G. Compton, *Physical Chemistry Chemical Physics* **2018**, *20*, 15795–15806.

[20] C. Zhang, N. Driver, Q. Tian, W. Jiang, H. Liu, *Journal of Biomedical Materials Research - Part A* **2018**, *106*, 1887–1895.

[21] D. Li, C. Batchelor-McAuley, L. Chen, R. G. Compton, *Physical Chemistry Chemical Physics* **2019**, *21*, 9969–9974.

[22] S. Eloul, R. G. Compton, *ChemElectroChem* **2014**, *1*, 917–924.

[23] J. Ellison, S. Eloul, C. Batchelor-McAuley, K. Tschulik, C. Salter, R. G. Compton, *Journal of Electroanalytical Chemistry* **2015**, *745*, 66–71.

[24] K. Cinková, M. Clark, S. V. Sokolov, C. Batchelor-McAuley, L. Švorc, R. G. Compton, *Electroanalysis* **2017**, *29*, 1006–1013.

[25] K. B. Oldham, C. G. Zoski, *Journal of Electroanalytical Chemistry and Interfacial Electrochemistry* **1988**, *256*, 11–19.

[26] C. Amatore, B. Fosset, *Analytical Chemistry* **1996**, *68*, 4377–4388.

[27] Z. Deng, R. Elattar, F. Maroun, C. Renault, *Analytical Chemistry* **2018**, *90*, 12923–12929.

[28] A. J. Bard, L. R. Faulkner, C. G. Zoski, J. Leddy, *Electrochemical methods: fundamentals and applications*, Second edition., New York ; Chichester, **2001**.

[29] G. Billon, C. M. G. van den Berg, *Electroanalysis* **2004**, *16*, 1583–1591.

[30] P. Salaün, C. M. G. van den Berg, *Analytical Chemistry* **2006**, *78*, 5052–5060.

[31] B. J. Privett, J. H. Shin, M. H. Schoenfisch, *Analytical Chemistry* **2010**, *82*, 4723–4741.

[32] K. E. Toghill, R. G. Compton, **2010**, *5*, 1246–1301.

[33] J. C. Harfield, C. Batchelor-McAuley, R. G. Compton, *Analyst* **2012**, *137*, 2285–2296.

[34] J. R. Windmiller, J. Wang, *Electroanalysis* **2013**, *25*, 29–46.

[35] M. Pumera, *ACS Nano* **2014**, *8*, 7555–7558.

[36] R. A. S. Couto, L. Chen, S. Kuss, R. G. Compton, *Analyst* **2018**, *143*, 4840–4843.

[37] X. Li, C. Batchelor-McAuley, R. G. Compton, *ACS Sensors* **2019**, *4*, 464–470.

[38] K. Aoki, K. Honda, K. Tokuda, H. Matsuda, *Journal of Electroanalytical Chemistry and Interfacial Electrochemistry* **1985**, *182*, 267–279.

[39] K. Aoki, K. Honda, K. Tokuda, H. Matsuda, *Journal of Electroanalytical Chemistry* **1985**, *186*, 79–86.

[40] A. Szabo, D. K. Cope, D. E. Tallman, P. M. Kovach, R. M. Wightman, *Journal of Electroanalytical Chemistry* **1987**, *217*, 417–423.

[41] H. Le, E. Kätelhön, R. G. Compton, *Journal of Electroanalytical Chemistry* **2019**, *855*, 113602.

[42] R. G. Compton, E. Laborda, K. R. Ward, *Understanding Voltammetry: Simulation of Electrode Processes*, Imperial College Press, **2013**.

[43] D. Peaceman, H. Rachford, Jr., *Journal of the Society for Industrial and Applied Mathematics* **1955**, *3*, 28–41.

[44] J. Heinze, *Journal of Electroanalytical Chemistry and Interfacial Electrochemistry* **1981**, *124*, 73–86.

[45] J. A. Alden, R. G. Compton, *The Journal of Physical Chemistry B* **1997**, *101*, 8941–8954.

[46] E. Kätelhön, R. G. Compton, *Analyst* **2015**, *140*, 2592–2598.

[47] R. G. Compton, C. E. Banks, *Understanding Voltammetry*, Third, World Scientific Press, **2018**.

Chapter 7: Electrochemical Processes Mediated via Adsorbed Enzymes: Flat and Porous Electrodes Compared. Understanding Nano-confinement.

This chapter presents theory for electrolysis at electrode surfaces modified by a layer of electroactive enzyme which can mediate the reduction of a substrate to a product. In particular, this chapter compares and contrasts immobilisation on flat surfaces with that on porous surfaces, identifies the conditions under which the adoption of porous electrodes facilitates markedly improved turnover rates and develops the analysis on the basis of the porous layer conferring a much-increased *effective* surface coverage. For both types of electrodes, the role of the electrode potential in controlling the thermodynamics of the binding of the substrate with the reduced layer of immobilised enzymes is quantified and the observation of apparent potential dependent Michaelis constants is explained. Four distinct classes of voltammetric responses are categorised allowing bottom-up process optimisation. The results reported in this chapter are based on a first-author paper submitted to *Journal of Electroanalytical Chemistry*.

7.1 Introduction

Immobilisation offers to improve the performance of enzyme-based catalytic systems notably in terms of stability, efficiency and selectivity [1,2] as a result of the enzyme species being attached to a solid supporting material, where the catalytic reaction takes place. The two most important improvements the immobilisation bring to the overall catalytic performance are, first, the nature of the catalytic processes of the

immobilised enzyme shifts from homogeneous to heterogeneous, leading to a better separation of the enzyme and the product, potentially increasing the reusability of the enzyme system and possibly leading to a higher purity of the product [3]. Second, the enzyme is attached to the supporting surface, which can make the catalytic system more durable allowing more repeated use and application for long periods [1]. Immobilising enzymes in nano-scale structures, so-called nano-confinement, has been realised in diverse structures including nanopores [4-7], nanochannels [8-11], etc, to take advantage of the large reaction area to volume ratios offered at the nanoscale.

Whilst immobilised enzymes have been rigorously investigated in fundamental electrochemical studies [7, 12-18] the application to electro-synthesis of using immobilised enzymes to mediate electron transfer may offer new possibilities in electrosynthesis combining the advantages of heterogeneous catalysis with the selectivity of enzyme chemistry and the intrinsically green nature of electrochemical reaction where oxidising and reducing agents are replaced by electricity. In key studies Ania et al. studied the electro-oxidation of glucose using enzymes immobilised in carbon nanopores made by sol-gel polymerisation of resorcinol-formaldehyde mixtures and claimed promoted heterogeneous electron transfer and stable electrocatalysis of glucose oxidation [6]. Armstrong et al. used catalytic systems where the enzymes are immobilised in nanopores formed by electrophoretic deposition of materials such as indium tin oxide (ITO) nanoparticles and reported the cycling of nicotinamide adenine dinucleotide phosphate (NADPH) and the enantioselective oxidation of alcohols [7,12,13]. They suggested that the high local concentration of NADP(H) enzymes helped increase the efficiency of cofactor recycling and realised selective oxidation of organic compounds. From a more fundamental perspective, Xia et al. insightfully studied glucose oxidation kinetics in nano-channels and asserted the possible

acceleration of rate and decrease of the Michaelis-Menten constant [8,9].

A generic feature of electrochemical approaches is the necessity of modelling the electrode processes in terms of diffusion, convection, adsorption, electron transfer, chemical reaction so as to permit realistic mechanistic analysis via voltammetry and the prediction of synthetic yields in terms of kinetic, thermodynamic and transport properties. This chapter seeks to develop a theory accounting for both apparently altered (and potential dependent) Michaelis-Menten constants and for nano-confinement effects. This builds on prior models developed by Lyons [19-21] and Bartlett [22-24] but is based on bespoke, newly derived kinetic expressions which recognise the surface immobilised nature of the redox enzyme and its reaction with a solution-phase substrate, *S*. The full kinetic scheme addressed is shown in Figure 7.1. Our approach emphasises the importance of the active electrode area to the volume of the solution, especially that under nano-confinement.

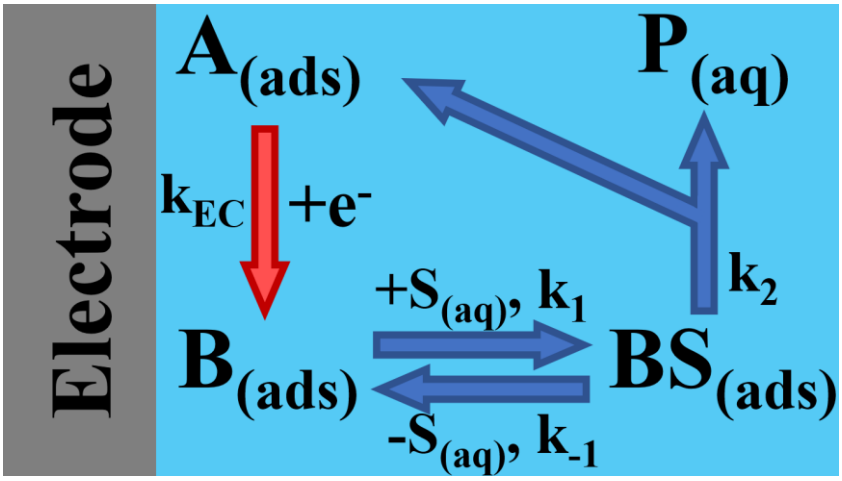


Figure 7.1: Illustrations of the electrode kinetics and enzyme mechanism studied in this work. The red arrow shows the electrochemical reaction for *A* to *B* on the electrode surface, while the blue arrows show the follow up chemical reactions.

The kinetics of enzymes in this chapter is described by a classical, time-invariant Michaelis-Menten-type mechanism [25, 26] but adapted to recognise the biphasic nature of the reaction between an adsorbed enzyme and a solution-phase substrate. A theoretical model is presented below before developing a further model of the catalytic

reaction in nanopores. Subsequently, in following sections, we then report, interpret, and discuss simulated voltammetry and its implications for practical electro-synthesis.

7.2 Theory

The simulation models are presented in this section with the dimensionless parameters and computational methods used. The current responses are calculated for cyclic voltammetry experiments.

It is worth noting that the mass transport in this model is assumed to be dominated by diffusion. As discussed in Chapter 1, in the 'Non-Porous Immobilised-Enzyme' model, in comparison between the simulated results and experimental data, migration and convection could have their influences on the experimental current responses at very short timescales or long timescales, respectively. In the 'Nanopore' model, as the depletion of the species within the particles are rapid, convection has a negligible impact on the experimental data in this system. However, extra attention should be paid in comparison between experimental results with simulated currents as migration could influence the experimental current responses at very short timescales.

7.2.1 The 'Non-Porous Immobilised-Enzyme' Model

The immobilised-enzyme-mediated electrochemical reaction is first modelled at a flat and non-porous planar electrode. The enzyme *A* and its reduced form *B* are assumed to be immobilised on the electrode throughout with a total enzyme coverage Γ_{max}. The bulk concentration of the substrate species *S* is set to be c_S^* and uniform before any potential is applied to the electrode. As shown in Figure 7.1 the reaction scheme is:

$$A_{(ads)} + e^- \rightleftharpoons B_{(ads)} \tag{7.1}$$

$$B_{(ads)} + S_{(aq)} \underset{k_{-1}}{\overset{k_1}{\rightleftarrows}} [BS]_{(ads)} \overset{k_2}{\rightarrow} A_{(ads)} + P_{(aq)} \tag{7.2}$$

where k_1, k_{-1} and k_2 are rate constants.

The electrode potential scans in the following way:

$$E(t) = \begin{cases} E(t_0) - \nu t & where \quad t < \dfrac{t_{sim}}{2} \\ E\left(\dfrac{t_{sim}}{2}\right) + \nu\left(t - \dfrac{t_{sim}}{2}\right) & where \quad t \geq \dfrac{t_{sim}}{2} \end{cases} \tag{7.3}$$

where $E(t)$ is the potential applied at t time point, $E(t_0)$ is the initial potential, t_{sim} is the total simulation time, and ν is the potential scan rate. t_{sim} is chosen to correspond to that of a full, single cyclic voltammogram with a forward sweep and a reverse one.

The velocity of the electro-catalysis, υ_C, is:

$$\upsilon_C = D_S \frac{\partial c_S}{\partial x}\Big|_{x=0} = -D_P \frac{\partial c_P}{\partial x}\Big|_{x=0} = k_2 \Gamma_{BS} \tag{7.4}$$

where D_S, D_P, c_S and c_P are the diffusion coefficients and concentrations for species S and P, respectively, x is the coordinate normal to the electrode surface ($x = 0$), and Γ_{BS} is the surface coverage of species BS.

By applying the steady-state approximation to BS, $\frac{\partial \Gamma_{BS}}{\partial t} = 0$, we obtain:

$$k_1 \Gamma_B c_S|_{x=0} = (k_{-1} + k_2)\Gamma_{BS} \tag{7.5}$$

which leads to:

$$\Gamma_{BS} = \frac{k_1 c_S|_{x=0}}{k_{-1} + k_2}\Gamma_B = \frac{c_S|_{x=0}}{K_m}\Gamma_B \tag{7.6}$$

where K_m is the Michaelis-Menten constant for the catalytic reaction, and $K_m = \frac{k_{-1}+k_2}{k_1}$.

If reaction (7.1) is fully electrochemically reversible, according to the Nernst equation [27], we have:

$$\frac{\Gamma_A}{\Gamma_B} = e^{\theta} \tag{7.7}$$

where $\theta = \frac{F(E(t)-E_f^0)}{\boldsymbol{RT}}$, and E_f^0 is the formal potential of the redox couple A/B. If we combine Eqn (7.6) and Eqn (7.7) with the conservation of surface coverage:

$$\Gamma_A + \Gamma_B + \Gamma_{BS} = \Gamma_{max} \tag{7.8}$$

we can obtain an expression for Γ_B:

$$\Gamma_B = \frac{\Gamma_{max}}{e^{\theta} + 1 + \frac{c_S|_{x=0}}{K_m}} \tag{7.9}$$

Therefore, we have:

$$D_S \frac{\partial c_S}{\partial x}\Big|_{x=0} = -D_P \frac{\partial c_P}{\partial x}\Big|_{x=0} = k_2 \Gamma_{BS} = \frac{k_2 \Gamma_B c_S|_{x=0}}{K_m} = \frac{k_2 \Gamma_{max} c_S|_{x=0}}{(e^{\theta} + 1)K_m + c_S|_{x=0}} \tag{7.10}$$

The diffusion equations for species in the solution phase during the simulations are:

$$\frac{\partial c_S}{\partial t} = D_S \left(\frac{\partial^2 c_S}{\partial x^2}\right); \frac{\partial c_P}{\partial t} = D_P \left(\frac{\partial^2 c_P}{\partial x^2}\right) \tag{7.11}$$

Before the simulation starts ($t = 0$), Γ_A, Γ_B, Γ_{BS}, c_S and c_P are set as following:

$$\begin{aligned} &\text{At } x = 0\text{: } \Gamma_A = \Gamma_{max};\ \Gamma_B = 0;\ \Gamma_{BS} = 0 \\ &\text{For } 0 \le x \le x_m\text{: } c_S = c_S^*;\ c_P = 0 \end{aligned} \tag{7.12}$$

where the maximum simulation space x_m is set according to total simulation time t_{sim}:

$$x_m = 6\sqrt{D t_{sim}} \tag{7.13}$$

where x_m is large enough so that the simulation is not affected by the far end boundary due to the Brownian motion of the solution phase [28, 29].

After the potential is applied ($t > 0$), at the electrode surface ($x = 0$):

$$\Gamma_A = \frac{e^{\theta}\Gamma_{max}}{e^{\theta}+1+\frac{c_S|_{x=0}}{K_m}};\ \Gamma_B = \frac{\Gamma_{max}}{e^{\theta}+1+\frac{c_S|_{x=0}}{K_m}};\ \Gamma_{BS} = \frac{c_S|_{x=0}}{K_M}\frac{\Gamma_{max}}{e^{\theta}+1+\frac{c_S|_{x=0}}{K_m}} \tag{7.14}$$

$$D_S \frac{\partial c_S}{\partial x}\Big|_{x=0} = -D_P \frac{\partial c_P}{\partial x}\Big|_{x=0} = k_2 \Gamma_{BS} = \frac{k_2 \Gamma_{max} c_S|_{x=0}}{(e^{\theta} + 1)K_m + c_S|_{x=0}} \tag{7.15}$$

and in the bulk of the solution phase ($x = x_m$):

$$\frac{\partial c_S}{\partial x}\Big|_{x_m} = \frac{\partial c_P}{\partial x}\Big|_{x_m} = 0 \tag{7.16}$$

Therefore, we can calculate the catalytic current I_C by:

$$I_C = -FA_e J_C = -FA_e D_S \frac{\partial c_S}{\partial x}\Big|_{x=0} = -\frac{FA_e k_2 \Gamma_{max} c_S|_{x=0}}{(e^{\theta} + 1)K_m + c_S|_{x=0}} \tag{7.17}$$

where J_C is the catalytic flux, and A_e is the electrode area. Moreover, the *A*/*B* current I_A can be calculated by:

$$I_A = FA_e J_A = FA_e \frac{\partial \Gamma_A}{\partial t} \tag{7.18}$$

where J_A is the flux for Eqn (7.1). Therefore, we have the total current I_T as:

$$I_T = I_C + I_A = -\frac{FA_e k_2 \Gamma_{max} c_S|_{x=0}}{(e^{\theta}+1)K_m + c_S|_{x=0}} + FA_e \frac{\partial \Gamma_A}{\partial t} \tag{7.19}$$

7.2.1.1 Dimensionless Parameters

Dimensionless parameters are introduced to generalise the output of simulations and to economise on simulation times [29]. In this model, the conversion from dimensional parameters to their dimensionless counterparts are shown in Table 7.1.

Table 7.1: Transformation of dimensional parameters to dimensionless ones in the 'non-porous immobilised-enzyme' model, where ***R*** is the Universal Gas Constant, and ***T*** is the temperature.

Dimensional Parameters	Dimensionless Forms	Conversions
Concentration of species j $c_j/(mM)$	C_j	$C_j = \frac{c_j}{c_S^*}$
Surface coverage of species j $\Gamma_i/(mol\ m^{-2})$	ξ_i	$\xi_i = \frac{\Gamma_i}{\Gamma_{max}}$
Diffusion coefficient of species j $D_j/(m^2\ s^{-1})$	d_j	$d_j = \frac{D_j}{D_S}$
Distance $x/(m)$	X	$X = \frac{x}{x_m}$
Time $t/(s)$	T	$T = \frac{t}{t_{sim}}$
Scan rates $\nu/(V\ s^{-1})$	σ	$\sigma = \frac{Ft_{sim}}{\boldsymbol{RT}}\nu$
Potential $E/(V)$	θ	$\theta = \frac{F}{\boldsymbol{RT}}(E - E^0_{f,A/B})$
BS decomposition rate constant $k_2/(s^{-1})$	K_2	$K_2 = \frac{x_m \Gamma_{max}}{D_S c_S^*} k_2$
Michaelis-Menten Constant $K_m/(mM)$	K_{mm}	$K_{mm} = \frac{K_m}{c_S^*}$
A/B Flux $J_A/(mol\ s^{-1}\ m^{-2})$	j_A	$j_A = \frac{t_{sim}}{\Gamma_{max}} J_A$
Catalytic Flux $J_C/(mol\ s^{-1}\ m^{-2})$	j_C	$j_C = \frac{x_m}{D_S c_S^*} J_C$

The dimensionless diffusion equations are:

$$\frac{\partial C_S}{\partial T} = \frac{d_S}{36}\left(\frac{\partial^2 C_S}{\partial X^2}\right); \frac{\partial C_P}{\partial T} = \frac{d_P}{36}\left(\frac{\partial^2 C_P}{\partial X^2}\right) \tag{7.20}$$

and the dimensionless expressions for the boundary conditions before the simulation starts (T = 0) become:

$$\begin{aligned} &\text{At } X = 0\text{: } \xi_A = 1;\ \xi_B = 0;\ \xi_{BS} = 0 \\ &\text{For } 0 \le X \le 1\text{: } C_S = 1;\ C_P = 0 \end{aligned} \tag{7.21}$$

As the simulation starts (T > 0), at the electrode surface (X = 0):

$$\xi_A = \frac{e^{\theta}}{e^{\theta}+1+\frac{C_S|_{X=0}}{K_{mm}}};\ \xi_B = \frac{1}{e^{\theta}+1+\frac{C_S|_{X=0}}{K_{mm}}};\ \xi_{BS} = \frac{C_S|_{X=0}}{K_{mm}}\frac{1}{e^{\theta}+1+\frac{C_S|_{X=0}}{K_{mm}}} \tag{7.22}$$

$$d_S \left.\frac{\partial C_S}{\partial X}\right|_{X=0} = -d_P \left.\frac{\partial C_P}{\partial X}\right|_{X=0} = \frac{K_2 C_S|_{X=0}}{(e^{\theta}+1)K_{mm} + C_S|_{X=0}} \tag{7.23}$$

and in bulk solution (X = 1):

$$\left.\frac{\partial C_S}{\partial X}\right|_{X=1} = \left.\frac{\partial C_P}{\partial X}\right|_{X=1} = 0 \tag{7.24}$$

We can relate the dimensional catalytic current I_C to the dimensionless flux j_C by:

$$I_C = -\frac{FA_e D_S c_S^*}{x_m} j_C = -\frac{FA_e D_S c_S^*}{x_m}\frac{K_2 C_S|_{X=0}}{(e^{\theta}+1)K_{mm} + C_S|_{X=0}} \tag{7.25}$$

where $j_C = d_S \left.\frac{\partial C_S}{\partial X}\right|_{X=0}$. Similarly, we can relate the dimensional *A*/*B* current I_A to the dimensionless flux j_A by:

$$I_A = \frac{FA_e \Gamma_{max}}{t_{sim}} j_A = \frac{FA_e \Gamma_{max}}{t_{sim}}\frac{\partial \xi_A}{\partial T} \tag{7.26}$$

where $j_A = \frac{\partial \xi_A}{\partial T}$. The dimensional total current I_T is:

$$I_T = I_C + I_A = -\frac{FA_e D_S c_S^*}{x_m}\frac{K_2 C_S|_{X=0}}{(e^{\theta}+1)K_{mm} + C_S|_{X=0}} + \frac{FA_e \Gamma_{max}}{t_{sim}}\frac{\partial \xi_A}{\partial T} \tag{7.27}$$

Eqn (7.27) is interesting. The first term corresponding to I_C indicates the role of the Michaelis constant in controlling the rate of turnover of *S* into *P*. As in conventional Michaelis-Menten kinetics, the constant K_m appears in the denominator of the

expression. However, in contrast to the kinetics describing purely homogeneous enzyme kinetics, the impact of the Michaelis constant is moderated by the factor $(e^{\theta} + 1)$ where the exponential term describes the role of the electrode potential. For very negative potentials the factor tends to unity corresponding to the case where all the immobilised enzyme on the surface is available for binding to the substrate *S*. At less negative potentials the factor is greater than unity so that the product $(e^{\theta} + 1)\ K_m > K_m$ corresponding to an apparent weaker binding of *B* and *A* arising since not all the immobilised enzyme is present on the form *B*. The composite term, $(e^{\theta} + 1)\ K_m$, can be thought of as the *effective Michaelis constant* and explains the potential-dependent apparent K_m values observed as discussed above.

7.2.2 The 'Nanopore' Model

Next we consider the same enzyme-mediated process where the electrode is covered by a layer of nanopores which contain solution and where the reaction of *S* takes place on the conductive walls of the pores via the reactions Eqn (7.1) and Eqn (7.2). Again, the applied potential follows Eqn (7.3), and, before the reactions start, the initial surface coverages and concentrations follow Eqn (7.12).

Consider a single pore of volume *V* and internal surface area A_S. We assume the electrolysis within the nanopore is "thin layer" [27, 30, 31]:

$$\sqrt[3]{V} \ll \sqrt{D\frac{\boldsymbol{RT}}{F\nu}} \tag{7.28}$$

where ν is the scan rate (*V/s*). c_S is assumed to be uniform within the cell throughout the voltammetry. Note that for a sweep rate of 0.1 *V/s* and $D = 10^{-5}\ cm^2/s$, we have $\sqrt{D\frac{\boldsymbol{RT}}{F\nu}}$ at about 16 μm which is much greater than the radius of typical "nano" pores.

We therefore have:

$$\frac{\partial c_S|_{x=0}}{\partial t} = -\frac{\partial c_P|_{x=0}}{\partial t} = -k_2\Gamma_{BS}\cdot\frac{A_S}{V} = -\frac{\frac{k_2 A_S \Gamma_{max}}{V}\cdot c_S|_{x=0}}{(e^{\theta}+1)K_m + c_S|_{x=0}} \tag{7.29}$$

Similarly, the total current in this model can be calculated by:

$$I_{PT} = I_{PC} + I_{PA} \tag{7.30}$$

where:

$$I_{PC} = FN_tVJ_{PC} = FN_tV\frac{\partial c_S|_{x=0}}{\partial t} \tag{7.31}$$

$$I_{PA} = FN_tA_SJ_{PA} = FN_tA_S\frac{\partial \Gamma_A}{\partial t} \tag{7.32}$$

where Γ_A can be calculated by Eqn (7.14), N_t is the total number of nanopores in the nanoporous layer, J_{PC} and J_{PA} are the catalytic flux and *A*/*B* reaction flux, respectively. Please refer to Section 7.2.5 for the calculations of N_t, A_S and V. Note again the appearance of the effective Michaelis constant, $(e^{\theta}+1)\,K_m$, in Eqn (7.29).

7.2.2.1 Dimensionless Parameters

Table 7.2: Transformation of dimensional parameters to dimensionless parameters where r_r is the radius of the nanopores. Note that the dimensionless conversions for c_j, Γ_j, D_j, x, E, and K_m are the same as those in Table 7.1 with x_m being replaced by r_r for conversion of x.

Dimensional Parameters	Dimensionless Forms	Conversions
Time $t/(s)$	T	$T = \frac{D_S}{r_r^2}t$
Scan rates $\nu/(V\ s^{-1})$	σ	$\sigma = \frac{r_r^2}{D_S}\frac{F}{\boldsymbol{RT}}\nu$
BS decomposition rate constant $k_2/(s^{-1})$	K_2'	$K_2' = \frac{A_S\Gamma_{max}r_r^2}{Vc_S^*D_S}k_2$
A/B Flux $J_{PA}/(mol\ s^{-1}\ m^{-2})$	j_{PA}	$j_{PA} = \frac{r_r^2}{\Gamma_{max}D_S}J_{PA}$
Catalytic Flux $J_{PC}/(mol\ s^{-1}\ m^{-2})$	j_{PC}	$j_{PC} = \frac{r_r^2}{D_Sc_S^*}J_{PC}$

In this model, the conversion from dimensional parameters to the dimensionless ones are shown in Table 7.2.

Before the simulation starts ($T = 0$), ξ_A, ξ_B, ξ_{BS}, C_S and C_P are set as shown in Eqn (7.21). Note that in this model C_S and C_P are assumed to always be uniform within the nanopores. As the simulation starts ($T = 0$), at the electrode surface ($X = 0$), ξ_A, ξ_B, ξ_{BS} follow Eqn (7.22). C_S and C_P within the nanopores follow:

$$\frac{\partial C_S|_{x=0}}{\partial T} = -\frac{\partial C_P|_{x=0}}{\partial T} = -\frac{K_2' C_S|_{X=0}}{(e^{\theta}+1)K_{mm} + C_S|_{X=0}} \tag{7.33}$$

We can relate the dimensional catalytic current I_{PC} to the dimensionless flux j_{PC} by:

$$I_{PC} = \frac{FN_t V c_S^* r_r^2}{D_S} j_{PC} = -\frac{FN_t V c_S^* r_r^2}{D_S} \frac{K_2' C_S|_{X=0}}{(e^{\theta}+1)K_{mm} + C_S|_{X=0}} \tag{7.34}$$

where $j_{PC} = \frac{\partial C_S|_{X=0}}{\partial T}$. Similarly, we can relate the dimensional *A*/*B* current I_{PA} to the dimensionless flux j_{PA} by:

$$I_{PA} = \frac{FN_t A_S \Gamma_{max} r_r^2}{D_S} j_{PA} = \frac{FN_t A_S \Gamma_{max} r_r^2}{D_S} \frac{\partial \xi_A}{\partial T} \tag{7.35}$$

where $j_{PA} = \frac{\partial \xi_A}{\partial T}$. The dimensional total current I_{PT} is:

$$\begin{aligned} I_{PT} &= I_{PC} + I_{PA} \\ &= -\frac{FN_t V c_S^* r_r^2}{D_S} \frac{K_2' C_S|_{X=0}}{(e^{\theta}+1)K_{mm} + C_S|_{X=0}} + \frac{FN_t A_S \Gamma_{max} r_r^2}{D_S} \frac{\partial \xi_A}{\partial T} \end{aligned} \tag{7.36}$$

7.2.3 Computational Methods

The simulation of the 'non-porous immobilised-enzyme' model was developed in *C++*, and the results were processed via *Python* using the *NumPy* and *matplotlib* libraries. The diffusion equations were solved using matrices resulting from a finite difference formulation together with the Thomas Algorithm [32–34]. Please refer to the textbook [29] for more details.

The simulation of the 'nanopore' model was developed in *Python*, and the simulation results were processed via *Python* using the *NumPy* and *matplotlib* libraries.

Testing and validation [35–37] were performed including studies of error of mass

conservation and convergence, which are shown in later sections.

7.2.4 Simulation Grids

In the 'Non-Porous Immobilised-Enzyme' model and the 'Nanopore' model, all cyclic voltammetry simulations adopt an equally spaced time grid based on an equally spaced potential grid:

$$\begin{cases} T(i) = T(i-1) + dT \quad where \quad i \geq 1; T(f) \leq T_{max} \\ dT = d\theta/\sigma \\ T_{max} = 2\left|\theta_f - \theta_i\right|/\sigma \end{cases} \tag{7.37}$$

where $T(i)$ is the dimensionless time at point i in the simulation time grid as $T(0)$ is the starting time point and $T(f)$ is the end time point of the simulation, dT is the dimensionless time step, T_{max} is the total simulation time, $d\theta$ is the dimensionless potential scan step, σ is the dimensionless potential scan rate, and θ_i and θ_f are the starting and end time points of the simulation.

The 'Non-Porous Immobilised-Enzyme' model features a single-expanding space grid as shown in Figure 7.2:

$$X(i) = X(i-1) + dX \times \omega X^{i-1} \quad where \quad i \geq 1; X(f) \leq X_{max} \tag{7.38}$$

where $X(i)$ is the dimensionless space length at space grid point i as $X(0)$ is the starting point of the simulation space, dX is the dimensionless space step, ωX is the expanding factor of the space step, $X(f)$ is the end point of the simulation space, and X_{max} is the length of the space field. Note that at the last point of the simulation space, $X(f)$ is rounded to X_{max}.



Figure 7.2: Illustration of the simulation space point for the 'Non-Porous Immobilised-Enzyme' model. $X = 0$ represents the point at the electrochemically active electrode surface shown in red, and $X = X_{max}$ represents the outer boundary of the simulation space.

7.2.5 Calculations of parameters for the 'Nanopore' model

In the 'Nanopore' model, the corresponding parameters were selected and calculated based on the experimental parameters in literature [7, 12, 13]. Particularly, the total number of nanopores per square meter of electrode N_t, the internal area of a single pore A_S and the volume of a single pore V were calculated as follows.

In the literature [7, 12, 13], the average radius of a single nanoparticle which forms the nanoporous layer is 25 *nm*, and the average thickness of the nanoporous layer is ~ 2 μm. Therefore, we simplified and assumed the radius of nanopores to be 25 *nm* and the packing of nanopores to be as shown in Figure 7.3 where for a single layer of nanopores on a 1 m^2 electrode surface, the total number of pores N_l is calculated by:

$$N_l = N_c \times N_r \approx \frac{2l_l}{l_p} \times \frac{l_l}{d_p} = \frac{2 \times 1\ m}{2 \times \sqrt{(50\ nm)^2 - (25\ nm)^2}} \times \frac{1\ m}{50\ nm} = 4.62 \times 10^{14} \quad (7.39)$$

where l_l is the side of the electrode surface (1 *m*). Therefore, the total number of nanopores N_t for a 2-μm-thick nanoporous layer is:

$$N_t = N_l \times N_t = N_l \times \frac{l_t}{d_p} = 4.62 \times 10^{14} \times \frac{2\ \mu m}{50\ nm} = 1.85 \times 10^{16} \quad (7.40)$$

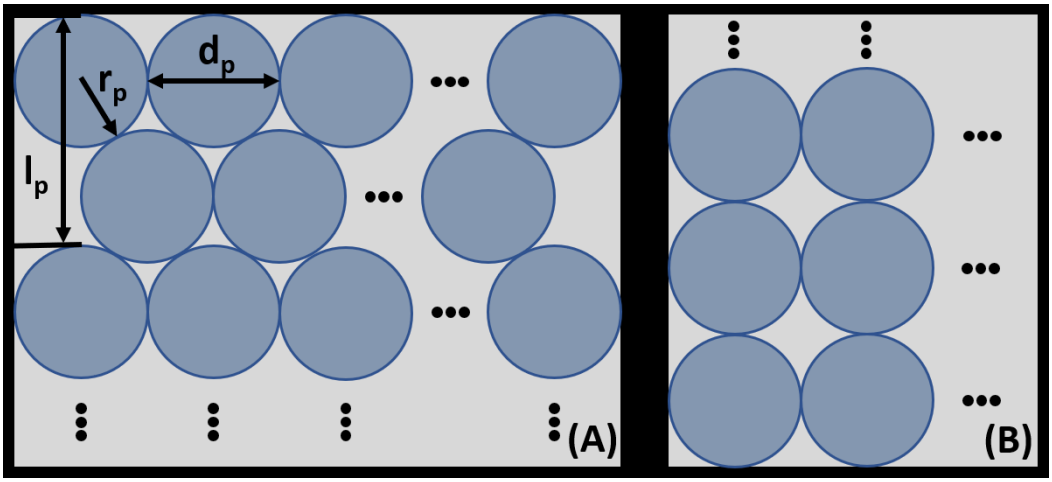


Figure 7.3: The demonstrations of the packing of nanopores in calculations for the number of nanopores: (A) Top view of the nanoporous layers. (B) Side view of the nanoporous layers.

The internal area A_S and volume V for a single pore are:

$$A_S = 4\pi r_p^2 = 4 \times \pi \times (25\ nm)^2 = 7.85 \times 10^{-15}\ m^2 \tag{7.41}$$

$$V = \frac{4}{3}\pi r_p^3 = \frac{4}{3} \times \pi \times (25\ nm)^3 = 6.54 \times 10^{-23}\ m^3 \tag{7.42}$$

7.3 Results and Discussion

This section reports and discusses simulation results for different models in the order in which the respective systems were introduced. First, the rigorous and careful testing and validation are presented first.

7.3.1 Testing Numerical Simulations

To test and validate the models [35-37], the errors of mass conservation for the substrate *S* and convergence studies of the voltammograms were conducted by varying the corresponding simulation parameters as detailed in this section. In both models, the errors of mass conservation E_{MC} for the species *S*, *P* and *BS*, were calculated by:

$$E_{MC} = \frac{M_T - M_S^*}{M_S^*} \times 100\% \quad where \quad M_T = M_S + M_P + M_{BS} \tag{7.43}$$

where M_S* is the total molar amount of species *S* before the simulations start, M_T is the total molar amount of species *S*, *P* and *BS*, M_S, M_P, M_{BS} are the molar amounts for species *S*, *P* and *BS* at the end of the simulation.

In the 'Non-Porous Immobilised-Enzyme' model, for the convergence studies, here we present two examples of which the first one features a forward peak with a diffusion-controlled decaying tail. Therefore, we used the values of peak potentials E_{PP} and peak current densities I_{PC} to test the convergence. For the second example where the voltammogram has a steady-state current, we used the potential where the current reaches half of the value of the steady-state current, also known as the half peak potential $E_{1/2}$, to test the convergence.

One of the potential step $d\theta$, the space step dX, and the space grid expanding factor

ωX in the simulation was varied while other two parameters were kept constant, and appropriate dimensionless parameter sets were obtained for every cyclic voltammogram of this model for K_m = 10 and 0.01 *mM* at k_2 = 1 s^{-1} under the conditions shown in Table 7.5 unless otherwise stated. The obtained parameters sets are shown in Table 7.3, and the errors of mass conservations introduced above and convergence studies are shown in Figures 7.4 to 7.6.

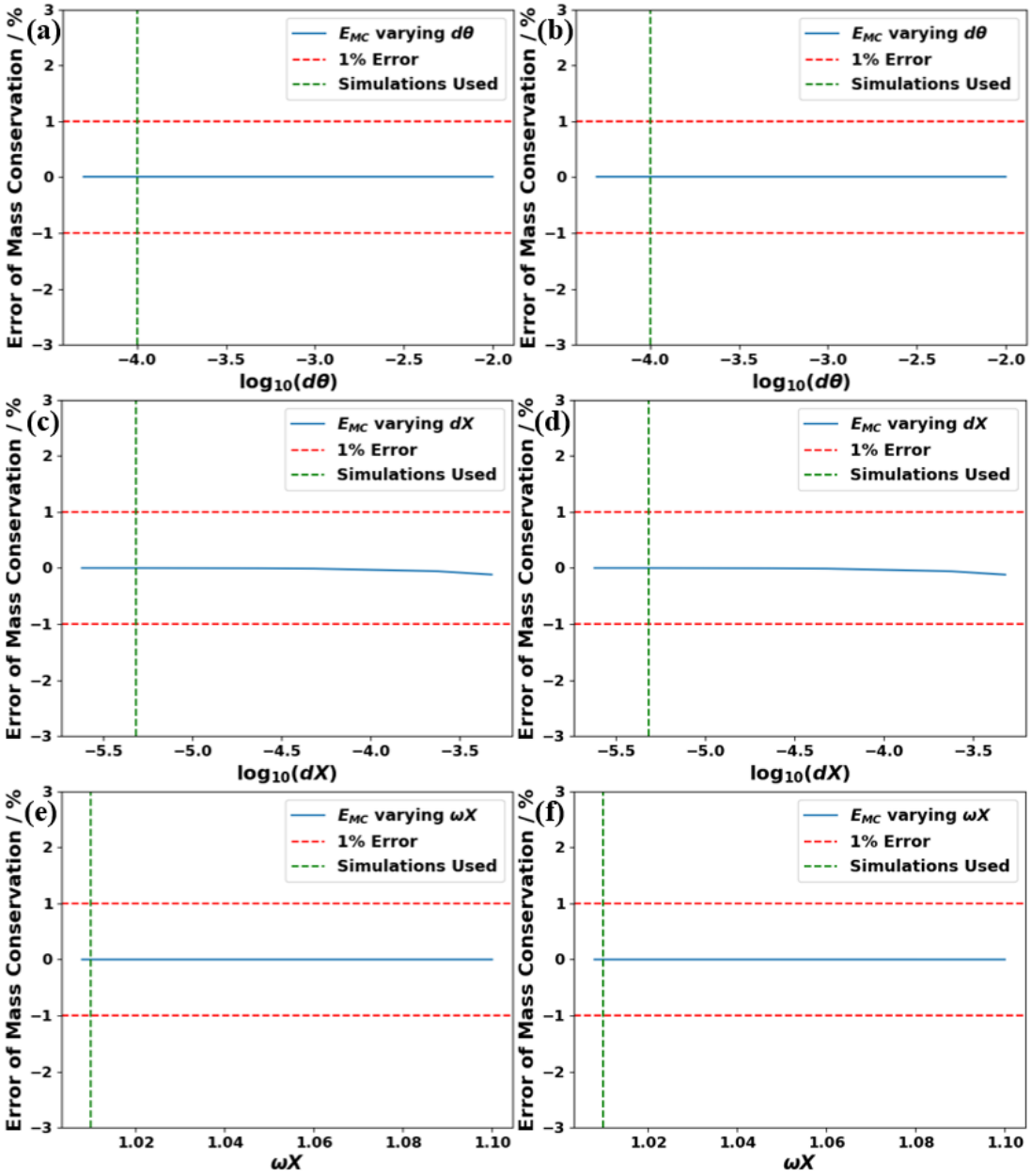


Figure 7.4: Errors of mass conservation calculated for K_m = 10 *mM* (a, c, e) and 0.01 *mM* (b, d, f) at k_2 = 1 s^{-1} for the 'Non-Porous Immobilised-Enzyme' model varying $d\theta$, dX, and ωX.

Table 7.3: Dimensionless parameter sets used for 'Non-Porous Immobilised-Enzyme' model.

Dimensionless Parameters	K_m = 10 mM, k_2 = 1 s^{-1}	K_m = 0.01 mM, k_2 = 1 s^{-1}
Potential Range (θ)	30 to -30	30 to -30
Potential Step ($d\theta$)	10^{-4}	10^{-4}
Space Step (dX)	4.8×10^{-6}	4.8×10^{-6}
Expanding factor (ωX)	1.01	1.01

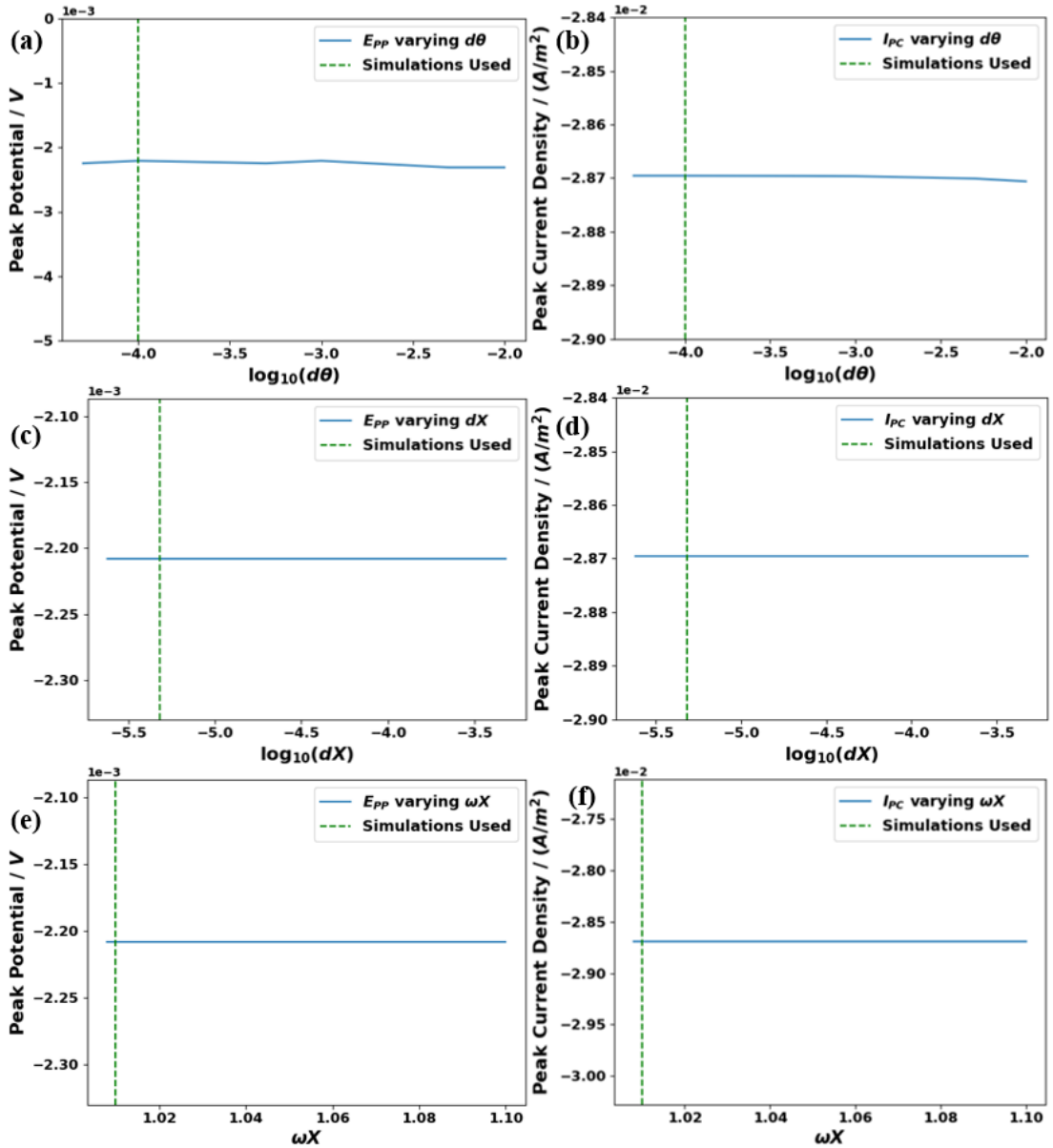


Figure 7.5: Peak potentials E_{pp} (a, c, e) and peak currents I_{PC} (b, d, f) at K_m = 10 mM and k_2 = 1 s^{-1} for the 'Non-Porous Immobilised-Enzyme' model varying $d\theta$, dX, and ωX.

The errors of mass conservation for the species *S*, *P* and *BS* are plotted in Figure 7.4 for K_m = 10 and 0.01 mM at k_2 = 1 s^{-1}. As shown in the plots, the simulations chosen for

these two sets of parameters are kept at a very low level, and if the parameters are decrease the simulation parameters, which gave more accurate results, the errors did not decrease much.

For the convergence studies, the peak potentials, peak currents for K_m = 10 *mM* and the half peak potentials for K_m = 0.01 *mM* all stay at a similar level even if we decrease the simulation parameters ($d\theta$, dX, and ωX) to more accurate levels. Together with the errors of mass conservation presented above, we confirm that these parameter sets are converged. We tested all the voltammograms for this model the same way shown above.

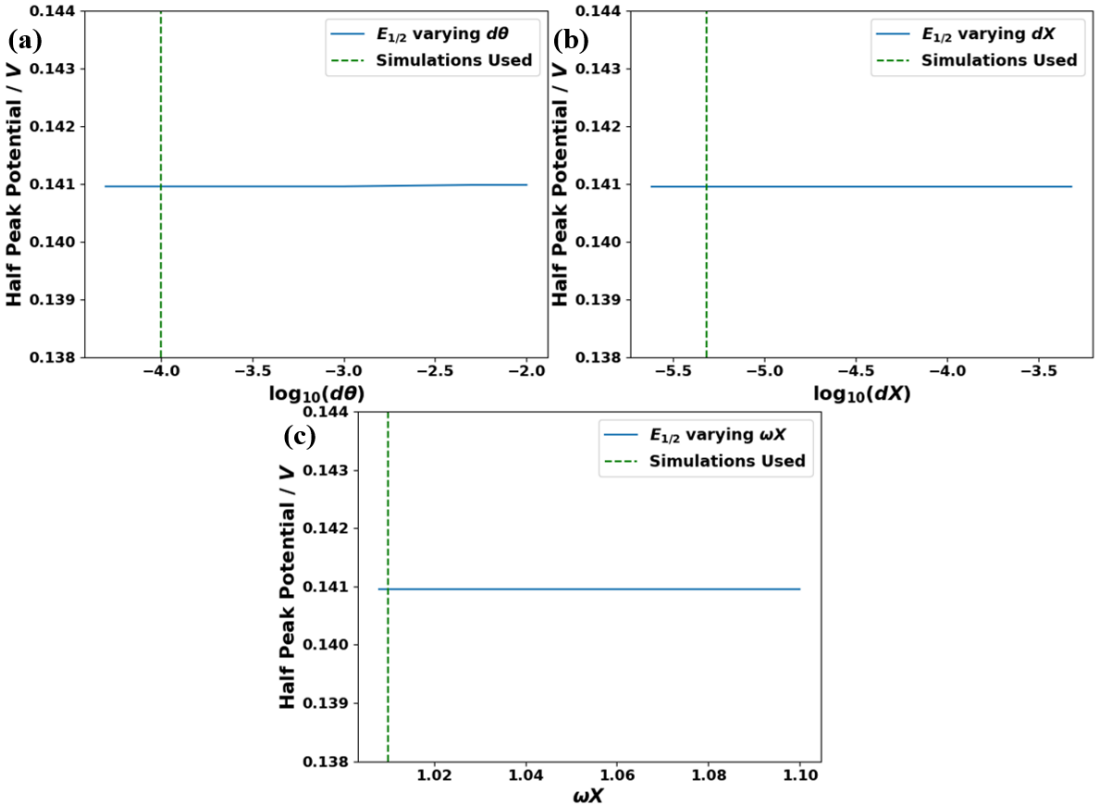


Figure 7.6: Half peak potentials $E_{1/2}$ for voltammograms at K_m = 0.01 *mM* and k_2 = 1 s^{-1} for the 'Nanopore' model varying $d\theta$, dX, and ωX.

For voltammograms in the 'Nanopore' model, we used the peak potentials and peak current of the pre-peak to test the convergence as these parameters are more sensitive than those of the *A*/*B* peak. The potential step $d\theta$ in the simulation was varied to obtain appropriate parameter sets for this model as shown in Table 7.4 under the conditions described in Section 7.3.3 unless otherwise stated. The obtained parameters

sets are shown in Table 7.4, and the errors of mass conservations for the species *S*, *P* and *BS* using Eqn (7.43) and convergence studies are shown in Figures 7.7 for K_m = 0.01 *mM* at k_2 = 1000 s^{-1}.

Table 7.4: Dimensionless parameter sets obtained for the 'Nanopore' model.

Dimensionless Parameters	K_m = 0.01 *mM*, k_2 = 1000 s^{-1}
Potential Range (θ)	30 to -30
Potential Step ($d\theta$)	10^{-4}

As shown in Figure 7.7, the error of mass conservation for the species *S*, *P* and *BS* stays at a very low level for the simulations. Moreover, E_{MC}, E_{PP}, I_{PC} extracted for simulations all do not vary much as we decrease $d\theta$, which indicates that this parameter set is converged. We tested all the voltammograms for this model in this manner.

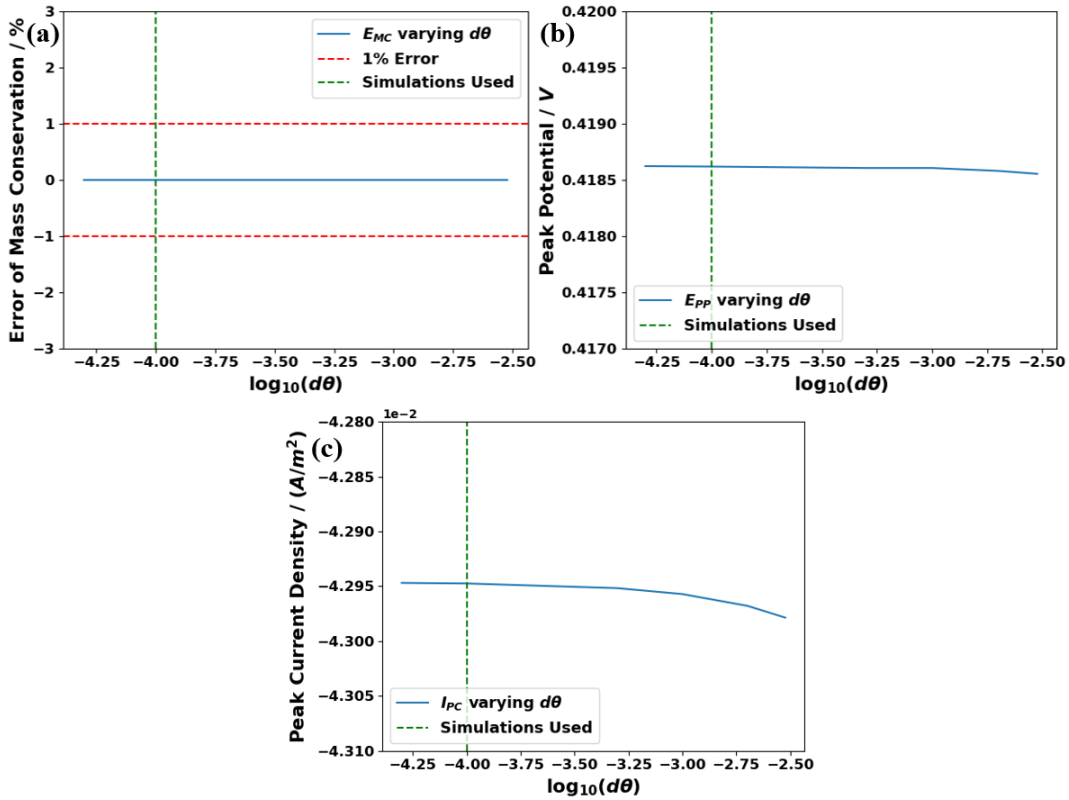


Figure 7.7: (a) Errors of mass conservation, (b) peak potentials E_{pp} and (c) peak current densities I_{PC} at K_m = 0.01 *mM* and k_2 = 1000 s^{-1} for the 'Non-Porous Immobilised-Enzyme' model varying $d\theta$.

Below, we present and interpret the simulation results for the cyclic voltammetric response of both models and then evaluate the possible influence of nano-porosity on

the electrochemistry of enzyme-mediated redox reactions and the implications for practical electrosynthesis.

In discussing the various voltammograms, references are made in the following discussions to several limits familiar from the voltammetry of flat, non-porous electrodes. First, we note that the maximum steady-state current [38] for an electrode modified with *A* arising from the reduction of *S* is:

$$I_{mss} = FA_e k_2 \Gamma_{max} \tag{7.44}$$

Second, the case of the *A*/*B* system immobilised on a flat electrode with no reaction with *S* leads, for the case of reversible electrode kinetics, to a symmetrical 'thin-layer' type cyclic voltammogram for which the forward peak current is [39, 40]:

$$I_{tlc} = \frac{F^2 A_e \nu \Gamma_{max}}{4\boldsymbol{RT}} \tag{7.45}$$

Third, if the enzyme reaction is so efficient that the electrolysis of *S* is under diffusion control, the forward peak current can be calculated from the Randles-Ševčík equation for a fully reversible one-dimensional macroelectrode system [41, 42]:

$$I_{RS} = 0.446FA_e c_S^* \sqrt{\frac{FD\nu}{\boldsymbol{RT}}} \tag{7.46}$$

For a reductive electrochemical reaction, these three cases are shown in Figure 7.8.

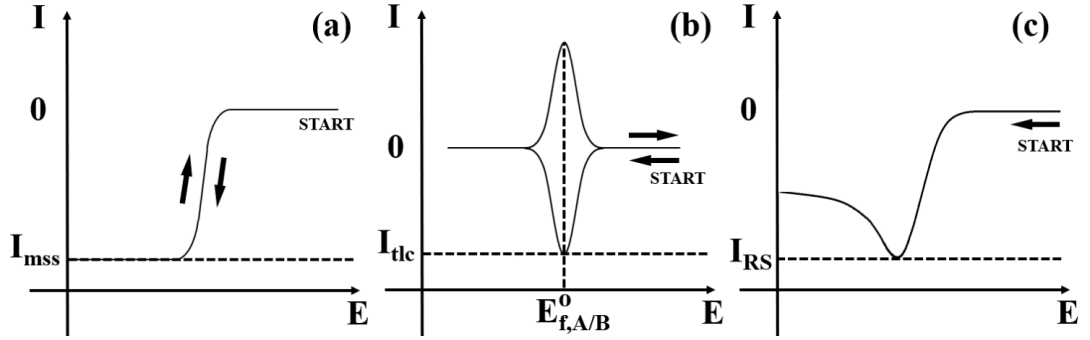


Figure 7.8: Illustration of the currents (a) I_{mss}, (b) I_{tlc} and (c) I_{RS} defined by Eqn (7.44), Eqn (7.45) and Eqn (7.46), respectively and the associated voltammetry. In this figure and figures below, the black arrows indicate the direction of scans of the cyclic voltammograms.

7.3.2 The 'Non-Porous Immobilised-Enzyme' Model

Simulations were carried out varying k_2, K_m, c_S* and v to investigate the nature and trends of the voltammetry of the immobilised-enzyme-mediated electrochemical reaction at a flat and non-porous planar electrode. Initially various simulations were computed for a series of combinations of k_2 and K_m to investigate the trends of the cyclic voltammograms based on the experimental parameters shown in Table 7.5, where c_S*, Γ_{max}, D_S and v were selected based on commonly used experimental conditions [43-45] from which x_m and t_{sim} were calculated. Currents are reported as current densities I_d (A/m^2) to ultimately obtain comparable results between models.

Table 7.5: Dimensional parameters set used in the 'non-porous immobilised-enzyme' model.

Dimensional Parameter	Value
Initial Concentration of *S*, c_S^*	$1\ mM$
Initial Surface Coverage of *A*, Γ_{max}	$10^{-6}\ mol\ m^{-2}$
Diffusion Coefficient of *S*, D_S	$10^{-9}\ m^2\ s^{-1}$
Scan Rate, v	$2.57 \times 10^{-2}\ V\ s^{-1}$
Simulation Distance, x_m	$2.08 \times 10^{-3}\ m$
Simulation Time, t_{sim}	$120\ s$

In general, the current responses were found to approximate to one of four limiting cases, shown in Figure 7.9, which can be understood with reference to the catalytic mechanism, Eqn (7.1) and Eqn (7.2), as follows.

In Case I, the binding of the substrate, *S*, to the active form of the enzyme *B* is negligible, corresponding to the limit where $K_m >> c_S$*, and k_2 is so small that the voltammogram reflects the equilibrium:

$$A_{(ads)} + e^- \rightleftharpoons B_{(ads)} \tag{7.47}$$

The voltammetry resembles that in Figure 7.9, Case I where the charge passed under each of the forward and backward peaks is the same and reflects the total coverage Γ_{max}.

The peak currents are close to I_{tlc} as shown in Eqn (7.45), and the peak potentials correspond to the formal potential of the *A*/*B* couple, $E^o_{f,A/B}$, which is set at zero in the simulations reported below.

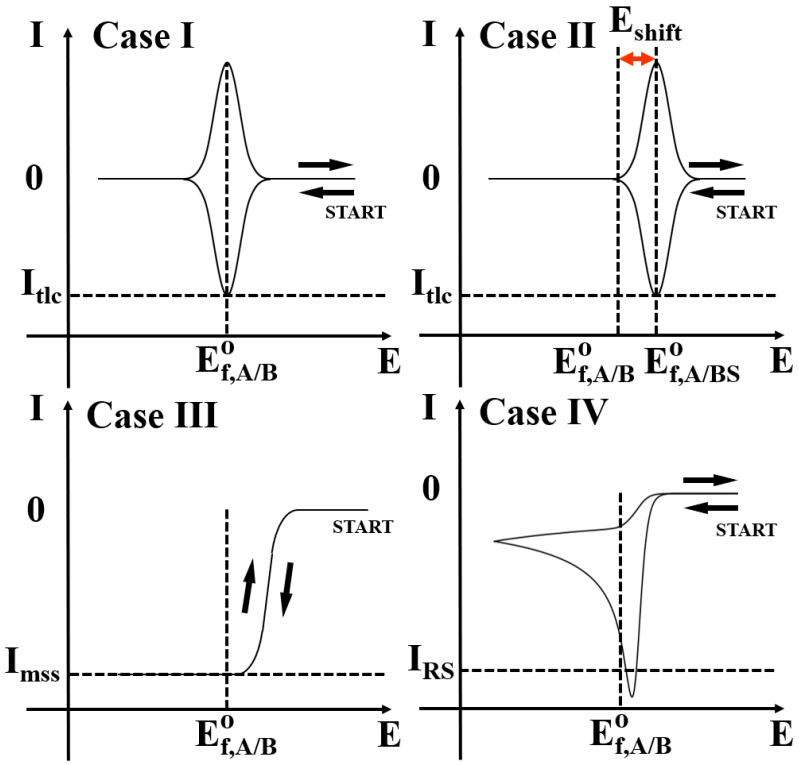


Figure 7.9: Illustrations of four limiting cases under extreme conditions.

In Case II, enzyme *B* binds the substrate *S* strongly, $K_m << c_S^*$, but the rate constant for decomposition of *BS*, k_2, is sufficiently tiny, $k_2 << vF/\boldsymbol{RT}$, that the voltammetry, shown in Figure 7.9, Case II, reflects the equilibria:

$$A_{(ads)} + e^- \rightleftharpoons B_{(ads)} \tag{7.48}$$

$$B_{(ads)} + S_{(aq)} \rightleftharpoons [BS]_{(ads)} \tag{7.49}$$

In this case, the voltammetry is similar to what is seen in Case I, with nearly symmetrical forward and reverse waves but in this limit both peaks are shifted to more positive potentials by an extent reflecting the strength of the binding given by K_m. The shift, E_{shift}, in peak potential E_{peak} which is given by:

$$E_{shift} = E_{peak} - E^o_{f,A/B} \tag{7.50}$$

reflects the formal potential of *A*/*BS* redox couple, $E^o_{f,A/BS}$ relative to that of

$E^o_{f,A/B}$where in the case that $K_m << c_S^*$ corresponding to strong binding of *S* with *B*:

$$E_{peak} = E^o_{f,A/BS} + \frac{RT}{F}\ln c_S^* \tag{7.51}$$

where $E^o_{f,A/BS}$ relates to the half-cell reaction:

$$A_{(ads)} + S(aq) + e^- \rightleftharpoons BS_{(ads)} \tag{7.52}$$

Thus the peak potential, E_{peak}, varies by ~59 mV (2.303$\boldsymbol{RT}/\boldsymbol{F}$) per decade of c_S^* at 25 °C.

In Cases III and IV, $K_m << c_S^*$, and k_2 is larger than in Case II. The voltammetry resembles the full mechanism shown in Eqn (7.1) and Eqn (7.2). In Case III, as shown in Figure 7.9, Case III, but k_2 is not large enough to significantly deplete *S* local to the electrode so that the total mechanism is under kinetic control with the concentration of *S* remaining nearly constant; quantitatively, $k_2\Gamma_{max} << D_S^{0.5}\, c_S^*(vF/\boldsymbol{RT})^{0.5}$. Therefore, the voltammogram shows steady-state behaviour and has a limiting current as shown in Eqn (7.44). The half-wave potential is again shifted anodically relative to $E^o_{f,A/B}$.

In Case IV, k_2 is large enough, where $k_2\,\Gamma_{max} >> D_S^{0.5}\, c_S^*(vF/\boldsymbol{RT})^{0.5}$, so that there is significant depletion of *S* near the electrode, the voltammetry is under diffusion control, and the forward voltammetric scan has a peak as shown in Figure 7.9, Case IV. The forward peak potential is shifted to a more positive potential relative to $E^o_{f,A/B}$ depending on the value of $E^o_{f,A/BS}$ or, equivalently, K_m. Note that there is no backward peak here since the formation of *P* is chemically irreversible. The following sections illustrate the transition between the different cases as various parameters are varied.

7.3.2.1 Varying the rate constant, k_2 and the Michaelis constant, K_m

Illustrative voltammograms are presented in Figures 7.10 and 7.11 in each plot of which one of either k_2 or K_m was fixed while the other was varied. In Figure 7.10a, k_2 was fixed at 1 s^{-1}, and K_m was set at 10^{-2}, 10^{-1}, 10^0 and 10^1 mM with c_S^* fixed at 1 mM. The currents are compared to I_{mss} and I_{tlc}. On the forward scans, all four voltammograms

start from zero current corresponding to potentials which are insufficient to reduce *A* to *B*. As the potentials are swept negative, currents onset at potentials which are progressively less negative as K_m decrease corresponding to enhanced binding with *S* which is set at a concentration of 1 *mM* throughout at the beginning of simulations. Thus, for high values of K_m relative to c_S*, a simple voltammogram corresponding almost to the reversible adsorbed *A*/*B* couple is seen (red line in Figure 7.10a) in terms of the peak potential (corresponding to that of $E^o_{f,A/B}$ set at 0 V in the simulations). This corresponds to the Case I limit. As K_m is decreased, the backward peak is reduced in size due to the absence of enzyme in the reduced form *B* on the reverse sweep and a non-zero steady current develops at negative potentials which increases as K_m decreases ultimately maximising at a current value controlled by k_2 and given by Eqn (7.44) (blue line in Figure 7.10a). This reflects limiting Case III.

In Figure 7.10b, k_2 was fixed at 1000 s^{-1}, and K_m was set at 10^{-2}, 10^{-1}, 10^0 and 10^1 *mM* with c_S* again fixed at 1 mM. The currents were compared to I_{RS} calculated for ν = 25.7 *mV/s*. On the forward scans, all four voltammograms start from zero current where the potentials are not negative enough to reduce *A*. The potentials are then swept negative where *A* starts to be reduced, and currents onset at different potentials with relatively more positive potentials observed for smaller K_m. The substrate *S* close to the electrode is depleted as potentials sweep negative for each voltammogram since the large k_2 enables rapid catalytic reaction of *S* which produces a diffusive forward peak in each plot voltammogram and corresponds to the limiting Case IV. For higher values of K_m relative to c_S*, the peak potential is observed to approach $E^o_{f,A/B}$ (red line in Figure 7.10b) whereas for small values of K_m the peak potential is shifted to more positive potentials due to the stronger binding of *S* (blue line in Figure 7.10b). The forward currents are increased for a smaller K_m and the reach a limiting value at high

overpotential reflecting the value of k_2. The expected value of I_{mss} is 98.5 A/m^2. On the backward scan, there is no peak for any K_m value since conversion to P is irreversible.

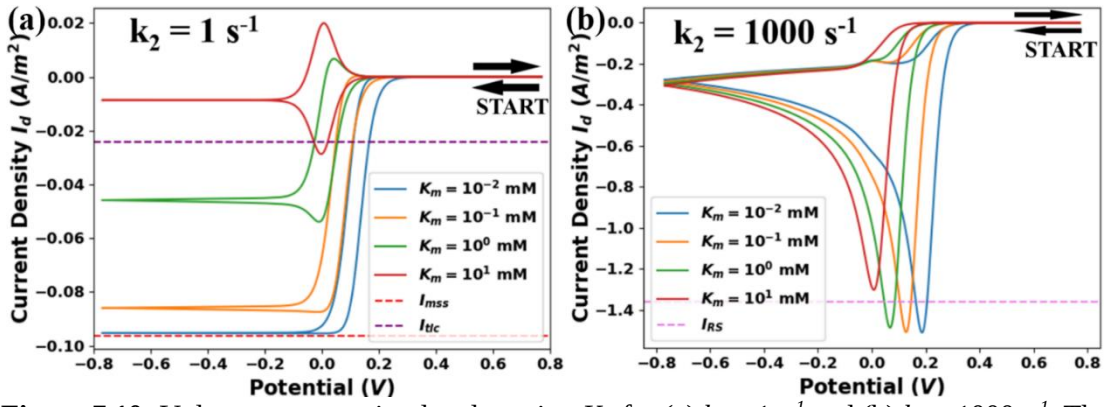


Figure 7.**10:** Voltammograms simulated varying K_m for (a) k_2 = 1 s^{-1} and (b) k_2 = 1000 s^{-1}. The calculated value of I_{mss} is 98.5 A/m^2 in (b).

In Figure 7.11a, K_m was fixed at 10^{-2} *mM*, and k_2 was set at 10^{-1} to 10^{2} s^{-1} with v and c_S* again as given in Table 7.5. The currents were compared to I_{RS} calculated for v = 25.7 *mV/s*, I_{tlc} from Eqn (7.45) and I_{mss} for the pertinent k_2 values of 0.1, 1 and 10 s^{-1}, respectively. On the forward scans, all four currents start at zero current and onset at potentials which are progressively more positive as k_2 increases corresponding to a more favourable catalytic reaction as the potential sweeps negative. For very small k_2 ($k_2 << vF/RT$, the blue line in Figure 7.11a), the voltammogram has almost symmetrical forward and reverse peaks, which are near the size of I_{tlc}, both shifted to more positive potentials than $E^o_{f,A/B}$ corresponding to limiting Case II with a limiting current close to I_{mss} at high overpotentials. As k_2 increases [but subject to $k_2\Gamma_{max} << D_S^{0.5}\, c_S^*(vF/\boldsymbol{RT})^{0.5}$, orange line in Figure 7.11a], as discussed above, the voltammogram corresponds to the limiting Case III and a limiting current is observed at high overpotential. As k_2 increases yet further a diffusive forward peak is formed reflecting the depletion of S close to the electrode. At the same time the forward peak potential shifts to more positive potentials. Thus, the voltammogram tends to the limiting Case IV as k_2 increases, and the forward peak current eventually approaches and slightly exceeds I_{RS} limiting when $k_2\Gamma_{max}$ >>

$D_S^{0.5}\, c_S^*(vF/\boldsymbol{RT})^{0.5}$ (red line in Figure 7.11a). The increase of current over and above that calculated from I_{RS} is characteristic of a so-called $E_{rev}C$ process in which a reversible electrode process is followed by a chemical reaction [27, 43, 44].

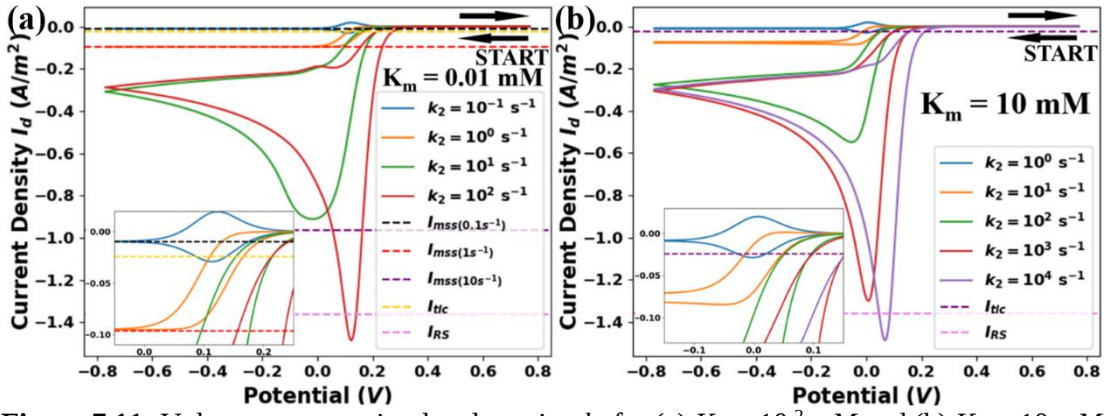


Figure 7.11: Voltammograms simulated varying k_2 for (a) $K_m = 10^{-2}$ *mM* and (b) $K_m = 10$ *mM*. In (a), I_{mss} is plotted for $k_2 = 0.1$ (black dashed), 1 (red dashed) and 10 (purple dashed) s^{-1}, respectively.

In Figure 7.11b, K_m was fixed at 10 *mM*, and k_2 was set at 10^0 to 10^4 s^{-1} with v and c_S^* as given in Table 7.5. The currents were compared to I_{tlc} and I_{RS} with the latter calculated for 25.7 mV/s. On the forward scans, all five currents start at zero current and catalytic currents onset at different potentials corresponding to relatively more negative potentials for smaller k_2 as the potential sweeps negative. For small k_2 ($k_2 << vF/RT$, blue line in Figure 7.11b), as discussed above, the voltammogram corresponds to the limiting Case I. As k_2 increases, the current on the forward scan increases but is markedly less than I_{mss}. The backward peak is reduced in size due to the absence of *B* on the reverse scan since it is in the form of *BS*. A diffusive forward peak is formed as a result of depletion of *S* close to the electrode, which again shifts the forward peak potential more positive. The voltammogram tends to resemble the limiting Case IV as k_2 increases. However, it requires a higher k_2 [$k_2\Gamma_{max} >> D_S^{0.5}\, c_S^*(vF/\boldsymbol{RT})^{0.5}$, purple line in Figure 7.11b], as compared to the case of the smaller K_m in Figure 7.11a, to exceed I_{RS} due to thermodynamically weaker binding of *S* with *B*.

7.3.2.2 Varying the bulk substrate concentration, c_S*

The bulk concentration of substrate *S*, c_S*, has a significant impact on the current responses depending on its magnitude relative to K_m. Illustrative voltammograms are presented in Figures 7.12 and 7.13 in which c_S* was varied while k_2 and K_m were fixed. In Figure 7.12, c_S* was set at 0.1, 1, 10 *mM*, K_m was fixed at 0.1 and 10 *mM* for Figures 7.12a and 7.12b, respectively, and k_2 was fixed at 1 s^{-1}. The currents are compared to I_{mss} and I_{tlc} in both plots. The plots span the full range of behaviour from negligible catalysis (K_m = 10 *mM*, c_S* = 0.1 *mM*, blue curve in Figure 7.12b) corresponding to Case I through to Case III with strong catalysis under kinetic control (K_m = 0.1 *mM*, c_S* = 10*mM*, green curve in Figure 7.12a).

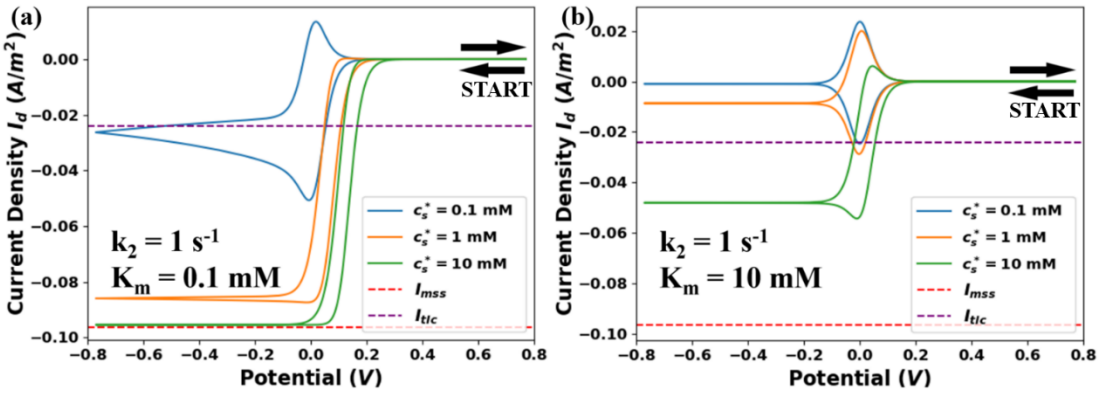


Figure 7.12: Voltammograms simulated at c_S* = 0.1, 1, 10 *mM* for K_m = 0.1 and 10 *mM* at k_2 = 1 s^{-1}.

In Figure 7.13, c_S* was set at 0.1, 1, 10 *mM*, and K_m was fixed at 0.1 and 10 *mM* for Figures 7.13a and 7.13b, respectively, but k_2 was fixed at the higher value 1000 s^{-1} as for the Figures 7.12. The currents are compared to I_{RS} calculated for c_S* = 0.1, 1 and 10 *mM*. In this set of figures, the further transition into Case IV can be followed as a consequence of the increased value of k_2 in comparison with Figure 7.12. Thus, the development of diffusional peaks is evident in both plots in Figures 7.13.

Further insights emerge from Table 7.6, which compares the values of the forward peak currents, I_p, to the corresponding I_{RS} calculated for the pertinent concentration and

gives the ratio of these two quantities as a function of different K_m and c_S* values.

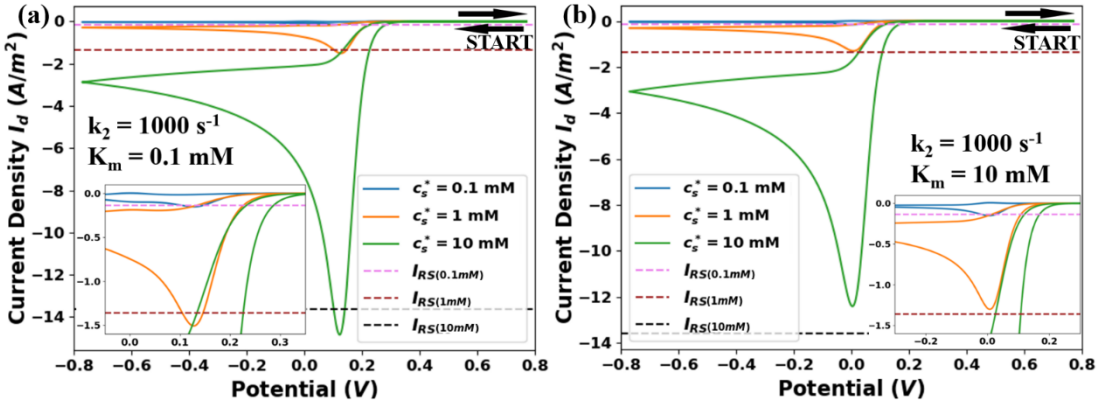


Figure 7.13: Voltammograms simulated at c_S* = 0.1, 1, 10 *mM* for K_m = 0.1 and 10 *mM* at k_2 = 1000 s^{-1}.

Table 7.6: Values of I_p, I_{RS} and their ratios at c_S* = 0.1, 1, 10 *mM* for K_m = 0.1 and 10 *mM* at k_2 = 1000 s^{-1}. The corresponding voltammograms are shown in Figure 7.13.

c_S* / *mM*	I_{RS} / (A/m^2)	K_m = 0.1 *mM*		K_m = 10 *mM*	
		I_p / (A/m^2)	I_p / I_{RS}	I_p / (A/m^2)	I_p / I_{RS}
0.1	-0.136	-0.152	1.114	-0.152	1.115
1	-1.361	-1.508	1.108	-1.301	0.956
10	-13.613	-14.841	1.090	-12.415	0.912

Note that the values of the peak currents are close to those expected for a simple diffusion-controlled process testifying to the diffusional character of the catalysed reaction. The deviation of the ratio from unity reflects two factors. First, as identified above, in the case of a reversible electron transfer process followed by irreversible chemical reaction the peak currents are expected to rise above those predicted by the Randles-Ševčík equation for a simple one electron transfer. Second, the most effective catalysis in terms of a comparison with what is expected for a simple diffusion-controlled electrolysis, is seen for small values of K_m and low values of c_S*, even though the absolute values of the current are higher in the latter case. These factors are best seen in the data for K_m = 10 *mM* where the first factor is evident for c_S* = 0.1 *mM* whilst for c_S* = 10 *mM* the substrate concentration is comparable to the K_m value so that the catalysis is less effective and the ratio of currents drops below unity.

7.3.2.3 Varying the scan rate, *v*

The scan rate of the applied potential in the electrochemical processes also influences the current responses significantly. Illustrative voltammograms are presented in Figures 7.14 and 7.15 in which the scan rate, *v*, was varied while k_2 and K_m were fixed. In Figure 7.14, *v* was set at 2.57, 25.7, 257 *mV/s*, K_m was fixed at 0.01 and 10 *mM* for Figures 7.14a and 7.14b, respectively, and k_2 was fixed at 1 s^{-1}. The currents are compared to I_{mss} and I_{tlc} calculated at corresponding scan rates in both plots. Similar to Figure 7.12, the plots span the full range of behaviour from negligible catalysis to Case III with strong catalysis under kinetic control (K_m = 0.01 *mM*, *v* = 2.57 *mV/s*, blue curve in Figure 7.14a). However note that in Figure 7.14a the negligible catalysis limit (K_m = 0.01 *mM*, *v* = 257 *mV/s*, green curve in Figure 7.14a) corresponds to Case II with shifted peak potentials, but in Figure 7.14b the negligible catalysis limit (K_m = 10 *mM*, *v* = 257 *mV/s*, green curve in Figure 7.14b) corresponds to Case I.

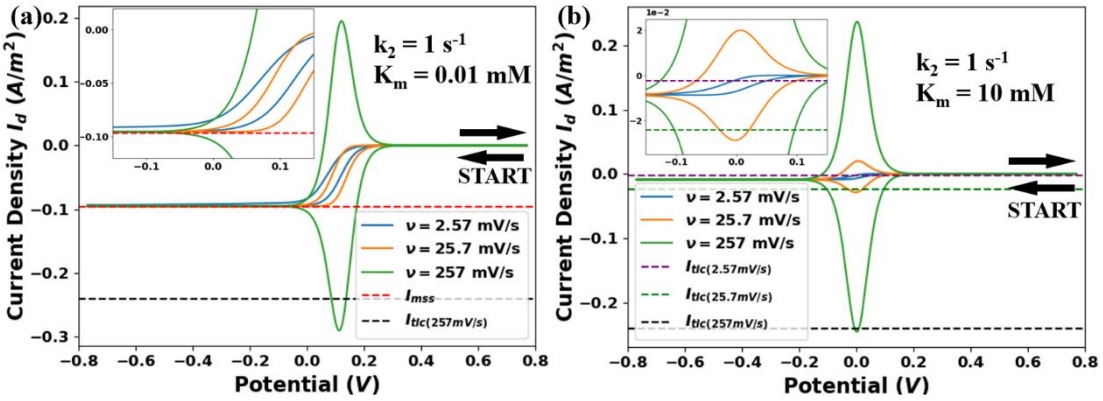


Figure 7.14: Voltammograms simulated at *v* = 2.57, 25.7, 257 *mV/s* for K_m = 0.01 and 10 *mM* at k_2 = 1 s^{-1}.

In Figure 7.15, *v* was set at 2.57, 25.7, 257 *mV/s*, and K_m was fixed at 0.1 and 10 *mM* for Figures 7.15a and 7.15b, respectively, but k_2 was fixed at the higher value 1000 s^{-1} as for the Figures 7.14. The currents are compared to I_{RS} calculated for *v* = 2.57, 25.7, and 257 *mV/s*. In this set of figures the further transition to Case IV is observed due to an increased value of k_2 in comparison with Figure 7.14. Therefore, diffusional peaks

are well developed in both Figures 7.15, especially at higher scan rates.

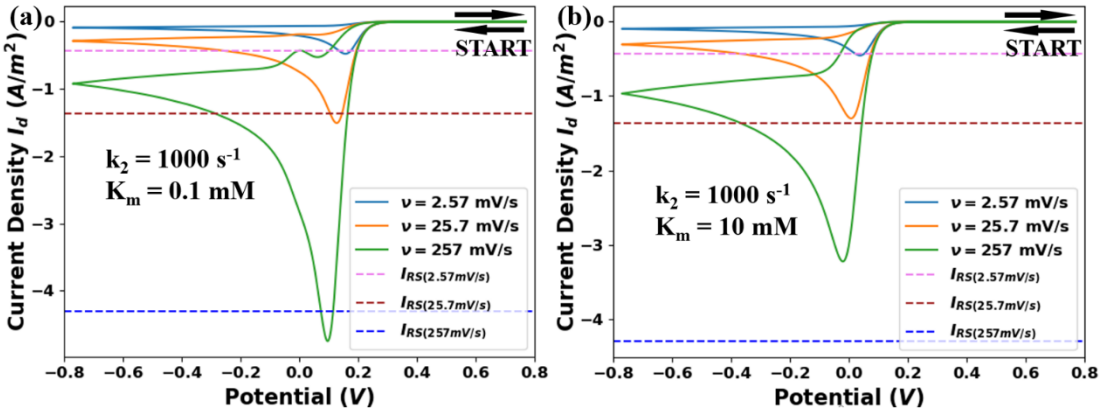


Figure 7.15: Voltammograms simulated at v = 2.57, 25.7, 257 *mV/s* for K_m = 0.1 and 10 *mM* at k_2 = 1000 s^{-1}.

Table 7.7 compares the values of I_p to the corresponding I_{RS} value calculated for the pertinent scan rate and presents the ratio of these two values. Both values increase with scan rate, but the I_{RS} values increases more strongly explaining the decrease in the ratio with scan rate. Further, as discussed above, Case IV mechanism can lead to a forward peak current exceeding the peak current predicted by the Randles-Ševčík equation for a small K_m relative to c_S* whereas, for a large K_m, I_{RS} is lower than I_{RS}. The strongest relative catalysis is seen for the lowest scan rates tabulated although of course these correspond to lower absolute currents.

Table 7.7: Values of I_p, I_{RS} and their ratios at v = 2.57, 25.7, 257 *mV/s* for K_m = 0.1 and 10 *mM* at k_2 = 1000 s^{-1} as shown in Figure 7.15.

v / (*mV/s*)	I_{RS} / (A/m^2)	K_m = 0.1 *mM*		K_m = 10 *mM*	
		I_p / (A/m^2)	I_p / I_{RS}	I_p / (A/m^2)	I_p / I_{RS}
2.57	-0.430	-0.478	1.110	-0.453	1.053
25.7	-1.361	-1.508	1.108	-1.301	0.956
257	-4.305	-4.751	1.104	-3.227	0.750

7.3.3 The 'Nanopore' Model

Calculations were carried out varying k_2, K_m, c_S* and v to investigate the features of the voltammetry for the electrochemical reaction mediated by an enzyme immobilised in a porous layer on the electrode surface using the experimental parameters shown in Table 7.8, where c_S*, Γ_{max}, D_S and v were, unless themselves varied, based on the values in Table 7.5. r_r, N_t, A_S and V were selected and calculated based on literature [7, 12, 13] shown above. Note that the current densities I_d (A/m^2) presented in the figures reported for this model refer to current per square meter of electrode area, ***not*** per square meter of internal area of pores.

Table 7.8: The dimensional parameters set used in the 'nanopore' model based in part in data reported in reference [7, 12, 13].

Dimensional Parameter	Value
Pore Radius, r_r	$25 \times 10^{-9}\ m$
Total Number of Nanopores per Square Meter of Electrode, N_t	$1.85 \times 10^{16}\ m^{-2}$
Internal Area of a Single Pore, A_S	$7.85 \times 10^{-15}\ m^2$
Volume of a Single Pore, V	$6.54 \times 10^{-23}\ m^3$

7.3.3.1 Varying the rate constant, k_2 and the Michaelis constant, K_m

In this section, k_2 and K_m are varied to investigate the shapes and trends of cyclic voltammetry for the 'nanopore' model. We first investigated the voltammograms where the catalytic effect is tiny. Illustrative voltammograms are presented in Figures 7.16a where k_2 was fixed at 10^{-9} s^{-1} while K_m was varied for c_S* = 1 mM.

Figure 7.16a shows voltammograms simulated for K_m = 10^{-3} to 10^{1} mM at k_2 = 10^{-9} s^{-1} and c_S* = 1 mM and with the standard potential for the A/B couple fixed at 0 V. Note the infinitesimally slow rate constant. We observe a clear transition from Case I (purple line in Figure 7.16a) to Case II (blue line in Figure 7.16a) in the voltammograms as K_m decreases. Figure 7.16b, shows that as K_m decreases the peak shifts to progressively

more positive values consistent with the stronger binding of *S* to *B*. Furthermore, for sufficiently small K_m, E_{peak} decreases by an amount ~59 *mV* (2.303***RT***/***F***) per decade of K_m. Conversely, as K_m increases E_{peak} approaches the standard formal potential for the *A*/*B* redox couple.

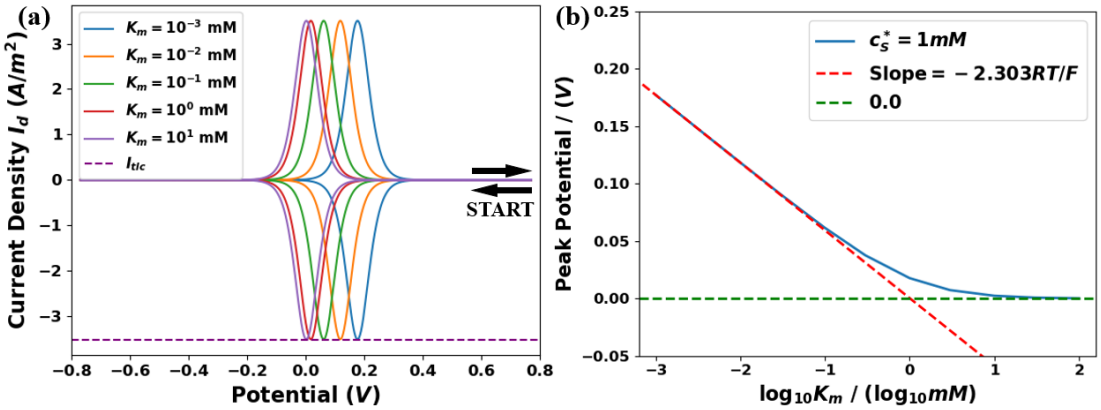


Figure 7.16: Voltammograms (a) and peak potentials (b) simulated for K_m = 10^{-3} to 10^{1} *mM* at k_2 = 10^{-9} s^{-1} and c_S* = 1 *mM*.

Similarly, voltammograms were simulated, as shown in Figures C1-C3 in Appendices, varying K_m for 10^{-3} to 10^{2} *mM* at k_2 = 1, 10^{3} and 10^{5} s^{-1} with c_S* = 1 *mM*. For larger k_2, introducing a stronger catalytic effect, a pre-peak will form in the voltammogram before the *A*/*B* redox peak at 0 *V*. The peak potentials E_{peak} for the pre-peak in the forward scans were extracted and are shown in Figure 7.17. These can be compared with pre-peak potentials for a negligible k_2 = 10^{-9} s^{-1} (Figure 7.16b). Note that for k_2 = 1 s^{-1} shown as the orange line in Figure 7.17, fewer points can be plotted as the pre-peak is merged with the *A*/*B* peak. As shown in Figure 7.17, the pre-peaks shift to more positive potentials due to increased catalytic effects for larger k_2. For k_2 = 1, 10^{3} and 10^{5} s^{-1}, the variations of the peak potentials for the pre-peaks follows the expected slope of ~ -59 *mV* (-2.303***RT***/***F***) per decade of K_m over the range of K_m values studied. Note that for k_2 = 1 and 10^{3} s^{-1}, for sufficiently large K_m, the pre-peak potentials tend to the value expected for a simple *A*/*B* peaks as the binding becomes increasingly negligible.

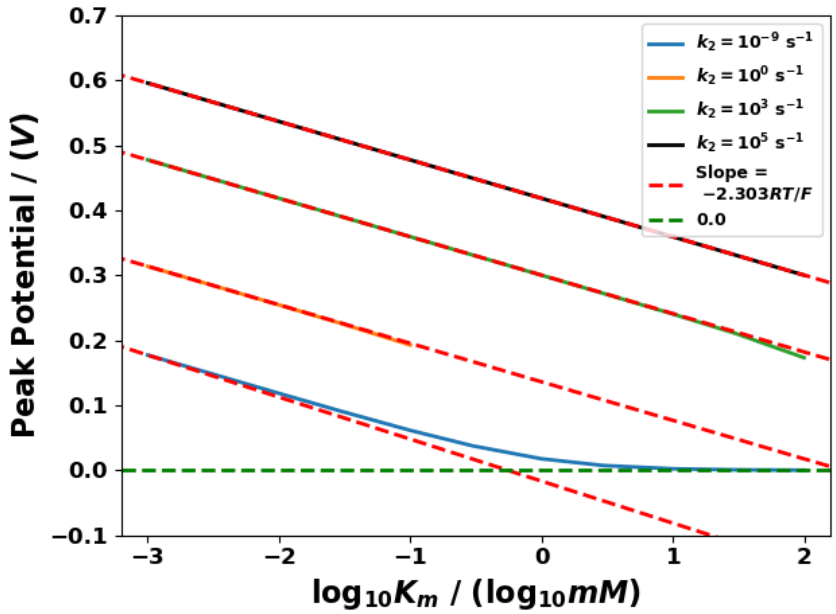


Figure 7.17: Peak potentials for the simulated voltammograms varying K_m at k_2 = 10^{-9}, 1, 10^3 and 10^5 s^{-1} at c_S* = 1 *mM*.

7.3.3.2 Varying the bulk substrate concentration, c_S*

Next, we varied the bulk concentration of substrate *S*, c_S*, at fixed k_2 and K_m to show its impact on the current responses. Figures 7.18a and 7.18b show the voltammetry and the variation of the peak potential for the case where the value of K_m is fixed but the substrate concentration is varied, again in the limit of infinitesimal k_2. The value of $E^o_{f,A/BS}$ is again fixed at 0 *V*. It can be seen that the simulated peak potential E_{peak} shifts to more positive potentials as c_S* increases whereas for smaller c_S*, E_{peak} tends to 0 *V*. In the limit of high c_S*, E_{peak} increases ~59 *mV* (2.303***RT***/***F***) per decade of c_S*.

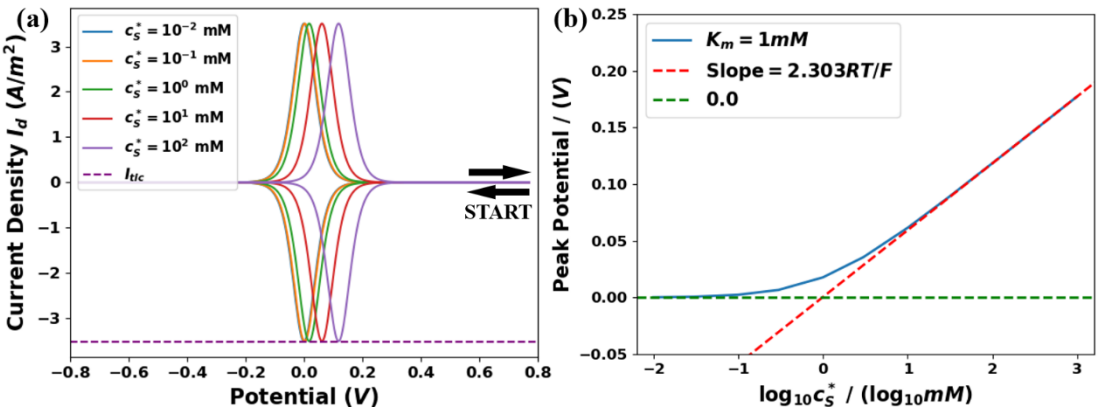


Figure 7.18: Voltammograms (a) and peak potentials (b) simulated for c_S* = 10^{-2} to 10^2 *mM* at k_2 = 10^{-9} s^{-1} and K_m = 1 *mM*.

Particularly interesting voltammetry is observed as k_2 is increased to progressively enhance the catalytic effect, so starting the transition to Case III. Figures 7.19a and 7.19b show the voltammograms simulated varying c_S* for 10^{-2} to 10^2 *mM* at k_2 = 1 and 1000 s^{-1}, respectively, with K_m = 1 *mM*. We see that, compared to Figure 7.18a, a pre-peak to the main *A*/*B* peak is formed as a consequence of the catalytic reaction. For voltammograms in both Figure 7.19a and 7.19b, as c_S* increases, the size of the pre-peak current increases whilst the peak potential E_{peak} for the pre-peak in the forward scans stays near a fixed potential. For Figure 7.19a, the peak potentials are shifted less positively due to the relatively smaller k_2. Therefore, the pre-peak is partially merged with the *A*/*B* peak, especially for a smaller c_S* (blue line in Figure 7.19a) where the peak current for the pre-peak is tiny compared to the *A*/*B* peak. Furthermore, as discussed in the previous section, a peak showing oxidative currents is formed after the pre-peak for a large c_S* (purple line in Figure 7.19a) due to formation of *BS* in the process as shown in Figure C4 in Appendices. The *BS* which survives the voltammetric scan through the pre-peak is re-oxidised to *A* at potentials anodic of the formal potential of the *A*/*B* couple. For Figure 7.19b, for a large k_2, the pre-peaks are shifted to more positive potentials due to the stronger catalytic effect. Such observations hint at the possibility of studying the enzyme complexes *BS* voltammetrically.

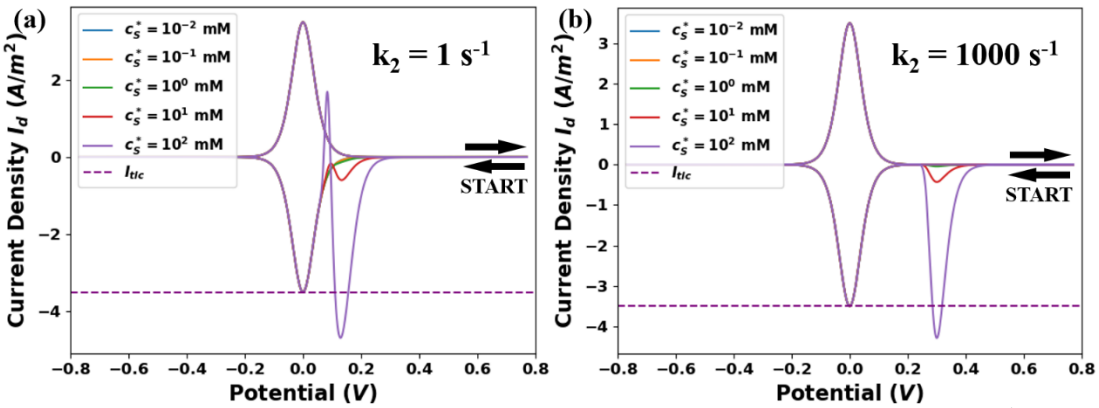


Figure 7.19: Voltammograms simulated for c_S* = 10^{-2} to 10^2 *mM* at k_2 = 1 and 1000 s^{-1} and K_m = 1 *mM*.

7.3.3.3 Varying scan rate *v*

Voltammograms were simulated, as shown in Figure C5-C7 in Appendices, varying *v* for 0.257 *mV/s* to 2.57 *V/s* at k_2 = 1, 10^3 and 10^5 s^{-1} with c_S* = 1 *mM* and K_m = 1 *mM*, and the peak potentials for the pre-peaks were extracted and plotted in Figure 7.20 comparing to the peak potentials for k_2 = 10^{-9} s^{-1} which is at the standard formal potential of *A*/*B* redox couple (0 *V*). For k_2 = 1 s^{-1} shown as the orange line in Figure 7.20, fewer points can be plotted as the pre-peak is merged with the *A*/*B* peak. Similar to Figure 7.17, the peak potentials of the pre-peaks shift to more positive potentials for increased k_2. For k_2 = 1, 10^3 and 10^5 s^{-1}, the varying rates of the peak potentials for the pre-peaks correspond to the expected slope of ~ -59 *mV* (-2.303***RT***/***F***) per decade of *v* over the range of *v* values studied.

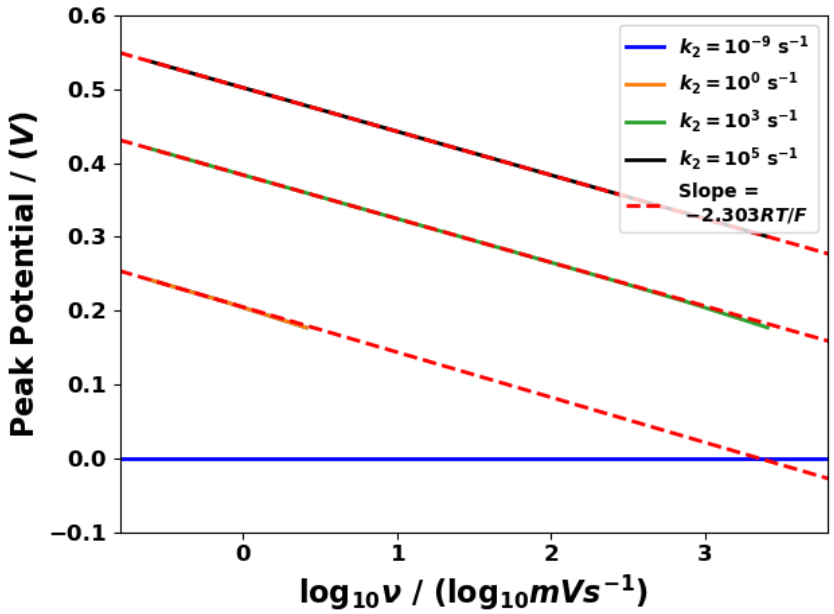


Figure 7.20: Peak potentials for the simulated voltammograms varying *v* at k_2 = 10^{-9}, 1, 10^3 and 10^5 s^{-1} at c_S* = 1 *mM* and K_m = 1 *mM*.

7.3.4 A Comparison of Flat and Nano-Porous Electrodes: Appreciating the Role of Nanoporosity and Optimising Substrate Conversion to Product

In this section. we compare the responses of the flat, non-porous electrode and a nano-porous electrode. In the first case we examine a typical macroelectrode whereas in the latter case we assume, based on the seminal work of Armstrong et al [7, 12, 13], that the porous layer comprises a dense network of pores of radius 25 nm within a 2-micron-thick layer on the electrode surface. We estimate above that the layer comprises ca 1.85×10^{16} such pores per square metre. Note that in the model developed above, the pores are considered isolated and not in diffusional communication with either each other or with the bulk solution. Nevertheless, the pore content is assumed to be solution of the same composition (concentration of *S*) as pertains in the bulk solution considered for the flat electrode. We return to these assumptions below.

In the first instance we compare these responses of the electrodes under conditions in which the enzyme is adsorbed at the same coverage on the surface of the flat macro-electrode and on the surface of each of the 1.85×10^{16} pores per square metre. We then compare the currents flowing through the same geometric area of the electrode surface. Thus, each of the pores contributes its own flux to the current density (A/m^2) of the porous electrode as a whole which is calculated by $I_{PT} = N_t\, A_s\, I_P$ (see Eqn 7.36). where N_t is the total number of pores per square metre, A_s is the internal area of a single pore, and I_P is the current response for a single pore. Note that the coverage chosen for these simulations approximately corresponds to ca monolayer coverage of a surface corresponding to 6.02×10^{13} molecules per square centimetre.

In Figure 7.21 we compare the responses for the values of K_m of either 0.1 *mM* or 10

mM and k_2 of either 1 s^{-1} or 1000 s^{-1} leading to the four possible cases of (Figure 7.21a), K_M = 10 *mM* and k_2 = 1 s^{-1} (weak catalysis) through K_m = 10 *mM* and k_2 = 1000 s^{-1} (Figure 7.21b), K_m = 0.1 *mM* and k_2 = 1 s^{-1} (Figure 7.21c) and K_m = 0.1 *mM* and k_2 = 1000 s^{-1} (Figure 7.21d) corresponding to increasing catalytic activity. Note that pre-peaks which are tiny on the scale of the main voltammograms in each figure are shown as amplified on the insets where the scale difference of a factor of 100 should be noted in Figures 7.21a, 7.21b and 7.21d.

In the four figures the transition from Case I to Case IV can be easily discerned for the planar electrode. A similar behaviour is seen for the pre-peak of the porous electrode. However, the dominant feature of the latter is that the size of the peak associated with *A*/*B* reduction is much greater in size than the pre-peak which involves the consumption of *S*. This in turn arises because for a typical single pore the number of moles on the surface is 7.85×10^{-21} moles of *A* whereas in the volume of the pore there are 6.54×10^{-23} moles of *S*. Thus, the size of the immobilised feature is much greater.

In the second instance we compare the responses of flat electrodes either modified as for Figure 7.21 or with a coverage corresponding to the total enzymes per geometric square metre of a porous electrode. Thus, we consider the case of an electrode with an effective loading of $N_t A_s \Gamma_A$ where Γ_A is the loading used above. Note that this is a hypothetical case since the resulting enzyme loading is multilayer and much greater than monolayer. However we argue that an optimal form of porous electrode will be one in which the pores are in full or at least substantial diffusional communication with the bulk solution and hence the amount of substrate that can be converted to product is that within the diffusion layer of the electrode and not limited to the content of the pores. This offers a substantial enhancement because of the greater extent of the diffusion layer of the accessible surface in comparison with the 2-micron thickness of the porous

layer. A flat electrode under conditions of semi-infinite diffusion has a diffusion layer of the size of tens or hundreds of microns depending on scan rate allowing a significant fraction of the substrate *S* within the layer to be converted into *P*.

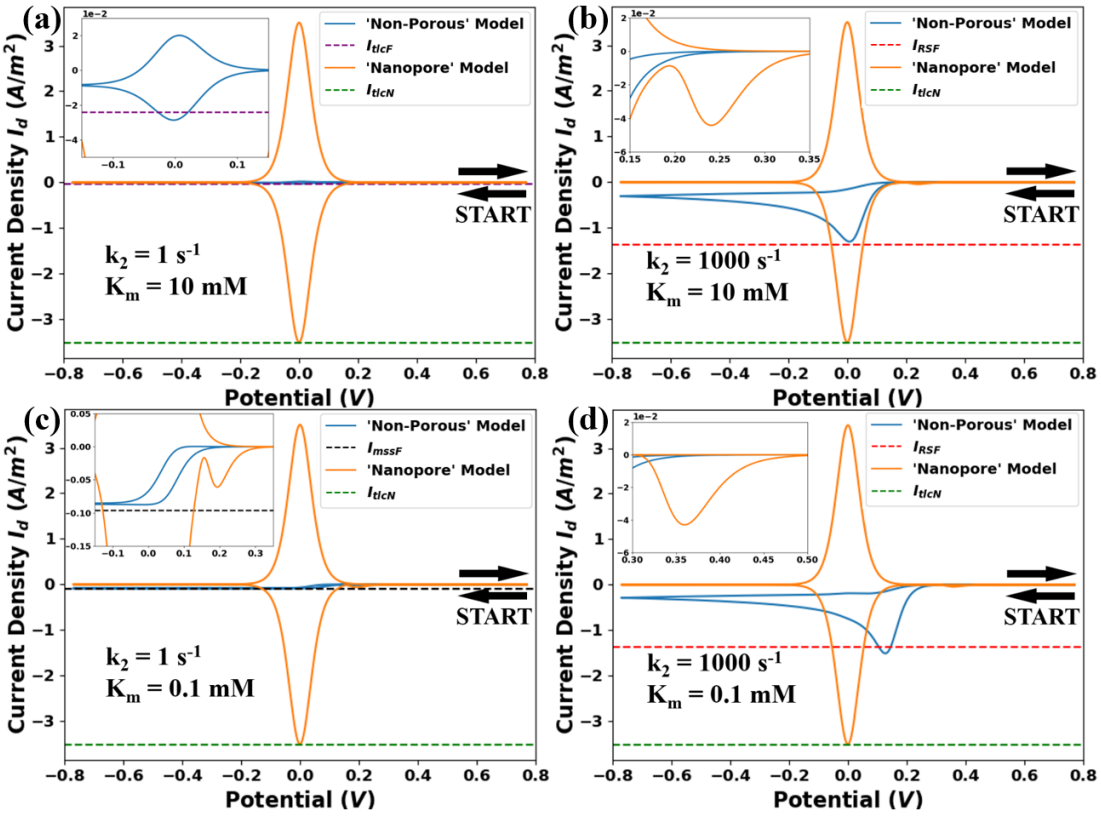


Figure 7.21: Voltammograms simulated for two models of K_m of either 0.1 *mM* or 10 *mM* and k_2 of either 1 s^{-1} or 1000 s^{-1} at c_S* = 1 *mM*, and v = 25.7 *mV/s*. Note that 'Non-Porous' Model is short for the 'Non-Porous Immobilised-Enzyme' model. I_{tlcF} and I_{tlcN} are I_{tlc} calculated for the 'Non-Porous Immobilised-Enzyme' model and the 'Nanopore' Model, respectively. I_{RSF} and I_{mssF} are the Randles-Ševčík Equation and I_{mss} calculated for the 'Non-Porous Immobilised-Enzyme' model. Initial surface coverages for enzyme *A* for both models are set to 10^{-6} mol/m^2.

From a diffusional perspective a fully accessible thin layer of pores can be realistically modelled as a flat electrode with an increased overall average coverage to reflect the total amount of enzyme immobilised over the *geometric* area of the electrode. With this is mind we consider the equations developed above for voltammetric response to identify those conditions under which the use of porosity to create an effective high surface coverage might be useful. Eqn (7.27) in particular shows first that for effective conversion of *S* to *P* (current I_C) it is essential that, in dimensional terms, $K_m << c_S$*

corresponding to the effective binding of S with B to create BS. In the event that the enzyme used has a relatively large K_m value then the deployment of an increased coverage Γ_A can compensate. This is illustrated by Figure 7.22 in which $K_m = 1\ mM$ and $c_S^* = 1\ mM$. and the voltammetric response for the two coverages 10^{-6} and 1.45×10^{-4} mol/m^2 are compared. Figures 7.23a and 7.23b show the two responses dissected into the contributions I_C and I_A. This is important since the signal from the immobilised enzyme electrochemistry (I_A) obscures the response from the substrate conversion (I_C). Importantly for the low coverage the substrate conversion is much below that expected for the diffusional discharge of S as estimated by the Randles-Ševčík equation for the (electrochemically reversible) discharge of S at a flat electrode. In contrast I_C in Figure 7.23b calculated for the porous electrode mimic (that is the flat electrode with a higher coverage), a near diffusional response is seen. This is because although not all the reduced enzyme, B, is in the form BS because of the high value of K_m, increasing the coverage increased the amount of BS present and hence the overall turnover of S to P.

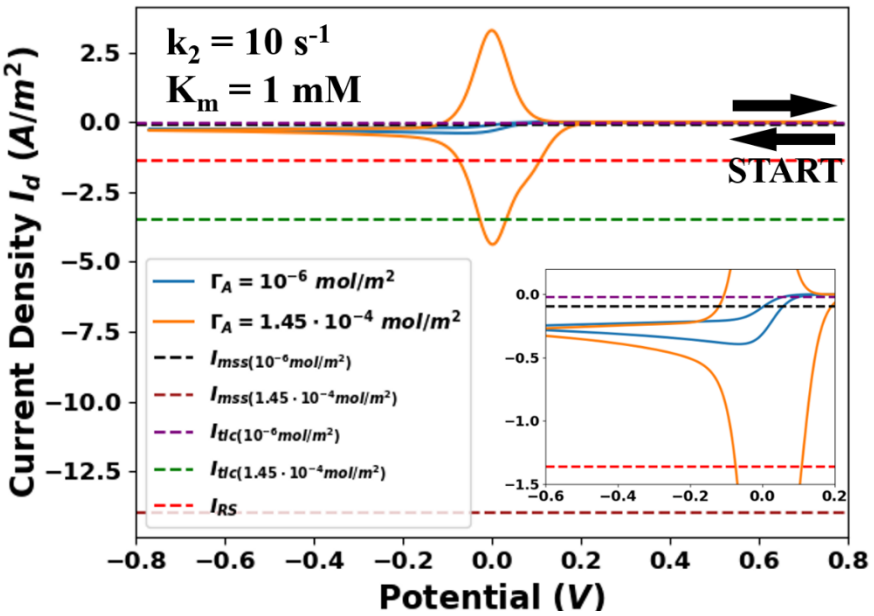


Figure 7.22: Voltammograms simulated for the 'Non-Porous Immobilised-Enzyme' model for $\Gamma_A = 10^{-6}$ and 1.45×10^{-4} mol/m^2 at $k_2 = 10\ s^{-1}$, $K_m = 1\ mM$, $c_S^* = 1\ mM$, and $v = 25.7\ mV/s$.

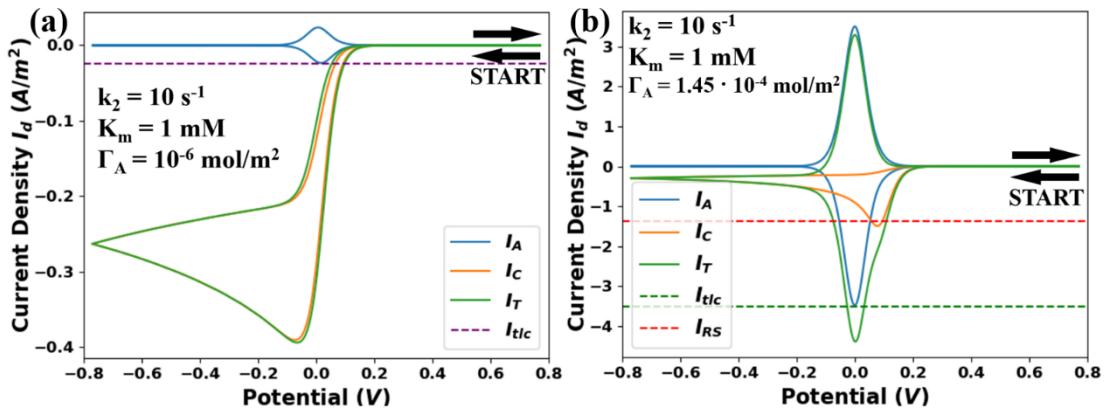


Figure 7.23: Voltammograms simulated including I_C, I_A and I_T from Eqns (7.25) – (7.27) for the 'Non-Porous Immobilised-Enzyme' model for (a) $\Gamma_A = 10^{-6}\ mol/m^2$ and (b) $\Gamma_A = 1.45 \times 10^{-4}\ mol/m^2$ at $k_2 = 10\ s^{-1}$, $K_m = 1\ mM$, $c_S^* = 1\ mM$, and $v = 25.7\ mV/s$. In (b), I_{RS} is calculated to be 1.36 A/m^2.

Second, returning to Eqn (7.23), and assuming the $K_m << c_S^*$, it is evident that if k_2, the rate constant for the decomposition of *BS*, is sluggish then again improved catalysis can be realised via the porous electrode strategy and the creation of an effective very high coverage. This is illustrated in Figure 7.24 where $K_m = 0.1\ mM$ and $c_S^* = 1\ mM$ meeting the first criterion, but it is assumed that $k_2 = 0.3\ s^{-1}$. Again, the responses for the high and low coverages of 10^{-6} and $1.45 \times 10^{-4}\ mol/m^2$ are plotted and decomposed in Figures 7.25a and 7.25b into the components I_A and I_C. It is apparent that I_C reaches the diffusional limit for the discharge of *S* with the high coverage but is substantially less for the lower coverage.

The above comparisons confirm the enormous potential for the use of surface porosity in creating an effective ultrahigh surface loading of enzyme which can offset limitations arising from both the thermodynamic parameters K_m and the kinetic constant k_2. However, in order for the porous layer to be effective we stress the essential need for the porous layer to have diffusional communication with the bulk solution so as to turn usefully large amount of *S* into *P*. Thus, for effective catalysis the nano-porosity needs to create surface roughness as opposed to 'nano-confinement' at least in the

diffusional sense. That said, roughness at the *nano*scale is especially effective in creating the increased area need for enhanced enzyme adsorption.

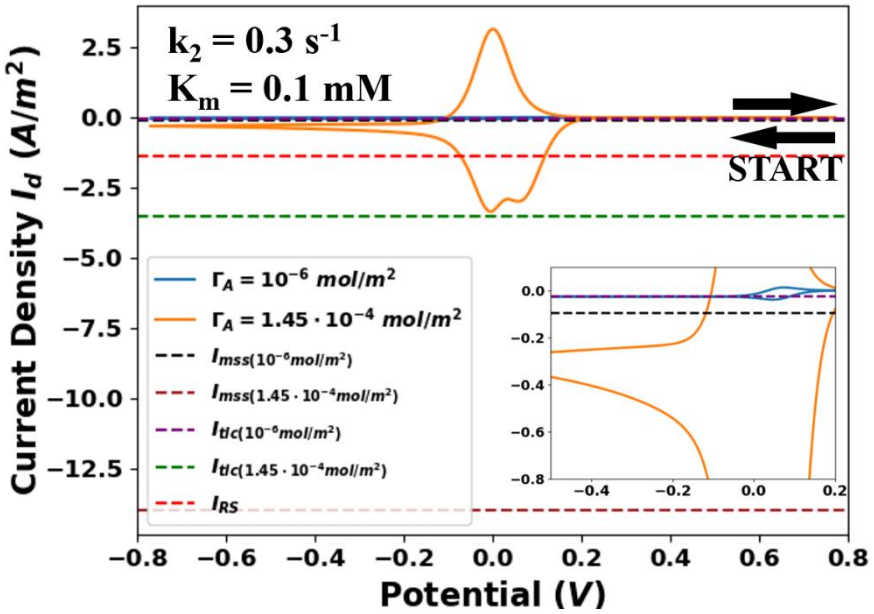


Figure 7.24: Voltammograms simulated for the 'Non-Porous Immobilised-Enzyme' model for $\Gamma_A = 10^{-6}$ and 1.45×10^{-4} mol/m^2 at $k_2 = 0.3\ s^{-1}$, $K_m = 0.1\ mM$, $c_S^* = 1\ mM$, and $v = 25.7\ mV/s$.

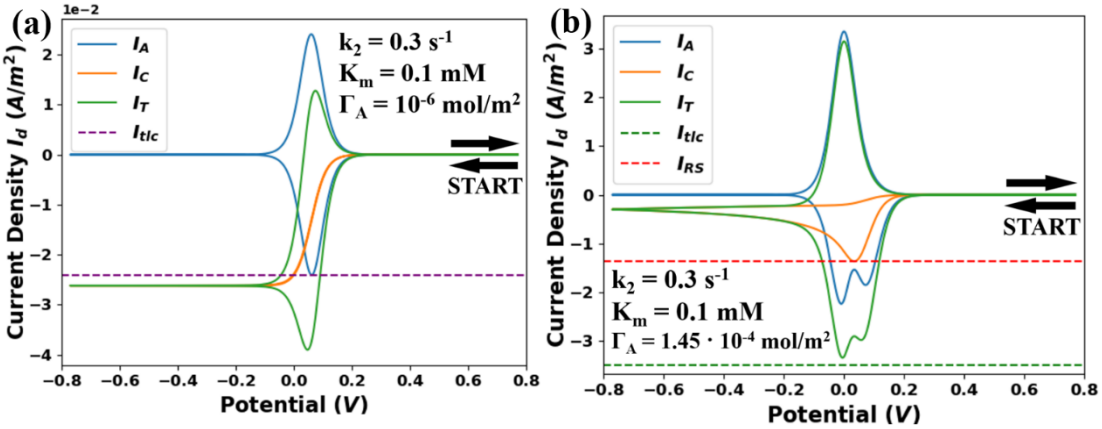


Figure 7.25: Voltammograms simulated including I_C, I_A and I_T from Eqns (7.25) – (7.27) for the 'Non-Porous Immobilised-Enzyme' model for (a) $\Gamma_A = 10^{-6}$ mol/m^2 and (b) $\Gamma_A = 1.45 \times 10^{-4}$ mol/m^2 at $k_2 = 0.3\ s^{-1}$, $K_m = 0.1\ mM$, $c_S^* = 1\ mM$, and $v = 25.7\ mV/s$. In (b), I_{RS} is calculated to be 1.36 A/m^2.

7.4 Conclusions

This work has utilised modelling and simulation tools to predict the cyclic voltammetry with immobilised-enzyme-mediated electrochemical processes on a flat electrode and on a porous electrode. The simulations were based on Fickian diffusion and Michaelis-Menten enzyme kinetics. For the model with flat electrodes, four limiting cases were identified and reflected first feeble binding between the enzyme and the substrate and negligible catalysis (Case I), second strong binding and tiny catalysis (Case II), third strong binding and significant but slow turnover (Case III), and fourth, in Case IV, strong binding and fast formation of the products. The latter case, corresponding to efficient electrochemical enzyme catalysis and leads to marked depletion of the substrate local to the electrode and hence voltammetric signals of a diffusional character which fingerprints the sought high turnover of *S*. The kinetic equations developed explain reported *apparent* potential dependence of the Michaelis constant in controlling the catalytic currents

Comparison of the flat and porous electrodes suggests that the latter best operate when in diffusional communication with the bulk solution and serve to create an effective high surface coverage of enzyme on the electrode surface. The conditions under which this is beneficial shown to be either where the Michaelis constant shows less than strong binding to the substrate or when the rate constant for the decomposition of *BS* is slow.

References

[1] C. Mateo, J.M. Palomo, G. Fernandez-Lorente, J.M. Guisan, R. Fernandez-Lafuente, *Enzyme Microb. Tech.*, 2007, **40**,1451-1463.

[2] R.A. Sheldon, *Adv. Synth. Catal.*, 2007, **349**, 1289-1307.

[3] Y, Zhang, J. Ge, Z. Liu, *ACS Catal.*, 2015, **5**, 4503-4513.

[4] H. Bi, L. Qiao, J. Busnel, B. Liu, H.H. Girault, *J. Proteome Res.*, 2009, **8**, 4685-4692.

[5] Q. Li, X. Tu, J. Ye, Z. Bie, X. Bi, Z. Liu, *Chem. Sci.*, 2014, **5**, 4065-4069.

[6] C.O. Ania, A. Gomis-Berenguer, J. Dentzer, C. Vix-Guterl, *J. Electroanal. Chem.*, 2018, 808, 372-379.

[7] C.F. Megarity, B. Siritanaratkul, R.S. Heath, L. Wan, G. Morello, S.R. FitzPatrick, R.L. Booth, A.J. Sills, A.W. Robertson, J.H. Warner, N.J. Turner, F.A. Armstrong, *Angew. Chem. Int. Ed.*, 2019, **58**, 4948-4952.

[8] C. Wang, Z. Sheng, J. Ouyang, J. Xu, H. Chen, X. Xia, *ChemPhysChem*, 2012, **13**, 762-768.

[9] C. Wang, D. Ye, Y. Wang, T. Lu, X. Xia, *Lab Chip*, 2013, **13**, 1546-1553.

[10] H. Dai, Y. Li, Y. Fu, Y. Li, *Electroanal.*, 2018, **30**, 328-335.

[11] M. Roushan, Z. Azad, S. Movahed, P.D. Ray, G.I. Livshits, S.F. Lim, K.R. Weninger, R. Riehn, *Sci. Rep.*, 2018, **8**, 10036.

[12] C.F. Megarity, B. Siritanaratkul, B. Cheng, G. Morello, L. Wan, A.J. Sills, R.S. Heath, N.J. Turner, F.A. Armstrong, *ChemCatChem*, 2019, **11**, 5662-5670.

[13] L. Wan, R.S. Heath, B. Siritanaratkul, C.F. Megarity, A.J. Sills, M.P. Thompson, N.J. Turner, F.A. Armstrong, *Green Chem.*, 2019, **21**, 4958-4963.

[14] J.D. Gwyer, J. Zhang, J.N. Butt, J. Ulstrup, *Biophys. J.* 2006, **91**, 3897 –3906.

[15] J. Zhang, Q. Chi, A.G. Hansen, P.S. Jensen, P. Salvatore, J. Ulstrup, *FEBS Lett.* 2012, **586**, 526– 535.

[16] J.J. Davis, D. Djuricic, K.K.W. Lo, E.N.K. Wallace, L. Wong and H.A.O. Hill, *Faraday Discuss*., 2000,**116**, 15-22.

[17] I. Willner, M. Lion-Dagan, S. Marx-Tibbon and E. Katz, *J. Am. Chem. Soc.*, 1995, **117**, 6581-6592.

[18] I. Willner and B. Willner, *Bioelectrochem. Bioenerg*., 1997, **42**, 43-57.

[19] M.E.G. Lyons, *Sensors*, 2006, **6**, 1765-1790.

[20] M.E.G. Lyons, *Int. J. Electrochem. Sci.*, 2009, **4**, 77-103.

[21] M.E.G. Lyons, *Int. J. Electrochem. Sci.*, 2009, **4**, 1196-1236.

[22] P.N. Bartlett, K.F.E. Pratt, *Biosens. Bioelectron.*, 1993, **8**, 451-462.

[23] V. Flexer, K.F.E. Pratt, F. Garay, P.N. Bartlett, E.J. Calvo, *J. Electroanal. Chem.*, 2008, **616**, 87-98.

[24] V. Flexer, E.J. Calvo, P.N. Bartlett, *J. Electroanal. Chem.*, 2010, **646**, 24-32.

[25] L. Michaelis, M.L. Menten, *Biochem. Z.*, 1913, **49**, 333-369.

[26] K.A. Johnson, R.S. Goody, *Biochem.*, 2011, **50**, 8264-8269.

[27] R.G. Compton and C.E. Banks, *Understanding Voltammetry* (3nd Edition), London, World Scientific Press, **2018**.

[28] I.B. Svir, A.I. Oleinick, R.G. Compton, *Russ. J. Electrochem.* 2003, **39**, 160–164.

[29] R.G. Compton, E. Laborda, E. Kätelhön, K.R. Ward, *Understanding Voltammetry: Simulation of Electrode Processes* (2nd Edition), World Scientific Press, **2020**.

[30] M.P. Soriaga, A.T. Hubbard, *J. Am. Chem. Soc.*, 1982, **104**, 2742-2747.

[31] I. Streeter, G.G. Wildgoose, L. Shao, R.G. Compton, *Sens. Act. B*, 2008, **113**, 462-466.

[32] D. Peaceman, H. Rachford, Jr., *J. Soc. Ind. Appl. Math.*, 1955, **3**, 28–41.

[33] J. Heinze, *J. Electroanal. Chem. Interf. Electrochem.*, 1981, **124**, 73–86.

[34] J.A. Alden, R.G. Compton, *J. Phys. Chem. B*, 1997, **101**, 8941–8954.

[35] E. Kätelhön, R.G. Compton, *Analyst*, 2015, **140**, 2592–2598.

[36] E. Kätelhön, R.G. Compton, *Analyst*, 2015, **140**, 3290–3290.

[37] E. Kätelhön, R.G. Compton, *Analyst*, 2016, **141**, 1154–1154.

[38] C. Amatore, In *Physical Electrochemistry: Principles, Methods and Applications*; I. Rubinstein, Ed.; Marcel Dekker: New York, **1995**; Chapter 4.

[39] R.S. Tyurin, Y.S. Lyalikov, S.I. Zhdanov, *Russ. Chem. Rev.*, 1972, **41**, 1086-1100.

[40] E. Laviron, *J. Electroanal. Chem.*, 1979, **100**, 263-270.

[41] J. E. B. Randles, *Trans. Faraday Soc.*, 1948, **44**, 327–338.

[42] A. Ševcík, *Collect. Czech. Chem. Commun.*, 1948, **13**, 349–377.

[43] H. Chen, A.K.S. Kumar, H. Le, R.G. Compton, *J. Electroanal. Chem.*, 2020, **876**, 114730.

[44] H. Chen, R.G. Compton, *J. Electroanal. Chem.*, 2021, **880**, 114942.

[45] H. Chen, J. Elliott, H. Le, M. Yang, R.G. Compton, *J. Electroanal. Chem.*, 2020, **869**, 114185.

Appendices

A. Simulation Grids

The expanding time and space grids used in the chapters are introduced in this section.

A.1 Expanding time grids

Expanding time grids were employed in the simulations, usually in chronoamperometric simulations, if needed. An expanding time grid is defined as:

$$T(i) = T(i-1) + dT \times \omega T^{i-1} \quad where \quad i \geq 1; 0 \leq \log_{10} T(i) \leq 6 \qquad \text{(A.1)}$$

where $T(i)$ is the dimensionless simulation time at the time grid point i as $T(0)$ is the starting time point of the simulation, T is the dimensionless time step, and ωT is the expanding factor of the time grid.

A.2 Expanding space grids

Expanding space grids were employed in the simulations, if needed, including a single-expanding space grid:

$$X(i) = X(i-1) + dX \times \omega X^{i-1} \quad where \quad i \geq 1; X(i) \leq X_{max} \qquad \text{(A.2)}$$

and a double-expanding space grid:

$$\begin{cases} X(i) = X(i-1) + dX \times \omega X^{i-1} & where \quad i \geq 1; X(i) \leq \frac{1}{2} X_{max} \\ X(i) = X(i-1) + dX \times \omega X^{n-i} & where \quad \frac{1}{2} X_{max} \leq X(i) \leq X_{max} \end{cases} \qquad \text{(A.3)}$$

where $X(i)$ is the dimensionless space length at the space grid point i as $X(0)$ is the starting space point of the simulation, dX is the dimensionless space step, ωX is the expanding factor of the space grid, and X_{max} is the length of the space field. It is worth noting that at the last point of the whole simulation space, the length is rounded to X_0.

B. Testing and Validating Simulations

All models reported in the thesis were tested through the error of mass conservation and convergence studies before analysing and discussing.

B.1 Errors of mass conservation

The errors of mass conservation E_{MC} are calculated, unless otherwise stated, as:

$$E_{MC} = \frac{\int_0^{T_f} J(T)dT - \Delta M}{\Delta M} \times 100\% \quad where \quad \Delta M = M_f - M_i \qquad \text{(B.1)}$$

where T_f is the total dimensionless simulation time, $J(T)$ is the dimensionless current at the T, M_i is the initial total mass of the analyte within the particle, and M_f is the final total mass of the analyte within the simulated system.

B.2 Convergence studies

As discussed in each chapter, the principles of testing the convergence studies are to fix all the parameters but varying one parameter at a time to make sure the obtained current response does not change much as a parameter is varied to a level, usually smaller, more accurately simulate the desired currents. In chronoamperometry, the steady-state, or quasi-steady-state current is used to observe the changes in current responses, whereas, in cyclic voltammetry, features such as the peak potential or peak current can be used.

C. Supplementary Figures for Chapter 7

In this section, several supplementary figures for corresponding figures in Chapter 7 are provided. Figures C1-C3 illustrate the voltammograms simulated for the 'Nanopore' model varying K_m from 10^{-3} to 10^{2} *mM* at k_2 = 1 (Figure C1), 10^{3} (Figure C2) and 10^{5} (Figure C3) s^{-1} with c_S* = 1 *mM* and v = 25.7 *mV/s*. The potentials for the pre-peaks shown in these voltammograms were extracted and used in Figure 7.17 in Chapter 7.

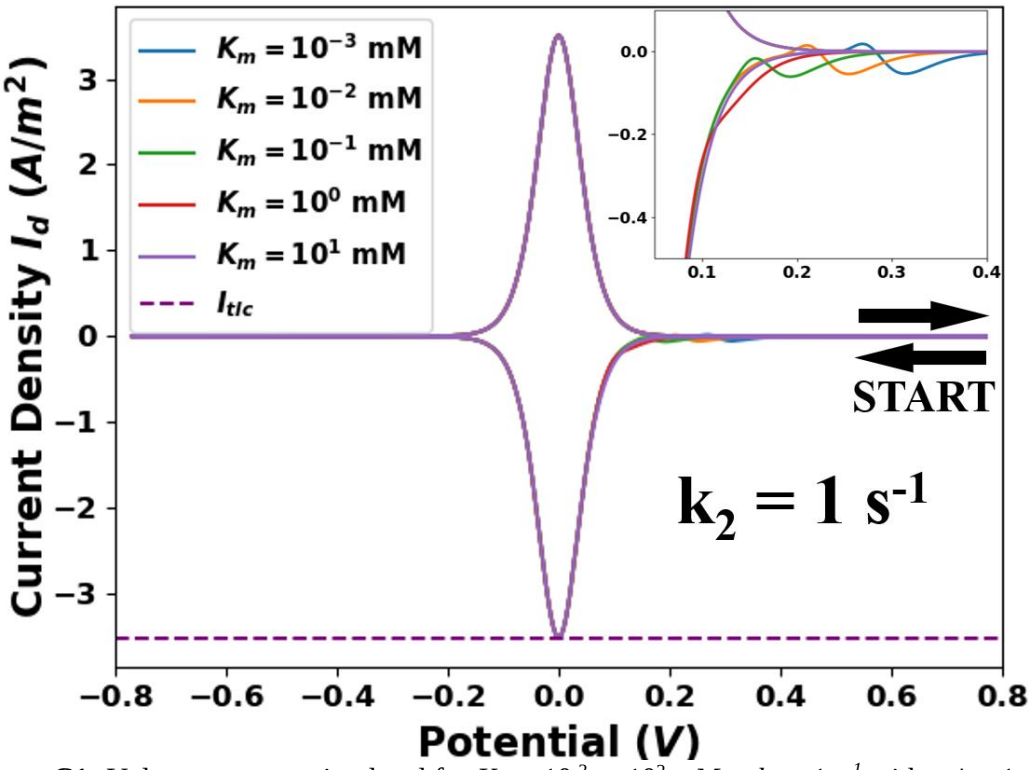


Figure C1: Voltammograms simulated for K_m = 10^{-3} to 10^{2} *mM* at k_2 = 1 s^{-1} with c_S* = 1 *mM* and v = 25.7 *mV/s*.

Figures C4 presents the temporal evolution of surface coverages for species *A*, *B* and *BS* for K_m = 1 *mM*, k_2 = 1 s^{-1}, c_S* = 100 *mM* and v = 25.7 *mV/s*. The expected total surface coverage Γ_T is also plotted in red dashed line. The formation of species *BS* as the simulation proceeds, which introduces the behaviour of species *A* as shown in Figure C4, and therefore leads to the positive current in Figure 7.19 on the forward scan.

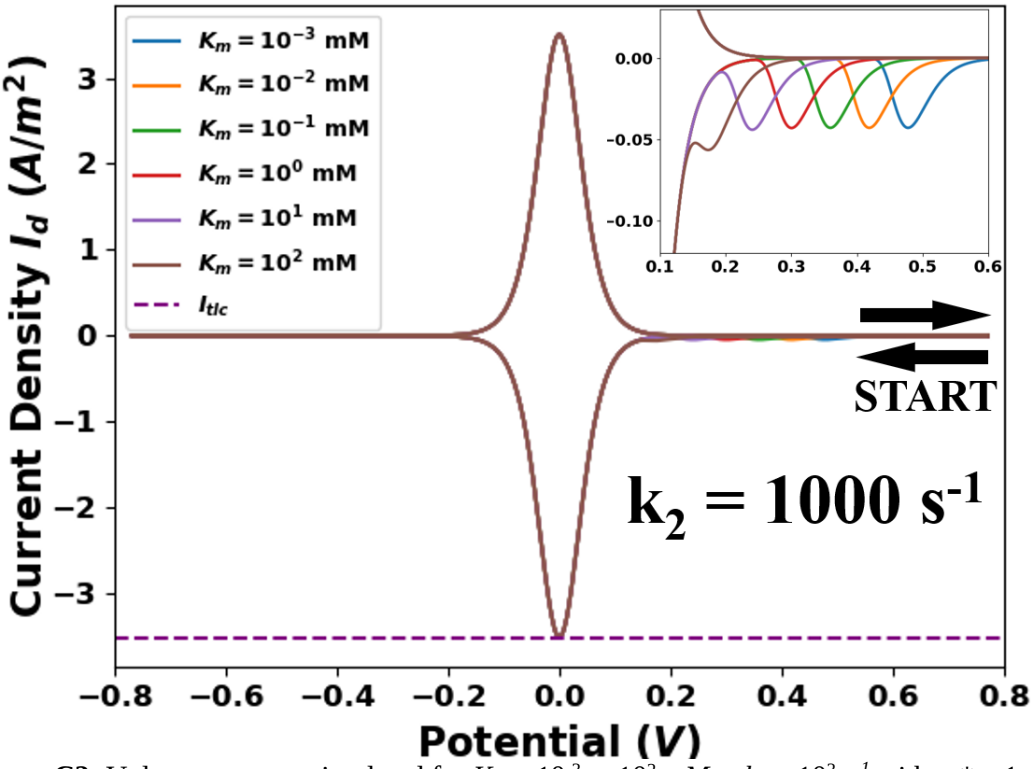


Figure C2: Voltammograms simulated for K_m = 10^{-3} to 10^{2} *mM* at k_2 = 10^{3} s^{-1} with c_S* = 1 *mM* and v = 25.7 *mV/s*.

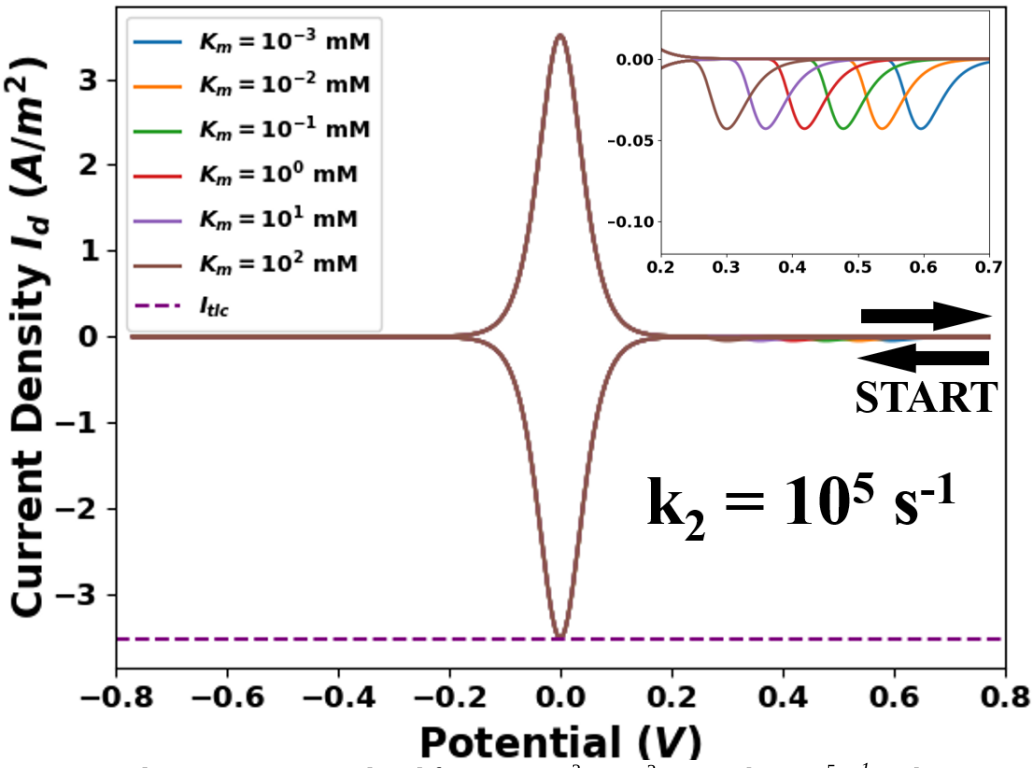


Figure C3: Voltammograms simulated for K_m = 10^{-3} to 10^{2} *mM* at k_2 = 10^{5} s^{-1} with c_S* = 1 *mM* and v = 25.7 *mV/s*.

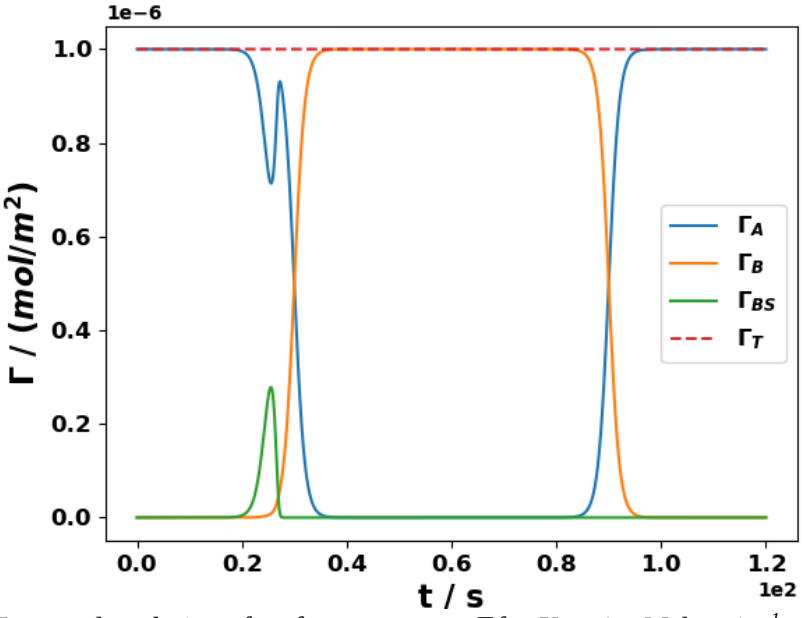


Figure C4: Temporal evolution of surface coverages Γ for K_m = 1 *mM*, k_2 = 1 s^{-1}, c_S* = 100 *mM* and v = 25.7 *mV/s*.

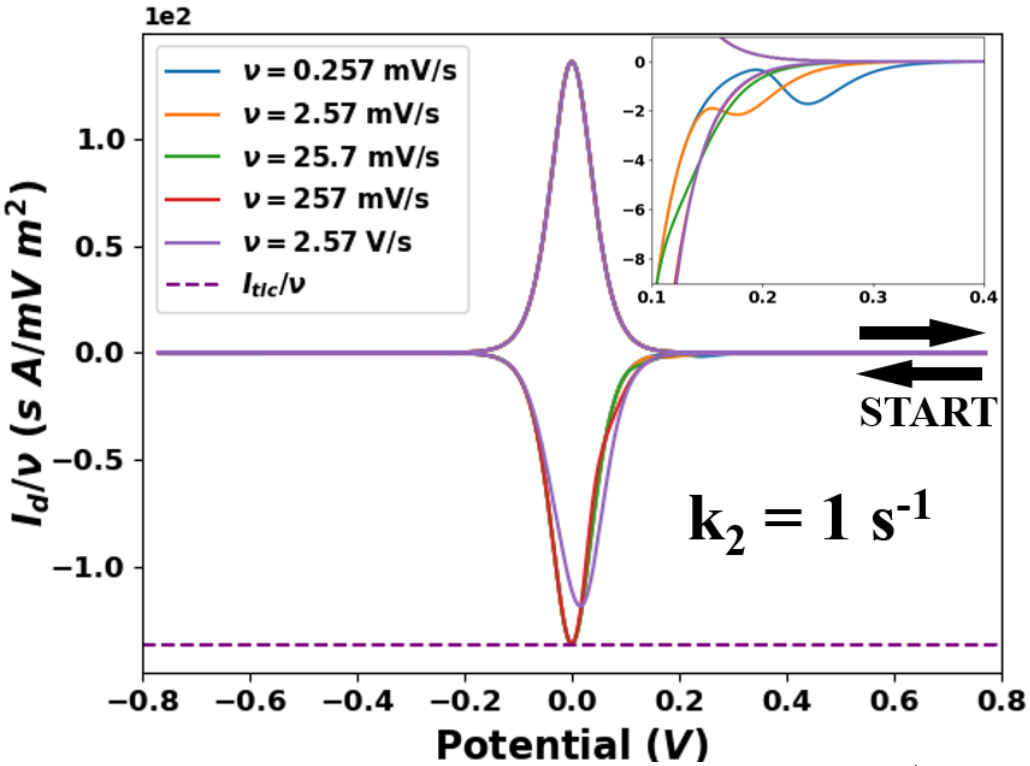


Figure C5: Voltammograms simulated for v = 0.257 *mV/s* to 2.57 *V/s* at k_2 = 1 s^{-1}, c_S* = 1 *mM* and K_m = 1 *mM*.

Figures C5-C7 illustrate the voltammograms simulated for the 'Nanopore' model varying v from 0.257 *mV/s* to 2.57 *V/s* at k_2 = 1 (Figure C5), 10^3 (Figure C6), 10^5 (Figure C7) s^{-1}, c_S* = 1 *mM* and K_m = 1 *mM*. Note in these three figures, the current responses were plotted as I_d/v to enable a more straightforward comparison between currents,

which did not alter the peak potentials extracted for Figure 7.20 in Chapter 7.

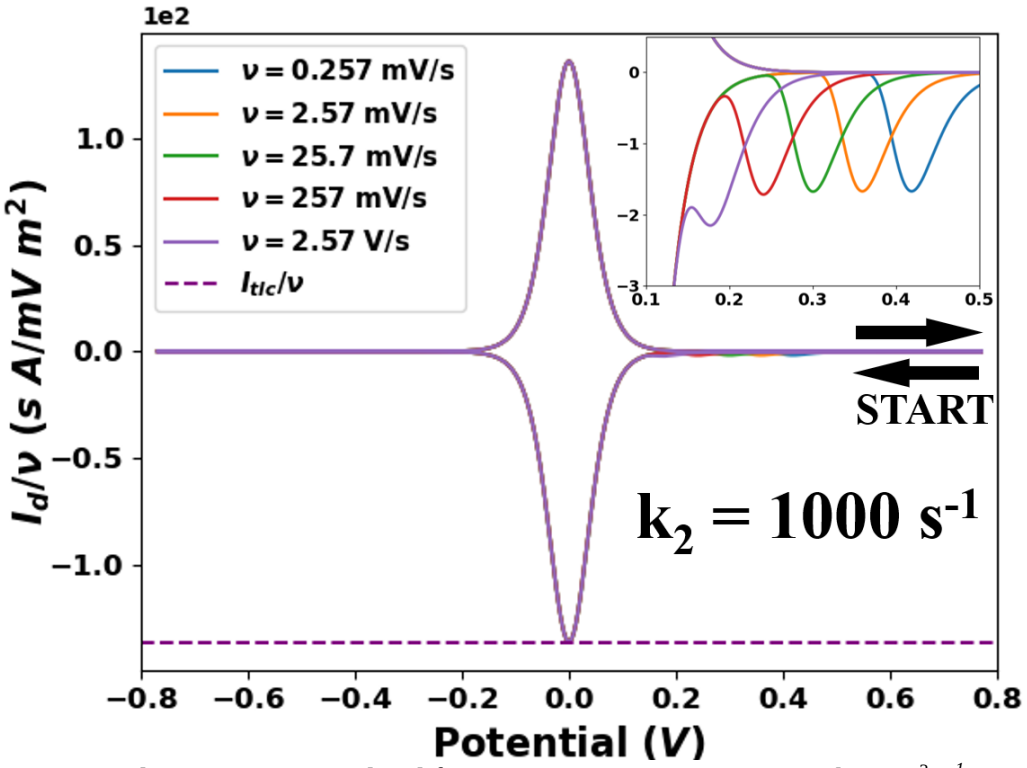


Figure C6: Voltammograms simulated for ν = 0.257 *mV/s* to 2.57 *V/s* at $k_2 = 10^3\ s^{-1}$, $c_S^* = 1$ *mM* and $K_m = 1$ *mM*.

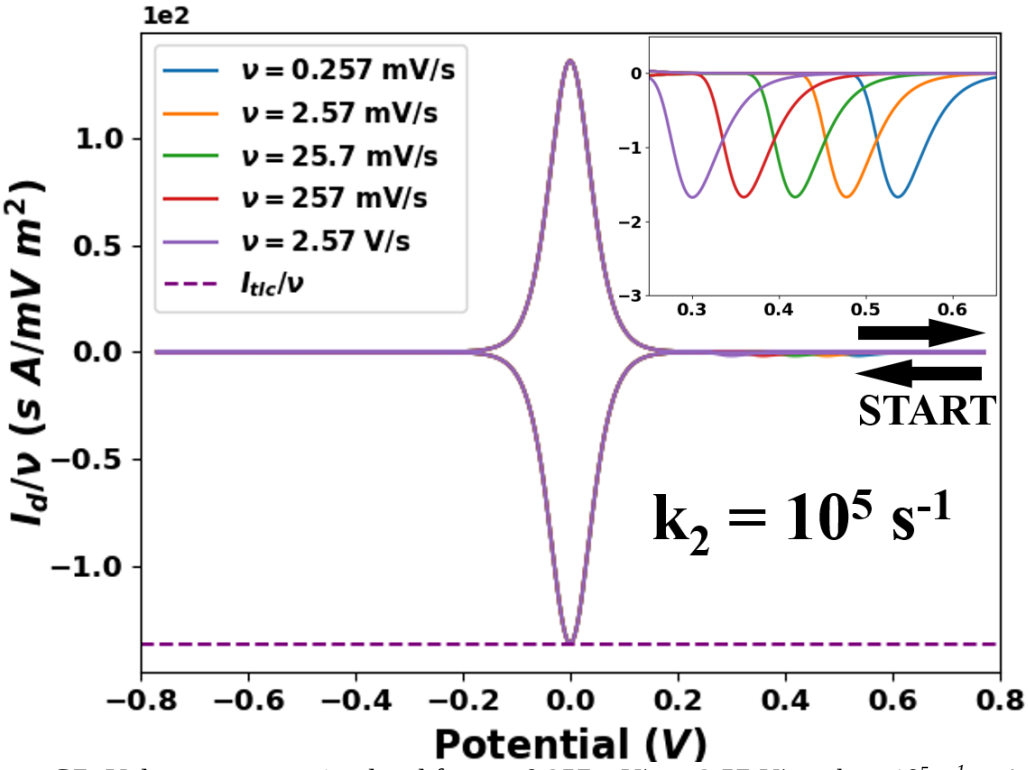


Figure C7: Voltammograms simulated for ν = 0.257 *mV/s* to 2.57 *V/s* at $k_2 = 10^5\ s^{-1}$, $c_S^* = 1$ *mM* and $K_m = 1$ *mM*.